DETERMINING, TREATING, AND PREVENTING MECHANISMS OF SUDDEN DEATH IN EPILEPSY USING MEDICAL IMPLANTABLE DEVICES

by

Daniel J. Pederson

A Dissertation

Submitted to the Faculty of Purdue University

In Partial Fulfillment of the Requirements for the degree of

Doctor of Philosophy

School of Electrical and Computer Engineering

West Lafayette, Indiana

December 2018

THE PURDUE UNIVERSITY GRADUATE SCHOOL
STATEMENT OF COMMITTEE APPROVAL

Dr. Pedro P. Irazoqui, Chair

    Department of Electrical and Computer Engineering

Dr. Edward J. Delp

    Department of Electrical and Computer Engineering

Dr. Michael G. Heinz

    Department of Speech, Language, and Hearing Sciences

Dr. John G. R. Jefferys

    Department of Pharmacology, University of Oxford, Oxford, UK

Approved by:

    Dr. Pedro P. Irazoqui

        Head of the Graduate Program

Dedicated to my extremely supportive and loving wife Christina and to my four amazing daughters, Abigail, Elizabeth, Allison, and Josephine.

To God be the glory

ACKNOWLEDGMENTS

I would like to acknowledge the many people and organizations who have assisted me during my time here at Purdue University.

- My committee members, Dr. Pedro Irazoqui, Dr. John Jefferys, Dr. Edward Delp, and Dr. Michael Heinz.
- Dr. Quan Yuan, Dr. Matthew Ward, and Dr. Edward Bartlett, of the Weldon School of Biomedical Engineering
- Bill Schoenlein, Susan Hardy, Asem Aboelzahab, and Melissa Bible of the Martin Jischke Hall of Biomedical Engineering
- Dr. Thelma Lovick of Bristol University, Bristol, UK
- My friends and lab-mates: Brandon Coventry, Jack Williams, Rebecca Bercich, Chris Quinkert, Henry Mei, Muhammad Arafat, Jesse Somann, Ryan Budde, Ethan Biggs, Rachael Swenson, Steven Lee, Kurt Quing, Zhi Wang, Henry Zhang, Gabriel Albors, Hans Ajieren, Kyle Thackston, Jay Shah, Curtis Slaubaugh, Jui-Wei Tsai, Kelsey Bayer, Kelsey Wasilczuk, Kaitlyn Neihouser, Vivek Ganesh, Gang Seo, Arvin Soepriatna, Shelby Olson, Mark Bevilacqua, Libby Wilger, Adam Scott, Trevor Meyer, Ahoura Mortazavi, and Georgia Lawlor.
- My wife Christina Pederson for her physical, emotional, and spiritual support as well as for her monumental efforts in raising our four daughters during my time here at Purdue.
- My parents Marcus and Joanne Pederson, my in-laws Wade and Jackie Calvin, and my grandparents John and Evelyn Stephens and Jean Pederson for their overwhelming support of my academic aspirations throughout various stages of my life.
- My pastor Bob Bolles and my church Providence Reformed Baptist Church in Fishers, IN.
- The National Science Foundation for funding three years of my research through the Graduate Research Fellowship Program.
- The Purdue Bilsland Dissertation Fellowship for funding the final year of my research.

TABLE OF CONTENTS

LIST OF TABLES

LIST OF FIGURES

LIST OF ACRONYMS

ADC... ....Analog to Digital Converter
AED... ....Antiepileptic Drug
AFE.... ....Analog Frontend
ASIC.. ....Application Specific Integrated Circuit
CBE..Charge Balance Error
CID..Center for Implantable Devices
CMRR ....Common Mode Rejection Ratio
CNAP..Compound Nerve Action Potential
COTS. ....Commercial Off-The-Shelf
CRC... ....Cyclic Redundancy Check
DAC... ....Digital to Analog Converter
DBS...Deep Brain Stimulation
ECG... ....Electrocardiogram
ECoG. ....Electrocorticogram
EMG..Electromyogram
GERD..Gastroesophageal Reflux Disease
GPIO.. ....General Purpose Input Output
GUI.... ....Graphical User Interface
HCS...Howland Current Source
IACUC..Institutional Animal Care and Use Committee
IP...Intraperitoneal
KA...Kainic Acid
LFP..Local Field Potential
NI-DAQ........ ....National Instruments Data Acquisition
PACUC........ ....Purdue Animal Care and Use Committee
PBS.... ....Phosphate Buffered Saline
PCA...Posterior Cricoarytenoid
PCB...Printed Circuit Board
PCBA. ....Printed Circuit Board Assembly
PMIC...Power Management Integrated Circuit
PPI...Parallel Peripheral Interface
PSD.... ....Power Spectral Density
RLN... ....Recurrent Laryngeal Nerve
RMS... ....Root Mean Square
RNS...Responsive neurostimulation
SPI...Serial Peripheral Interface
SpO2.. ....Peripheral Capillary Oxygen Saturation
SUDEP..Sudden Unexpected Death in Epilepsy
TeNT..Tetanus Neurotoxin
UDP... ....User Datagram Protocol
VNS... ....Vagus Nerve Stimulation
WFI.... ....Wait for Interrupt
WPT..Wireless Power Transfer

ABSTRACT

Author: Pederson, Daniel, J. PhD
Institution: Purdue University
Degree Received: December 2018
Title: Determining, Treating, and Preventing Mechanisms of Sudden Death in Epilepsy Using Medical Implantable Devices.
Committee Chair: Pedro Irazoqui

People with epilepsy have an increased risk of mortality when compared to the general population. These increased mortality risks include deaths related to status epilepticus and sudden unexpected death in epilepsy (SUDEP). Physiological data describing cardiac, respiratory, and brain function prior to sudden death in epilepsy is crucial to the studying the underlying mechanisms behind these deaths. Because it is unknown when sudden deaths in epilepsy may occur, continuous monitoring is necessary to guarantee the capture of physiological data prior to death.

I have used custom designed implantable devices to continuously measure cardiac, respiratory, and neurological signals in freely behaving rats with chronically induced epilepsy. Due to the continuous respiration measurements, the resultant dataset is the first of its kind. This dataset indicates that respiratory abnormalities (reduced respiration and short apneas) occur during and after seizures. These abnormalities may indicate SUDEP onset because obstructive apneas due to laryngospasm have been indicated as possible causes of SUDEP in other studies.

Laryngospasms can be caused by gastric acid coming into contact with the larynx. During a laryngospasm, intrinsic laryngeal muscles contract, resulting in the closure of the airway. Recently published research has indicated that acid reflux may be responsible for triggering fatal laryngospasms in rats with induced seizures. I have found that the larynx can be opened during a laryngospasm by electrically stimulating the recurrent laryngeal nerves. I have also found that performing gastric vagotomies leads to a statistically significant reduction in mortality due to fatal apneas in rats with induced seizures.

1. INTRODUCTION

1.1 Background

Epilepsy is a neurological disease that affects millions of Americans and their families [1]. People with epilepsy experience recurring seizures often without warning [2]. The disruptive and unpredictable nature of these seizures negatively affects quality of life in areas relating to school performance, independence, and cognition [3, 4]. While many people with epilepsy find relief from their seizures using antiepileptic drugs (AEDs), 30% of people with epilepsy suffer from medically intractable epilepsy, and are unable to achieve control over their seizures using AEDs [5, 6]. Up to 70% of people suffering from medically intractable epilepsy who have localization-related seizures find relief from their seizures by various resection and disconnection surgical procedures in the brain [5, 7, 8]. Many people suffering from medically intractable epilepsy who are not candidates for surgical resection or disconnection turn to implantable neuromodulation devices to help manage their seizures [9-11]. The two most popular neuromodulation devices for treating epilepsy in the United States are the vagus nerve stimulation (VNS) device produced by LivaNova and the responsive neurostimulation (RNS) device produced by NeuroPace [9]. VNS has been shown to reduce seizure frequencies in some patients by providing periodic electrical stimulation of the cervical vagus nerve [12]. RNS, which has also been shown to reduce seizure frequency in some patients, uses one or more deep brain stimulator (DBS) electrodes paired with a set of electrocorticogram (ECoG) electrodes that provides reactive DBS based on ECoG inputs [11, 13]. While both the VNS and RNS neuromodulation devices are configured to maximally reduce the number of seizures that people experience, it may be possible to configure them to provide additional forms of therapeutic stimulation. My work documented in this dissertation explores the possibility of treating and/or preventing mechanisms leading to sudden death in epilepsy using implantable neuromodulation technology.

People with epilepsy have an increased risk of mortality when compared to the general population [14-16]. These increased mortality risks include deaths related to status epilepticus and sudden unexpected death in epilepsy (SUDEP) [17, 18]. Status epilepticus is defined as a prolonged generalized, convulsive seizure or cluster of seizures that do not terminate in a normal fashion [17].

These prolonged seizures are associated with an increased mortality rate [19]. SUDEP is the leading cause of death in people with chronic, uncontrolled epilepsy and is defined as a sudden and unexpected non-traumatic, non-drowning death excluding status epilepticus experienced by a person with epilepsy without any post-mortem evidence of structural or toxicological cause of death [20]. Because people with implantable neuromodulation devices typically have medically intractable epilepsy, they represent a population within the epilepsy community with an increased risk of SUDEP [21]. The definition for SUDEP specifically excludes death related to status epilepticus, so I will use the term "sudden deaths" throughout this dissertation to refer to deaths from either SUDEP or status epilepticus.

The spontaneous and unexpected nature of most epileptic seizures and the sudden deaths associated with them make studying the mechanisms behind epileptic seizures and deaths difficult. Many people who suffer from sudden deaths in epilepsy were otherwise healthy and not medically monitored, so there is limited data regarding the state of their physiology in the moments leading up to their deaths [22]. Physiological data describing cardiac, respiratory, and brain function prior to sudden death in epilepsy is crucial to the studying the underlying mechanisms behind these deaths [22-24]. Because it is unknown when sudden deaths in epilepsy may occur, continuous medical monitoring is necessary to guarantee the capture of physiological data prior to death. The invasive and inconvenient nature of continuous medical monitoring in humans paired with the relative infrequency of sudden death in epilepsy makes this continuous physiological data collection in people with epilepsy impractical. For this reason, researchers have turned to collecting physiological data from animal models of epilepsy in an attempt to better understand the mechanisms behind sudden deaths in epilepsy [25].

While dogs and baboons experience epilepsy naturally [26, 27], studies involving these species are often prohibitively expensive because they require more specialized facilities and husbandry efforts than other smaller species (e.g. rodents) [28]. Because rodents do not experience epilepsy naturally, various genetic and injury models that produce chronic seizures mimicking epilepsy have been developed [29-33]. The work documented in this dissertation features physiological measurements taken before, during, and after seizing activity experienced by chronic tetanus neurotoxin (TeNT) and acute systemic kainic acid (KA) models of epilepsy in rats. The chronic

TeNT model involves injecting TeNT into the CA3 region of the rat hippocampus to chronically induce epilepsy in rats by reducing inhibitory neuronal responses in the hippocampus [34]. The acute systemic KA model involves injecting KA in the rat intraperitoneal (IP) space during an acute procedure to induce repeated seizing activity by increasing the activity of excitatory neurons [33]. We chose to focus our research on rodent models of epilepsy because rodents are relatively inexpensive to use in scientific studies due to their small size, minimal husbandry needs, and high availability. While mouse models of epilepsy exist, we chose to focus specifically on rat models of epilepsy because rats are larger than mice, making them better candidates for fully implantable devices designed to acquire continuous physiological data.

1.2   Bionode

After inducing epilepsy in rats, we needed to find a way to acquire continuous physiological data describing cardiac, respiratory, and brain functions in order to determine mechanisms behind sudden death in epilepsy. Because stress and environmental factors can affect the frequency and severity of seizures [35, 36], we needed to design a method of acquiring physiological signals in a way that allowed the rats to be freely behaving and untethered. This led to the design, fabrication, and deployment of a custom wireless, fully implantable device for rodents containing four channels of continuous biopotential recording. To study the feasibility of using presently available neuromodulation devices to treat and/or prevent sudden death in epilepsy, we also included a constant-current stimulator in the implantable device with the ability to provide either VNS or DBS.

Wireless implantable devices with the ability to record biopotential signals and electrically stimulate the nervous system have been used to study and treat a wide variety of neurological and neuropsychiatric disorders in humans including epilepsy, Parkinson's disease, depression, and drug addiction [13, 37-40]. To research these disorders in rodent models, various miniature wireless implantable devices have been developed [41-45]. To achieve a small size and reduce power requirements, many of these devices rely on application specific integrated circuits (ASICs), specifically designed packaging methods, and/or proprietary technologies. While these techniques can produce small and power efficient devices, the ability to reproduce them in typical laboratory settings is often prohibitively difficult and expensive. Additionally, the application-specific nature

of such devices introduces problems when adapting them to alternate applications. Chapter 2 of this dissertation documents the design, fabrication, and deployment of a miniature wireless implantable device for rodent through clinical models called the Bionode. The Bionode features customizable recording and stimulation channels in a flexible, modifiable, and re-useable package to accommodate a wide variety of use cases.

The Bionode was developed over the course of four years at the Center for Implantable Devices (CID) at Purdue University. With the ability to record up to four differential biopotential signals and provide up to 1 mA of biphasic constant current electric stimulation, its capabilities and performance exceeds that of currently available implantable devices for rodent models [41, 43, 44, 46]. Each input channel contains multiple gain and filtering stages that can be modified to accommodate a variety of input signals. Bi-directional communication between the implant and external systems allows for the real-time specification of stimulation wave-forms, providing a platform for closed-loop recording and stimulation studies. Furthermore, all components used to construct the Bionode are available as commercial off-the-shelf (COTS) components with the intent that any and all aspects of the Bionode's design can be reproduced by a typical university laboratory or small medical device company.

Over the past four years, the Bionode has been used by researchers at Purdue University to study epilepsy, Parkinson's disease, glaucoma, urinary incontinence, and vagus nerve stimulation for modulation of the inflammatory reflex and gastroparesis. Throughout the course of these studies, more than 100 Bionodes have been successfully implanted. Over the course of these implant procedures, the methods used to manufacture the Bionode have been refined to increase its ease of use and re-use.

1.3   Chronic Respiration Measurements in Rats with Epilepsy

Electrodes and transducers are necessary to interface the Bionode's analog front end circuitry with the source of its measurements. While methods for chronically measuring electrocardiograms (ECGs) and ECoGs are relatively straightforward [47, 48], no method of acquiring long-term chronic respiration data from rats has been documented. This led me to design, fabricate, validate,

and deploy a custom fully implantable respiration transducer based around a thermocouple that can sense temperature changes inside the nasal cavity during respiration.

While several methods of acquiring respiration data in rodent models already exist, most of them are difficult to implement in long-term studies involving freely-behaving rodents. Chest movements can often be correlated with respiration activity, so piezoelectric belts and/or video monitoring systems that detect chest movements can produce respiration data [49, 50]. These methods, while useful in their simplicity and relative non-invasiveness, are difficult to implement during long-term freely-behaving studies in rodents. Freely behaving rodents can remove piezoelectric belts, and they also may not always be oriented within the video's field of view in a way that is conducive to visually measuring respiration. These two methods are also unable to detect respiration accurately if respiration becomes uncorrelated with chest movements (e.g. during obstructive apnea). Plethysmography chambers can measure respiration by detecting the volumetric changes that occur during inspiration and expiration [51]. Because these chambers rely on measured pressure differences to detect changes in volume, the movement of freely-moving rodents within the chamber can induce large motion artifacts onto the respiration signal. Plethysmography chambers are also relatively expensive compared to other methods of recording respiration, and they require that the rodent live within a fairly confined space during data acquisition, a space considerably smaller than the regulatory minima for long-term housing both in the US and UK [52].

A more direct method of measuring respiration is to use a thermocouple to detect temperature variations inside the nasal cavity [53, 54]. Because rats breathe solely through their noses, a thermocouple implanted inside a rat's nasal cavity is able to detect thermal differences when cooler air enters the nasal cavity during inspiration and when warmer air exits the nasal cavity during expiration. Because this method relies on airflow to change the temperature inside the nasal cavity, it is a more direct measurement of respiration than measuring chest movements. It also is much less expensive and more easily deployable than using a plethysmography chamber. Current implementations typically rely on a trans-cutaneous link to provide access to the thermocouple, which requires the rat to be tethered during data collection and can lead to irritation and/or infection around the trans-cutaneous site. I have designed a fully implantable thermocouple that robustly

interfaces with the Bionode. I analyzed data collected from eight freely behaving rats over the course of two to six weeks using this thermocouple transducer to validate this method's ability to sense respiration during long-term chronic studies.

I used Bionodes equipped with my fully implantable thermocouple transducer along with ECG and ECoG leads to measure cardiac, respiratory, and neurological signals in freely behaving rats with chronically induced epilepsy using the TeNT model. An initial analysis of the data collected before seizures (the preictal phase), during seizures (the ictal phase), and after seizures (the postictal phase) shows reduced respiration during the ictal phase with increased respiration during the post-ictal phase. Additionally, in some cases, I have observed short (2 to 4 second) apneas during the transition from the ictal to the postictal phase. While these apneas are short, they may indicate possible SUDEP onset as obstructive apneas due to laryngospasm have been indicated as possible causes of SUDEP [55-57].

1.4 Treating Laryngospasm with Electrical Stimulation

A laryngospasm is a reflex response typically triggered by harmful manual or chemical stimulation of the larynx [58]. During a laryngospasm, intrinsic laryngeal muscles contract to force adduction of the larynx, resulting in the closure of the larynx over the lumen of the trachea [59, 60]. While laryngospasms are usually observed in anesthesiology, they can also be life-threatening symptoms of gastroesophageal reflux disease (GERD), various neurological diseases, and some genetic disorders [61-68]. Furthermore, recent work has indicated that laryngospasms may be a factor in SUDEP [55-57], and that acid reflux may be the trigger for some or all of those laryngospasm episodes [55]. Because laryngospasms close the larynx, they require immediate treatment. Laryngospasms are typically treated using active measures such as rapidly changing body position or breathing slowly [65]. While these treatments are often successful, they are impossible to self-administer by people who are alone and unconscious. This poses a particular risk to those with epilepsy. In these instances, a new form of treatment is needed. I have explored the possibility of treating laryngospasms by activating abductor muscles in the larynx during laryngospasms via electrical stimulation in an attempt to open the larynx.

Studies have shown that certain methods of VNS can have an effect on the larynx via the recurrent laryngeal nerve (RLN), which are branches of the vagus nerves [69-71]. It has also been shown that direct electrical stimulation of the RLN can cause abduction of the larynx [72]. To activate the abductor muscles in the larynx during a laryngospasm, we electrically stimulated the RLNs in rats after triggering a laryngospasm with hydrochloric acid topically applied to the larynx. The RLNs innervate the majority of the muscles in the larynx, including the posterior cricoarytenoid (PCA) muscles which control laryngeal abduction [73, 74]. The RLNs run parallel to the lateral edges of the trachea (See Figure 1.1), making them easy to identify and access for electrical stimulation. We were able to use the Bionode's stimulator circuit to produce a constant-current stimulation waveform that, when applied bilaterally to the RLNs, was able to open the larynx during acid-induced laryngospasms in rats.
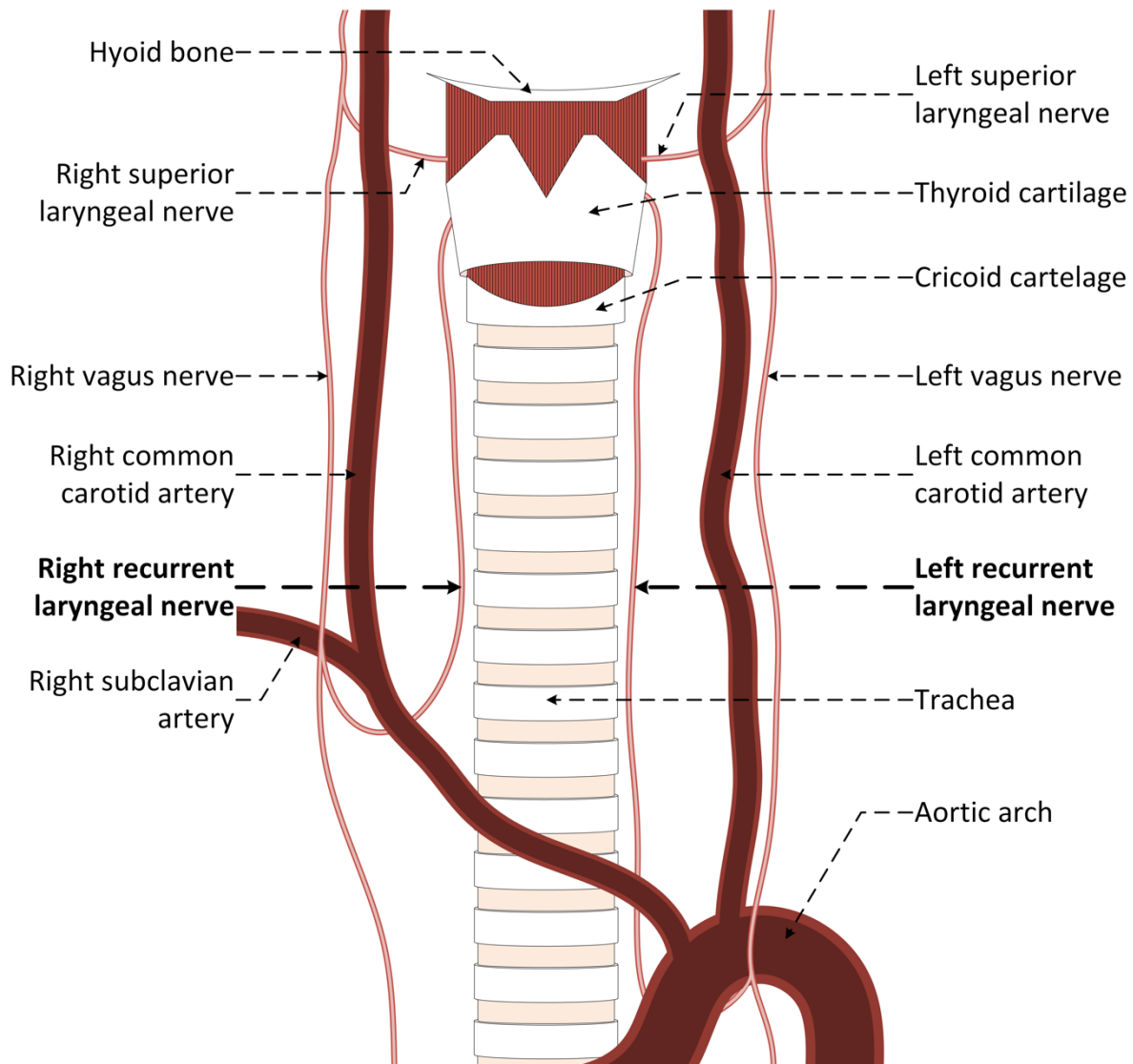
Figure 1.1: Both recurrent laryngeal nerves run parallel to the lateral edges of the trachea, making them easy to access and identify. Both the recurrent and superior laryngeal nerves are branches of the vagus nerve.

1.5   Preventing Laryngospasm via Gastric Vagotomy

Laryngospasm can be caused by gastric acid coming into direct contact with the larynx and activating chemoreceptors and/or mechanoreceptors responsible for triggering the laryngospasm reflex [58, 59]. While we found that this type of laryngospasm can be treated via electric stimulation of the RLNs, understanding the mechanism behind how seizing activity leads to gastric acid induced laryngospasm is important for exploring preventative treatments.

Gastric acid production in the stomach is regulated by the vagus nerve in two overlapping phases of digestion: the cephalic phase and the gastric phase. During the cephalic phase, gastric acid production is driven by sensory inputs (e.g. smell, sound, sight) to increase the amount of gastric acid in the stomach prior to and during the consumption of food [75]. During the gastric phase, vagus nerve mediated responses to both stretch receptors and chemoreceptors in the stomach increase gastric acid production while the stomach is distended as well as while the presence of peptides and amino acids freed from proteins during digestion is detected [76, 77]. It has been shown that performing gastric vagotomies (severing the gastric branch of the vagus nerve) leads to a reduction of gastric acid production during both of these phases [75, 78]. Additionally, particular forms of electrical stimulation of the vagus nerve can lead to an increased production of gastric acid [79].

The presence of acid in the esophagus of seizing rats is abnormal because rats are unable to vomit [80, 81]. This lack of ability to vomit rules out the possibility that seizing activity triggers an active vomiting reflex leading to gastric acid making contact with the larynx. Rats also do not experience acid reflux naturally, so a passive, natural migration of acid from the stomach to the larynx during seizing activity is unlikely [82, 83]. Rats do not experience acid reflux naturally because their typically closed gastroesophageal barrier (See Figure 1.2), which consists of both the crural sling and the lower esophageal sphincter, provides two separate closure points between the stomach and the esophagus [84]. When the crural sling, which is part of the diaphragm, contracts, it pinches the esophagus closed. Likewise, when more caudally located lower esophageal sphincter contracts, it closes off the esophagus from the stomach. Both the crural sling and the lower esophageal sphincter are innervated by the vagus nerve [85], and both of them must open in order for acid to leave the stomach and enter the esophagus as shown in [83].
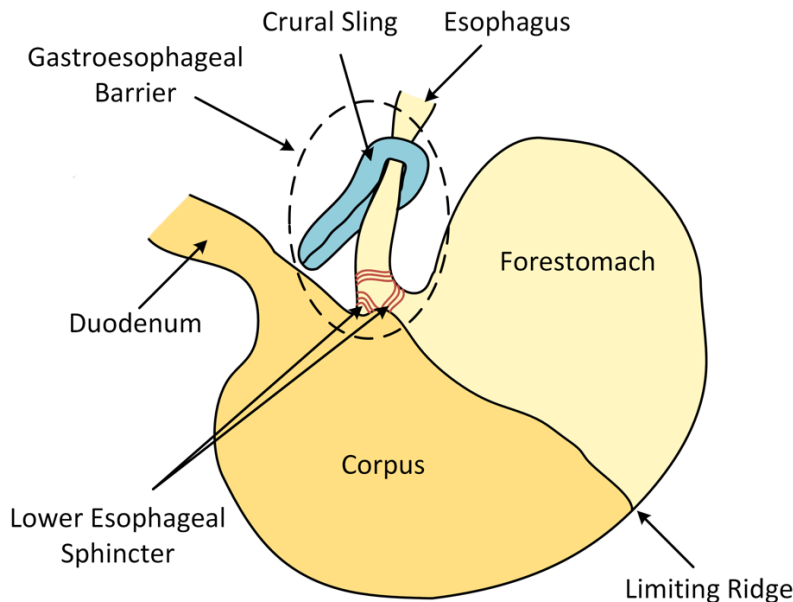
Figure 1.2: The gastroesophageal barrier is comprised of the crural sling located at the diaphragm and the lower esophageal sphincter located at the entrance to the stomach. Both the crural sling and lower esophageal sphincter are innervated by the vagus nerve. Adapted from [86].

During seizures, errant signals originating in the brain can affect various autonomic systems including cardiac, respiratory, and digestive systems [25, 87-89]. These effects can be caused by signals sent through the vagus nerve [89]. Because the vagus nerve regulates gastric acid, it is possible that errant signals on the vagus nerve caused by seizing activity could result in gastric acid overproduction. While rats cannot vomit, they are able to regurgitate which occurs when the stomach becomes over-filled, and stomach contents passively force their way through the lower esophageal sphincter and the crural sling [90]. Therefore, it may be possible for excessive gastric acid produced during seizing activity to force its way into the esophagus and subsequently make contact with the larynx. Because the vagus nerve innervates the lower esophageal sphincter and the crural sling, gastric acid may also be able to enter the esophagus if errant signals on the vagus nerve cause relaxation of the gastroesophageal barrier.

To determine if the vagus nerve plays a role in the mechanism behind how seizing activity leads to stomach acid induced laryngospasm during seizures, we performed a series of gastric vagotomies on rats prior to inducing seizures via systemic KA injections. We found that

performing gastric vagotomies on rats led to a statistically significant reduction in sudden death and incidences of acid reflux.

1.6 Possible Life-Saving Therapies for Patients with Implanted VNS Devices

Using Bionodes to measure respiration, ECG, and ECoG in freely behaving rats with epilepsy by means of the chronic TeNT model, we found that rats experience a suppression of respiration during the ictal phase, and sometimes experienced apneas during the transition between the ictal and post-ictal phase. These apneas may indicate possible SUDEP onset as obstructive apneas due to laryngospasm.

We found that a constant-current, alternating-phase stimulation waveform can open the larynx during acid-induced laryngospasms in rats when applied bilaterally to the RLNs. Evidence suggests that this stimulation waveform opens the larynx by contracting the PCA abductor muscles in the larynx via signals induced on the RLNs. Because the RLNs branch off of the vagus nerve, adaptation of this stimulation for use in unilateral vagus nerve stimulation could provide a crucial alternative treatment for laryngospasms for people with epilepsy who already have a VNS device.

We found that rats with gastric vagotomies had a statistically significant reduction in sudden death and acid reflux while seizing when compared to rats without gastric vagotomies. While this result indicates that errant signals on the vagus nerve may cause gastric acid induced laryngospasms leading to an increased risk of death in epilepsy, it does not directly provide a preventative treatment for increased risk of sudden death in epilepsy. While some people do have gastric vagotomies to treat stomach ulcers [91], the risk of sudden death in epilepsy may be too low for people with epilepsy to pursue invasive preventative surgery. It may be possible to stimulate the left cervical vagus nerve via electrical stimulation to block signals traveling from the brain to the gastric branch of the vagus nerve. If the risk of sudden death from epilepsy can be mediated by applying blocking electrical stimulation to the left cervical vagus nerve during seizures, then people already outfitted with VNS devices may be able to reduce their risk of death in epilepsy via a modification to the algorithm driving the stimulation output of their device to provide blocking stimulation during seizing activity.

1.7   Specific Aims

My research documented in this dissertation can be broken into three specific aims.

Aim 1: Design a chronic, wireless implantable device with the ability to acquire long-term cardiac, respiratory, and brain signals in freely behaving rodents as well as provide electrical stimulation to the nervous system. I was integrally involved in the design and testing of the analog front-end, stimulator, power management circuitry, and packaging of this device. I was also the lead developer of the firmware on the implantable device as well as the graphical user interface PC application used to communicate with the device.

Aim 2: Acquire and analyze cardiac, respiratory, and brain signals from freely behaving rats with induced chronic epilepsy. I built all of the implants used to acquire these signals and was directly involved in developing the implant surgical procedure. I also designed all of the electrodes and transducers used to acquire the respiration, ECG, and ECoG signals. After the rats were implanted, I was in charge of all animal husbandry and data collection responsibilities, although I did receive assistance from Ethan Biggs in latter experiments.

Aim 3: Stimulate the nervous system via electrical stimulation to treat and/or prevent the onset of sudden death in epilepsy. The end goal of this aim is to inform possible life-saving therapies using neuromodulation devices currently used by people with epilepsy. I was the lead developer of the RLN stimulation experiments aimed at treating laryngospasms via electrical stimulation and performed all of the surgical procedures myself with assistance from Ethan Biggs. I also had the initial idea that gastric acid overproduction during seizures may lead to fatal acid-induced laryngospasms. I was the lead developer of the gastric vagotomy experiments aimed at preventing sudden death in epilepsy by removing the possible mechanism leading to gastric acid overproduction during seizing activity. I worked closely with Ryan Budde and Ethan Biggs to perform all of the surgeries and analyze survival and stomach content measurement data acquired during these experiments.

2. AIM 1: THE DESIGN OF THE BIONODE: A FULLY IMPLANTABLE DEVICE FOR RECORDING AND STIMULATING BIOELECTRIC EVENTS IN RODENTS.

Much of the content contained in this chapter has been submitted for publication in a paper titled "The Bionode - A Closed-Loop Neuromodulation Implant," of which I am the first author. It has been accepted for publication in the Association for Computing Machinery (ACM) Transactions in Embedded Computing Systems (TECS) journal.

2.1 Motivation/Overview

The Bionode was developed over the course of four years at the CID at Purdue University. With the ability to record up to four differential biopotential signals and provide up to 1 mA of biphasic constant current electric stimulation, its capabilities and performance exceeds that of currently available implantable devices for rodent models [41, 43, 44, 46]. Each input channel contains multiple gain and filtering stages that can be modified to accommodate a variety of input signals. Bi-directional communication between the implant and external systems allows for the real-time specification of stimulation wave-forms, providing a platform for closed-loop recording and stimulation studies. Furthermore, all components used to construct the Bionode are available as COTS components with the intent that any and all aspects of the Bionode's design can be reproduced by a typical university laboratory or small medical device company. The unforeseen difficulties presented by these challenges have motivated the detailed documentation of their various solutions in this dissertation in the hopes that they will be of use to others designing and utilizing electroceutical devices. It is my desire that the documented design of the Bionode will enable more investigators to be able to use implantable device technology in their work.

2.2 Bionode Device

Over the past four years, the Bionode has been used by researchers at Purdue University to study epilepsy, Parkinson's disease, glaucoma, urinary incontinence, and vagus nerve stimulation for modulation of the inflammatory reflex and gastroparesis. Over 100 Bionodes have been have been successfully implanted throughout the course of these studies. The methods used to manufacture the Bionode have been refined to increase its ease of use and re-use.

This chapter is organized in sections that document the design challenges and solutions for the various systems on the Bionode. When applicable, in-vivo results are reported and discussed in each section. These sections include descriptions of the Bionode's recording channels, stimulation circuitry, bi-directional communication scheme, communication antenna design, wireless power capabilities, and packaging techniques. The challenges outlined in these sections have been thoroughly studied by current and past members of the CID at Purdue University. The unforeseen difficulties presented by these challenges have motivated the detailed documentation of their various solutions in this paper in the hopes that they will be of use to others designing and utilizing electroceutical devices.

2.2.1   Bionode System Overview

The Bionode implant consists of three printed circuit board assemblies (PCBAs): The Bionode mainboard, the Powernode, and the Feedthrough board. The Bionode mainboard contains all circuitry for the recording and stimulating channels as well as a microcontroller, radio, and antenna for data transmission and reception (See Sections 2.2.2-2.2.4). The Powernode provides power rails to the Bionode mainboard (See Section 2.2.5). Electrodes are connected to the Bionode mainboard via a feedthrough board (See Section 2.2.6). Fully assembled and fully packaged Bionodes are pictured in Figure 2.1. We implant Bionodes like the one shown in Figure 2.1 in the subcutaneous space on the side of rats.
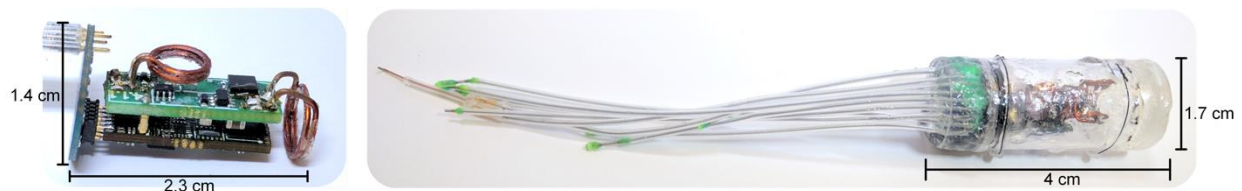
Figure 2.1: Bionode implant assembly (left) and 4-channel Bionode fully packaged inside glass packaging with electrodes attached and rechargeable batteries included (right)

The Bionode is supported by various external systems as seen in Figure 2.2. A Wireless Powering Transfer (WPT) chamber provides both power to the Bionode and a living space for the implanted rodent (See Section 2.2.5). External video cameras attached to the WPT chamber provide 24/7 video recordings of the rat while it lives in the cage. All data transmitted to and from the Bionode passes through an external Base Station that provides a communication interface between the

Bionode and a PC via a Wi-Fi link (See Section 2.2.4). A custom-designed cross-platform application provides a graphical user interface (GUI) allowing users to view and save data transmitted by the Bionode as well as specify various settings (i.e. stimulation waveform parameters) on the Bionode.
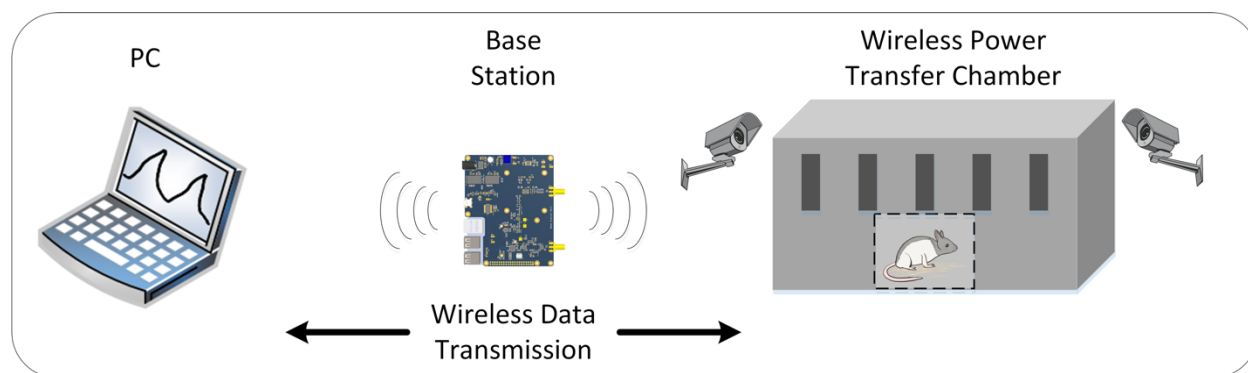
Figure 2.2. External support systems for the Bionode include the wireless power transfer chamber, external video cameras, a Base Station, and a PC equipped with a custom cross platform application that provides a graphical user interface for controlling the Bionode.

A functional block diagram of the Bionode with its external systems is shown in Figure 2.3. The Bionode and external systems consist of five custom PCBAs, two firmware programs (one for the Bionode microcontroller and one for the Base Station microcontroller), and two software applications (one for the Base Station Raspberry Pi, and one for the PC graphical user interface). All hardware, software, and firmware was designed, fabricated, and deployed by members of the CID at Purdue University. I was a major contributor to all of these projects and was the lead designer and author of the Bionode DataView GUI application, the Bionode firmware, and the daughter board PCBA. I also assisted in the assembly of each PCBA and hand built, packaged, and deployed over 50 Bionode implants for various tests and experiments during my time at the CID.
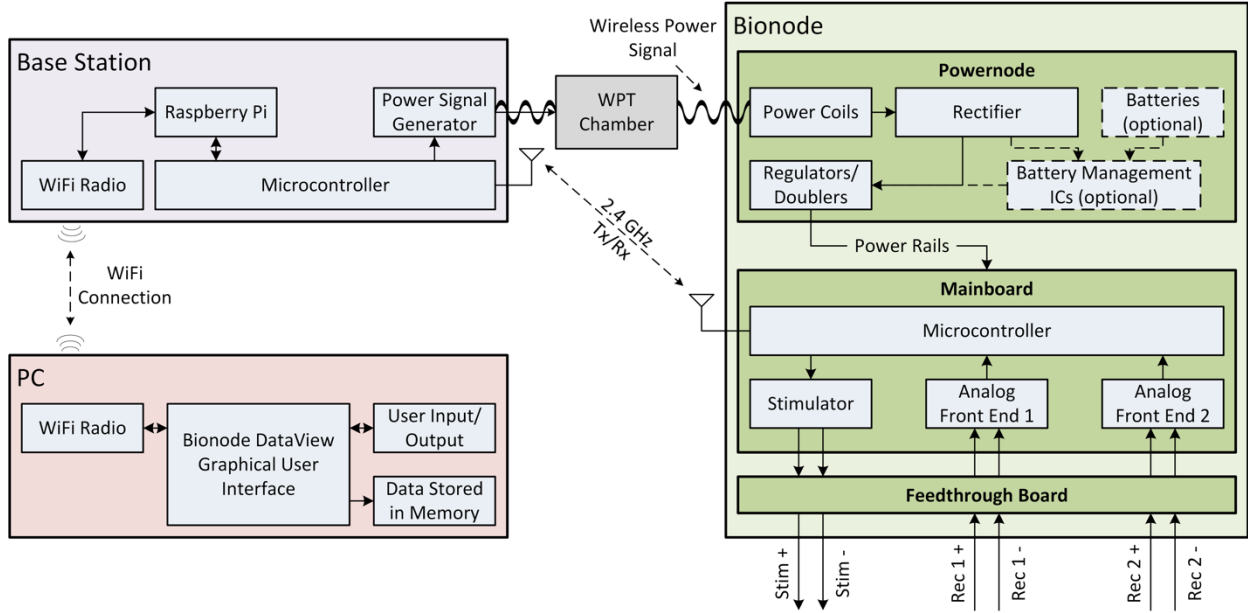
Figure 2.3. Bionode settings are updated and acquired data is displayed on a PC via Bionode DataView, a custom designed cross-platform graphical user interface. Bi-directional communication is facilitated via the Base Station which also provides the wireless power source that drives the wireless power transfer (WPT) chamber. The WPT chamber houses the implanted rodent and carries the circulating magnetic field that powers the device.

2.2.2   Bio-signal Acquisition

In order to acquire small electric signals generated by biological processes, an analog front end (AFE) is needed to amplify and filter the signals before they can be digitized.

2.2.2.1   AFE Design Considerations

The AFE features high differential input impedance, low noise, a high common mode rejection ratio (CMRR), and sufficient gain and bandwidth [92]. The gain and bandwidth are specified for each input channel in order to properly condition the various signals that may be sensed by the AFE (i.e. ECG, ECoG, electromyogram (EMG), local field potential (LFP), compound nerve action potential (CNAP), thermocouple sensor inputs, or pressure sensor inputs). While this AFE is able to filter out noise generated by typical sources (i.e. nearby radiated signals, motion artifacts, and other biological signals), it also can filter out high frequency RF noise injected into the signal from the WPT chamber (Section 2.2.5).

2.2.2.2   AFE Design Overview

The Bionode has two parallel dual ended AFEs; one for each input channel. Two additional channels can be added to the Bionode via an expansion board. Each AFE consists of passive front-end filtering followed by two stages of gain amplification (Figure 2.4). The two stages of gain amplification include a first stage of differential amplification and a second stage that provides bandpass filtering and additional gain. These parallel AFEs are dual ended with ±0.9V rails to allow the AFE to have a zero dc bias voltage. This is necessary because the stimulation circuit requires that the negative stimulation electrode is connected to the Bionode's ground (See Section 2.2.3). If the AFE had a non-zero dc bias voltage, a static potential would exist between the recording electrodes and the negative stimulation electrode; causing possible tissue damage, electrode erosion, and unwanted stimulation performance. Alternatively, inputs and outputs can be ac coupled, but that introduces different signal processing challenges for stimulus artifact cancellation in the recorded signal, and lowers the CMRR for the AFE.
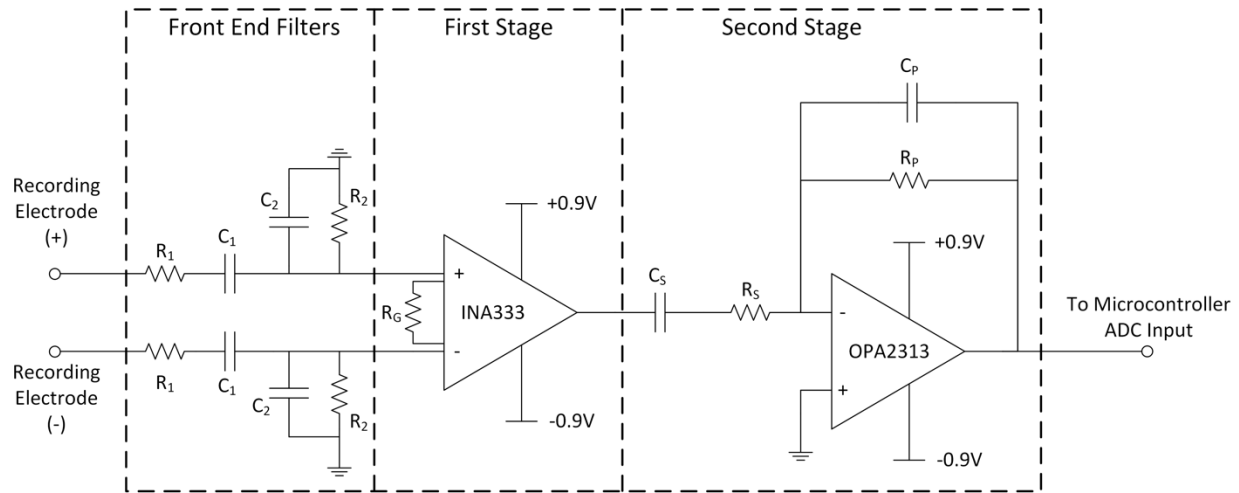
Figure 2.4. Signals are acquired via an analog frontend consisting of front-end filtering and two amplification stages. Front-end filters provide passive bandpass filtering prior to amplification. The first stage differentially amplifies the signal using an instrumentation amplifier. The second stage provides additional gain and active bandpass filtering.

2.2.2.3   Front End Filtering

The optional passive front-end filters allow for the inclusion of a high pass filter, low pass filter, or bandpass filter before the first stage differential amplifier. While adding these filters reduces

the CMRR and differential input impedance of the AFE (Table 2.1), they have been found to be necessary under certain conditions. When directly sensing bio-signals with differential leads (i.e. ECG, ECoG, or EMG), a drifting dc offset voltage has been observed which can cause the inputs to the first stage to drift out of the dc voltage input range of the instrumentation amplifier. This slowly drifting DC can be seen in Figure 2.5.
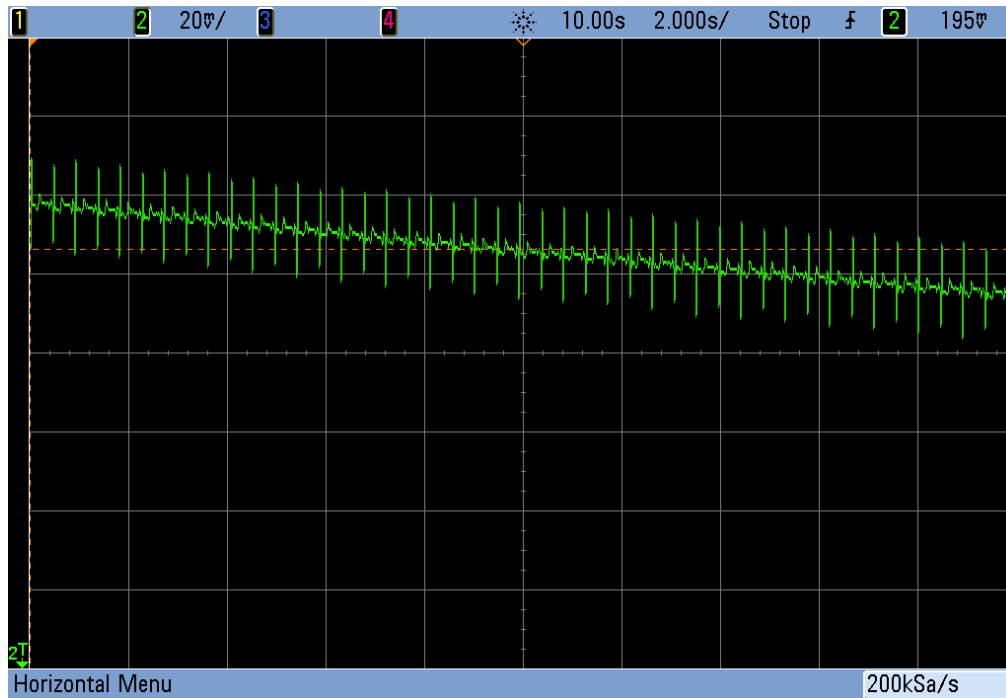
Figure 2.5: DC drift on a simulated electrocardiogram signal on the input to the amplifier in the first stage of the analog front end

The signal in Figure 2.5 was obtained via a bench test fixture designed to test each AFE of the Bionode. This fixture simulates an ECG signal in a saline bath, which is subsequently measured using electrodes connected to the Bionode's AFEs (See Figure 2.6).
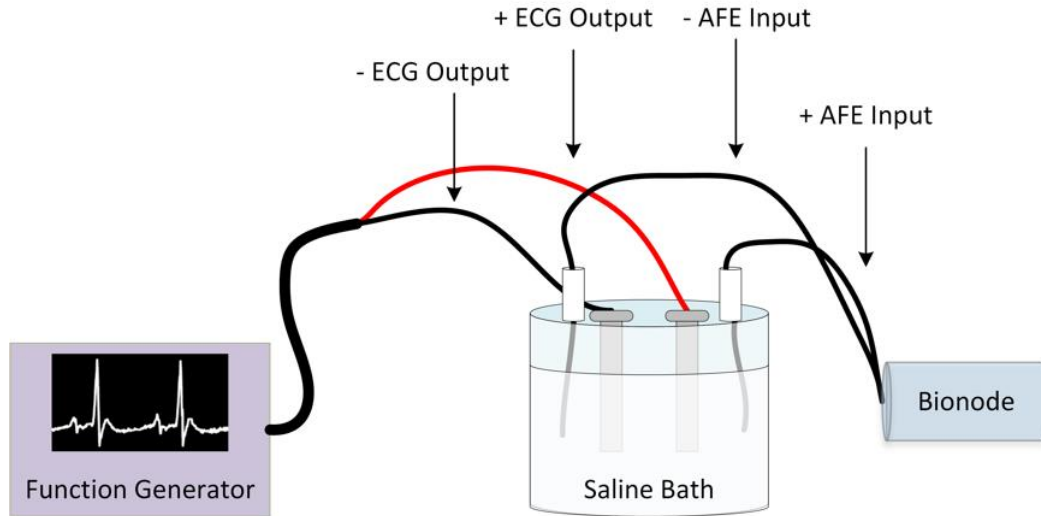
Figure 2.6: Test setup for sending simulated bio-signals into the Bionode's analog front end through saline which better simulates how signals are sensed by the Bionode's leads in-vivo.

The signal in Figure 2.5 is a measurement of the input to the instrumentation amplifier of a Bionode without front-end filters populated. The DC drift only presents itself when the signals are fed into the Bionode's AFE through the saline bath. It has never been observed when the ECG signals are fed directly into the Bionode. Feeding signals into the Bionode's AFEs in this manner more closely resembles how the Bionode actually acquires signals in-vivo, which provides a more complete test of the Bionode's AFEs than if signals were directly wired into the Bionode. Figure 2.7 contains ECG data chronically recorded from a freely behaving rat that suffers from a loss of signal due to this drifting DC offset at the input of the AFE.
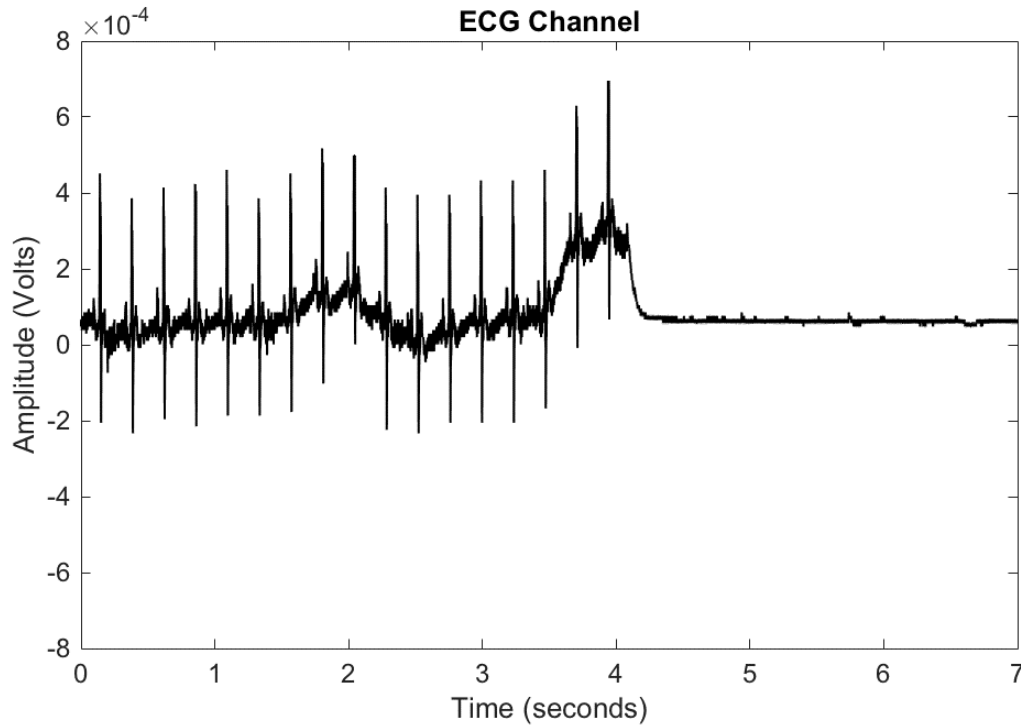
Figure 2.7: This electrocardiogram signal was acquired from a freely behaving rat implanted with a Bionode without frontend filters. The signal loss is characteristic of observed signal loss due to DC drift at the input to the analog front end.

To avoid this issue, we populate a passive high-pass filter in the front-end filtering stage of the AFE, and leave it out for smaller and higher frequency recording where high CMRR is paramount. A similar issue is also observed when providing power to the Bionode using a high frequency inductive link. High frequency RF noise can couple onto the leads and traces of the Bionode when inductively powering. We remove this noise by populating a passive low-pass filter in the front-end filtering stage of the AFE. If operating the Bionode under conditions where both of these problems may occur, we populate a passive band-pass filter. Alternatively, we can bypass all of the front-end filtering section by populating the R_1 and C_1 pads with zero ohm resistors and not populating the R_2 or C_2 pads; providing input channels with much higher differential input impedance and CMRR. When recording small signals requiring high differential gain, maximized CMRR is necessary to cancel noise common to both differential inputs. Additionally, high CMRR is needed when stimulation artifact cancellation is required because the stimulation artifacts are common to both differential inputs.

Table 2.1: Measured Performance Characteristics of the Bionode AFE

	No front-end filters	**Low-pass front-end filter**	**Bandpass front-end filter**	**Units**
Gain	60	60	59.9	dB
High-pass cutoff	10.47	4.9	6.0	Hz
Low-pass cutoff	1,410	1,480	1,460	Hz
CMRR	100	43	72	dB
Input Impedance	100,000	3.61	2.03	MΩ
Input-referred noise	51.85	101	97.3	nV/√Hz

2.2.2.4 First Stage Differential Gain

The first stage consists of an instrumentation amplifier (INA333) that differentially amplifies its input signal. The INA333 is used because of its high input impedance (100 GΩ) and low current draw (50 µA). We typically set the gain of the INA333 to 20 dB by setting R_G to 11 kΩ. For higher CMRR, higher first-stage gain settings should be used.

2.2.2.5 Second Stage Gain and Filtering

The second stage consists of an inverting band-pass filter [93] using an operational amplifier (OPA2313). The OPA2313 is used because of its sufficient gain bandwidth (>1MHz), low noise (25 nV/√Hz), and rail-to-rail output. The OPA2313 has the added benefit of being available in a dual-package form factor allowing one IC to be used for both AFEs. The gain and bandwidth of this stage can be set individually by choosing appropriate component values for R_S, C_S, R_P, and C_P [94]. The gain for this stage is typically set to between 20 and 50 dB. Table 2.2 contains values for all of the passive components in the AFE that we have used when measuring respiration (via a thermocouple), ECG, ECoG, and CNAP signals. Note that for neural signals, we chose a high-pass filter to remove motion artifact for the specific application of seizure detection. Typical neural recordings which require sub 1-Hz recordings can be achieved by altering Cs and Rs. Also, using smaller values for R1 would help reduce input referred noise.

Table 2.2: Passive component values for desired gain and bandwidth for various bio-signals

	Respiration	ECoG	ECG	CNAP	Units
Desired Gain	70.5	60	54	60	dB
Desired Bandwidth	0.53-371.6	3.62-1400	3.62-1500	15-2500	Hz
R_1	10	20	20	Short	kΩ
C_1	Short	100	100	1000	nF
R_2	Open	1000	1000	100	kΩ
C_2	1	0.1	0.1	Open	nF
R_G	11	11	11	11	kΩ
R_S	30	20	20	10	kΩ
C_S	10000	2200	2200	1000	nF
R_P	10000	2000	1000	1000	kΩ
C_P	0.039	0.047	0.1	0.053	nF

The outputs of the each of the AFE's are routed directly into two of the NRF51822 microcontroller's ADC inputs. The NRF51822 is powered at the same (±0.9) voltages that power the AFEs, which remove the necessity for the outputs of the second stages to be transformed into single-ended signals. This allows them to be routed directly into the ADC inputs of the microcontroller. Depending on desired device size, and sensitivity to noise at the input, these supply voltages can be generated jointly or separately for AFE and microcontroller. The NRF51822 microcontroller's ADC can be configured to acquire samples at either 8-bit or 10-bit resolution with a total sample rate of up to 25 kHz, which is selectable by the user via the bidirectional communication interface (See Section 2.2.4).

In order to measure respiration, ECG, ECoG, and LFP signals, either two Bionodes must be implanted, or the Bionode must be upgraded to include two additional recording channels. The latter option was chosen to reduce risk to the animal model, as well as to increase the usability of a single Bionode implant. Two more AFE channels were added to the Bionode implant by connecting a two-channel AFE board called the daughter board. The daughter board contains two more AFE channels that are made up of exactly the same components as the two AFE channels on the Bionode Mainboard. The daughter board has two outputs that are connected directly into two

additional ADC inputs on the NRF51922 microcontroller on the Bionode Mainboard. Figure 2.8 below shows a fully assembled Bionode with an attached 2-channel AFE daughter board on its side.
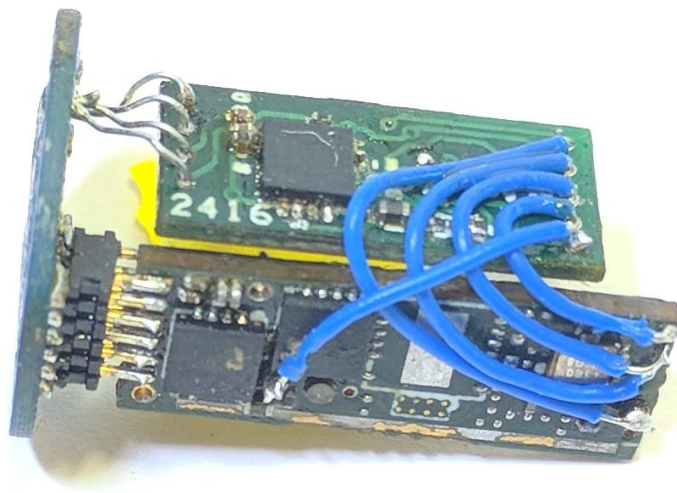
Figure 2.8: Bionode implant with attached daughter board. The daughterboard provides two additional analog front ends to the Bionode. Blue jumper wires are used to connect power rails to the daughter board and to connect the two analog outputs from the daughter board to analog-to-digital converter inputs on the Bionode mainboard.

2.2.2.6   In-Vivo Results

Fifty-one rats have been implanted with 4-input-channel Bionodes configured to record respiration, ECoG, and ECG signals in the lead I and lead II positions. Examples of signals acquired during these studies can be seen in Figure 2.9. All signals depicted in Figure 2.9 were acquired wirelessly from freely behaving rats. Chapter 3 documents the acquisition and validation of these signals.
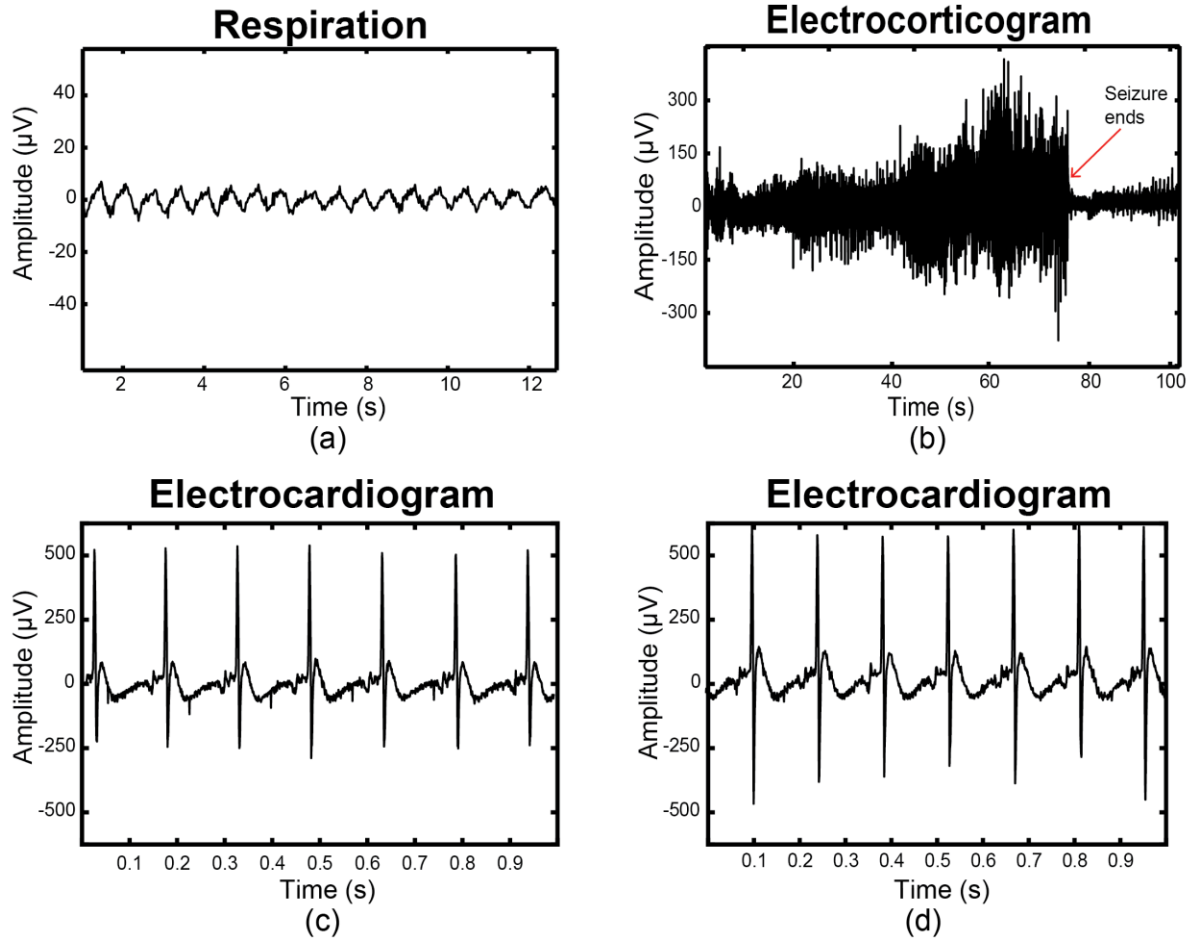
Figure 2.9. Wirelessly acquired biopotential signals from freely behaving rodents. (a) Respiration signal acquired using a thermocouple implanted in the nasal cavity of a rat. (b) Electrocorticogram signal acquired from the cortex of a rat at the end of a seizure using a differential pair of helical leads. (c) Electrocardiogram (ECG) signal acquired one week after implantation. (d) ECG signal acquired six weeks after implantation.

2.2.3   Electrical Stimulation

Many open loop implantable systems have been designed to either record biological signals [95] or to produce a physiological response by means of electrical, mechanical, or optical excitations [96, 97]. For a closed-loop study however, both capabilities are required. Therefore, the Bionode is designed with a flexible single electrical stimulation channel to supplement its recording capabilities. Alternatively, the stimulation channel is able to drive an LED for optogenetic stimulation if desired [98].

2.2.3.1 Stimulation Circuit Design Considerations

When designing an electrical stimulator, the specific type of stimulation that is needed must be considered. Constant voltage stimulation between a reference and counter electrode is relatively easy to implement, but suffers from the drawback of variable charge injection due to the capacitive nature of the electrode/body interface, leading to variable and unreliable stimulation efficacy. Constant current (galvanostatic) stimulation is more difficult to implement, but has the advantage of attaining a consistent and knowable charge injection throughout a stimulation pulse [99]. We implemented a constant current stimulator on the Bionode using a Howland current source (HCS) to ensure stimulation consistency and efficacy.

Another consideration in electrical stimulation is the flexibility of the stimulation waveform generated. Stimulation parameters such as amplitude, pulse width, frequency, and charge balancing are adjusted to meet the safety and efficacy needs of a given study. For example, while using a monophasic pulse train stimulus will likely result in an increased amount of action potential responses in nerves, this stimulus waveform will also likely cause tissue damage and electrode erosion over time. This might be sufficient for short-term acute studies, but for long-term chronic experiments, a charge-balanced biphasic pulse train is more appropriate to prevent future tissue and electrode damage in the subject. The tradeoffs of efficacy and safety in stimulation protocols are studied at length in the literature [100]. The Bionode allows the stimulation amplitude, pulse width, and frequency to be defined by an outside user in real time using its bidirectional communication capabilities (See Section 2.2.4). For the long-term safety reasons mentioned previously these parameter choices force the stimulation to be biphasic and charge balanced, although a simple firmware change will allow for non-balanced and/or mono-phasic stimulation if needed or desired.

A final important consideration in electrical stimulation is the accuracy and precision of the output of the stimulation circuit. Safe stimulation requires an accurate delivery of the desired stimulation waveforms. Unbalanced pulses, inconsistent pulse delivery times, and DC offsets on the stimulation waveform can cause unintended damage to the nerve and compromise electrode integrity. The Bionode is measured to have an acceptable charge balance ($\leq$0.3% error), and has

the added safety of a stimulation glitch switch and discharge switch built in to prevent unintended charge release during device startup.

2.2.3.2 Stimulation Circuit Design

We construct the constant current stimulation waveform using a current source (LT6375) driven by a DAC7551 digital to analog converter (DAC) as seen in Figure 2.10.
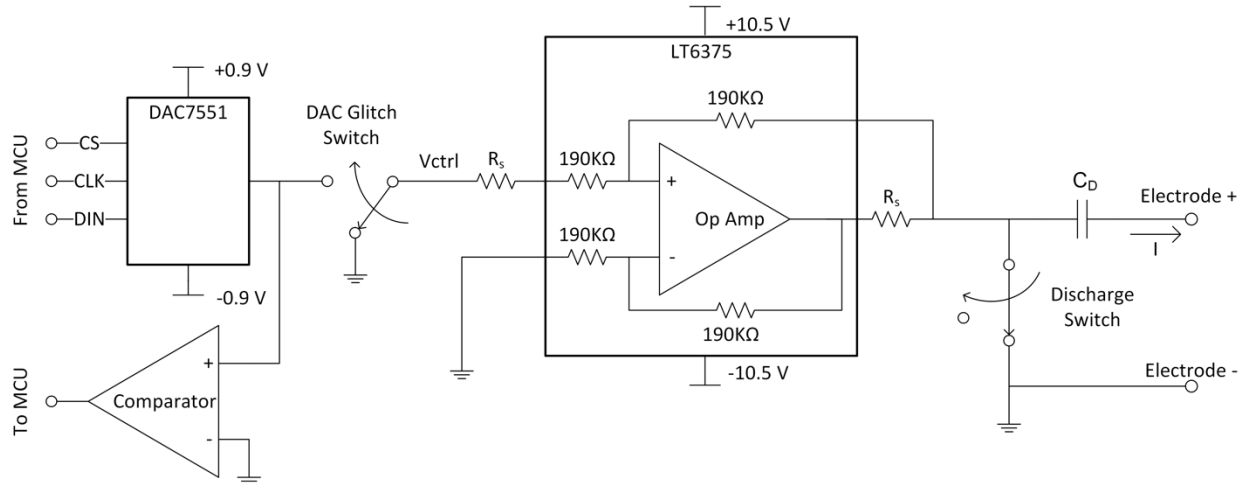
Figure 2.10. Constant current stimulation is generated via an LT6375 Howland current source. The output of the Howland current source is set by the microcontroller on the Bionode via a 12-bit digital to analog converter (DAC7551). A comparator connected to the output of the DAC7551 compares the DAC output to ground which allows the microcontroller automatically compensate for DC offset errors presented by the DAC7551. A normally grounded control switch is used to ensure that unwanted stimulation does not occur during the Bionode power-on sequence. To ensure true bi-phasic stimulation, the positive stimulation electrode swings around the negative stimulation electrode which is directly tied to the Bionode's ground. The positive stimulation electrode is AC coupled to the stimulator output through a DC-blocking capacitor (C_D) to ensure that unwanted DC stimulation is blocked. During startup and between stimulation pulses, the output of the stimulator circuit is grounded via a normally closed switch which discharges C_D, and shunts any unwanted stimulation output to ground.

The LT6375 improved HCS converts a control voltage provided by the DAC into a current waveform to achieve constant current stimulation [101]. We prefer the HCS topology over other topologies like current mirroring or electrode polarity switching (where the positive and negative electrodes are physically switched) because the HCS can generate reliable symmetric bipolar current pulses. It is difficult to achieve symmetric pulses using current mirroring topologies due to

part tolerances, and electrode polarity switching can sometimes create asymmetric responses in stimulated nerves due to the physical change in anodic and cathodic electrode placement.

In the LT6375, the output current I is related to the control voltage V_{CTRL} by equation (2.1) below.

$$I = \frac{V_{CTRL}}{R_S} \tag{2.1}$$

Here, R_S is a current limiting resistor which we choose while populating the Bionode PCBA such that the specified stimulation current amplitude and precision are met. For example: let's say the Bionode is designed to provide a maximum stimulation current of 1 mA through a 10 kΩ electrode impedance. Because the output voltage range for the DAC which provides V_{CTRL} is -0.9V to 0.9V, R_S is set to 800 Ω; allowing the HCS to provide current outputs ranging from -1.125 mA to 1.125 mA. In order to drive this current across a 10 kΩ electrode impedance, the HCS is powered by a ± 10.5 V supply allowing a maximum voltage of 10.5V to appear at the output terminal.

Stimulation waveforms are created by the 12-bit DAC7551 DAC which is controlled by the Bionode's onboard NRF51822 microcontroller via a serial peripheral interface (SPI). These stimulation waveforms are biphasic rectangular pulses defined by the user in terms of amplitude, pulse width (T$_{PW}$), interphasic delay (T$_{IPD}$), and pulse repeat time (T$_{PRT}$) (Figure 2.11).
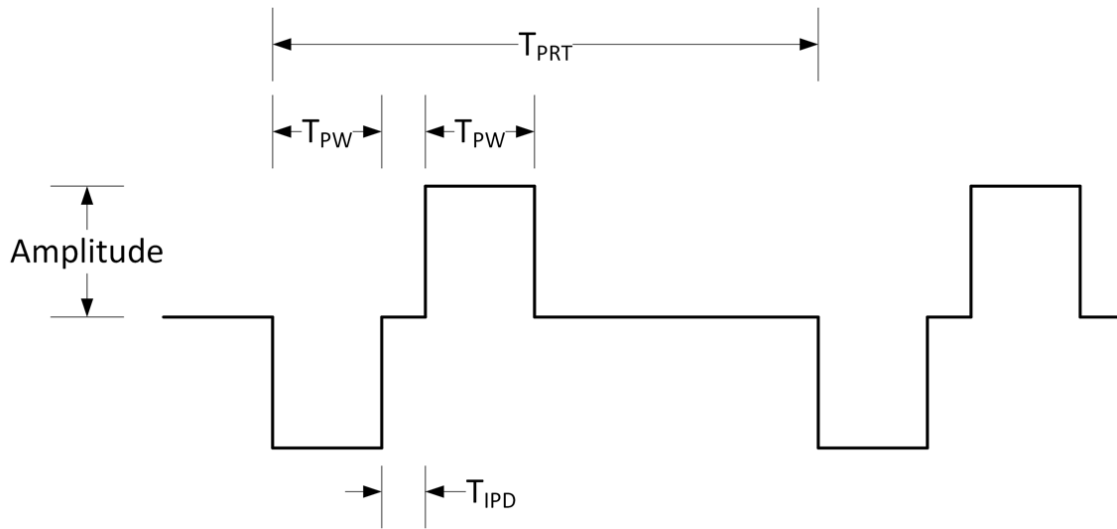
Figure 2.11. The biphasic stimulation waveform is defined in real time by the user via the Bionode's bi-directional communication interface. The aspects of the stimulation waveform that are settable by the user are its amplitude, pulse width (T_{PW}), interphasic delay (T_{IPD}), and pulse repeat time (T_{PRT}).

The user defines these parameters using the Bionode DataView application (See Section 2.2.4) which subsequently instructs the Bionode to set interrupt registers in its onboard NRF51822 microcontroller. These interrupt registers define the stimulation waveform by specifying when DAC output voltage updates must occur.

A single-pull double-throw switch between the DAC output and the HCS input avoids a documented start-up glitch on the output of the DAC that appears when the DAC is first powered on. If not avoided, this glitch will cause the HCS to output an unwanted stimulus pulse every time the Bionode is powered on. This switch is controlled by the onboard NRF51822 microcontroller and has a pull-down resistor attached to the control line which ensures that the switch is in position 0 even when the microcontroller is powering on. When at position 0, the switch connects the V_{CTRL} line of the HCS to ground, causing the stimulator to not output any current. When at position 1, the switch connects the output of the DAC to V_{CTRL}, allowing the DAC to control the current output of the stimulator circuit. For safety reasons, the switch is only set to position 1 when the user has specified that stimulation should occur. Table 2.3 shows a list of key performance specifications for the stimulator.

Table 2.3: Performance characteristics of the Bionode Stimulator

	Value	**Units**
Voltage headroom	10.5	V
Current amplitude[1]	0.0005-1.050	mA
Current amplitude resolution	0.513	μA
Pulse width (T_{PW})	25-8.36e6	μs
Pulse width resolution	1	μs
Pulse rate	1e-5-20	kHz
Charge balance error[2]	<0.3	%

[1]Over a 10 kΩ load

[2]PW = 200 μs, IPD = 500 μs, PRT = 1000 μs, amplitude = 500 μA

The voltage headroom is determined by the maximum voltage provided to the Bionode by the Powernode (See Section 2.2.5). Current amplitude limits are set by the maximum voltage headroom available over a 10 kΩ load. The current amplitude resolution is determined by the 12-bit DAC, which can set V_{CTRL} to 4096 distinct levels. This translates to 4096 different current amplitudes available over a 2.1 mA range. The pulse width's lower limit is determined by the maximum speed at which the 12-bit DAC can be updated via the SPI interface. The upper limit of the pulse width is set by the maximum value of the timer in the microcontroller that controls the stimulation waveform timing (See Section 2.2.4). We pre-scale the onboard high frequency clock to drive this timer at a rate of 1 MHz, which sets the pulse width resolution. If higher resolution is desired, this timer can be set to increment as fast as 16 MHz by modifying the pre-scaling factor of the high frequency clock. Similarly, the pulse rate timing limits are set by the timers in the microcontroller. Section 2.2.4 describes these timers in more detail.

We determined the charge balance error (CBE) by connecting the output of the stimulator across a 9.65 kΩ load and applying an alternating-phase stimulation waveform with a pulse width of 200 μs, pulse repeat time of 500 μs, and amplitude of 500 μA. We created the alternating-phase stimulation waveform by setting the inner-phasic delay to be equal to half of the pulse repeat time. This allowed the stimulator to produce both the negative and positive stimulation pulses from a

consistent baseline. While stimulating, we measured the voltage across the load with an oscilloscope. One period of this stimulation is shown in Figure 2.12.
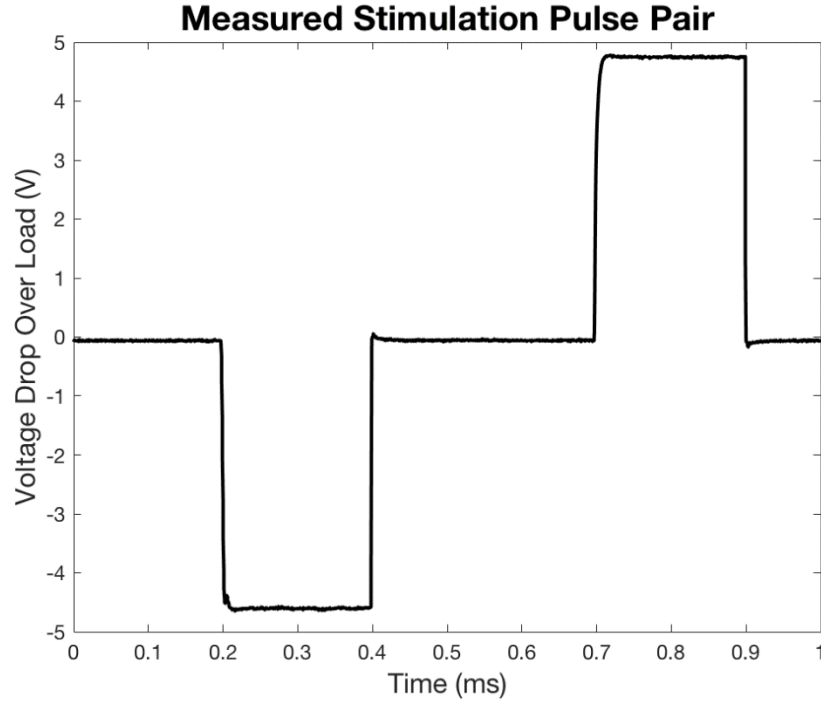
Figure 2.12. Measured voltage drop over a 9.65 kΩ load while stimulating with an alternating phase constant current waveform with PW=200 µs, IPD = 500 µs, and Amplitude = 500 µA.

We calculated the CBE using equation (2.2) as provided by [102].

$$CBE\ Percentage = \frac{\sum cations - |\sum anions|}{\sum cations + |\sum anions|} * 100 \tag{2.2}$$

To calculate the summations of cations and anions, we first converted the voltage waveform into current by dividing each data point shown in Figure 2.12 by the value of the load (9.65 kΩ). The $\sum cations$ is equal to the total positive charge injected, which is equal to the sum of all data points during the second half of the stimulus pulse phase. The $\sum anions$ is equal to the total negative charge injected, which is equal to the sum of all data points during the first half of the stimulus phase. Therefore, the CBE percentage in this case is the total charge accumulated across the load during a single period of alternating-phase stimulation as a percentage of total charge injected across the load during the same period.

Initially, the comparator, blocking capacitor (C_D), and discharge switch seen in Figure 2.10 were not included in the stimulator circuit. We added these elements to the stimulator circuit after we observed unwanted DC offsets in the stimulator output. Some of these offsets were due to documented offsets that exist in the DAC7551. The comparator allows the microcontroller to determine if the DAC7551 is properly centered around ground by periodically reading the output of the comparator between stimulation pulses and updating the DAC output to compensate. We added the blocking capacitor C_D to further ensure that no unwanted DC offsets in the stimulator are transferred to the positive stimulation electrode. Between stimulation pulses, the output of the stimulator is connected to ground via the discharge switch which discharges C_D and shunts any unwanted stimulation output to ground. The discharge switch is normally closed, so unwanted stimulator circuit outputs experienced during startup are shunted to ground as well.

While updating the stimulation circuit, I noticed that a start-up glitch was appearing across the load resistor that we were using to test the circuit. This was not due to the known start-up glitch output of the DAC because the DAC Glitch Switch was properly working. Because unwanted electrical stimulation is unacceptable in a chronically implanted device, it was imperative that this start-up glitch was removed. I determined through experimentation that the unwanted stimulation during start-up was being caused by an undocumented output glitch on the LT6375 current source when it was turning on. We removed this glitch by inserting two normally open switches (Analog Devices ADG1401) between the LTC6375's rails and their power supplies (See Figure 2.13). This allows us to keep the LTC6375 unpowered until we can shut the Discharge Switch. Once the Discharge Switch is shut, we power on the LTC6375. Because the Discharge Switch is shut, the output glitch shunts directly to ground instead of to the stimulation leads. These switches when working in conjunction with the DAC Glitch Switch and the Discharge Switch have allowed us to completely remove start-up stimulation glitches from the stimulation circuit.
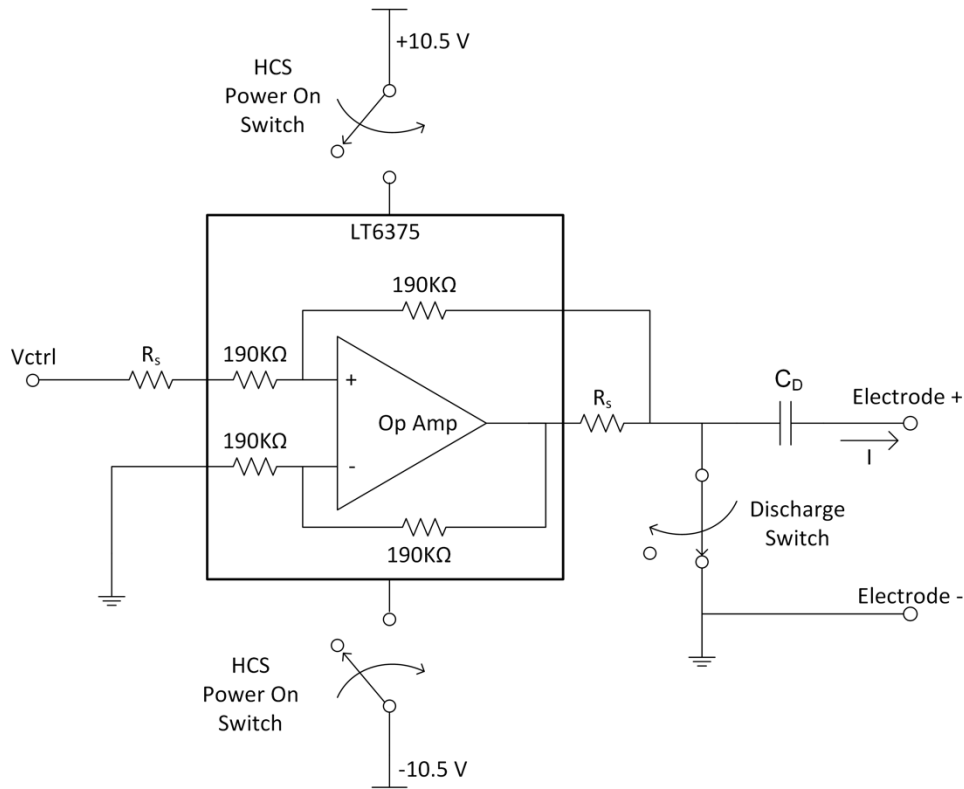
Figure 2.13. Two normally open switches (Analog Devices ADG1401) ensure that the Howland current source (HCS) is not powered on until the NRF51822 microcontroller can ensure that the Discharge Switch is closed. This shunts the start-up glitch outputs of the HCS directly to ground instead of across the electrodes.

2.2.3.3 In-Vivo Results

We tested stimulation and recording with the Bionode on a rat under isoflurane anesthesia [103]. The rat's body temperature was controlled to 36.5-37.0 °C using a heating pad with a rectal thermometer feedback sensor (Harvard Apparatus 50-7212). Twisted pair 125-µm insulated stainless steel electrodes were placed in left fimbria and right CA1 stratum radiatum. In this configuration, the postsynaptic response is mediated by axons of CA3 pyramidal neurons on the left, and is recorded as a negative wave lasting about 7 ms. The 6 stimuli delivered at 20 ms reveal the phenomenon of frequency potentiation, as expected for this pathway. Each stimulus pulse was of the form of a bi-phasic negative-leading pulse with an amplitude of 1 mA, a pulse width of 100 µs, an interphasic delay of 100 µs, and a pulse repeat time of 50 ms.
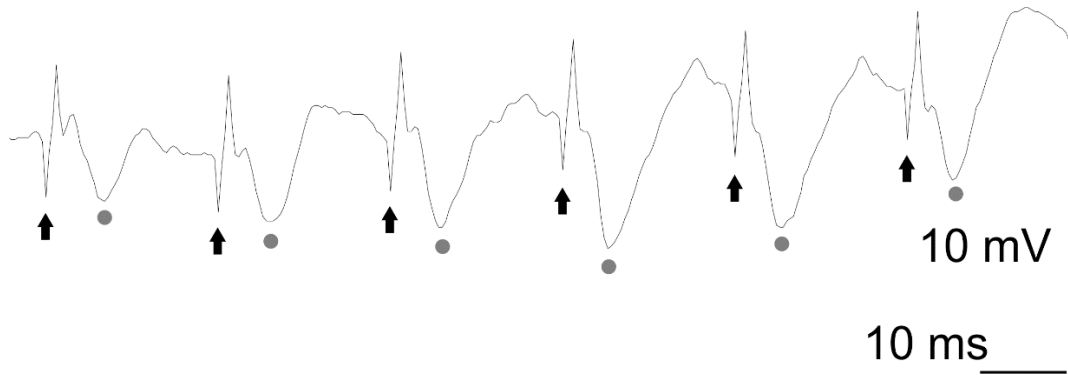
Figure 2.14. Evoked responses in the hippocampus in-vivo. Responses recorded in the right hippocampal CA1 stratum radiatum evoked by stimuli to the left fimbria. Arrows mark the stimuli and grey circles mark the peak postsynaptic responses.

2.2.4 Bi-directional Communication

Bidirectional communication (the ability to transmit and receive data) greatly increases the flexibility and possible application space of an implantable device. Not only does the ability to transmit data remove the burden of on-board data storage from the implantable device, it also allows the device to communicate its current status and settings in real time. Furthermore, the ability to receive data allows the implantable device to be configured, calibrated, and instructed before, during, and after implantation; increasing its adaptability to varying circumstances. An implantable device that can both receive and transmit data has the added benefit of allowing an external user or system to reactively send instructions to the implantable device based on recorded data obtained by the implantable device; effectively creating a closed-loop system.

While the benefits of bidirectional communication are great, it poses some specific challenges to the design of a small, power efficient implantable device. These challenges, namely power consumption and data robustness are addressed in the design of the Bionode, and our custom bidirectional communication system is described here.

2.2.4.1 Bionode and Base Station Firmware

The major challenge of implementing bidirectional communication in an implantable device is handling the increased power consumption introduced by radio communication circuitry. In many cases, including in the Bionode, the most power-hungry system on an implantable device is the

transmit/receive radio. Power consumption for the Bionode is greatly reduced while transmitting and receiving data by tightly coordinating when data transmissions occur.

The Nordic NRF51822 microcontroller on the Bionode handles all data telemetry moving into and out of the device. This microcontroller was specifically chosen because of its low-power sleep states, small size, on-board radio, and on-board analog to digital converter (ADC). Because this microcontroller only draws 2µA of current when it is in sleep mode, and draws 20mA of current when the radio is activated, I designed an interrupt-driven firmware program to keep the microcontroller in sleep mode with the radio deactivated as long as possible. This interrupt driven design is illustrated in Figure. 2.15.

Figure. 2.15. When the microcontroller turns on, it begins executing code starting at the firmware entry point. Once the initialization code is completed, the microcontroller enters "Wait for Interrupt" (WFI) mode. In the WFI mode, the microcontroller remains in sleep mode until an interrupt triggers an interrupt request handler function. When the microcontroller completes all instructions in a triggered interrupt handler function, it re-enters the low-power sleep mode if no other interrupts are pending. The microcontroller executes concurrent interrupts based on their priority setting (low priority setting = high priority). The parallel peripheral interface (PPI) allows interrupts generated by peripheral devices to trigger events in other peripherals without waking up the microcontroller.

Firmware Entry Point

Power On → Start clocks → Initialize peripherals and PPI → Set interrupt priorities → Enable interrupts → Start acquisition timer → Enter "Wait for Interrupts" (WFI) mode

Stimulation Timer Interrupt

Stimulator IRQ Handler (Priority 0)

Start

Disable stimulator interrupt

Update stimulator switch logic

Update DAC Level

Clear timer compare registers

Enable stimulator interrupt

End

ADC Data Ready Interrupt

Acquisition IRQ Handler (Priority 1)

Start

Disable ADC data ready interrupt

Update current ADC input

Shift ADC buffer data into radio buffer

Radio buffer full? — No

Yes

Construct radio packet and initiate TX

Handshake interval met? — No

Yes

Set handshake flag

Enable ADC data ready interrupt

End

Radio RX Interrupt

Radio IRQ Handler (Priority 2)

Start

Disable radio interrupt

Handshake expected? — No

Yes

Update all registers using RX packet info

Acquisition registers modified? — No

Yes

Reset acquisition timer

Stimulation registers modified? — No

Yes

Reset stimulation timer

Enable radio interrupt

End

DAC Out Compare Timer Interrupt

DAC Out Compare IRQ Handler (Priority 3)

Start

Disable DAC out compare interrupt

Stimulator activated? — No

Yes

DAC out compare low? — No

Yes

Increase zero calibration point

Decrease zero calibration point

Update DAC output

Enable DAC out compare interrupt

End

Parallel Peripheral Interfaces (PPI)

Acquisition Timer Interrupt → Trigger ADC Sample

Handshake Timeout Timer Interrupt → Turn off Radio RX

When the NRF51822 powers on, it loads the Bionode firmware image from its onboard non-volatile flash memory and begins executing instructions at the firmware entry point. The firmware entry point is an initialization function that first activates high and low frequency on-board clocks which are used to run various on-board timers to drive interrupts. The initialization function then initializes and activates onboard ADC, radio, and timer peripherals as well as the parallel peripheral interface (PPI) and general purpose input/output (GPIO) pins. The timer peripherals (See Table 2.4) coordinate the microcontroller's handling of the stimulation, acquisition, and radio circuits by generating interrupts at set intervals. The PPI allows peripheral interrupts (in this case timers) to directly trigger actions in other peripherals (e.g. the ADC or radio) without waking up the microcontroller. The GPIO pins allow the microcontroller to write or read transistor-transistor logic levels to other integrated circuits on the Bionode (e.g. SPI pins on the DAC and switch logic inputs in the stimulator circuit).

Table 2.4: NRF51822 Peripheral Timers

Timer Name	Description
Stimulation Timer	Coordinates the timing of the stimulation circuit to generate user-specified stimulation waveforms (See *Figure 2.11*)
Acquisition Timer	Sets the acquisition sample rate by directly triggering the ADC (via the PPI) to sample data from the AFE output.
Handshake Timeout Timer	Shuts down the radio RX circuitry (via the PPI) when a handshake timeout has occurred.
DAC Out Compare Timer	Indicates when it is time to poll the DAC output comparator (See *Figure 2.10*) and update the DAC zero-level.

After the microcontroller has initialized the peripherals, PPI, and GPIO pins, it sets the priority levels for each of the four interrupts as indicated in Figure. 2.15. These priority levels instruct the microcontroller how to handle concurrently occurring interrupts. If the microcontroller is executing the interrupt request handler function of a particular interrupt and an interrupt request is generated by an interrupt of a higher priority (indicated by a lower priority number), the microcontroller will halt execution of the current interrupt request handler and begin executing the interrupt request handler of the new, higher priority interrupt. When the microcontroller finishes

handling the new interrupt, it will resume executing the next highest priority pending interrupt's interrupt request handler function. The stimulator interrupt handler has the highest priority because the timing of the stimulation waveform must be as precise as possible to best reflect the user's desired waveform (See Section 2.2.3). Precise timing of the stimulator circuit is also important to achieve proper charge balancing. The acquisition interrupt handler has the second highest priority because maintaining a consistent sample interval is important to properly discretize continuous signals with uniform sampling [104]. Using the PPI to directly trigger ADC samples provides an additional level of precision because the ADC can be told to sample data even if the microcontroller is busy handling a higher priority interrupt. As long as the acquisition interrupt is fully handled before the next ADC sample is ready, the sample interval remains consistent. The radio and DAC out compare interrupt request handlers have lower priorities because their tasks are not as time sensitive as the stimulator or acquisition interrupt request handlers.

Once the priorities of the interrupt request handlers have been set, the initialization function enables all four interrupts, starts the acquisition timer, and enters "Wait for Interrupt" (WFI) mode. While in WFI mode, the microcontroller stays in a low-power sleep mode, drawing minimal current (~2 µA). The microcontroller only wakes up when an interrupt triggers one of the four interrupt requests.

Bidirectional communication is achieved by enforcing a coordinated handshake protocol with the custom designed external Base Station to facilitate all communication between the Bionode and any outside user (Figure. 2.16). After the Bionode acquires 40 data samples from its ADC, the Bionode's microcontroller initiates a data-packet transmission to the base station using the onboard 2.4 GHz ISM band radio. In most cases, the radio is only activated during this transmission which lasts approximately 1 millisecond. However, the 100th data packet initiates a hand-shake with the Base Station. Immediately after transmitting the 100th data packet, the Bionode sets its radio to receive mode, and listens for a data packet from the Base Station for no more than 10 milliseconds. This gives the base station an opportunity to send a single data packet to the Bionode. The 10 millisecond time-limit is enforced by the handshake timeout timer (See Table 2.4). The single data packet contains a 45-byte long payload, which is used to set firmware registers in the Bionode microcontroller that store data acquisition, stimulation, and communication settings. Because the

payload contains values for all writeable firmware registers on the Bionode, the Bionode is fully configured and instructed during this single transmission.
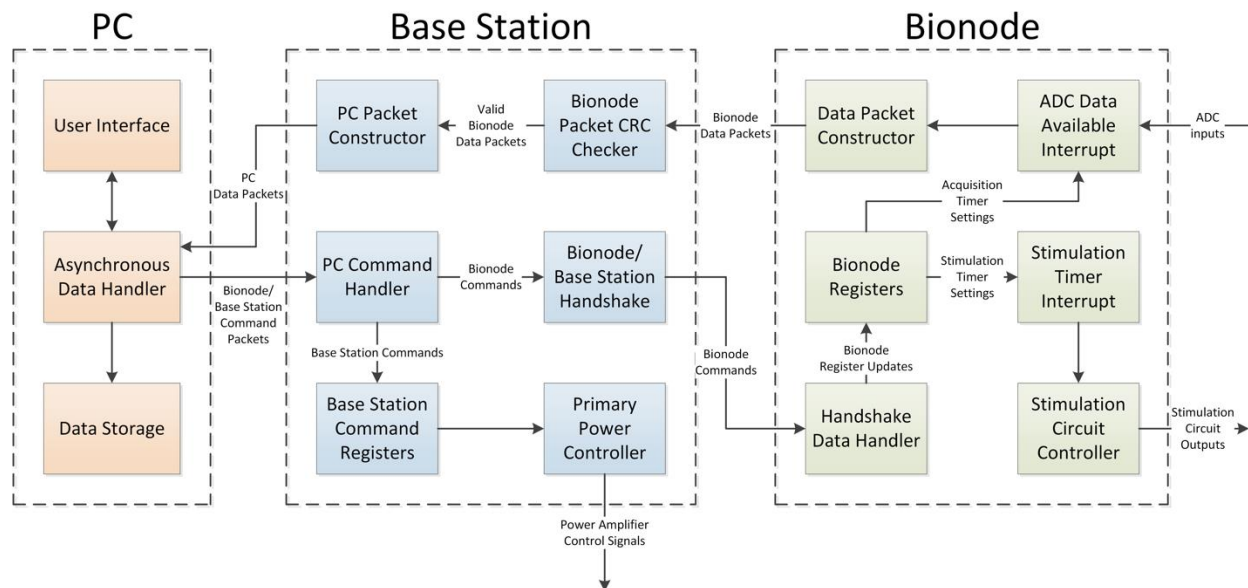
Figure. 2.16. The Base Station facilitates all communication between the PC and the Bionode. The user can specify Bionode recording and stimulation parameters or Base Station settings by sending an update packet to the Base Station via the PC application. The Base Station then relays the packet to either to its own register update or to the Bionode during the next Base Station handshake. All data recorded by the Bionode is packetized and wirelessly transmitted to the Base Station via the Bionode's onboard radio. These packets are then relayed to the PC the Base Station's Wi-Fi link to the PC. All incoming data to the PC can be stored on the PC's onboard hard drive.

This handshake driven communication scheme allows the Bionode to transmit acquired data rapidly, while maintaining the ability to receive data from an outside source with minimal radio activation time. For example: given a data acquisition sample rate of 5 kHz, the Bionode's radio will transmit 125 data packets per second and initiate a handshake once every 800 milliseconds. Given the described radio on-time, bidirectional communication can be achieved with the radio being deactivated 86.7% of the time. If this handshake latency is too large for a particular application, it can be reduced at any time by ether increasing the sample rate or by reducing the handshake packet interval.

Another challenge in any wireless communication scheme is increasing data robustness. In order to properly analyze any data recorded by the Bionode, the ability to identify when data has been

corrupted or lost is essential. Data can be corrupted or lost during wireless transmission if it is blocked by something that can absorb RF energy, if a nearby device communicating on the same frequency creates interference, or if the distance between the Bionode and the base station exceeds the transmission range of the Bionode. Data can also be lost if the Bionode suddenly loses power during data acquisition or transmission.

We design methods into the Base Station to detect corrupted or lost data packets. Before sending data packets to the Base Station, the Bionode appends a 2-byte cyclic redundancy check (CRC) to the end of the packet (See Figure 2.17). The base station uses this CRC to determine the validity of all incoming data packets. Corrupted data packets failing this CRC are discarded by the Base Station. To make lost data packets detectable, the Base Station appends a time stamp at the end of all incoming packets. These time stamps can be used to determine not just if data samples are missing from the acquired data stream, but how many data samples are missing, which is crucial for data analysis. The use of these time stamps to generate a uniformly sampled data stream is covered in more detail in Chapter 3.
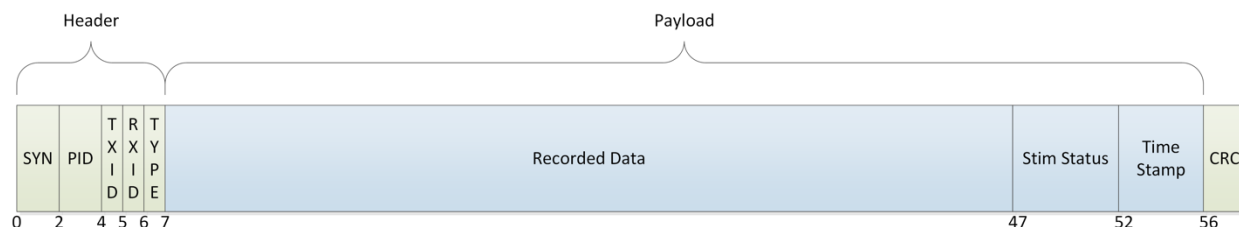
Figure 2.17: The wireless data packet is comprised of a header, payload, and CRC. The header contains information regarding packet synchronization, transmission ID, intended receiver ID, and packet type. The payload contains different types of data defined by the packet type specified in the header. The packet shown here is a data packet, so the payload contains recorded data samples, stimulation status bits for each recorded sample, and a timestamp. The CRC at the end of the packet is used to ensure that invalid packets are detectable.

The data packet shown in Figure 2.17 consists of three sections: a header, a payload, and a CRC. All packets that are transmitted to and from the PC, Base Station, and the Bionode contain the same header and CRC sections. The payload section varies depending on the type of data being transmitted in the packet. The header section is used by the Base Station to properly route all packets it receives, and can also be analyzed to determine if a packet has been routed incorrectly.

The leading "SYN" bytes consists of the bit-code 0xA55A (1010 0101 0101 1010). These bytes allow the beginning of a data packet to be found in cases where partial packets may be missing from the data stream. This is most likely to occur during a serial transmission that occurs between the Base Station's NRF51822 microcontroller and the Base Station's onboard Raspberry Pi. The next bytes in the data packet contain an incrementing packet ID number. This number is set and incremented by whatever is sending the data packet (the PC, the Base Station, or the Bionode) and is used to determine if packets have been missed by the receiver. The next two bytes in the packet contain the ID numbers of who sent the packet (0 = PC, 1 = Base Station, 2 = Bionode, 3 = Invalid), and who the intended receiver is. These bytes tell the Base Station where to route all incoming packets and inform the receiver of where the incoming data packet came from. The final byte of the header contains the type ID of the packet which indicates what kind of data is contained in the payload. The types of payload data and their associated type IDs are shown in Table 2.5.

Table 2.5: Packet Type Identification Numbers

Type ID	Packet Type
0	8-bit data sampled by the Bionode
1	10-bit Data sampled by the Bionode
2	Lead impedance measurement (legacy)
3	Thermistor reading from the Bionode (legacy)
4	Bionode register configuration
5	Base station register configuration
6	Identification response
7	Identification ping
8	Invalid packet
255	Shutdown Base Station Command

Some of the data contained in the header of the transmission packet contain redundancies which are useful for determining if corrupted data has been transmitted. For example, it has been observed that a data-packet containing all zeros is sometimes transmitted over the UDP interface between the Base Station and the PC. This packet was marked as valid by the Bionode DataView software because a packet containing all zeros passes the CRC check. However, this packet could be later

determined to be invalid by noting that the data packet had a type ID of zero which corresponds to an 8-bit data sample packet from the Bionode while the TXID of the packet was also zero, indicating that the packet originated from the PC. Because the PC cannot generate a packet of this type, the data packet could be deemed as invalid. This check is now in place to filter out these errant all-zero packets.

When the Bionode is instructed to record in 8-bit mode, it saves one sample in each byte of the Recorded Data section of the Payload; allowing it to send 40 samples per packet. However, if the Bionode is instructed to record in 10-bit mode, it records each sample using 1.2 bytes of the Recorded Data section of the Payload; allowing it to send 32 samples per packet. The Bionode stuffs these 10-bit samples together so that no space is wasted in the Payload. Because of this, it is crucial that the packet header indicates what the data resolution is in order for it to be properly decoded down the line.

Finally, the Bionode has the ability to request a re-transmission of a missed handshake by simply not incrementing its packet ID counter whenever an expected handshake is not received. This causes the Base Station to continually re-transmit the handshake packet until the Bionode indicates that it has received the handshake by incrementing its packet ID counter.

2.2.4.2 PC Graphical User Interface

Users communicate with the Bionode via the Base Station using a software application called Bionode DataView. This application is implemented in Python (Figure. 2.18). I decided to use Python because it is open source and easily portable to Macintosh, Windows, and Linux operating systems, which allows the application to be built and deployed to a wide range of computing devices. To further increase the ease of deployment, I designed the base station to create its own Wi-Fi connection which allows any device with Wi-Fi capabilities to communicate with the base station without the need of additional drivers. The Bionode DataView application provides a GUI that displays all acquired data and current Bionode and Base Station settings in real time. The user interface allows the user to set Bionode stimulation parameters as well as initiate and terminate stimulation sessions. All incoming data packets can be recorded into a binary data file. These raw binary files can be either analyzed directly, or exported as .wav files and easily imported by

multiple data analysis tools (e.g. MATLAB®, Spike2, etc.). When the binary data file is generated, the application automatically generates a header packet that contains the date and time that the file was generated, as well as the sample frequency and number of recording channels being used by the Bionode at the time of the generation of the file. This information is important when analyzing the recorded data as shown in Chapter 3.
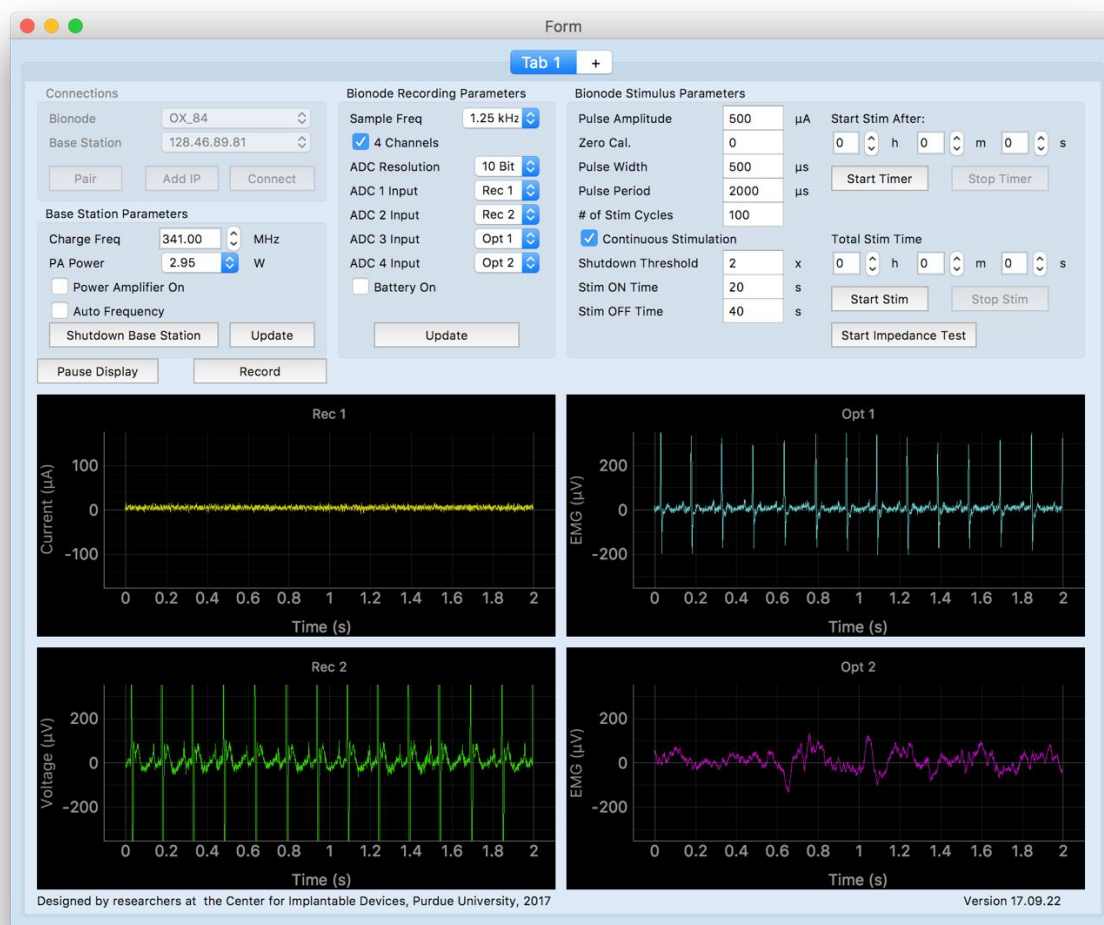
Figure. 2.18. The Bionode DataView application provides access to all of the settings for the Bionode and Base Station. All incoming biopotential recordings are displayed in real-time.

The Bionode DataView application's main two tasks are to give the user the ability to update Bionode and Base Station registers and to acquire, record, and display incoming data packets from the Base Station. Upon startup, the application first reads in configuration files that contain information about both the Bionode and the Base Station (e.g. Bionode communication frequency,

AFE gain settings, Base Station IP address, etc…). These configuration files are plaintext files that allow the user to add any number of Bionodes and/or Base Stations to their environment. Once the configuration files are loaded, the Bionode Dataview application loads and displays the graphical user interface. A software flow diagram of the Bionode DataView application is shown in Figure 2.19.
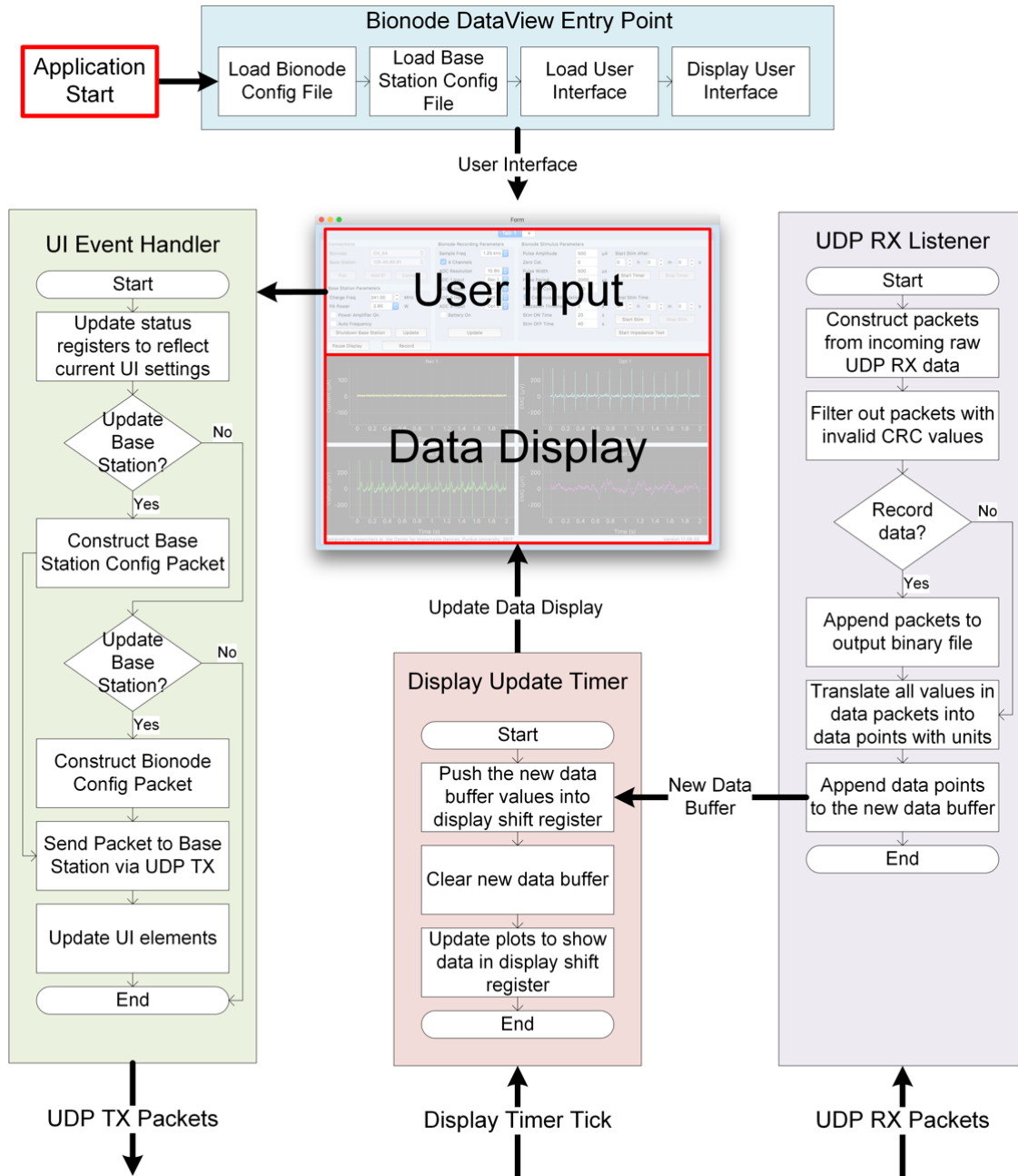
Figure 2.19: After loading the configuration files, the Bionode DataView application loads and displays the graphical user interface (GUI). User input is handled by an event handler that updates UI registers and constructs and transmits Bionode or Base Station configuration packets when necessary. Incoming data is packetized and saved in a buffer by the UDP RX Listener thread. The data plots on the GUI are refreshed at a rate of 50 Hz as defined by the free-running display timer which runs the Display Update Timer function once per tick. User inputs via the GUI trigger the UI Event Handler which updates status registers and initiates handshake packet transmissions to the Base Station when the user indicates that updates should be pushed out to the Base Station or the Bionode.

Upon starting the Bionode DataView application, the user must choose both a Base Station and a Bionode to connect to. Once the user makes these selections and presses the "Connect" button, the Bionode DataView application initiates a User Datagram Protocol (UDP) connection to the Base Station to allow for both TX and RX via UDP. The Bionode DataView application sends an initial ID packet to the Base Station so that the Base Station can bind its TX port to the Bionode DataView's RX port and vice versa. At this time, the all packets sent out by the Base Station are routed directly to the Bionode DataView's RX UDP Port. Likewise, all packets sent out by the Bionode DataView's TX UDP Port are routed to the Base Station's RX UDP Port.

When the user inputs data into the user interface, the UI Event Handler records the Base Station and Bionode settings into internal status registers. If the user indicates that a Bionode or Base Station configuration setting should be sent to the respective device, the UI Event Handler constructs either a Base Station or Bionode configuration packet using the current values of the internal status registers. Once the configuration packet has been constructed, it is sent to the Base Station via the UPD TX interface. The Base Station subsequently routes the configuration packet to the correct device (See Figure. 2.16). After the packet is sent, the UI Event Handler may need to update certain UI elements to reflect the new Base Station or Bionode configuration settings (e.g. change the display plot time axis to reflect an updated sample rate).

A separate thread called the UDP RX Listener acquires raw data from the Base Station in the background while the GUI runs. Whenever data comes in on the UDP RX port, the UDP RX Listener thread packetizes the raw data and checks each packet's CRC to filter out invalid packets and determine if a loss of packet synchronization has occurred. If the user has indicated that incoming data should be saved, all valid packets are appended to a binary output file. All Bionode Data packets are then translated into data points with units as described by the Bionode configuration file which specifies each Bionode's recording channel gain, units, and offsets. This allows the data points to be properly displayed on the plots in the GUI. The data points are finally written to a new data buffer which holds all data points that have not yet been displayed on the GUI. Because the UPD RX Listener function is in a different thread than the Bionode DataView UI elements, it is should not modify the UI elements directly. Therefore, to display the data points held in the new data buffer a free-running timer called the Display Update Timer is used to trigger

display updates at a rate of 50 Hz. The display is updated by pushing all of the data points in the new display buffer into the display data shift register and then clearing the new display buffer. This simultaneously shifts the newest data into the display data shift register while shifting out the oldest data. The data plots in the GUI are then updated to display the data contained in the display data shift register. The free running Display Update Timer and the UDP RX Data Listener enable the Bionode DataView plots to update in real time at a rate of 50 Hz for total sample rates as fast as 25 kHz without noticeable lag when running on most modern laptops.

When the Bionode DataView application records data in binary format, all information from all valid incoming data packets is saved (including the header, payload, and CRC). This is vital for finding and fixing corrupted data packets, data packets sent out of order, or duplicate data packets. Because all bytes from every packet are recorded, the raw data from every data packet can be easily viewed within the binary file if the data is organized in 58 byte columns as shown in Figure 2.20 below.

	SYNC	PID	TXID	RXID	TTYPE	Recorded Data	Stim Status	Time Stamp	CRC
58	A55A	0000	0200	00F0	F0F0 F1F1 F1F2 F2F2 F3F3 F3F3 F4F3 F4F4 F4F4 F5F5 F5F5 F5F5 F6F6 F6F6 F6F6 F7F7 F7F7 F7F7 F8F7 F800	0000 0000	000B 0EE6	0022
116	A55A	0000	0200	00F1	F2F2 F2F3 F3F3 F4F4 F4F4 F5F5 F5F5 F6F6 F6F6 F7F6 F7F7 F7F7 F8F8 F8F8 F8F8 F9F9 F9F9 F9F9 FAF9 FA00	0000 0000	000B 1135	CF4C
174	A55A	0001	0200	033B	7BA5 6157 F03C 3561 57F2 3CB5 6156 F3FD 2561 56F5 7D75 6156 F6FD D561 56F7 FE25 6156 F93E 6561 5602	8000 0000	000B 1224	3A6E
232	A55A	0002	0200	01F7	FD15 6156 F57D 8561 56F7 3DE5 6156 F87E 3561 56F9 BE85 6156 FABE C561 56FB 7EF5 6156 FC7F 3561 5600	0000 0000	000B 12EC	0071
290	A55A	0003	0200	01FA	FDD5 6156 F87E 3561 56F9 BE95 6156 FB3E E561 56FC 3F25 6156 FD3F 5561 56FD FF95 6156 FEBF B561 5602	8000 0000	000B 13B4	6CFC
348	A55A	0004	0200	01FC	FE65 6156 FA7E C561 56FB FF15 6156 FCFF 6561 56FE 3F95 6156 FEFF D561 56FF BFF5 6156 FFFF F561 5600	0000 0000	000B 147C	A7D6
406	A55A	0005	0200	01FE	BED5 6156 FC3F 2561 56FD 7F75 6156 FE7F B561 56FF 7FF5 6156 FFFF F561 56FF FFF5 6156 FFFF F561 5602	8000 0000	000B 1544	8CC2
464	A55A	0006	0200	01FF	BF25 6156 FD3F 7561 56FE 7FC5 6156 FFBF F561 56FF FFF5 6156 FFFF F561 56FF FFF5 6156 FFFF F561 5600	0000 0000	000B 160C	0C0D
522	A55A	0007	0200	01FF	FF55 6156 FDFF A561 56FF 3FE5 6156 FFFF F561 56FF FFF5 6156 FFFF F561 56FF FFF5 6156 FFFF F561 5602	8000 0000	000B 16D4	BFFF
580	A55A	0008	0200	01FF	FF75 6156 FE7F C561 56FF BFF5 6156 FFFF F561 56FF FFF5 6156 FFFF F561 56FF FFF5 6156 FFFF F561 5600	0000 0000	000B 179C	2919
638	A55A	0009	0200	01FF	FF85 6156 FEFF D561 56FF FFF5 6156 FFFF F561 56FF FFF5 6156 FFFF F561 56FF FFF5 6156 FFFF F561 5602	8000 0000	000B 1864	88EA
696	A55A	000A	0200	01FF	FFA5 6156 FF7F F561 56FF FFF5 6156 FFFF F561 56FF FFF5 6156 FFFF F561 56FF FFF5 6156 FFFF F561 5600	0000 0000	000B 192C	95DB
754	A55A	000B	0200	01FF	FFC5 6156 FFFF F561 56FF FFF5 6156 FFFF F561 56FF FFF5 6156 FFFF F561 56FF FFF5 6156 FFFF F561 5602	8000 0000	000B 19F4	4C34
812	A55A	000C	0200	01FE	FED5 6156 FC3F 2561 56FD 3F65 6156 FE3F 9561 56FE BFC5 6156 FF3F E561 56FF BFF5 6156 FFFF F561 5600	0000 0000	000B 1ABC	F304
870	A55A	000D	0200	01FE	3EB5 6156 FBBF 0561 56FC FF55 6156 BFB5 6156 FE3F F561 56FF BFF5 6156 FFFF F561 5602	8000 0000	000B 1B84	0EED
928	A55A	000E	0200	01FE	7EC5 6156 FBFF 1561 56FD 3F65 6156 FE3F A561 56FE FFD5 6156 FFBF F561 56FF FFF5 6156 FFFF F561 5600	0000 0000	000B 1C4C	14B8
986	A55A	000F	0200	01FE	FEE5 6156 FC7F 3561 56FD BF85 6156 FEBF C561 56FF 7FF5 6156 FFFF F561 56FF FFF5 6156 FFFF F561 5602	8000 0000	000B 1D14	87A4
1044	A55A	0010	0200	01FF	7F05 6156 FCFF 6561 56FE 3FA5 6156 FF3F E561 56FF FFF5 6156 FFFF F561 56FF FFF5 6156 FFFF F561 5600	0000 0000	000B 1DDC	9C06
1102	A55A	0011	0200	01FF	FF25 6156 FDBF 8561 56FE FFD5 6156 FFFF F561 56FF FFF5 6156 FFFF F561 56FF FFF5 6156 FFFF F561 5602	8000 0000	000B 1EA4	4C5E
1160	A55A	0012	0200	01FF	FF45 6156 FE3F A561 56FF 7FF5 6156 FFFF F561 56FF FFF5 6156 FFFF F561 56FF FFF5 6156 FFFF F561 5600	0000 0000	000B 1F6C	5925
1218	A55A	0013	0200	01FF	FF75 6156 FEBF C561 56FF FFF5 6156 FFFF F561 56FF FFF5 6156 FFFF F561 56FF FFF5 6156 FFFF F561 5602	8000 0000	000B 2034	897B
1276	A55A	0014	0200	01FF	FF95 6156 FF7F F561 56FF FFF5 6156 FFFF F561 56FF FFF5 6156 FFFF F561 56FF FFF5 6156 FFFF F561 5600	0000 0000	000B 20FC	586C
1334	A55A	0015	0200	01FF	FFB5 6156 FFFF F561 56FF FFF5 6156 FFFF F561 56FF FFF5 6156 FFFF F561 56FF FFF5 6156 FFFF F561 5602	8000 0000	000B 21C4	86DA
1392	A55A	0016	0200	01FF	FFE5 6156 FFFF F561 56FF FFF5 6156 FFFF F561 56FF FFF5 6156 FFFF F561 56FF FFF5 6156 FFFF F561 5600	0000 0000	000B 228C	2FE6
1450	A55A	0017	0200	01FF	FFF5 6156 FFFF F561 56FF FFF5 6156 FFFF F561 56FF FFF5 6156 FFFF F561 56FF FFF5 6156 FFFF F561 5602	8000 0000	000B 2354	B95A
1508	A55A	0018	0200	01FF	FFF5 6156 FFFF F561 56FF FFF5 6156 FFFF F561 56FF FFF5 6156 FFFF F561 56FF FFF5 6156 FFFF F561 5600	0000 0000	000B 241C	90D7

Figure 2.20: Viewing the raw binary file generated by Bionode DataView with 58 bytes per row shows the packet structure. Saving all raw data allows for better analysis of possible device failures and/or communication glitches.

In most use cases, the Bionode DataView application on a PC communicates directly with a single Base Station to control and acquire data from a single Bionode as shown in Figure 2.2. There have

been instances, however, where a single PC needs to control multiple Bionodes via multiple Base Stations. In these cases, instead of directly connecting to the PC via a WiFi interface, the Base Stations connect to the PC via a network switch as shown in Figure 2.21. In this use case, each Base Station is given its own static IP address. The Bionode DataView application is wrapped inside a top-level tabular interface, which allows multiple instances of the Bionode DataView GUI to be called inside one instance of the application. For each Base Station connection, a separate instance of the Bionode DataView GUI is instantiated. When connecting to the Base Stations in this way, dynamic port allocations are used to give each Base Station its own set of UDP TX and RX ports.
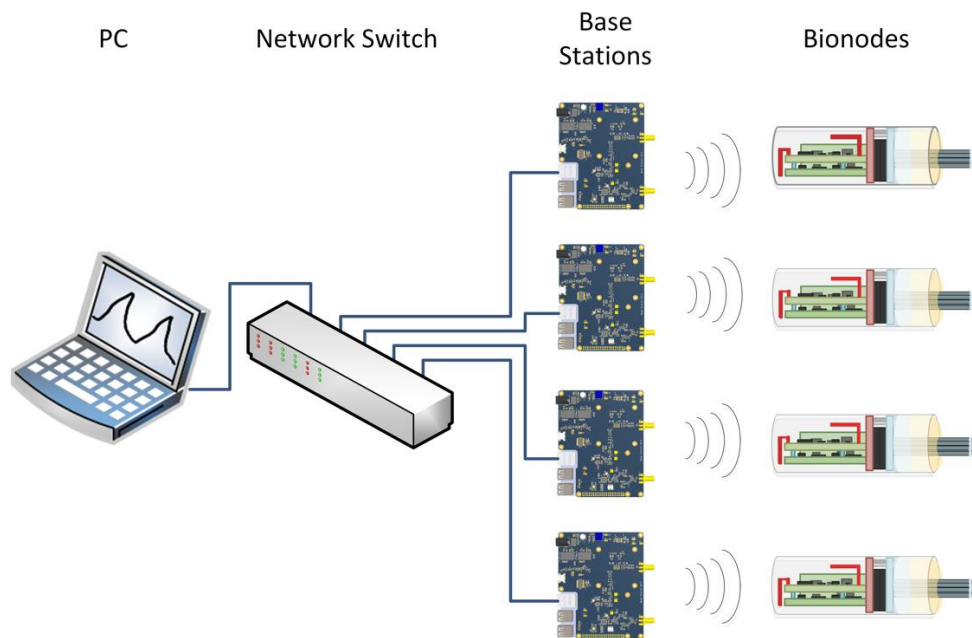
Figure 2.21. To control multiple Bionodes via multiple Base Stations, the PC can connect to the Base Stations via a network switch. In this use case, each Base Station is given its own static IP address, and multiple instances of the Bionode DataView graphical user interface are instantiated within the main Bionode DataView application.

2.2.5   Powering

Active implantable devices requiring power in the milliwatt range are typically powered using wireless EM fields, batteries, or a combination of the two [105, 106]. Other powering methods such as ambient energy harvesting, optical coupling, or ultrasonic excitation become difficult to implement when higher power is needed, deeper implantation sites are required, or small implant

size is paramount [105]. Battery solutions offer a robust method for powering implantable devices by providing stable powering during the battery's lifetime. However, this solution comes at the cost of requiring a relatively large footprint that scales with capacity [107]. Furthermore, implantable devices relying on battery power have an inherently limited device lifetime.

2.2.5.1 Wireless Powering Systems

Our way of powering an implantable device is to generate a circulating magnetic field inside a WPT chamber using resonant cavity theory [108] which removes the necessity for any primary transmit coils because the entire WPT chamber resonates. Secondary coils in the implantable device can harvest energy from the magnetic field as long as the device is appropriately oriented inside the WPT chamber. Thus, the WPT chamber provides a space where a freely moving implanted rodent can live while the implanted device is wirelessly powered [108]. Alternatively, an external wand can be used to generate a magnetic field to power and recharge the device when the WPT chamber cannot be used (e.g. when implanting a subject that cannot fit inside the chamber). The Bionode leverages either method of wireless powering through a custom designed powering module called the Powernode (Figure 2.22).
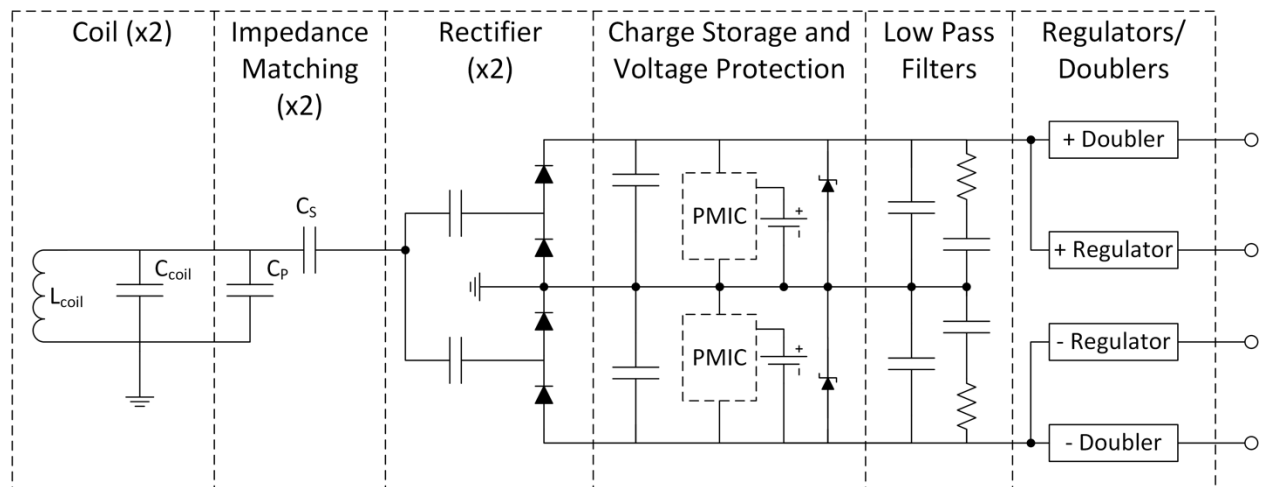
Figure 2.22. Each coil (modeled here by C_{coil} and L_{coil}) is connected directly to an impedance matching network which maximizes power transfer efficiency. Acquired AC signals are then rectified using a dual-ended rectifier to produce positive and negative DC voltages. Both rectifier outputs are then passed through passive low pass filters to remove high frequency RF noise. Positive and negative power rails for the Bionode are generated by regulating the filtered outputs of the rectifiers. Higher voltages needed by the stimulator are generated by passing the filtered rectifier outputs through positive and negative voltage doubler circuits. Optional battery charging/discharging is handled by PMICs attached to the rectifier outputs.

2.2.5.2 Powernode

The Powernode is designed as a modular board that can provide sufficient power to the Bionode. Figure 2.23 illustrates the typical power consumption of the Bionode while acquiring data at 5000 samples per second.

Bionode Power Consumption
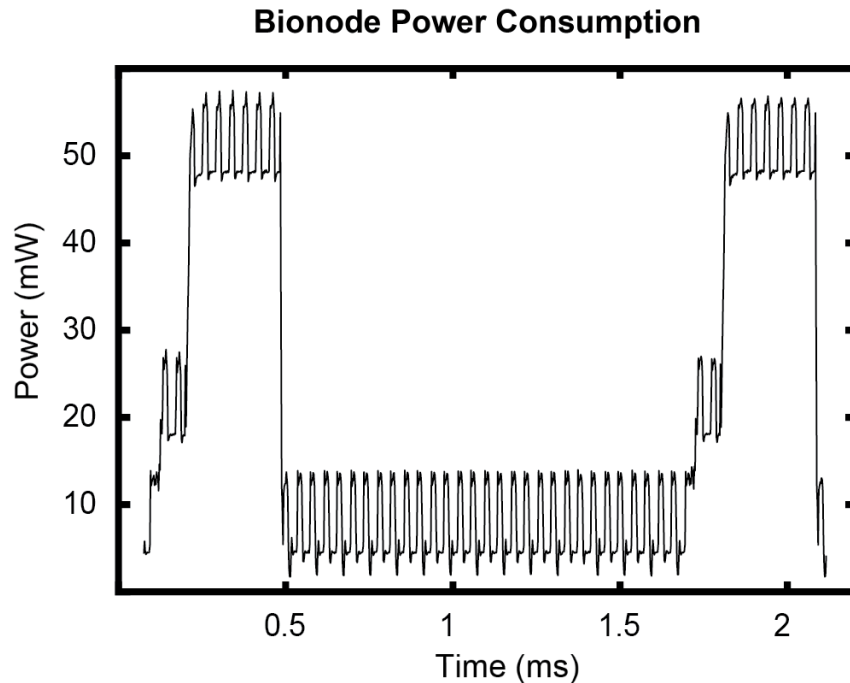
Figure 2.23. Power consumption greatly increases during the activation of the Bionode's onboard radio as illustrated in this figure between t=0 and t=0.5, and t=1.7 and t=2.2 ms. Power consumption also increases whenever the microcontroller on the Bionode initiates a sampling of the onboard ADC as illustrated by the periodic ~10 mW spikes in this figure.

To accommodate the powering requirements of the Bionode, the Powernode is designed to provide 16 milliwatts of average power with the ability to produce up to 60 milliwatts of peak power. This power is transferred to the Bionode through voltage rails that are used by the Bionode's acquisition and stimulation circuitry.

The Powernode uses two secondary coils oriented orthogonally to each other to collect energy from the circulating magnetic field inside the WPT chamber. The orthogonal orientation of these two coils allows the Powernode to more consistently collect energy while the implant is in varying orientations within the WPT chamber. The power transferred to each coil is maximized via an impedance-matching admittance inverter network on the Powernode tuned to the resonant

frequency of the WPT chamber (approximately 340 MHz). This resonant frequency is determined by the geometry of the WPT chamber. This high frequency allows us to apply up to 2 Watts of power to the chamber while staying within SAR limits. The impedance matching network consists of two capacitors (C_P and C_S in Figure 2.22) which initially have values predicted by bandpass filter theory [109-111]. These capacitor values are further tuned based off of measured resonant responses of the system. Because the coils are perpendicular to each other and their rectifiers provide high reactance between the two coils, the coils minimally affect each other's energy transfer.

The AC voltages coupled onto each coil are converted into both positive and negative DC voltages using a full wave rectifier. High amplitude voltages coming out of the rectifier are clamped using Zener diodes to protect low-voltage circuitry on the Bionode. Furthermore, to provide stable voltage rails to the Bionode, we implement RC-based low-pass filters on both the positive and negative rectifier outputs to reduce coupled AC noise from non-idealities present in the rectifier. The rectified voltages are then fed into regulators to provide the digital and recording circuitry on the Bionode with accurate, low ripple voltage supplies. To supply the higher headroom voltage required by the Bionode's stimulation circuitry, we double both outputs of the full wave rectifier using a Texas Instruments TI7660 boost converter for the positive output and an inverting charge pump for the negative output. The outputs of these doubler circuits provide the voltages required by the Bionode's stimulation circuitry to drive its constant current stimulation output.

2.2.5.3 In-Vivo Results

To determine the effectiveness of the Powernode's ability to provide power to the Bionode inside a WPT chamber, we analyzed the data gathered during a study involving a freely moving rat with an implanted Bionode. We placed the rat inside the WPT chamber for 1.6 hours, and continuously recorded two channels of biopotential data (ECG and respiration). During the recording, we manually tuned the driving frequency of the WPT chamber to maximize device on-time. PID and timestamp information (Section 5) in the recorded data file can then be used to determine that the Bionode was receiving sufficient power to acquire and transmit biopotential data 85.43% of the time. While the powering of the Bionode during this session is not perfect, it is sufficient to provide useable biopotential signals over the duration of the study (Figure 2.9).

This method of wirelessly powering implantable devices addresses many of the issues present with powering devices inside freely moving rodents. However, improvements to power transfer efficiency can still be made. Secondary coil misalignment created when the rodent is aligned in certain orientations within the WPT chamber's circulating magnetic field can cause insufficient coupling to either coil, resulting in insufficient power generation for the Bionode. Furthermore, the resonant frequency of the WPT chamber is modified when the rodent changes radial positon within the chamber, causing the Powernode to become de-tuned which reduces the power transfer efficiency of the system. These challenges are currently being addressed by incorporating dynamic impedance matching on both the WPT chamber power source as well as the Powernode to allow the system to dynamically tune itself in response to the rodent's radial motion [112]. No wireless powering scheme can provide 100% on-time, and so a determination of what is good enough falls to the application needs. For required on-times approaching 100%, rechargeable batteries are added to the Bionode as described below.

Two LIR1220 lithium-ion rechargeable coin-cell batteries can be connected to the Powernode to provide a supplemental power source. Each battery is connected between ground and either the positive rectifier output or the negative rectifier output via two Linear Technology LTC4071 power management integrated circuits (PMICs). These PMICs ensure that the batteries are connected to the outputs of the rectifier circuits whenever the coils are unable to provide sufficient voltage through the rectifier. Furthermore, whenever excessive power is provided to the Powernode through the coils, the PMICs direct this power to recharge the batteries. When equipping Bionodes with these backup batteries in chronic implant studies, we have achieved 100% on-times for over three hours at a time. These batteries also allowed us to successfully implant the Bionode into three pigs for a multi-week chronic study [113]. Because the pigs could not fit into the WPT chamber, we activated and charged the implanted Bionodes using the external wand.

2.2.6   Manufacturing and Packaging

Successfully fabricating and packaging a device for chronic implantable applications depends greatly on miniaturized form-factors and robust device encapsulation. All physical aspects of the Bionode implant are designed with the goal of creating an adaptable, inexpensive, robust, and fully implantable device with a form factor allowing for long-term chronic implantation in rodents or

minimally invasive implantation in humans. These design considerations were further constrained by the desire to use only COTS components as well as a need to maximize manufacturing yield. The components of the Bionode that most define its form factor and manufacturability are its PCBAs, electrodes, wireless powering coils, and packaging used to encapsulate the implant.

2.2.6.1   PCBA Considerations

The Bionode implant contains either three or four PCBAs: The Bionode mainboard, the optional daughter board, the Powernode, and a feedthrough board. The mainboard contains the AFE, stimulator, microcontroller, radio, and antenna while the optional daughter board contains two additional AFE circuits. The Powernode contains all circuitry necessary to provide power rails to the Bionode mainboard and wirelessly recharge battery if used (See Section 2.2.5). All electrode connections are made via the feedthrough board which connects the electrode pins to the Bionode mainboard and/or daughter board. The main function of the feedthrough board is to prevent leakage into the implant via faulty leads. Lead breaks are often a cause for implant failure [114]. The feedthrough board isolates the leads from the inside of the implant case, which ensures that broken leads do not provide a path for fluid to enter the implant.

Because these boards were developed in a modular fashion, each board could be designed, optimized, fabricated, and tested independently. The ability to fabricate and test the four Bionode PCBAs separately made manufacturing defects easier to find and repair, which increased device manufacturing yield. This approach also allowed a modular design where different Powernodes (e.g. with and without rechargeable batteries) could be used in different applications.

All four PCBAs were optimized for size by selecting small component packages and laying out all pads and traces on the printed circuit board (PCB) using a minimum spacing and width of 0.127 mm wherever possible. The Bionode mainboard is a 6-layer board, while the Powernode, daughter board, and feedthrough board are 2-layer boards. Figure 2.24 shows the top and bottom layers of all four PCBs. Chris Quinkert was in charge of the layout for the Bionode Mainboard, Powernode, and Feedthrough board, while I was in charge of the layout for the daughter board. All PCBs were fabricated by Advanced Circuits, Pentalogix, or at the CID using an LPKF ProtoMat S100 milling

machine. We populated all of the boards in-house using solder paste, solder paste stencils, reflow ovens, reflow guns, soldering irons, and microscopes.
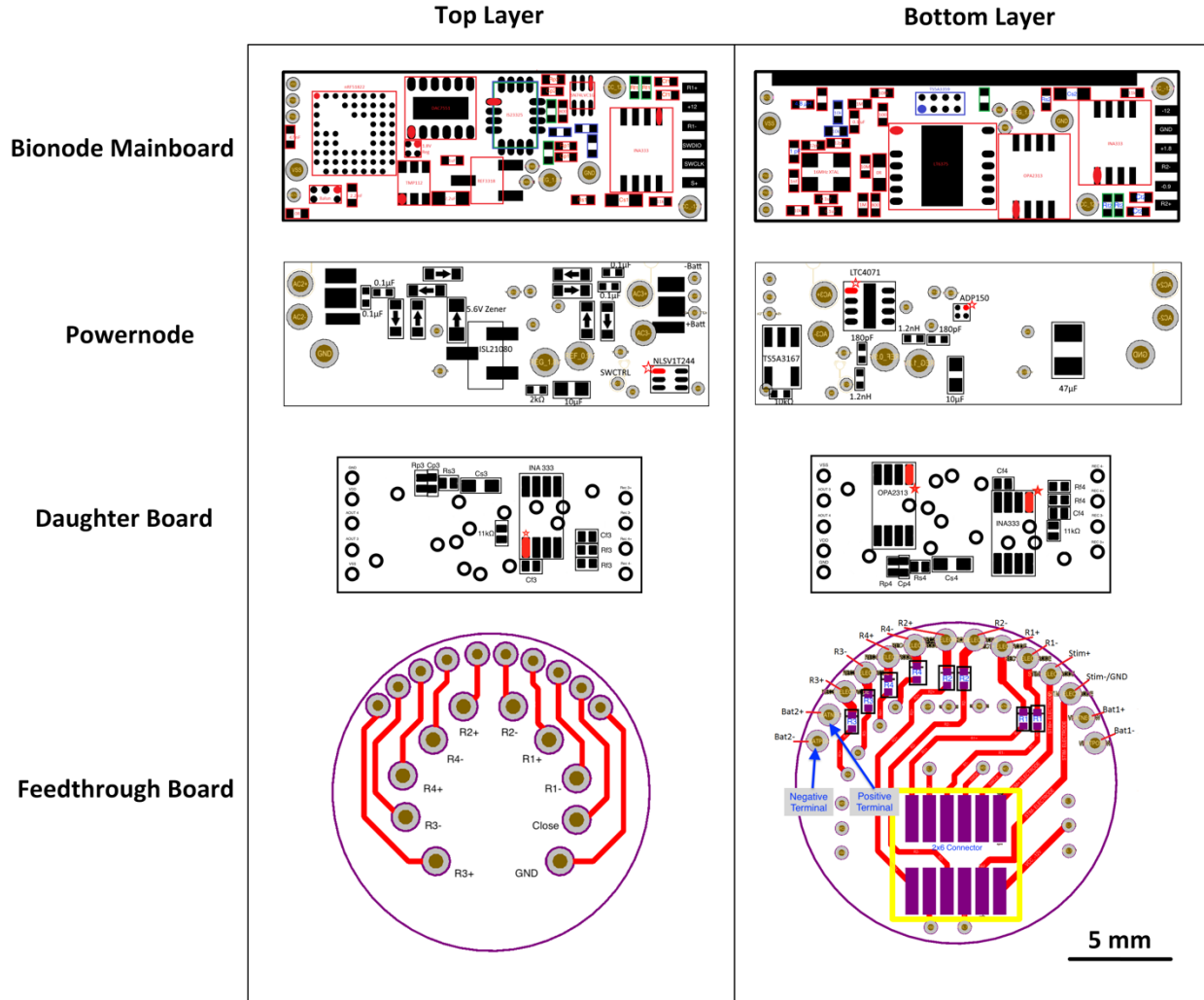
Figure 2.24: Top and Bottom layers of all four printed circuit boards (PCBs) that make up the Bionode. All PCBs were optimized for size by using a minimum spacing and width of 0.127 mm wherever possible.

2.2.6.2 Electrode Connection Considerations

A variety of electrodes and leads can be successfully used with the Bionode for both recording and stimulating including nerve cuffs, helical leads, pressure sensors, thermocouples, deep brain electrodes, and bone screws. All of these electrodes connect to the Bionode by means of low-impedance commercial pins. This interface allows virtually any electrode to be terminated with a

0.46 mm – 0.51 mm diameter pin and connected to the Bionode. Design and construction of the electrodes and transducers that I used with the Bionode are covered in Section 2.3.

2.2.6.3 Coil Considerations

Both wireless powering coils (See Section2.2.5) were hand-wound at the CID using 22-gauge wire. The front-coil has a 7 mm inner diameter and the top-coil has a 5 mm inner diameter. These dimensions were constrained so that the coils could fit inside the cylindrical package described next. We optimized for number of turns and wire-gauge choice by iterative experimentation.

2.2.6.4 Final Board Assembly

Once all of the Bionode PCBAs had been tested and the electrodes had been constructed (See Section 2.3), we hand-assembled all of the components together to make the final implant as shown in Figure 2.25.
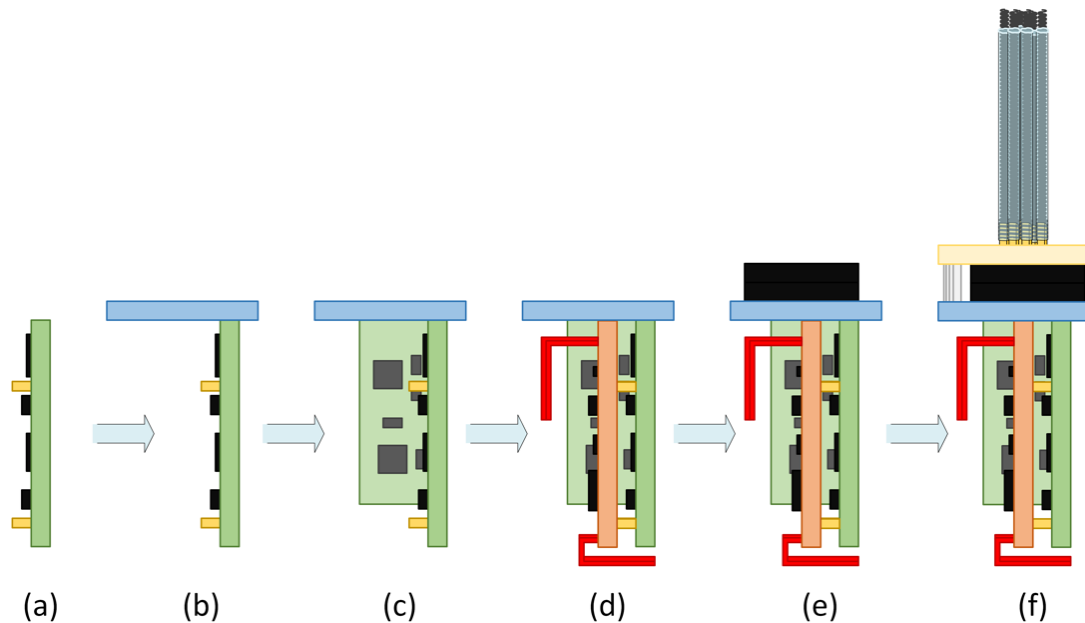
Figure 2.25: This figure provides a side-view of the Bionode assembly process. (a) The Bionode mainboard is prepped for final assembly with Powernode and feedthrough board connection pins attached. (b) The feedthrough board is attached to the Bionode mainboard. (c) The daughter board is attached to the feedthrough board and the mainboard. (d) The Powernode is connected to the Bionode mainboard. (e) The optional batteries are installed on top of the feedthrough board. (f) If optional batteries are installed, the electrodes are connected to a cap-board which insulates the batteries from the electrodes. If the optional batteries are not used, the electrodes are connected directly into the feedthrough board.

While most of the steps shown in Figure 2.25 are straight-forward, the attachment of the daughter board to the feedthrough board and mainboard is more involved and requires more detailed explanation. When the Bionode was first designed, it was made with only two AFEs. It became apparent soon after the Bionode was made that my specific research needs required four channels of biopotential recordings (See Chapter 3). During the design phase of the Bionode mainboard, I had pushed that two GPIO ports be routed to accessible vias just in case we decided we wanted to expand the capabilities of the Bionode. These two GPIO pins were selected specifically because they could be configured as digital input or output pins or as analog ADC inputs. The availability of two additional ADC inputs allowed for the possibility of making a daughter board with two additional AFEs that could route directly into the ADC inputs. Because the daughter board was not initially planned to be part of the Bionode implant, it has to be manually wired to the Bionode feedthrough board and mainboard to provide for its power rails as well as its analog inputs and outputs. This connection is shown in Figure 2.26.
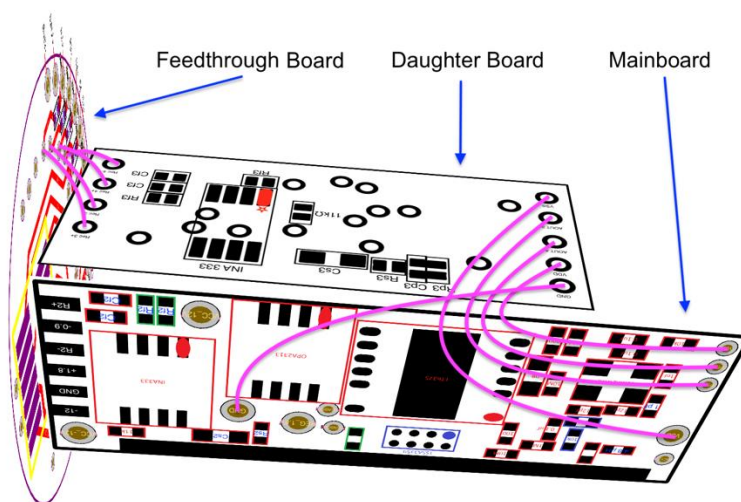
Figure 2.26: The daughter board is hand-wired to the feedthrough board and mainboard using insulated 30 AWG tin plated copper wire (PN: B-30-1000) indicated by the pink connections in this figure. The connections to the left connect the feedthrough board's electrode inputs to the daughter board's analog front end (AFE) inputs. The connections to the right connect the mainboard's power rails to the daughter board and also connect the daughter board's AFE outputs to the mainboards ADC inputs.

While this manual connection is time consuming, it has not been a failure point of any devices made this way. A future Bionode design has been created that uses a press-fit connector to make

these connections. Because this updated Bionode has not been used to generate any data being presented in this work, I will not document it here. An annotated diagram of the fully assembled Bionode is shown in Figure 2.27.
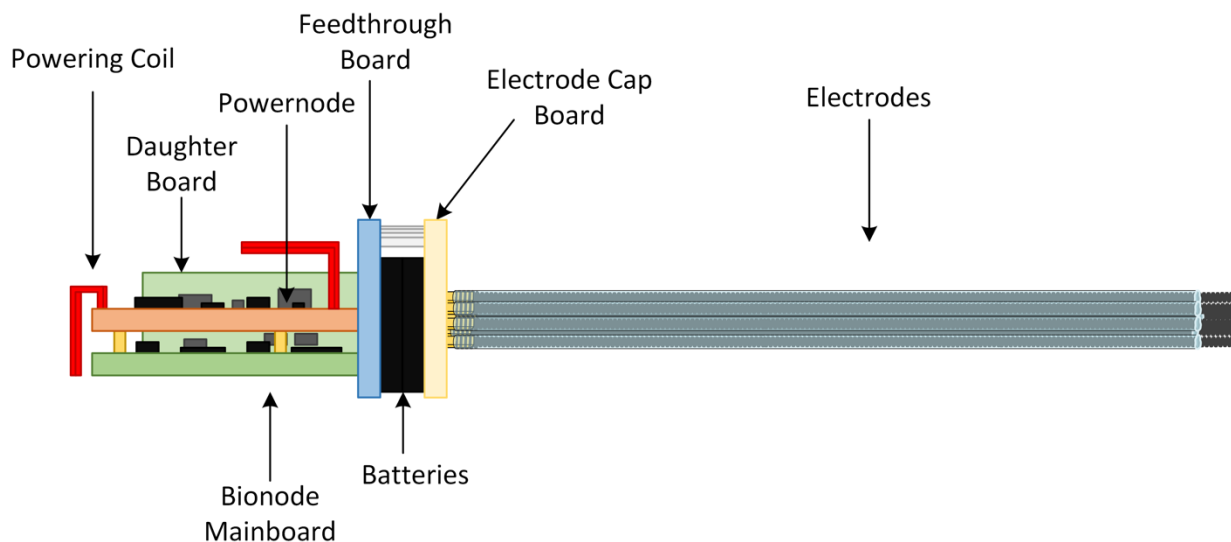
Figure 2.27: The fully assembled Bionode contains four PCBAs, two batteries, electrodes for each input channel, two powering coils, and an electrode cap board. The modular design of each of the four PCBAs allows them to be swapped out of existing Bionodes if changes or upgrades are desired.

2.2.6.5 Packaging Considerations

To chronically implant the Bionode in a rodent model for any length of time, it must be encapsulated in a package that insulates it from tissue. Many materials including polymers, metals, ceramics, and glasses have been used in recent years for hermetic and non-hermetic implantable device packaging [115-118]. While metal packages with glass or ceramic feedthroughs have become popular for long term medical implants, the sealing processes often require highly controlled environments and expensive precision equipment (i.e. infrared lasers to melt glass or laser-beam welders to fusion weld metals). Metal packaging also may require powering coils and communication antennas to be placed outside of the packaging to avoid power and communication losses; further complicating the packaging process[115].

With these considerations in mind, we initially used the inexpensive and flexible option of using medical grade epoxy to encapsulate the Bionode, which has been successfully verified as a legitimate option in other research[116, 119]. We fully encapsulated the Bionode in medical grade (Hysol Loctite M-31CL) epoxy once it was in a 3D printed package. This packaging approach optimized for customization and flexibility in the design and test cycle of the Bionode. Changes in the board shape, size, and architecture could be quickly accommodated with quick changes to device casing and feedthrough board layout, providing for fast turn-around and implementation. In addition, the interconnects utilized by the feedthrough board can be modified to meet the ever evolving attributes of future devices [120] such as capacitive feed-through systems [121, 122]. Unlike other hermetic sealing examples [117, 123, 124] have used alternative materials and methods, the materials and tools used in this method are relatively inexpensive and easy to obtain.

In more recent studies involving the long-term chronic implantation of the Bionode in rats, I replaced the 3D printed case with a glass cylinder. This reduced the amount of epoxy needed to seal the device because the glass case does not need to be fully encapsulated in epoxy. One of these devices is pictured in Figure 2.1. The glass cylinder was created by cutting quartz tubing to size and sealing one end of the cut tube at the Scientific Glass Blowing facility at Purdue University. Figure 2.28 shows the packaging process using this glass package.
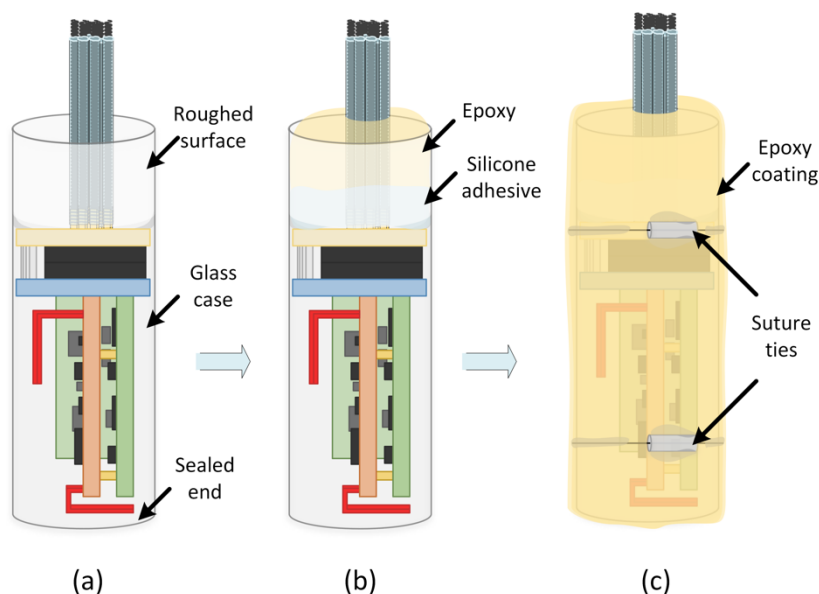
Figure 2.28: (a) Prior to inserting the Bionode into the glass case, I roughed up the inside of the case as shown using a rotary tool with a sand-paper attachment which promotes adhesion to the glass by the silicone and epoxy added in the next step. (b) I applied an initial layer of silicone adhesive to create a seal around the silicone electrodes. After the silicone adhesive dried, I applied medical grade epoxy to fill what space remained in the well at the top of the case. (c) Silicone tubes superglued and tied to the sides of the glass package provide tie points for suturing the device during implantation. I finalized the implant packaging by applying a thin epoxy coating around the entire device to ensure that the epoxy-glass seem was fully sealed and to further adhere the silicone suture ties in place.

When I decided to transition to a glass case, I initially had difficulty getting the medical grade epoxy to completely seal around the glass package. The medical grade epoxy provides the seal at the top of the glass case, so good adhesion is necessary. I found that roughing up the inside of the glass case with a sand-paper attachment connected to a rotary tool gave the epoxy a better surface to adhere to. After roughing up the inside of the case with the rotary tool, I initially secured the fully assembled Bionode in place using a small amount of carefully placed super glue on the interface between the glass case and the electrode cap board.

Sealing the top end of the glass case requires both medical grade silicone adhesive (NuSil Med 4-4420) and medical grade epoxy (Hysol Loctite M-31CL). Because the electrodes typically are insulated using silicone tubing, making an initial seal between the glass case, the electrode cap, and the electrodes using a silicone adhesive creates a semi-flexible plug that adheres well to the bottom of each electrode. This plug is important because it can stop fluids from entering into the

electrode-implant interface space via a broken or cut lead. If fluids were able to flow into this space, a single broken lead could cause all other leads to become shorted together, resulting in the loss of all channels of recording. This seal cannot be achieved using only the medical grade epoxy because when it cures, it is ridged. Because the silicone tubes that insulate the leads are flexible, an inadequate seal between the silicone tubes and epoxy is created if only epoxy is used to fill the well. Another benefit to using silicone adhesive in this step is that it provides for the possibility of removing the Bionode implant from the glass package for re-use purposes because It is not difficult to remove silicone adhesive from the electrode cap board, while it is much more difficult to remove epoxy from the cap board. While the silicone adhesive provides a good seal inside the electrode-implant interface space, it does not provide an adequate seal to the glass case itself. I use medical grade epoxy to achieve this seal by filling up the rest of the well at the top of the case after the silicone adhesive has cured.

When implanting the Bionode, it is important to assure that it does not migrate [125]. Aside from the adverse health effects of a migrating subcutaneous implant, the WPT chamber requires that the powering coils be aligned properly to the rotating electromagnetic field for optimal power transfer (See Section 2.2.5). If the Bionode migrates after implantation, the powering coils could be moved out of alignment which would adversely affect powering performance. To keep the Bionode from migrating, I attach silicone tubes to act as suture ties to the sides of the implant using super glue as shown in Figure 2.28 (c). Prior to super-gluing the tubes to the implant, I thread silk suture through the tubes and tie it around the case to further secure the tubes to the case. During the implant procedure, we thread suture through the tubes and then secure it to the muscle wall.

Once the suture ties are in place, I put a final coating of medical grade epoxy over the entire implant. I do this by putting some epoxy on my gloved hand, and then rubbing the epoxy over the entire surface of the implant. This provides a thin, full coating of epoxy around the implant which ensures a good seal around the top of the package and further adheres the suture ties to the sides of the case. After this final layer cures, we fully submerge the packaged implant in water for 48 hours (ideally) and no less than 12 hours before implantation. This soak test ensures that the Bionode has been fully sealed before it is implanted. If we can turn on the Bionode after the soak

test and if its tuning coils have not become de-tuned, we declare that the Bionode has passed the soak test.

The fully packaged Bionode is 4 cm long with a diameter of 1.7 cm and weighs 9 grams, which is comparable to other non-ASIC systems [126, 127]. This packaging method provides excellent reliability for medium to long term chronic studies. To date, using the glass packaging method, Bionodes have been successfully implanted in over 50 chronic studies lasting up to 71 days. No packaging failures have been observed during the course of these studies.

The use of removable packaging facilitates the ability to adjust and reuse explanted Bionodes. For devices that do not require any adjustments to the Bionode hardware, the leads can simply be cleaned and the Bionode can be reused. For devices needing adjustments to the Bionode hardware (e.g. devices needing different AFE passband values), the device can be completely removed from its packaging, adjusted, and then repackaged. While this process destroys the packaging as well as the electrodes, all circuit boards, powering coils, and batteries can be re-used. To date, 15 Bionodes have been reused using this process, with some being reused multiple times. A detailed flow chart of the entire manufacturing and testing process for the Bionode is shown in Figure 6.1 in the Appendix.

2.3 Electrodes and Transducers

All signals fed into the Bionode's AFEs are initially sensed using either an electrode or a transducer. When sensing signals originating at some distance from the Bionode implant, these electrodes or transducers are attached to leads which transport the sensed signals from the signal source to the Bionode's AFEs. All leads, electrodes, and transducers must be carefully designed to withstand long-term chronic implantation. Leads in particular must be designed to be particularly flexible and robust as they often experience repetitive torsion, compression, and strain within the implanted rodent.

2.3.1 Helical Leads

All leads used to record ECG, ECoG, and respiration were fabricated using custom made helical wire produced by Fort Wayne Metals. I specified the physical characteristics of the helical wire to

Fort Wayne Metals when experiments using solid-core and stranded wire electrodes resulted in multiple problems. Solid-core wire leads were prone to breakages within days of implantation, and sometimes even during the surgical procedures. This risk of solid-core wire lead breakage increased with the length of the electrode, making it difficult to acquire signals requiring long leads (i.e. ECG signals in the lead II configuration). The stranded wire leads used were more flexible than the solid-core wire leads and suffered less breakages. However, the stranded wire leads were subject to getting kinked during surgery, making them difficult to place correctly. Both the solid-wire and stranded leads suffered from an inability to stretch, which resulted in higher strain and torque experienced at the electrode or transducer interface as well as at the Bionode interface.

The helical form of the wires used for the leads in this work allows the leads to twist and stretch without compromising their structural integrity. The helical wire is composed of 35N-LT; a proprietary alloy of Fort Wayne Metals. This alloy has been shown to be bio-compatible, which allows the wire to be used as both an insulated lead as well as an exposed electrode that directly contacts tissue [128]. The main challenge to using this alloy as a lead is its low solderability; making it very difficult to electrically connect the helical lead to the Bionode. Conductive epoxy is challenging to work with, and the helical shape of the wire makes it difficult to crimp onto with a connector. I developed a robust wire-wrapping technique to attach a solderable pin to the helical wire, thereby making the lead easy to connect to a variety of receptacles. This technique is illustrated in Figure 2.29.
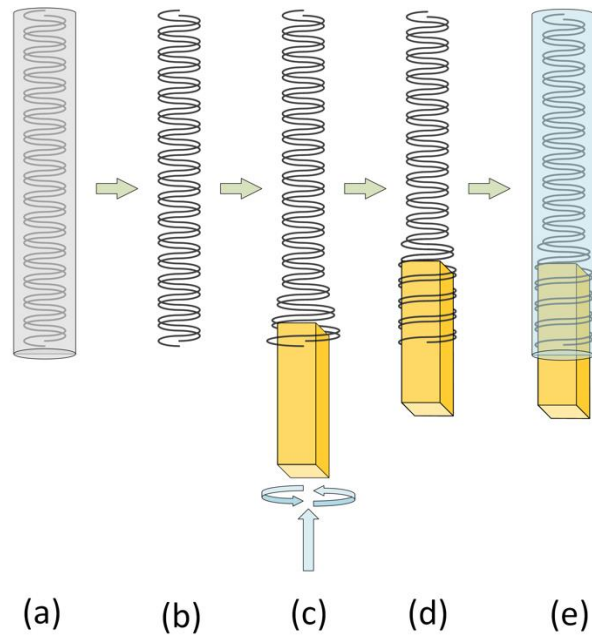
Figure 2.29: The ridged outer insulation on the helical lead shown in (a) is stripped off using a scalpel (b). (c) The helical wire is screwed onto a gold plated pin. (d) The pin has a larger diameter than the inner diameter of the helical lead, so a strong connection is made between the pin and the lead. (e) The helical lead is slipped into a flexible silicone tubing. This tubing provides a biocompatible insulating layer around the lead.

To connect the solderable pin to the helical lead, the insulation initially surrounding the helical wire must be removed. This is done using a scalpel because traditional wire strippers tend to deform the helical shape of the wire. The wire is then twisted around the solderable pin. Because the inner diameter of the helical wire is less than the diameter of the solderable pin, the twisted helical wire creates a strong connection to the pin. The helical wire is finally threaded through a silicone tube to provide insulation for the lead.

2.3.2   ECoG/ECG Electrodes

ECoG electrodes are constructed by simply removing some of the silicone tubing from the ends of the helical leads and plugging the end of the tubing with silicone adhesive (See Figure 2.30).
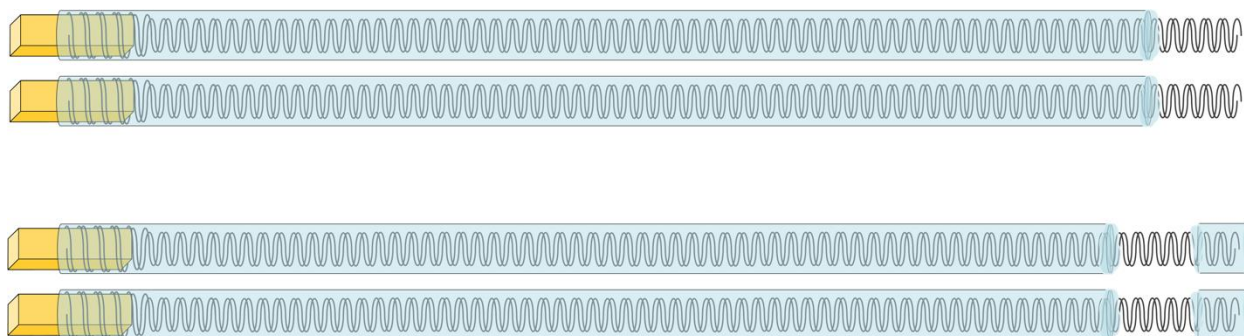
Figure 2.30: The differential pair of electrocorticogram (ECoG) leads (top) do not need a silicone cap like the differential pair of electrocardiogram (ECG) leads (bottom) do because the ECoG lead tips are covered in dental cement during implantation, so they will not damage tissue. The ECG leads are sutured directly to the muscle wall, so their potentially sharp tips need to be covered by the silicone cap to avoid tissue damage.

The exposed end of the lead senses ECoG signals, while the silicone adhesive plug prevents fluids from leaking into the lead body. ECG electrodes are similarly constructed with the additional step of adding a small length of tubing over the very tip of the exposed helical wire. This tubing covers the sharp end of the helical wire which reduces tissue damage. The ECoG electrodes do not need this covering because the entire electrode tip is covered in dental cement during the surgical procedure. Figure 2.31 shows the tips of an ECoG and an ECG electrode.
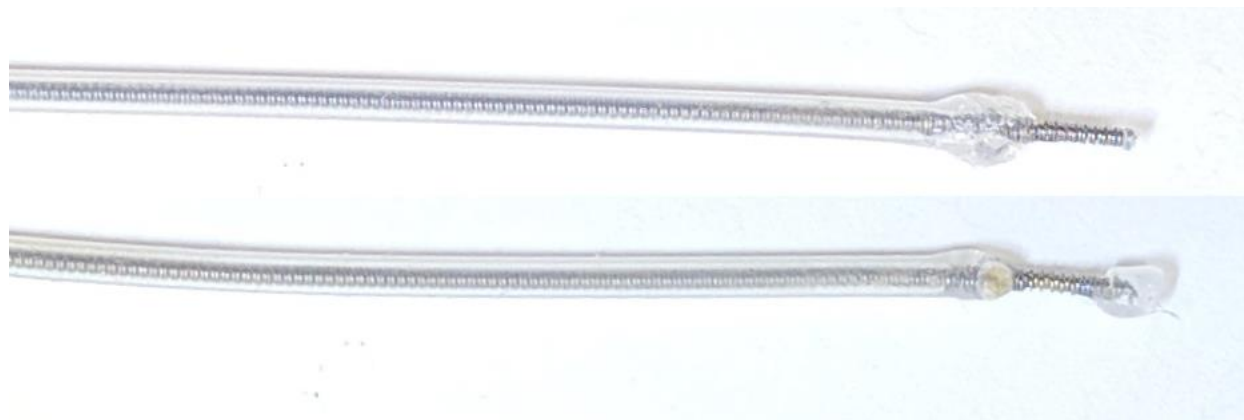
Figure 2.31: Tips of an electrocorticogram (ECoG) (top) and electrocardiogram (ECG) (bottom) electrode. The ECG electrode has a silicone cap on the end to insulate the sharp end of the lead from the subcutaneous space. Because the ECoG electrode tip is covered in dental cement, it does not require the silicone cap.

2.3.3 Respiration Transducer

Our method of acquiring respiration signals using a thermocouple implanted in the nasal cavity is derived from methods originally described in [53] and further demonstrated by [54, 129]. To achieve long-term respiration recordings using this method, I designed and fabricated fully implantable thermocouple transducers using biocompatible materials and helical leads. To make long-term chronic thermocouple transducers I modified 36 AWG type K thermocouples (Newport Electronics 5TC-TT-K-36-36/N) as depicted in Figure 2.32 below.
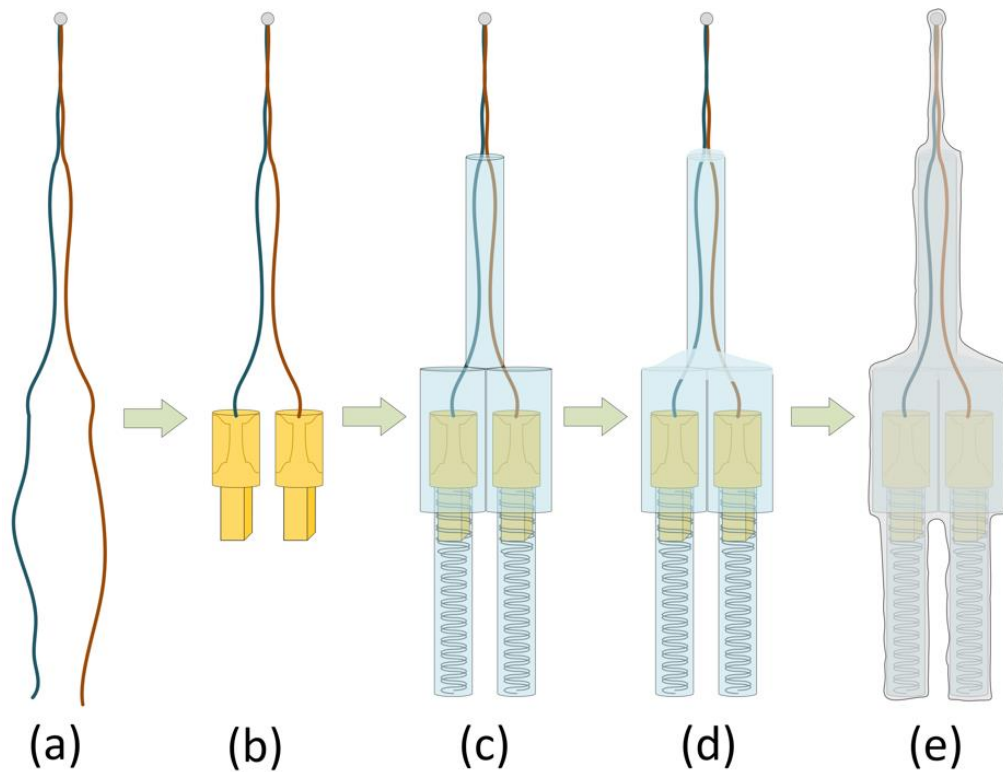
Figure 2.32: Chronic thermocouple transducer fabrication. We first trim the 36 AWG wires of a type k thermocouple shown in (a) and then attach pins shown in (b) via a crimping tool. We wire-wrap helical wires onto each pin, and insulate the pins, wires, and body of the thermocouple with silicone tubing shown in (c). To seal the silicone tubing shown in (d), we use a silicone adhesive. Finally, we apply a 5 µm thick Parylene coating as shown in (e) to insulate the non-biocompatible tip of the thermocouple transducer.

I first trimmed the thermocouple to a length of 7 cm and then crimped each terminating wire to a receptacle with a male pin at its base. I then wire-wrapped helical wires around each male pin to make robust solderless electrical connections. The sensing tip of the thermocouple is not

biocompatible, so it must be insulated. This poses a challenge because any method of insulation that thermally insulates the tip of the transducer will reduce the transducer's ability to sense thermal changes in its environment. I insulated the tip of the transducer by having a 5 µm thick Parylene coating deposited over the entire thermocouple transducer, which provides electrical and biological insulation while minimizing thermal insulation. Dr. Quan Yuan deposited the parylene coating for me using facilities in Wang Hall at Purdue University. Figure 2.33 shows a fully assembled thermocouple transducer.
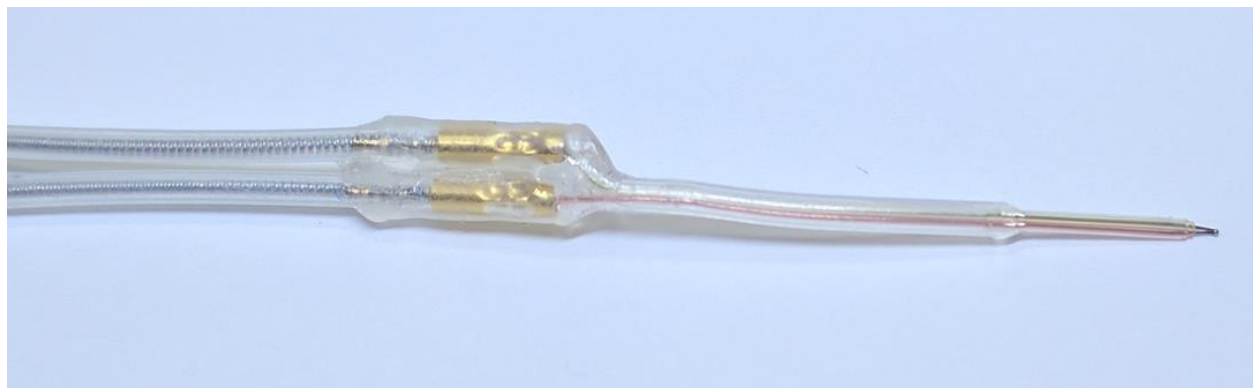
Figure 2.33: Fully assembled thermocouple transducer with parylene coating. This thermocouple transducer is ready for implantation. Prior to implanting, we connect it to one of the differential inputs of the Bionode implant with an analog front end configured for respiration recordings as shown in Table 2.2.

2.4   Conclusion of Specific Aim 1

My first specific aim was to design a chronic, wireless implantable device with the ability to acquire long-term cardiac, respiratory, and brain signals in freely behaving rodents as well as provide electrical stimulation to the nervous system. The Bionode's verified ability to acquire up to four channels of chronic biopotential data from freely behaving rodents as well as concurrently stimulate and record from the nervous system has met this aim, and has also led to its widespread use in research projects at Purdue University and at other institutions. This widespread usage is further facilitated by proven fabrication and packaging methods that make the Bionode a viable low-cost, reusable, and modifiable research tool. Improvements to the wireless power transfer methods including the addition of dynamic impedance matching on both the Bionode and the external power source are currently being developed with the goal of improving powering

performance. The use of only COTS components in the Bionode's design allows all aspects of the Bionode to be replicated and/or modified by a typical university lab.

The Bionode's ECG and ECoG electrodes have been used in multiple projects at Purdue to collect cardiac and brain signals. The respiration transducer has been used extensively to produce a novel dataset containing respiration data as well as ECG and ECoG data from freely behaving rats with chronically induced seizures. This is the first dataset of its kind, and is the subject of Chapter 3 of this dissertation.

3. AIM 2: ACQUIRING LONG-TERM ECG, ECOG, AND RESPIRATION FROM FREELY BEHAVING RATS WITH CHRONIC, SPONTANEOUS SEIZURES

Much of the material presented in this chapter will be included in a paper, of which I am the first author, titled "Respiratory changes during and following seizures in a chronic model of temporal lobe epilepsy." This paper is currently in preparation with a planned submission date of Q1 2019.

3.1 Motivation/Overview

Physiological data describing cardiac, respiratory, and brain function prior to sudden death in epilepsy is crucial to the studying the underlying mechanisms behind these deaths [22-24]. Because it is unknown when sudden deaths in epilepsy may occur, continuous monitoring is necessary to guarantee the capture of physiological data prior to death. I used Bionodes equipped with a respiration thermocouple transducer along with ECG and ECoG leads to measure cardiac, respiratory, and neurological signals in freely behaving rats with chronically induced epilepsy by means of the TeNT model. The TeNT model involves injecting TeNT into the CA3 region of the hippocampus to chronically induce epilepsy in rats [34, 130]. We chose to use TeNT for this work because of the spontaneous and chronic nature of the seizures that tetanus neurotoxin injected into the CA3 region of the hippocampus produces [32, 131]. After the toxin is injected, the rat will start experiencing spontaneous seizures within 4 to 20 days, and will typically continue to seize for 3 to 4 weeks. It is expected that the rat will experience a median of 10 seizures per day during this time. This time frame allows for baseline physiological data to be recorded by an implanted Bionode before seizures start as well as during the duration of the time that the rat is experiencing spontaneous seizures. The data gathered during these chronic experiments represents the first dataset where respiration data has been gathered from freely behaving rodents with chronically induced epilepsy.

3.2 Surgical Procedures

We implanted 51 rats with Bionodes equipped with daughter boards with the ability to record respiration, ECoG, and two channels of ECG (Lead I and Lead II configurations [132]). In 45 of these rats, we attempted to induce epilepsy by injecting TeNT into the CA3 region of the

hippocampus [131]. We performed this injection in the same surgery as the Bionode implantation. All of the rats we used for these experiments were female Long Evans rats weighing between 225 and 300 grams. We performed all chronic surgical procedures using aseptic techniques. Every surgical procedure that we performed was in accordance with the regulations of the Institutional Animal Care and Use Committee (IACUC) and using procedures approved by the Purdue Animal Care and Use Committee (PACUC).

3.2.1   Surgical Preparation

Prior to any chronic implant surgery, we perform various procedures to ensure that the implantable device, the surgical area, and the animal are well prepared for a successful surgery.

3.2.1.1   Implantable Device Preparation

Before beginning any implant surgery, we fully submerge the packaged Bionode implant in water as a soak-test. The goal of this test is to ensure that we discover any leaks in the packaging before we implant it in a rat. If the implant fails this soak test, the surgery is cancelled and the implant is re-packaged. This soak test lasts a minimum of 12 hours. When the soak test is completed, we power on the Bionode to ensure that it has not been damaged by the packaging process or the soak test. We initially turn on the implant using the powering wand (See Section 2.2.5). This allows us to check the electrodes and transducers by either shorting them together (in the case of the ECoG and ECG electrodes) or by breathing on them (in the case of the respiration transducer). In some cases, we also feed in known signals through the electrodes using a function generator to further ensure that the recording channels are ready to be implanted. Turning the implant on using the powering wand also allows us to ensure that the implant can properly transition to battery power if the optional batteries are installed.

After confirming that the Bionode implant can still turn on and sense signals after the soak test, we measure the resonant frequency of both coils using a vector network analyzer (Agilent E5071B) to determine if the coils and/or matching networks have become detuned (See Figure 2.22). Moisture inside the package could change either the inductance or capacitance of the coils or the capacitance values of the matching networks which would result in a change to the resonant frequency of the coil/matching network circuit. As a final check, we place the Bionode implant

into the WPT chamber to ensure that it is still able to be powered on inside the WPT chamber using similar power input levels that we used when we tuned the device. If the Bionode passes all of these final tests, we deem it acceptable for implantation.

After the Bionode implant has passed the soak test, we sterilize it. Because the Bionode implant can contain batteries, it cannot be passed through an autoclave, so we use a liquid cold sterilant instead. We sterilize the Bionode by fully submerging it (including the electrodes) in CIDEX OPA for at least 20 minutes; following the manufacturer's instructions. Immediately prior to implanting the device, we remove it from the CIDEX OPA and rinse it with sterile saline using aseptic techniques.

3.2.1.2   Tetanus Neurotoxin Preparation

We acquired tetanus neurotoxin from clostridium tetani in solid form from multiple vendors (List Labs, Cayman Chemicals, Sigma-Aldrich, and Alomone Labs). We obtained the tetanus toxin from multiple vendors because during the course of this work, we had some difficulty inducing seizures in rats. We determined that in most cases the tetanus neurotoxin had become ineffective somehow; possibly during the shipping process. This is discussed further in Section 3.6. We created a TeNT solution by dissolving the solid TeNT into sterile phosphate buffered saline (PBS) at a concentration of 100 µg/mL. We performed all of this work in a sterile cabinet using aseptic techniques. We created 50 µL aliquots of the whole solution and stored them in 1.5 mL vials. We stored the vials in a lock-box inside a -80 °C freezer between surgeries. Immediately prior to surgery, we removed a single vial from the freezer and placed it on ice until we were ready for injection. We disposed of all used vials and syringes that made contact with the toxin by placing them inside a bio-hazard sharps bin.

3.2.1.3   Surgical Area Preparation

We performed all of the chronic Bionode implant procedures documented in this work at the CID at Purdue University. Prior to beginning an implant surgery, we passed all surgical tools through an autoclave (20 psi, 250 °F, 20 minutes) to sterilize them. We also removed unnecessary equipment and supplies from the surgical station to provide an un-cluttered sterile field.

3.2.1.4   Animal Preparation

To reduce the risk of infection, we give each rat one dose of systemic antibiotics for three days, starting the day before the surgery and continuing on the day of the surgery and the day after. We give the rat antibiotics by subcutaneously injecting one dose of Cefazolin (15 mg/kg) each day. Each rat arrives at the animal facilities at Purdue University at least 48 hours prior to surgery to allow them to acclimatize to their new environment in accordance with PACUC guidelines.

3.2.2   Implanting the Bionode

When performing chronic surgical procedures at the CID, both a surgeon and at least one assistant are present. The assistant handles all non-sterile objects which allows the surgeon to maintain sterility during the duration of the procedure. While I performed some of the implant surgeries myself, the majority of them were performed by Professor John Jefferys of the Department of Pharmacology at Oxford University who has been a collaborator at the CID for many years and has worked directly with me for the majority of my time at Purdue University. Ethan Biggs, a graduate student in the Biomedical Engineering Department, has also performed some of the surgeries described here. The following procedure describes implanting a Bionode equipped with a respiration transducer, two ECG channels, and one ECoG channel. Note that during this procedure, we also injected the Tetanus Neurotoxin to induce seizures. I describe this injection step separately in the following sub-section (See Section 3.2.3).

Prior to initial incision, we gave the rat a subcutaneous dose of Butorphanol as an analgesic and anesthetized it using isoflurane in oxygen. Throughout the duration of the surgery, we monitored the rat's vitals using a pulse-oximetry system (Nonin 8600V). We recorded heart rate and peripheral capillary oxygen saturation (SpO_2) in a surgical log. Additionally, we manually monitored respiration rate by respiratory movements. Every 1 to 1.5 hours we also administered 1.5 mL of saline subcutaneously to keep the rat hydrated. We maintained the rat's core temperature using a heating pad with a rectal thermometer feedback sensor (Harvard Apparatus 50-7212). Once the rat was anesthetized, we kept its eyes hydrated using artificial tears (AKORN NDC 17478-062-35).

Our first task was to secure the Bionode implant inside a subcutaneous pocket on the side of the rat. With the rat in the prone position, we made an initial rostral-caudal incision left of midline, and created a subcutaneous pocket to house the Bionode implant. Once the Bionode implant was secured in place, we rotated the rat into the supine position and subcutaneously tunneled the ECG leads to the Lead I or Lead II position [132]. We secured these leads in place by suturing them directly to the muscle wall. In some surgical procedures, this step of tunneling and securing the ECG electrodes in place was postponed to the end of the surgery to allow us to focus on the more challenging portion of the surgery (specifically the placement of the thermocouple electrode in the nasal cavity) early on.

Next, we placed the rat into a stereotaxic frame in the prone position and made a rostral-caudal incision on the rat's scalp, exposing the skull. We then tunneled the ECoG electrodes and respiration transducer up to the scalp incision site. In order to place the ECoG electrodes onto the surface of the cortex, we drilled two bur holes into the skull to expose the dura, making sure to locate the caudal ECoG electrode over the hippocampus (See Figure 3.1). We then made a final rostral-caudal incision between the rat's eyes to expose the left nasal bone. To get the tip of the respiration transducer into the nasal cavity, we drilled a bur hole into the center of the left or right nasal bone 7-mm rostral to the naso-frontal suture (See Figure 3.1). Next, we tunneled the respiration transducer to the nasal incision site and inserted the tip of the transducer into the nasal cavity via the nasal bone bur hole. We secured the respiration transducer in place by covering the bur hole with dental cement, which we cured using ultra-violet light. Once the respiration transducer was secured, we inserted the ECoG electrodes into the bur holes in the skull and secured them with dental-cement as well. Finally, we closed all open incisions with sutures and allowed the rat to recover (See Section 3.2.4).
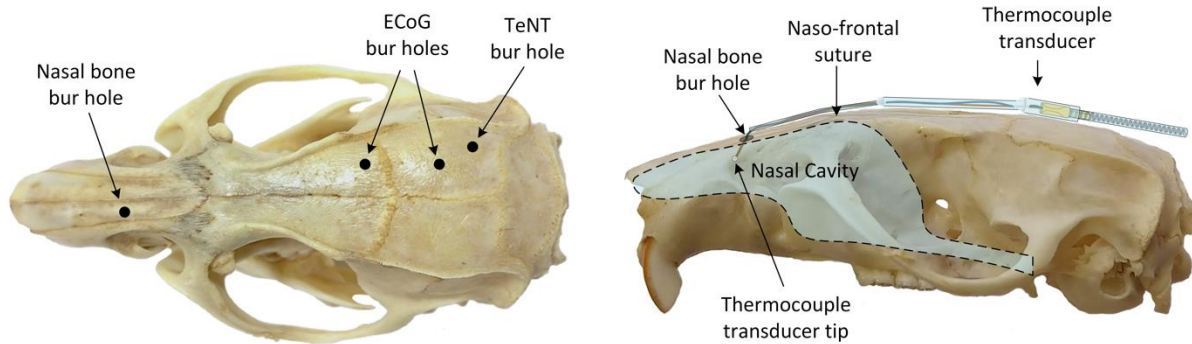
Figure 3.1: Locations of bur holes and transducer placement. We drill 1-mm diameter bur holes in the skull as shown to provide access for the ECoG electrodes, respiration transducer, and Tetanus Neurotoxin injection. We take precaution to ensure that the tip of the thermocouple electrode is located in the middle of the nasal cavity. Once the transducer and electrodes have been inserted into the bur holes, we seal them using ultraviolet curable dental cement.

One step in the above surgical procedure that deserves some extra precautionary detail is the insertion of the respiration transducer. During the surgical procedure, when inserting the respiration transducer tip, we had to take special care to ensure that it was located in the middle of the nasal cavity (See Figure 3.1). If we did not insert the respiration transducer low enough, it would not be in the path of the airflow within the nasal cavity and would be unable to sense thermal changes during respiration. If, however, we inserted the respiration transducer too low, it could make contact with the ventral surface of the nasal cavity, which in turn could cause bleeding that may insulate the thermocouple tip, lowering its sensitivity to thermal changes during respiration.

3.2.3   Tetanus Neurotoxin Injection

During the previously described surgical procedure, we also inject 5 to 20 ng of TeNT in a PBS solution (100µg/mL) into the CA3 region of the hippocampus. We perform the TeNT injection procedure after drilling the bur holes in the skull for the ECoG electrodes. To give us access to the CA3 region, we drill a 1-mm bur hole in the skull at coordinates 5.2 mm caudal and 2.5 mm lateral to the Bregma point (See Figure 3.1). We then carefully puncture the exposed dura using the tip of a 26-gauge needle. This is necessary to avoid bending the syringe that we use to inject the toxin and to avoid damaging the cortex via deflection of the dura. With the dura punctured, we withdrew the TeNT solution into a 1 µL Hamilton 7000 series syringe using World Precision Instruments (WPI) UMP3 micro pump. Once the toxin was inside the syringe, we positioned the syringe over

the TeNT bur hole, and lowered it until it was level with the cortex. At this point, we noted the starting coordinate, and lowered the syringe 6.8 mm to position the tip of the syringe inside the CA3 region of the hippocampus [133]. At this point, we instruct the pump controller (WPI Micro 4 MicroSyringe Pump Controller UMC4) to inject the neurotoxin over the course of five minutes. This allows the toxin to slowly be introduced into the CA3 region with physical minimal damage. After the injection is completed, we wait five more minutes before removing the syringe to ensure that the toxin does not follow the syringe back up the track when we remove it. At this point, we carefully rinse out the Hamilton syringe and then continue in the surgical procedure described in Section 3.2.2.

To determine if we were properly hitting the CA3 target in the brain, I removed the brain of a rat that we had injected with tetanus toxin and sliced it into 30 µm slices using a cryotome (Shandon Cryotome FE). I then applied a Nissl stain to each of the slices to visualize the structures and injection wounds. One of these stained brain slices can be seen in Figure 3.2.
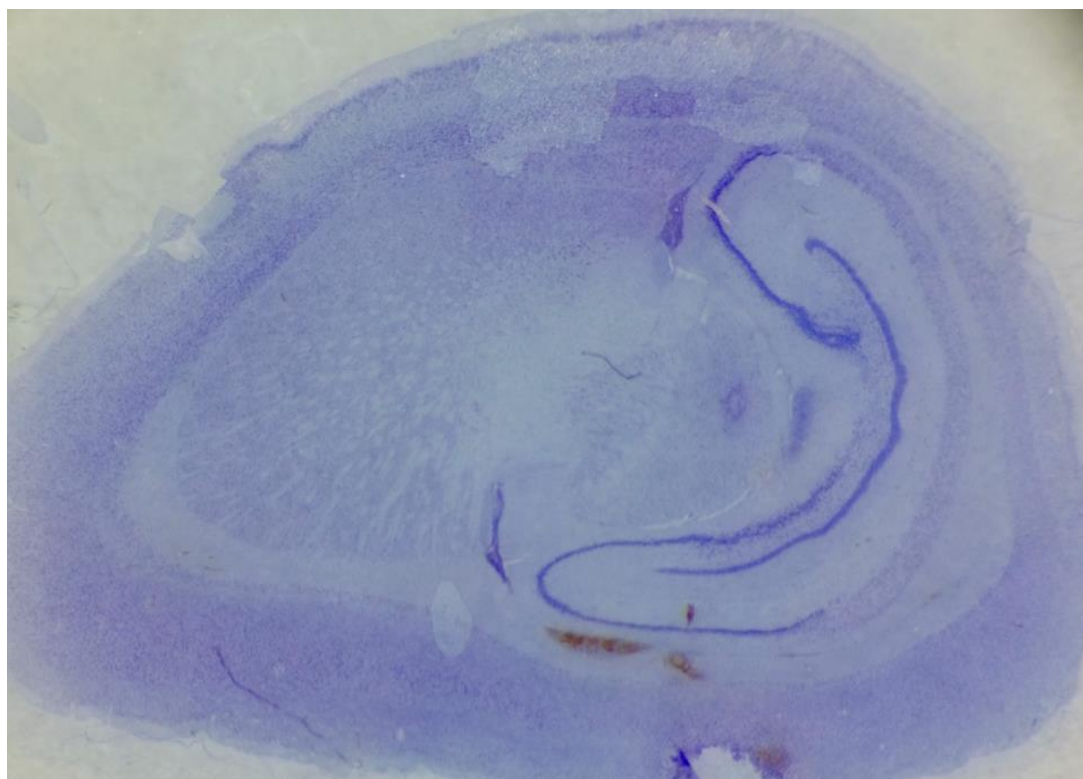
Figure 3.2: Nissl stained brain slice. The hippocampus is depicted on the right. Evidence of bleeding is shown around dorsal CA1.

3.2.4 Recovery and Postoperative Care

Upon conclusion of the surgery, we apply topical antibiotics to the incision sites and let the rat recover in the lab so that we can monitor her immediate recovery process. Using the VNA, we checked the resonance frequency of both coil circuits to ensure that they had not drifted during surgery. We typically noticed an approximately -1 MHz shift in both coil circuits' frequencies (both frequencies are in the range of 340 MHz). This is most likely caused by the rat's subcutaneous space slightly coupling to the coils. We have not observed any reductions of powering performance due to this slight drift.

Over the next 48-hours, we administer both systemic antibiotics (Cefazolin, 15 mg/kg subcutaneously once per day) and either Butorphanol (0.5-2 mg/kg subcutaneously every four hours) or Carprofen (5 mg/kg subcutaneously every twelve hours) for pain relief. While administering these injections, we record the rat's weight and our observations of each incision site as well as the rat's overall recovery progress in a post-operative log. To avoid dehydration, we also give the rat 1.5 mL of saline every twelve hours during this recovery period.

3.3 Data Acquisition

We implanted Bionodes into 51 rats over the course of 26 months using the procedures described in Section 3.2. After the rats were implanted, we allowed them to recover in their normal cages for at least 48 hours before transferring them to WPT chambers for long-term data and video acquisition (see Section 2.2.5). The majority of this recording took place in the animal facilities in the Martin Jischke Hall of Biomedical Engineering at Purdue University. During the data acquisition phase, we recorded continuous biopotential and video data from up to four rats at a time. I designed and deployed all four data acquisition setups and maintained them throughout the duration of these experiments with help from Ethan Biggs. Acquiring this data required a heavy investment of time, planning, effort, and diligence. I have documented my acquisition system setup as well as the procedures we followed to ensure that we properly collected biopotential data, video recordings, and seizure observations from each rat.

3.3.1 Concurrent Data Acquisition from Multiple Rats

To acquire continuous data and video from all four rats, I deployed four WPT chambers, four Base Stations, four Raspberry Pi Model 3B computers, a four port HDMI switch (Zettaguard ZW410), a four port USB switch (UGREEN 30346), on USB hub, eight video cameras connected to two DVR systems (2x Amcrest AMDV40M4-4B-B), a computer monitor, keyboard, and mouse. This setup is shown in Figure 3.3.
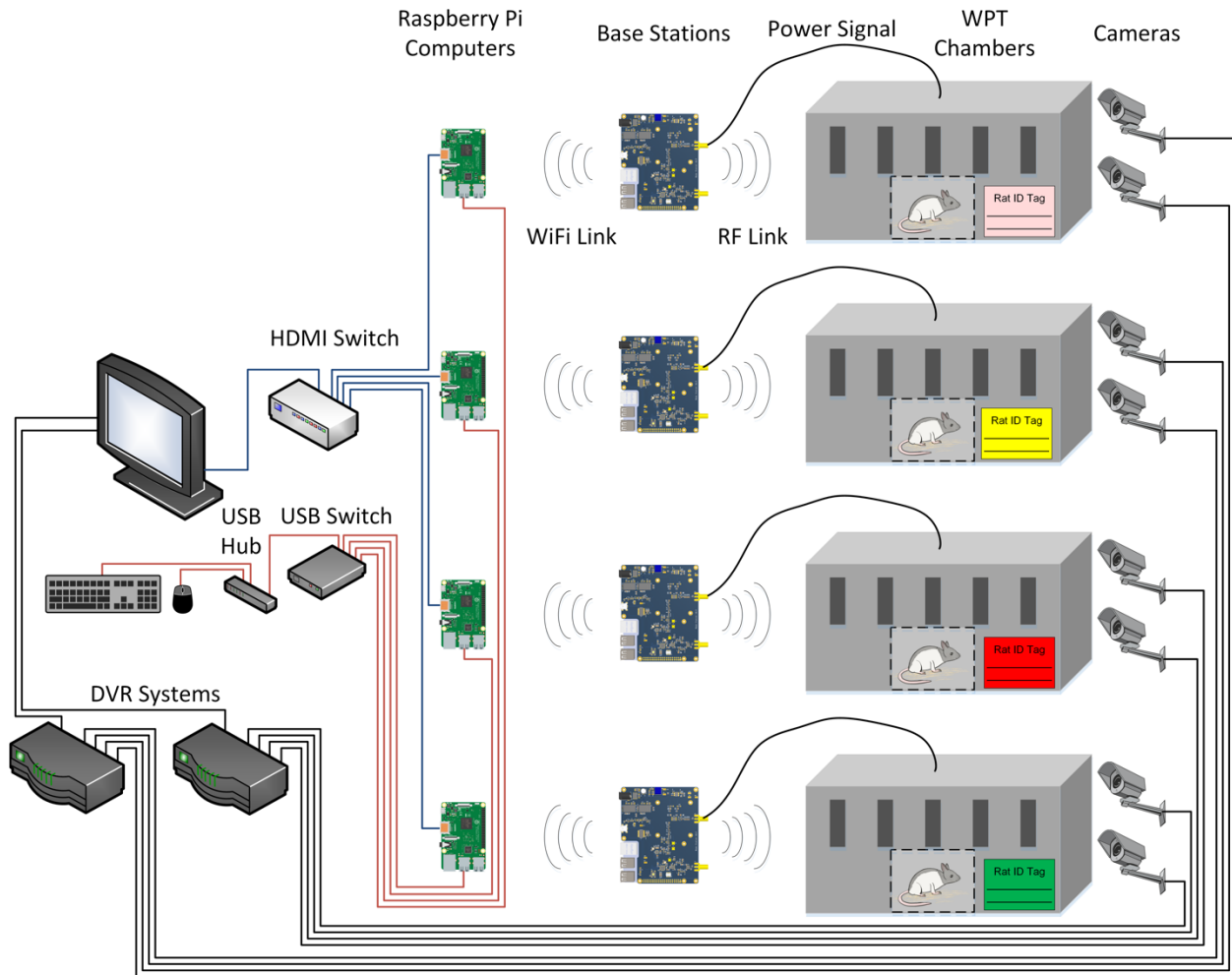
Figure 3.3: Biopotential data collected by each rat's Bionode implant is wirelessly transmitted to Base Stations paired to the implants via an RF link. These Base Stations each power their respective wireless power transfer (WPT) chambers using their on-board power amplifiers. The WPT chambers are clearly labeled and color-coded to ensure that the right dataset is properly attributed to each rat. Each Base Station sends data via a WiFi link to a Raspberry Pi Computer equipped with the Bionode DataView application. The monitor, keyboard, and mouse provide a user interface for each instance of the Bionode DataView application on the Raspberry Pi computers. These peripherals are connected to each Raspberry Pi computer via the HDMI Switch and USB Switch both of which connect the peripherals to the desired Raspberry Pi computer. Two video cameras are attached to each cage. All video is recorded by the DVR systems and is also viewable through the monitor VGA input.

I decided to collect all of the biopotential data using Raspberry Pi computers because they are inexpensive and relatively easy to maintain. The Raspberry Pi Model 3B has on-board WiFi capabilities, making it readily able to communicate with a Base Station. Because I created the

Bionode DataView application using Python (See Section 2.2.4), it was easy to build and install on the Linux operating system installed on the Raspberry Pi computers. After installing the Bionode DataView software on each Raspberry Pi computer, I paired each Raspberry Pi to one Base Station. The wireless link between the Raspberry Pi computers and the Base Stations allowed me to locate the Raspberry Pi's and the monitor, keyboard, and mouse in the animal handling facility without being tethered to the Base Stations and WPT chambers.

To avoid having to deploy four sets of keyboards, mice, and monitors inside the animal facility, I used HDMI and USB switches to connect these user interface peripherals to all four Raspberry Pi computers. This scheme allows me to control a particular Raspberry Pi by simply selecting it on the USB switch to send the keyboard and mouse signals and HDMI switch to receive the video signals. This greatly reduced the amount of equipment that I had to purchase and deploy in the confines of the rat-room in the animal facility.

I attached two cameras (Amcrest 960H AMC960HBC36-B) to the sides of each WPT chamber to acquire videos of each rat as shown in Figure 3.4. The placement of these cameras on opposite corners of the cage provide full video coverage of the inside of the WPT chamber. To achieve full coverage, I removed each camera from its outer casing and inserted the lens directly inside the chamber through one of its open side slots. These cameras are part of the Amcrest 4-channel video security system (AMDV40M4-4B-B) that I purchased for this work. I chose this video recording system because of its low cost and ease of use. Each camera has light sensors and infrared LEDS for low-light recording which is important because rats are nocturnal creatures and often seize when the lights are turned off in the animal facility.
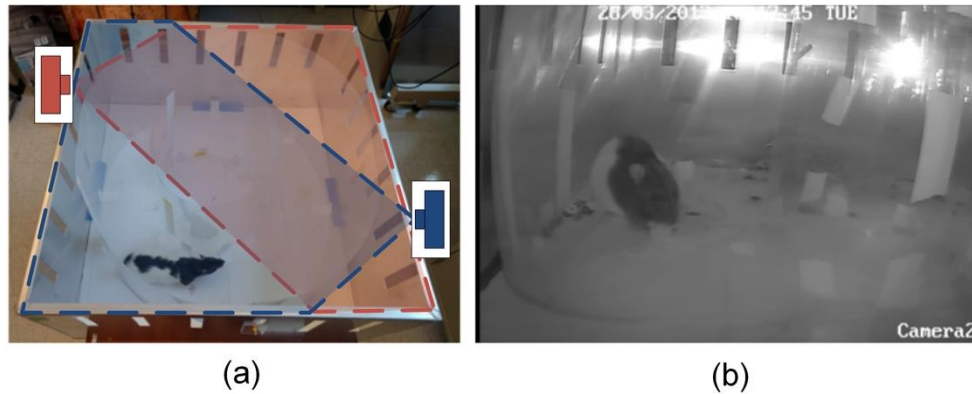
Figure 3.4: (a) Two cameras provide full video coverage of the inside of the WPT chamber. (b) Screen grab of video captured during data acquisition.

All videos recorded by the video surveillance system are stored in the system's internal hard drive in a circular buffer. A timestamp and camera identification label are superimposed onto the video frames which is essential for data-video synchronization. During initial experiments, I noticed that the video surveillance system clock and the Raspberry Pi computer clocks did not stay synchronized. I typically observed a 1 to 2 second drift per day. Over the course of a month of data collection, this drift became a real problem, so I started recording each Raspberry Pi's system time in relation to its associated video time on a daily basis. I later removed any discrepancies on order to synchronize the data to the video (See Section 3.4.1).

3.3.2 Data Storage

Because of the spontaneous nature of the rats' seizures, we had to gather continuous data from each rat. We typically recorded four channels of 10-bit data with a 5 kHz total sample rate (1.25 kHz per channel). This produced up to 783 MB of data per day per rat. Additionally, the video recordings produced approximately 30 GB of data per cage (two video streams at ~166 kB/s each). When acquiring data from four rats concurrently, we generated up to 3.1 GB of biopotential data and 120 GB of video data per day. Due to time constraints, we were unable to actively filter out unneeded data in real time, so we had to store and back-up all of the data until we had opportunity to review it. We did this by copying data from the Raspberry Pi computers and the DVR at a rate of to external hard drives 2 to 3 times per week. Additionally, we uploaded all of this data to servers made available to us by the Purdue Institute of Integrated Neuroscience to increase ease of data sharing.

3.3.3 Animal Husbandry

It is important to know when the rats begin to seize because some rats experience abnormal weight fluctuations when they begin seizing and may require supplemental food and/or water. It is also important to observe the health of the implant location to ensure that any abnormalities are immediately caught and dealt with (e.g. implant migration, open sutures, dermal necrosis, etc.) Because of these concerns, we undertook all animal husbandry responsibilities ourselves for the rats during the data acquisition phase. This included daily feeding, weighing, and health observations as well as weekly WPT chamber cleaning. Additionally, we recorded specific observations regarding seizing activity or other activity indicative of seizure onset on a daily basis. While the rats were in the WPT chambers, we fed them dry rat pellets, apple slices, and supplemental dietary gel food.

3.4 Data Translation

Data recorded by the Bionode DataView application is saved in its raw, binary form (See Section 2.2.4). Saving the data in its raw form allows us have a record of the original data as recorded by the implantable device. Any transforms performed on this data can therefore always be undone by referring to the original record. Additionally, as described in Section 2.2.4, we can analyze various fields within the raw-data communication packet structure to quantify various statistics regarding data telemetry and implant powering performance.

Because the data is recorded as raw, binary information we must translate the binary data files into a file format that is importable by common data analysis software (e.g. MATLAB, or Spike 2). Because of the high volume of large binary data files that we generated during the data acquisition phase, I created a Python script that is able to automatically translate the binary files into multi-channel .wav files that are easily importable into multiple signal analysis software packages. After translating the data into a .wav file, the Python script also analyzes the raw data packets and generates output files describing the telemetry and powering performance of the implant as indicated by the raw binary data.

3.4.1 Converting Binary Data

The Python script that I created to convert the binary data file generated by the Bionode DataView software into a .wav file is named Bin2wav.py, and it is outlined in Figure 3.5. I chose the .wav file format because it encodes the sample rate, number of channels, and data resolution in its header and because .wav files are easily importable into MATLAB and Spike 2, which are the two data analysis software packages that I used most when analyzing acquired biopotential data.
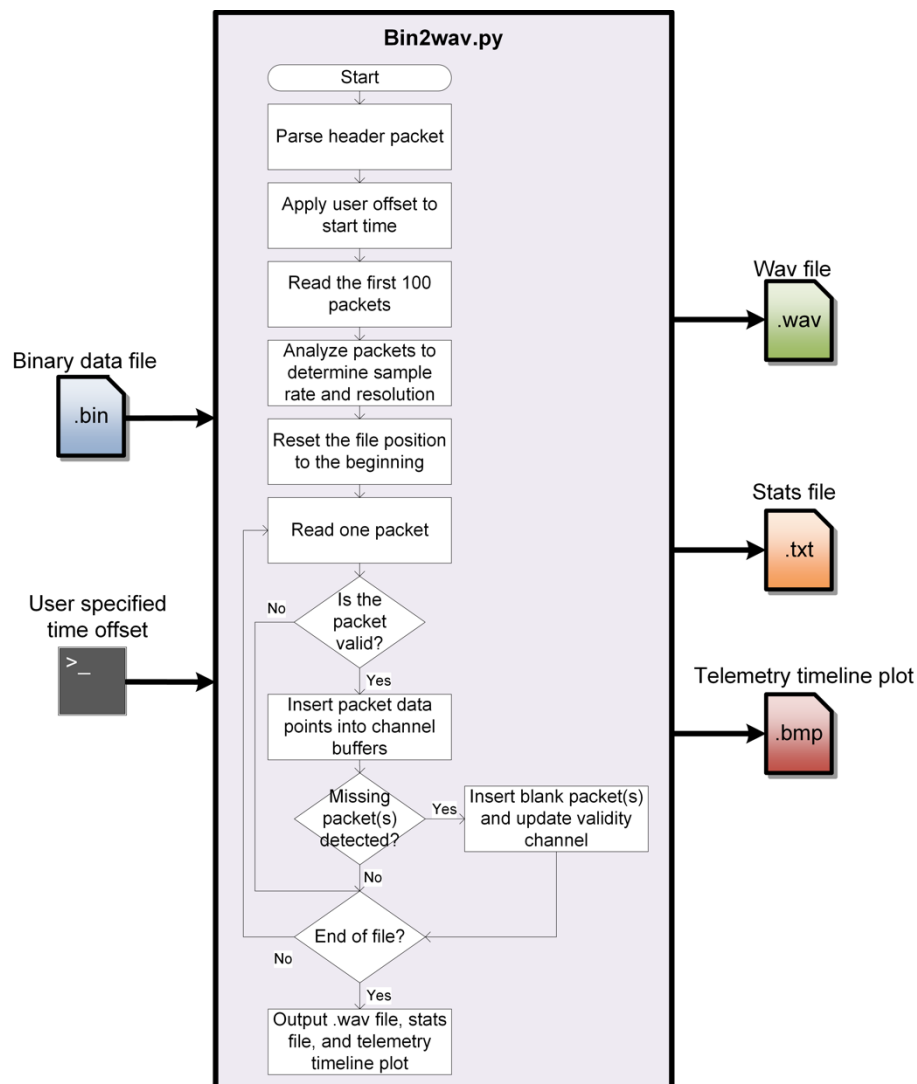
Figure 3.5: The Bin2wav.py script converts raw binary data files into .wav files. During this conversion, it inserts blank packets whenever it detects missing packets in order to ensure that the .wav file contains uniformly sampled data. Along with the .wav file, the Bin2wav.py script outputs various powering and telemetry fidelity performance statistics in the form of a text file and a visual telemetry performance timeline bitmap.

Because the Bionode implant relies on wireless data transmission and wireless powering, it is not uncommon to lose packets of data due to packet collision, attenuated telemetry, and/or insufficient implant powering. This causes packet-long gaps of data to exist in the raw binary data file. These gaps in the data file make the data non-uniformly sampled. Most common data spectral analysis techniques require a uniform sample rate [104]. The .wav file format assumes a uniform sample rate as well. For these reasons, the Bin2wav.py script must analyze the raw data to search for these gaps and fill them in when detected. Additionally, when filling in these gaps, the Bin2wav.py script must somehow alert the user as to when and where the data gaps have occurred in order to avoid mistaking filled-in data with acquired data.

The Bin2wav.py script finds gaps in the raw binary data file by analyzing the timestamp at the end of each packet. The Base Station appends these timestamps to the end of each packet, so the timestamp values increment independently of the implant's powering and wireless data transmission performance. This makes the timestamp values a much more reliable measurement of acquired data timing than other fields in the data packets. Because the sample rate of the data is known (as set by the user at the time of data collection), the number of data points per packet is known (40 for 8-bit recording and 32 for 10-bit recording), and the frequency of the timestamp increments is known, (31.25 kHz), the expected difference between the timestamps in subsequent packets can be calculated using Equation (3.1).

$$Expected\ Timestamp\ Diff = \frac{Samples\ Per\ Packet}{Sample\ Frequency * Timestamp\ Frequency} \qquad (3.1)$$

Missing data packets are detected by calculating the difference between the timestamps of every subsequent packet in the raw binary data file and comparing the difference to the expected difference. The number of missing data packets between two subsequent packets is found using Equation (3.2)

$$N_{missing\ packets} = \left| \frac{Calculated\ Timestamp\ Diff}{Expected\ Timestamp\ Diff * Samples\ Per\ Packet} \right| \qquad (3.2)$$

As the Bin2wav.py script parses through the entire raw data binary file, it reconstructs the Bionode transmission packets contained in the file. After constructing these packets, the script checks the packets to determine if they are valid (See Section 2.2.4). The script then separates the payloads of each valid packet into channels (2 for 2-channel data recording, and 4 for 4-channel data recording). Data from each channel is appended to temporary python lists. One additional list is constructed alongside the channel data lists called the validity channel. This list is used to indicate the validity of the data contained in the other channel lists. Whenever valid data is appended to the channel lists, a '1' value is appended to the validity channel list. While parsing through the raw data binary file, if any packets are determined to be missing using Equation (3.2), blank data is inserted into the channel lists, and a '0' is appended to the data validity channel list. When inserting blank data into the channel lists, the user can configure the script to insert a particular value (e.g. 0, or the value of the last data point), or an interpolated line of values between the last recorded data point and the next valid data point. In the data presented in this work, chose to configure the script to fill in missing data with the value of the last recorded data point. This reduces the choppy look of the data while also making it clear when data has been inserted without needing to refer to the validity channel.

After the Bin2wav.py script has fully parsed the raw data binary file, it bit-shifts all of the data points in the channel lists to force them to be 10-bit data. This unifies the output file format of the script, making it possible to scale data contained in the output .wav file without needing to know the original data resolution. The script then zips all of the channels together (including the data validity channel), and generates a .wav file using functions contained in the "wave" python module.

3.4.2   Implant Performance Statistics

Because the raw data binary file contains all of the information contained in a Bionode communication packet, certain implant performance metrics can be gleaned from analyzing various fields in the communication packets. Metrics of particular interest include data start date/time, actual sample rate, total packet count, telemetry fidelity, powering fidelity, and data validity over time. The Bin2wav.py script automatically determines these metrics and provides

them to the user in both an output stats file as well as a telemetry timeline plot (See Figure 3.8 at the end of this section).

The actual start time of the first data point is crucial for video/data synchronization. When the Bionode DataView application generates a new raw data binary file, it inserts a header packet at the beginning of the file which contains the current system date and time, the number of channels being recorded, and the sample rate of the data recordings. The Bin2wav.py script parses this header packet to determine the actual time of the first data point. It determines this time using the reported file start time, the timestamp of the first data packet, and the user specified time offset as shown in Equation (3.3). The user specified time offset allows the user to compensate for recorded time differences that may exist between the data acquisition PC and the video acquisition system (See Section 3.3).

$$Start\ Time = File\ Start\ Time + \frac{1st\ Timestamp}{32*10^{-6}} + User\ Specified\ Offset \qquad (3.3)$$

Before parsing the entire raw data binary file, the Bin2wav.py script collects an initial sample of 100 data packets and analyzes the timestamp differences of all subsequent data packets (indicated by subsequent Packet ID Numbers). The script then compares the average of all subsequent packet timestamp differences to the expected timestamp difference as calculated by the reported sample rate in the header of the file using Equation (3.1). Discrepancies between these two values indicates that the Bionode implant was unable to sample data at the desired sample rate. Both the calculated timestamp difference and the expected timestamp difference are recorded in the stats.txt output file.

Telemetry and powering fidelity metrics were of great interest especially while developing the Bionode implant's radio and powering circuitry. Because the rats can move freely within the WPT chamber, the data telemetry and powering efficiencies can fluctuate greatly over a 24-hour period depending on how much the rat is moving, what position it prefers, where it decides to sleep, and how long it sleeps. A robust telemetry and powering system should be able to successfully transmit data while staying powered in even the most inefficient of telemetry and powering situations. For

these reasons, I added the ability to record and report on these two metrics to the Bin2wav.py script.

Both telemetry and powering fidelity are calculated after the Bin2wav.py script has finished parsing the entire raw data binary file. The total data fidelity is easily calculated by analyzing the data validity channel to determine the number of missed packets vs. the total number of packets. Because the data validity channel list contains a '1' for every valid packet, and a '0' for every missed packet, the total data fidelity is given by Equation (3.4)

$$Total\ data\ fidelity = \frac{sum(validityChannel)}{len(validityChannel)} \tag{3.4}$$

While the data fidelity metric is a useful indication of overall implant performance, it is more useful to know what percentage of the missed data is due to telemetry drop-outs vs. insufficient implant powering. Because the implant cannot directly report on how long it has been powered off, these metrics must be acquired indirectly by analyzing the timestamp fields inserted in the communication packet by the Base Station. When a single packet is lost during a failed telemetry transmission, a gap in time equal to one expected timestamp difference is detected by the Bin2wav.py script. Likewise, whenever any number of packets are lost due to failed telemetry transmissions, the gap in time detected by the Bin2wav.py script is equal to a multiple of the expected timestamp difference between packets. If, however, the Bionode shuts down due to insufficient powering, the Bin2wav.py script will detect a gap in time equal to length of time that the Bionode was shut down. The probability that this gap in time is equal to a multiple of the expected timestamp difference is given by Equation (3.5)

$$P_{IsMultiple} = \frac{1}{Expected\ Timestamp\ Difference} \tag{3.5}$$

Because this probability is typically low (e.g. 0.005 when sampling at 5 kHz), the Bin2wav.py script determines that gaps in time that are multiples of the expected timestamp difference are due

to telemetry failures, and gaps that are not multiples of the expected timestamp difference are due to powering failures.

An example of the of this usefulness of these metrics is the difference in failure modes of the implantable devices implanted in ER129 and ER128. As shown in Figure 3.6, while both ER129 and ER128 had implants suffering from data fidelity issues, the reason behind their data telemetry issues was different. Over the course of approximately 18 days, ER129's implant achieved a data fidelity of 69.56%, while ER128's implant achieved a data fidelity of 55.75%. Of the packets lost by ER129's implant, 86.76% of them were due to telemetry failures, with the rest being attributed to powering failures. However, of the packets lost by ER128's implant, only 19.72% of them were caused by telemetry failures, with the rest of them being attributed to powering failures. The separate telemetry and powering metrics make it clear that the low data fidelity performances achieved by these two implants were caused by different issues.
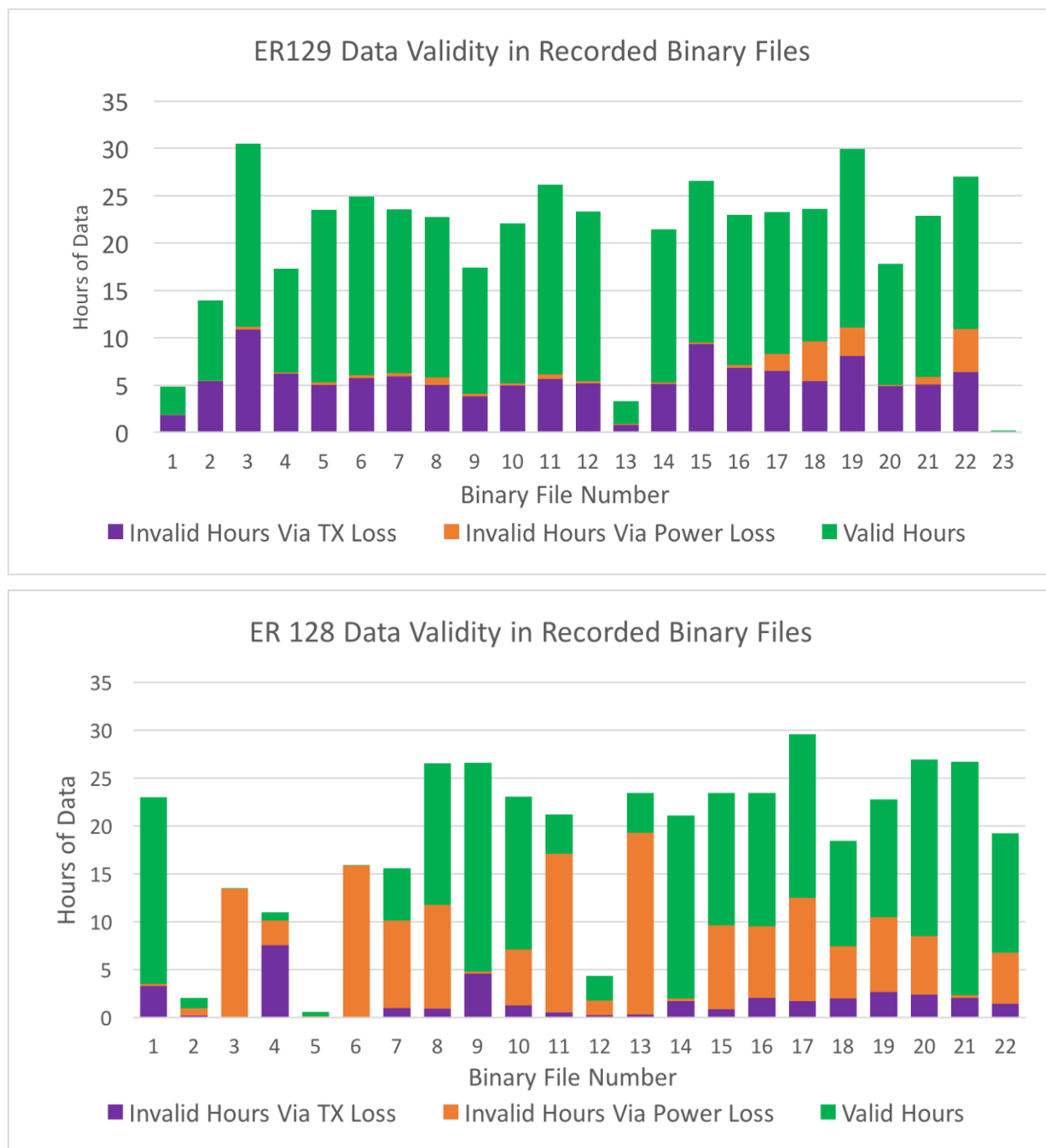
Figure 3.6: Both of these rats (ER129 and ER128) had implants suffering from higher than normal data loss. ER129's implant (top) suffered from data-loss due mainly to telemetry failures. ER128's implant (bottom) suffered from data-loss due mainly to power failures.

For comparison, Figure 3.7 shows the telemetry and powering metrics measured from an implant with more typical data fidelity performance. Over the course of approximately 18 days, ER165's

implant achieved a data fidelity of 95.97%. Of the packets lost by ER165's implant, 2.7% of them were due to telemetry failures, with the rest being attributed to powering failures.
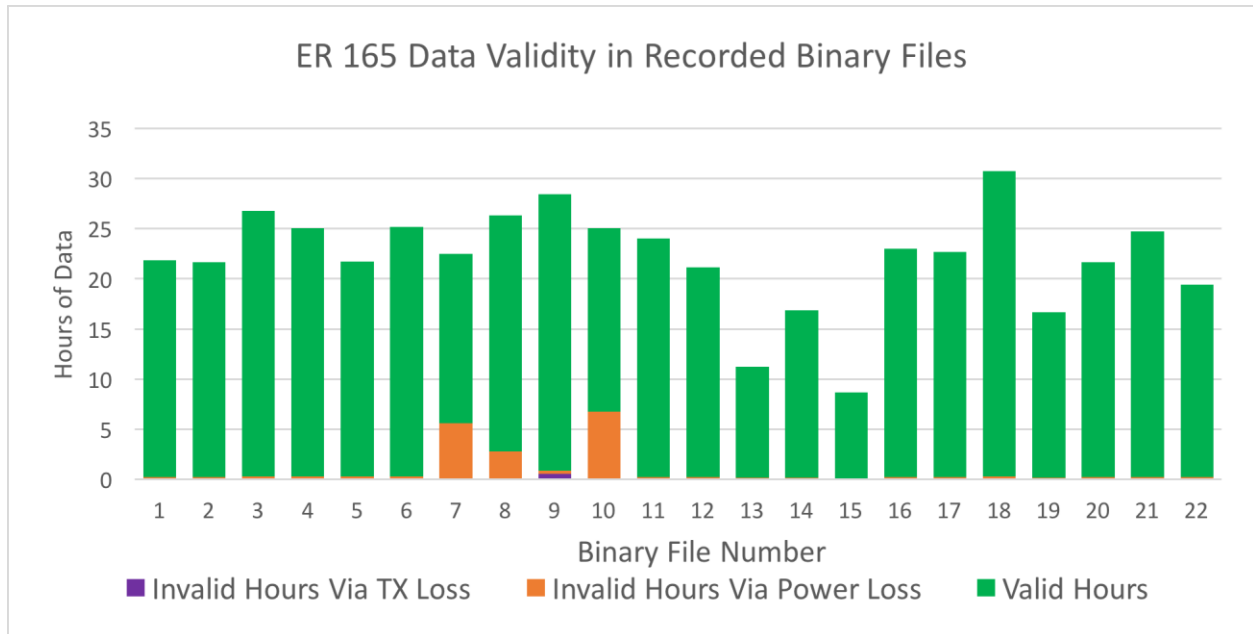
Figure 3.7: ER165's implants achieved data fidelity of over 95% during the course of approximately 18 days. The majority of the data loss occurred during 2 of these days, and was due to insufficient powering.

Both telemetry and powering fidelity are affected by the movements of the rat in the WPT chamber. If the Bionode's antenna is located far away from the Base Station's receive antenna, or if there are objects between the two antennas (e.g. the rat's body, food, or bedding), some packets may be lost. Also, if the rat spends long amounts of time in an orientation that is suboptimal for wireless power transfer (See Section 2.2.5), the Bionode may shut down due to insufficient powering. For these reasons, the data fidelity performance tends to change from hour to hour and from day to day. The location, duration, and frequency of these changes can point to the source of different data fidelity issues. For instance, multiple short losses of data indicate a small disturbance in data telemetry, while a single, long loss of data indicates something more serious like a power loss or telemetry dead spot. To visualize the data fidelity performance over time, the Bin2wav.py script auto-generates a data fidelity timeline report for each raw data binary file as shown in Figure 3.8.

Figure 3.8: Data fidelity timeline reports are auto-generated by the Bin2wav.py script. (a) This report indicates normal data fidelity with no major gaps in the data. (b) This report indicates that the Bionode shut down at around 3:00 AM on the 19th of May and stayed shut-down until approximately 8:50 AM the same day. This data fidelity report corresponds to ER-165's raw data binary file #7 as shown in Figure 3.7 which also indicates that the implant suffered from power-loss during this file. (c) The Raspberry Pi computer used to gather this data experienced periodic WiFi disconnect issues causing data loss with a consistent periodic pattern. (d) This Bionode was damaged post-implantation and suffered from both power losses and telemetry losses. It's Raspberry Pi computer also had WiFi disconnection issues as seen by the periodic data losses. In the background.

START   :2018-05-17 13:50:41.006720
END   :2018-05-18 14:51:57.980896
DURATION:1 DAY, 1:01:16.974176

START   :2018-05-18 14:55:17.009472
END   :2018-05-19 13:17:08.561472
DURATION:22:21:51.552000

(a)   (b)

START   :2018-07-22 14:34:11.884352
END   :2018-07-23 15:46:59.712672
DURATION:1 DAY, 1:12:47.828320

START   :2018-07-25 12:38:51.002464
END   :2018-07-26 14:46:08.669696
DURATION:1 DAY, 2:07:17.667232
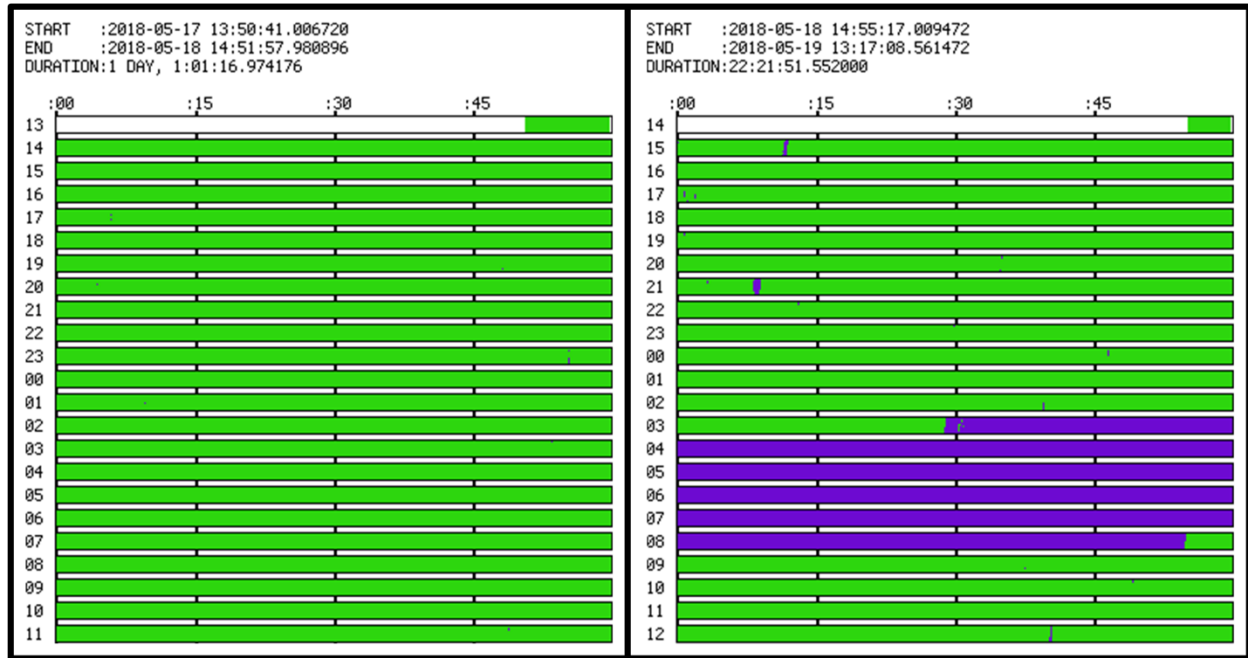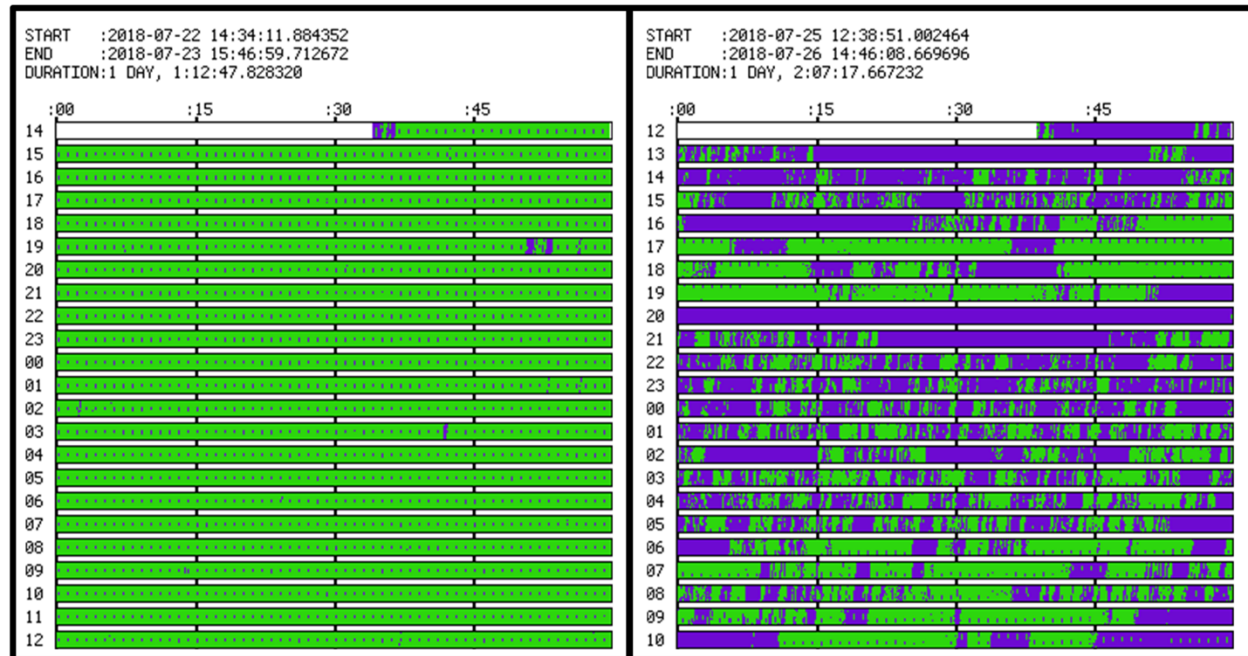
(c)   (d)

Lost Packets

The data fidelity timeline reports are simply a time-line plot of the data validity channel where each row depicts one hour of data collection. Each row is 360x10 pixels in size, making each pixel represent 1 second of data. Green pixels represent low packet loss ($< 50\%$ of packets lost), while purple pixels represent high packet loss ($> 50\%$ of packets lost). These charts make it easy to determine the state of the implant's data telemetry and powering performance over the course of hours and days at a glance. For instance, in Figure 3.8, it is easy to see that the implant performance indicated by report (a) is much better than the performance indicated by report (d). In Figure 3.7, it can be noted that the raw data binary file #7 contains greater packet loss due to power failure than normal. The data fidelity report for this file is shown in Figure 3.8 (b). This report shows that the power failure was most likely contained in a single event between the hours of 3 and 9 AM on May 18th, 2018. While the report does not tell us why the implant lost power, it is an important clue nonetheless because a single low-power event suggests a much different diagnosis than multiple, short power down events would (e.g. the rat falling asleep in a poor powering area vs. the battery being damaged and causing multiple restart events).

Failure modes that these data fidelity reports are particularly good at detecting are hardware failures in the data acquisition systems. Figure 3.8 (c) depicts one of these errors. During the course of data collection, we decided to upgrade the Raspberry Pi computers from Model 3 B boards to Model 3 B+ boards. We realized, however, that after making this upgrade, we started losing packets in a very uniformly periodic way as indicated by the repeated, short data loss events shown in Figure 3.8 (c). We determined that the Model 3B+ Raspberry Pi computers were having issues maintaining their WiFi connections with the Base Stations. Based off of this data, we rolled back the Raspberry Pi computers to their original Model 3B boards and the periodic dropped packets disappeared. I highlight this case because when looking at the data fidelity numbers alone, this issue would not have been found. Over the course of the file reported by Figure 3.8 (c), it achieved a total data fidelity of 95.44%, which we would not typically label as poor performance. The only way we found this issue was by looking at the data fidelity timeline report.

3.5   Signal Validation

Before analyzing the ECoG, ECG, and respiration signals that we acquired from the 51 rats that we implanted with Bionodes, we needed to validate that the signals gathered by the Bionode were

in actuality the signals that we desired to measure. While a representation of these signals has already been shown in Figure 2.9, this section will look more closely at each of these signals with the intention of validating them as properly measured physiological signals. The ECG and ECoG waveforms were relatively straightforward to validate because they are common signals that are well documented [134, 135]. We had to invest much more effort into validating the respiration signal because the method that we used to acquire this signal had never been reportedly performed in a long-term chronic implant with a fully implantable transducer.

3.5.1 ECG Signal Validation

I validated the ECG signals by visually confirming that the all PQRST complexes within the ECG waveform were present [134]. Because the ECG electrodes are sutured directly to the muscle wall, the electrode-tissue impedance may increase over time due to encapsulation [136], so I performed an analysis of the ECG waveform amplitude change over time as well. Figure 3.9 presents an ECG waveform that we acquired from a freely behaving rat (ER164) inside the WPT chamber. This data was gathered two weeks after the implant surgery. Figure 3.9 clearly shows that all PQRST complexes are readily identifiable in the signal.
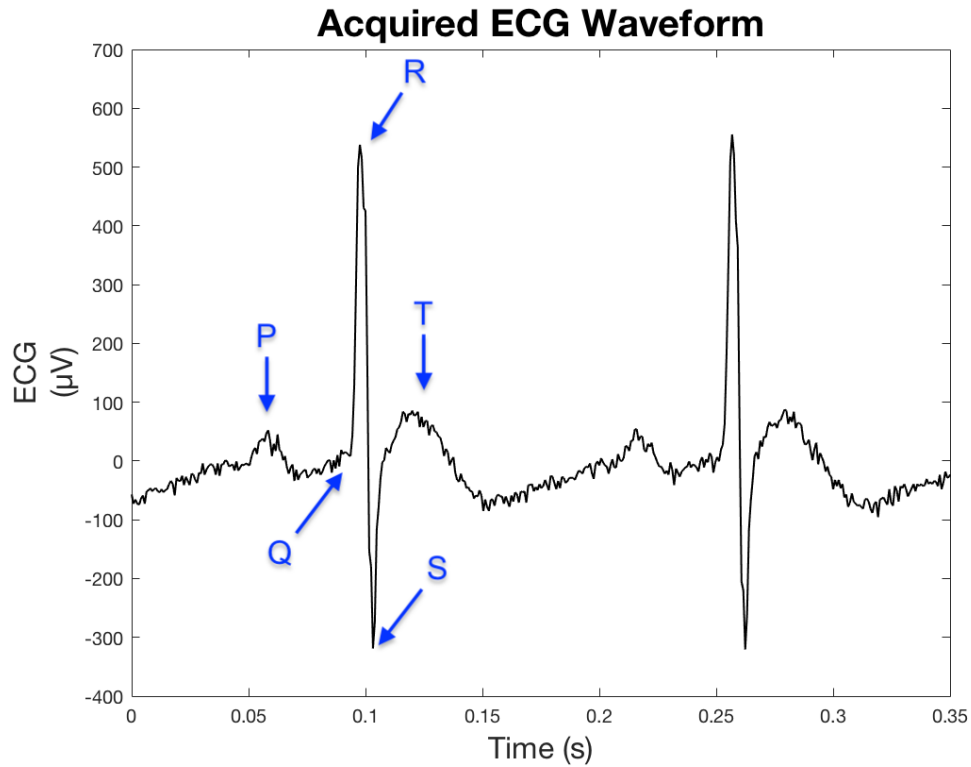
Figure 3.9: An electrocardiogram (ECG) signal recorded from a freely behaving rat (ER164). All PQRST ECG complexes are clearly shown.

After confirming that the chronic ECG measurements recorded a useful ECG signal, I looked at signals recorded from the same freely behaving rat (ER164) at 1, 2, 4, and 6 weeks after the implant surgery. For each week, I chose 1-second samples of the ECG signal that were comparable to each other (e.g. not affected by motion artifacts, and not near seizing activity). Figure 3.10 shows each of these 1-second samples.
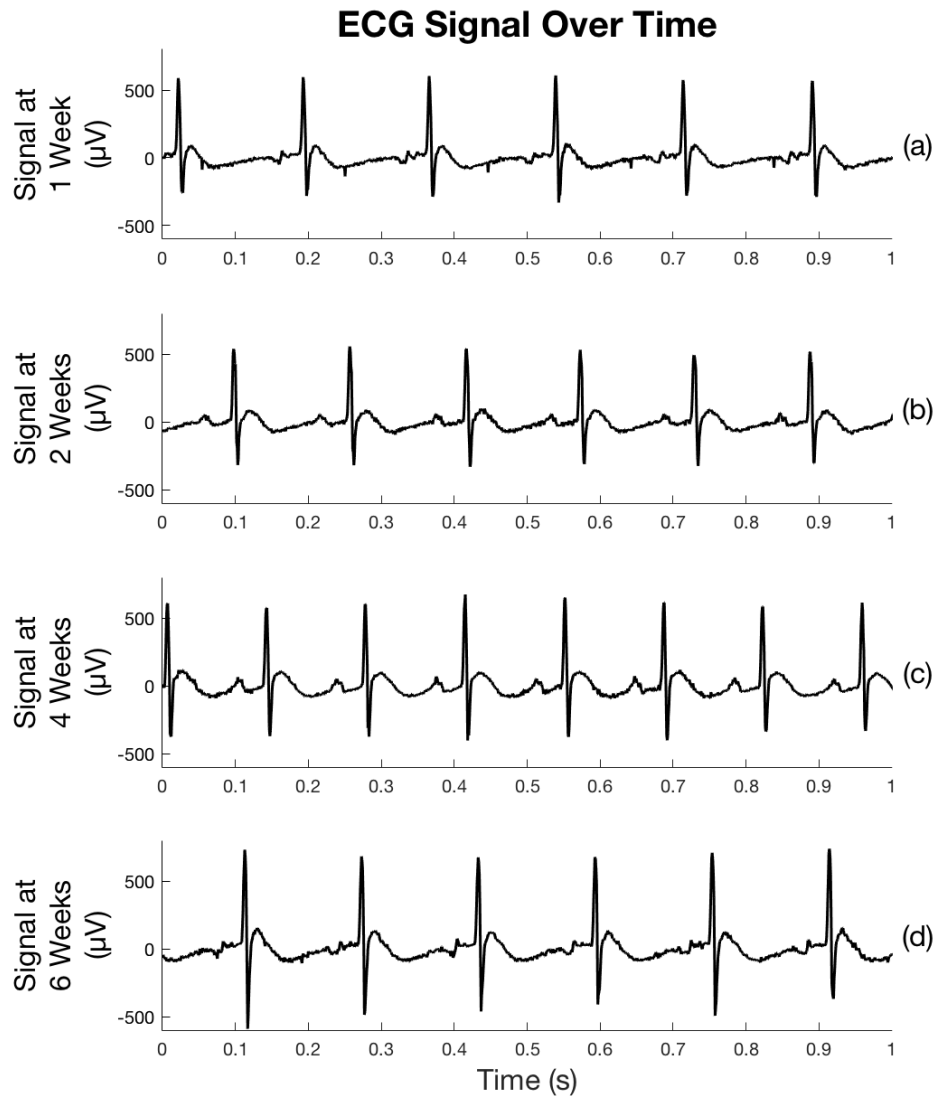
Figure 3.10: Electrocardiogram (ECG) signals recorded from a freely behaving rat (ER164) at 1, 2, 4, and 6 weeks after the implant surgery. No attenuation of the signal over time is present.

In general, it is clear that the overall amplitudes of the sampled ECG waveforms shown in Figure 3.10 do not decrease from week to week. I should note here that this form of evaluating the long-term chronic performance of the ECG recording channel will produce limited results. This is because the specific characteristics of the ECG input signal are unknown. This makes it difficult to apply typical noise measuring metrics. To further quantify the amplitude changes of the ECG waveforms, I calculated the average amplitude of the P, QRS, and T complexes contained in the sampled data displayed in Figure 3.10. These calculated amplitudes are displayed in Figure 3.11
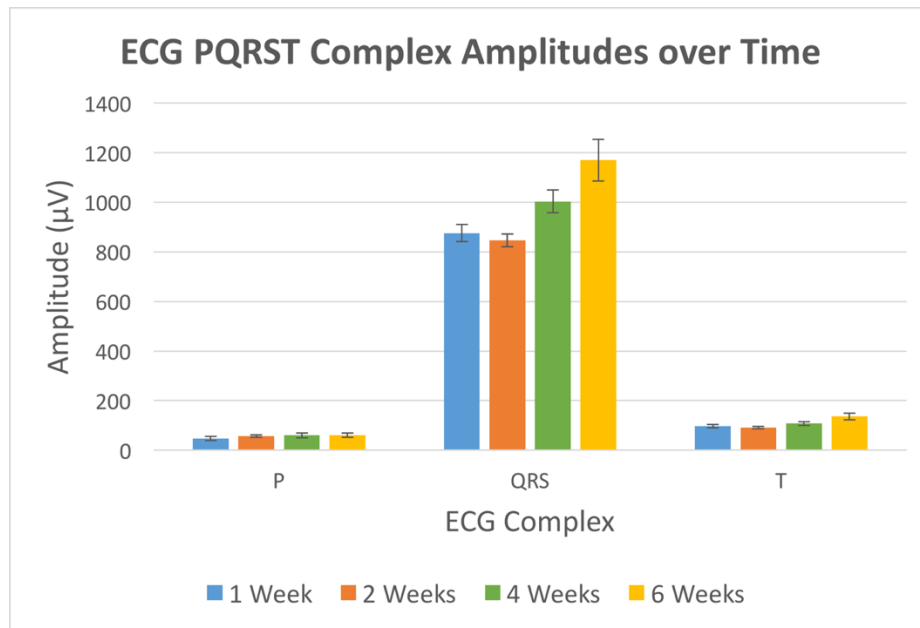
Figure 3.11: The amplitudes of the P, QRS, and T complexes of 1-second of sampled ECG data from 1, 2, 4, and 6 weeks after surgery do not indicate any reduction of amplitude in any of the complexes over time. Error bars represent ± standard deviation.

The sampled ECG data gives no indication that the amplitudes of the PQRST ECG complexes reduce from week to week. In fact, my analysis shows that the QRS and T complexes experience a slight increase in amplitude over time. While it is currently unclear if this increased amplitude in the QRS or T complexes is pathological, the increase does support the conclusion that the Bionode's ECG channel is not experiencing an acute loss of signal due to lead encapsulation over time.

3.5.2 ECoG Signal Validation

I validated the ECoG signals by analyzing the ECoG channels of rats during known and verifiable neurological events. Figure 3.12 displays ECoG data recorded during a seizure from ER164. The annotated start and end of the seizure as well as the head shake were verified by viewing the concurrent video recordings. The initial increase in amplitude of the ECoG signal at the start of the seizure, the period of neural suppression at the end of the seizure, and the head shake artifact following the end of the seizure is consistent with EEG recordings and observations of other work using the TeNT model [32].
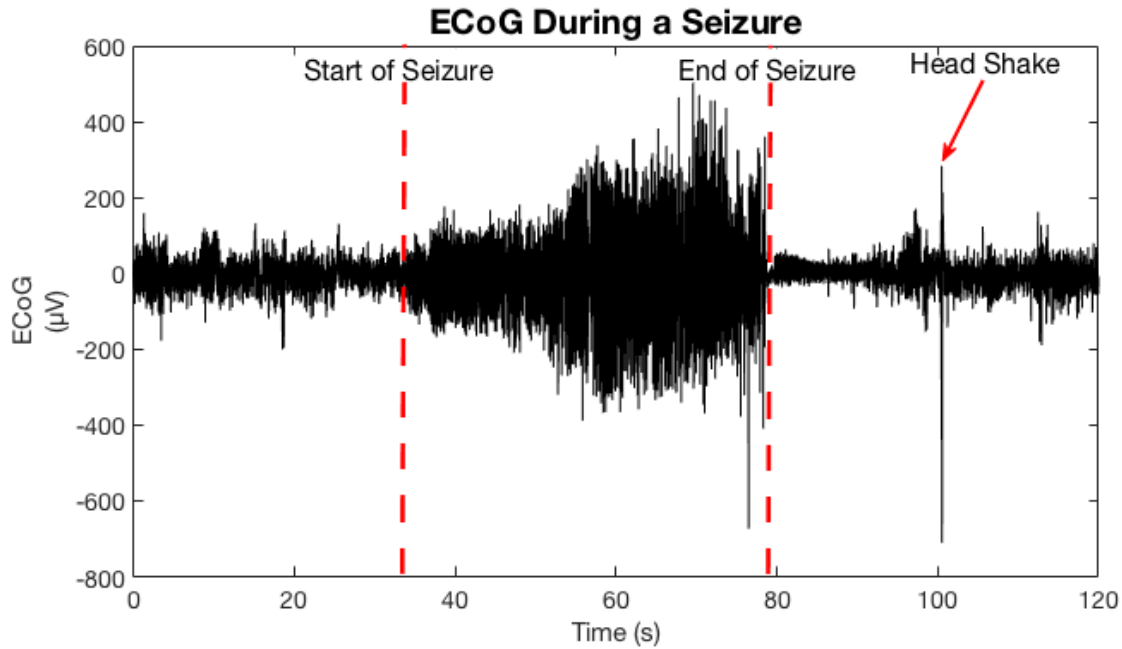
Figure 3.12: ECoG recorded from ER164 during a seizure. This seizure was verified via concurrent video recordings.

To validate the ECoG signal in the frequency domain, I took two 30-second samples of the ECoG signal shown in Figure 3.12, one during the preictal phase (before the seizure) and one during the ictal phase (during the seizure), and plotted the estimated power spectral density (PSD) of each sample using the Welch's method with a Hamming window [137]. This plot is shown in Figure 3.13. The increased power during the ictal phase seen below 40 Hz and specifically near 30 Hz and in the 9-16 Hz band is consistent with findings reported by [138] when using the TeNT toxin model.
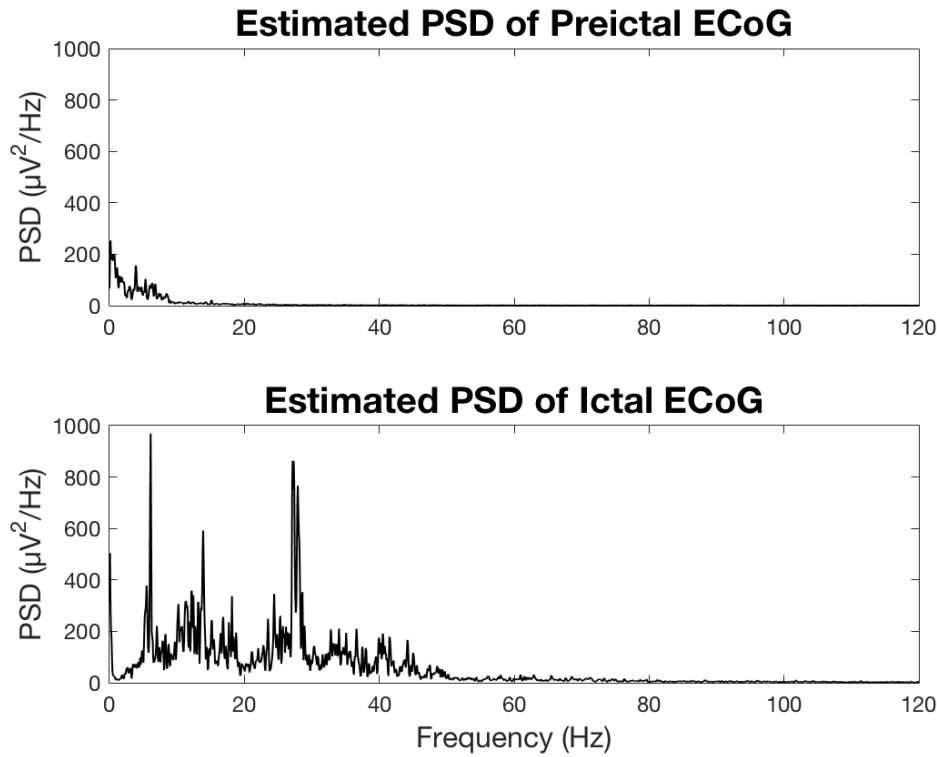
Figure 3.13: Estimated power spectrum density (PSD) of 30-second samples of the ECoG data shown in Figure 3.12 taken during the preictal (top) and ictal (bottom) phases. PSD is estimated using Welch's method with a Hamming window. The increased power during the ictal phase seen below 40 Hz and specifically near 30 Hz and in the 9-16 Hz band is consistent with findings reported by [138] when using the TeNT toxin model.

Another verifiable neurological event that I used to validate the ECoG channel is sniffing behavior. This behavior, which is verifiable via concurrent video recordings, leads to increased oscillations in the type 1 hippocampal theta rhythm band (6 to 12 Hz) [54, 139]. I used this behavior to validate the respiration channel, so this analysis is further explained in the following section. Figure 3.15 shows the respiration, ECoG, and ECG channels during sniffing events. The major frequency component of the oscillations observed on the ECoG channel is 8 Hz, which falls inside the aforementioned theta rhythm band.

3.5.3   Respiration Signal Validation

Validating the respiration signal involved a much more in depth process because of the novel way in which we measured it. We analyzed respiration gathered over time from 8 of the 51 rats

implanted with Bionodes equipped with respiration transducers. The durations of each of these studies is shown in Table 3.1.

Table 3.1: Implant study durations.

Rodent ID	Thermocouple Transducer ID	Study Duration (Days)
ER-119	1	44
ER-120	2	31
ER-121	3	24
ER-128	4	41
ER-129	5	23
ER-131	6	32
ER-134	4*	12
ER-138	6*	18

*Recycled transducers.

We performed initial validation of the acquired respiration signal visually by observing a rat's chest movements during respiration alongside a live feed of the implanted thermocouple's signal. Because the signal rose and fell in synchrony with chest movements related to respiration, and because it was similar to known respiration signals as shown in [53, 54], we determined that the acquired thermocouple data provided a valid respiration signal. We then validated the acquired respiration signals from each implanted rat by observing each rat alongside a live feed of their recorded respiration signal. If the recorded signal had a similar shape and frequency to that of our previously validated recordings while the rats were breathing at rest, we deemed the acquired thermocouple data as a valid respiration signal.

To validate the measured respiration signal quantitatively, I reviewed the video files that we recorded during data collection and manually counted respiration by annotating chest movements in the video recordings for ER138. I plotted these manual respiration annotations alongside the simultaneously recorded respiration data gathered from the thermocouple transducer. Figure 3.14 displays this data. I have removed the DC offset of the respiration signal and applied a digital low-pass filter with a time-constant of 0.1 seconds.
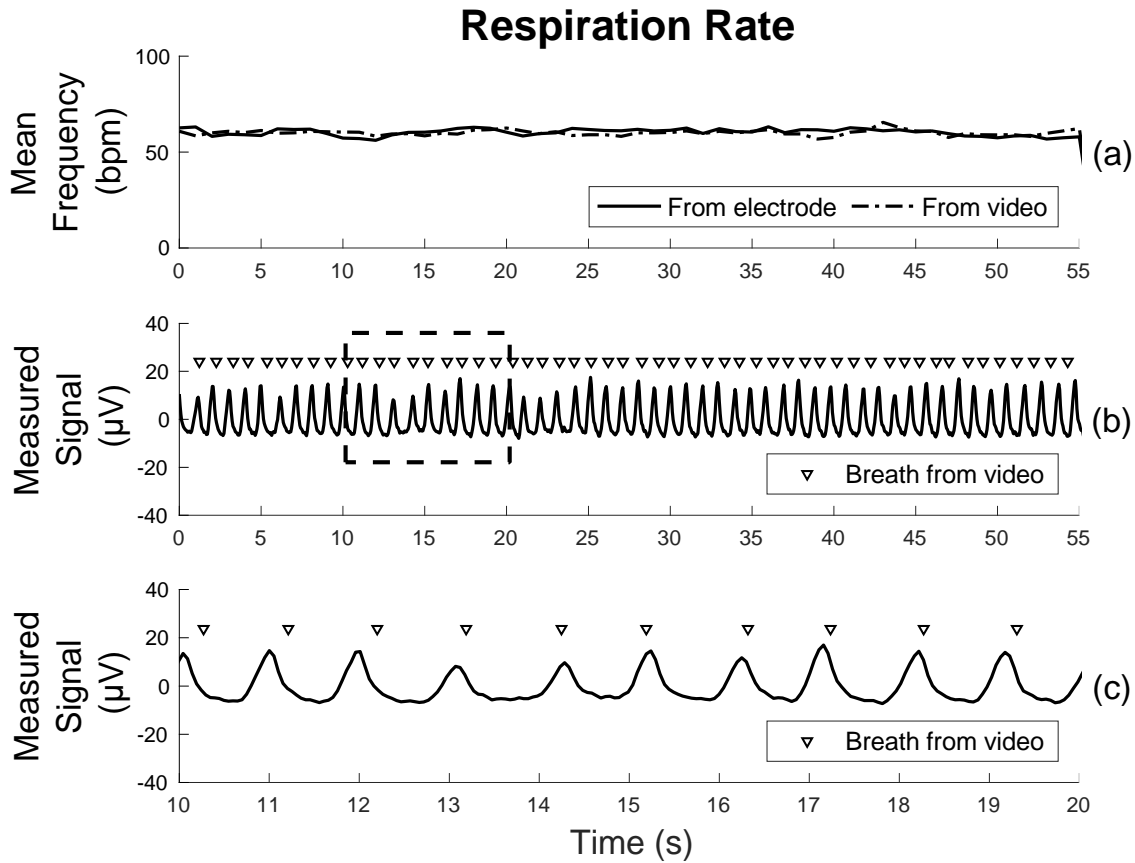
Figure 3.14: I gathered all of the data shown in these three plots from ER138. The plot in (a) displays the mean respiration frequency in breaths-per-minute for both manually counted breaths as well as breaths determined by locating peaks in the measured thermocouple transducer signal over a 55-second period. (b) displays the data that we used to determine the mean respiration frequencies shown in (a). (c) shows 10-second subset of the data displayed in (b) to illustrate the synchrony between the manually counted breaths and the signal recorded by the thermocouple transducer.

While reviewing video files for ER-138, I noted various times when the rat sniffed. Figure 3.15 shows the ECoG, ECG, and respiration signals that the Bionode recorded during sniffing activity. I have removed any DC offsets from each signal, and applied a digital low-pass filter to the respiration signal with a time-constant of 0.1 seconds.

Sniffing Activity
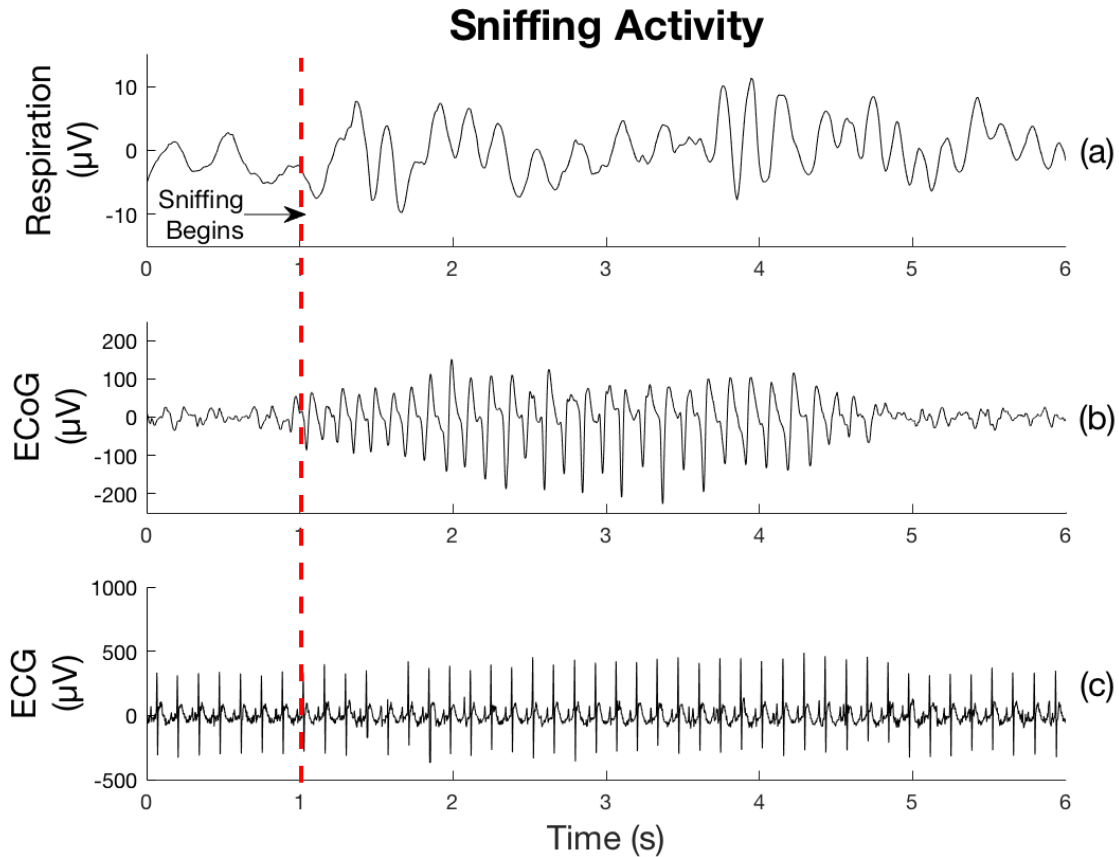
Figure 3.15: I gathered all of the data shown in these three plots from ER138 during the same 6 second time period. These plots show (a) respiration, (b) ECoG, and (c) ECG data that we recorded when the rat was sniffing. The rapid changes in the respiration channel as well as the characteristic 8-Hz theta wave in the ECoG channel indicate sniffing behavior. We validated this data as taking place during sniffing by reviewing the simultaneously recorded video files.

Table 3.1 shows that the rat identified as ER119 had an implanted thermocouple transducer for 44 days which is the longest duration of all the rats used for this study. Figure 3.16 depicts various 10-second snippets of respiration data recorded from ER119 during the approximately six-week long study. I have removed DC offsets from each signal, and applied a digital low-pass filter with a time constant of 0.1 seconds.
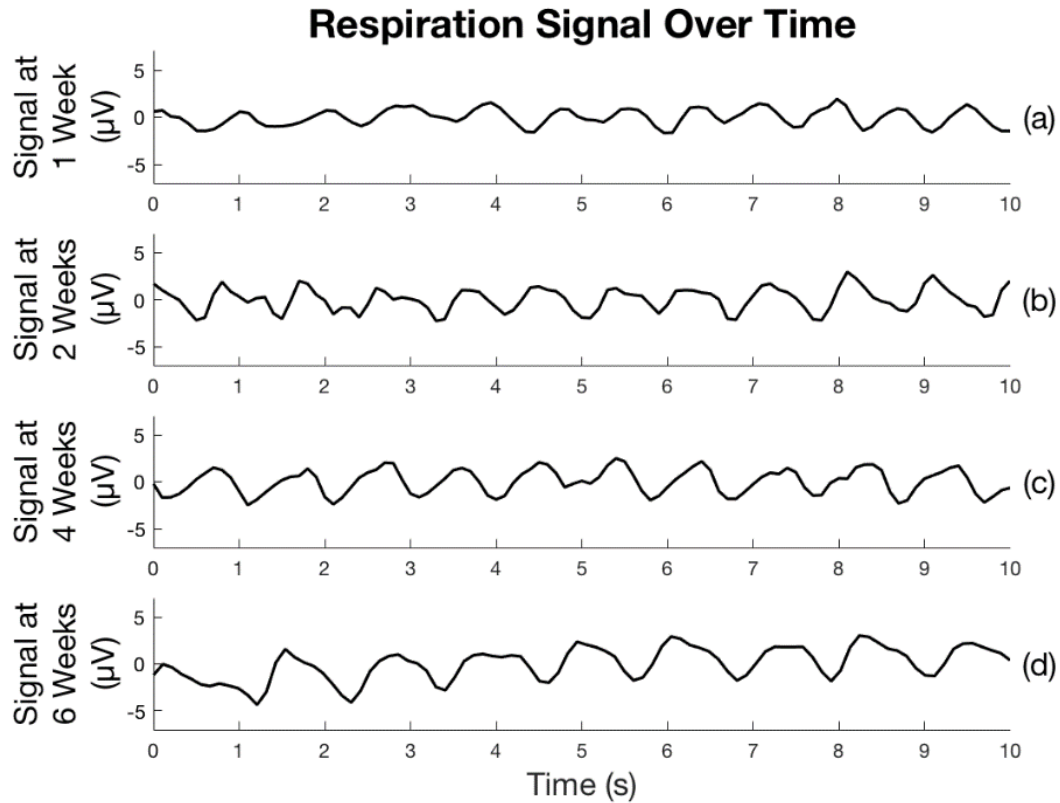
Figure 3.16: These four charts show 10-second snippets of respiration data measured by the thermocouple transducer from ER-119 over the course of 6 weeks. I removed the DC offset from each signal and applied a digital low-pass filter with a time constant of 0.1 seconds to reduce high frequency noise.

All of the respiration data I have presented in this section was recorded at least 48 hours after the implant procedure to give the rats time to recover from the operation. We occasionally ran into difficulty sensing a respiration signal while testing the implanted device during the surgical procedure as well as during the first 12 hours following the surgery. We believe that this may be due to inflammation or blood blocking the nasal cavity during the recovery period. In every study we have performed, this problem has cleared up by the end of the 48-hour recovery period.

I applied low-pass digital filters with a time constant of 0.1 Hz to all of the presented respiration data. While the Bionode implant contains analog filters to remove high frequency powering and digital noise from the incoming signals, the high gain of the respiration channel caused some of this attenuated noise to remain noticeable on the recorded signal. By universally applying a low-pass digital filter with a fixed cutoff frequency to all respiration recordings, I am able to obtain a

cleaner respiration signal. We may be able to obtain a more precise respiration measurement if we implement more aggressive passive low-pass filters in the analog front-end of the respiration channel in future studies.

We have occasionally observed a sudden loss of respiration signal that is similar to that illustrated in Figure 2.7 which may be related to the same DC drift issue that is described in Section 2.2.2. This may be because the AFE for the respiration circuit currently does not contain any passive high-pass filter, which means that the input is not biased to the midpoint of the INA333 instrumentation amplifier. This sudden loss of signal plagues certain implants more than others, which suggests that it could be exacerbated by surgical misplacement of the transducer. If the transducer makes contact with surrounding structures in the nasal cavity, it could result in a large change in signal level, which could saturate the instrumentation amplifier. In future deployments of the respiration transducer, we will add a 1 MΩ bias resistors in the R_2 position shown in Figure 2.4 to centrally bias the input of the respiration transducer.

To determine if the thermocouple transducer is a viable solution for long-term chronic respiration measurement, I will first show that signals recorded by the thermocouple transducer correspond to respiration events. Figure 3.14 (b) shows that the respiration events that we manually annotated when reviewing video of ER138 line up with individual peaks in the concurrently recorded signal measured by the thermocouple. The precision of annotating inspiration and expiration from video recording is limited. This is most likely the reason for the slight misalignments between annotated breaths and recorded peaks seen near the beginning of Figure 3.14 (c). These misalignments are relatively small, and do not result in any differences between manual respiration counts and measured signal peak counts. Figure 3.14 (a) shows that both the manual respiration annotations and the measured signal peaks result in similar mean respiration rate calculations over time.

To further validate the thermocouple transducer signal as a respiration signal, I analyzed the thermocouple signal during known sniffing events. Figure 3.15 presents the respiration signal alongside the ECoG and ECG signals measured during a sniffing event. I initially determined that the signals shown in Figure 3.15 were occurring when the rat was sniffing by observing high amplitude swings in the respiration signal concurrent with periodic oscillations in the ECoG signal.

The major frequency component of these oscillations in the ECoG signal is 8 Hz. This falls inside the band of type 1 hippocampal theta rhythms (6 to 12 Hz) that have been observed during sniffing behaviors [54, 139]. I corroborated that this data represents sniffing behavior by observing the rat sniffing in the corresponding video recordings. The measurements shown in Figure 3.14 and Figure 3.15 indicate that the signal recorded by the thermocouple transducer is a valid respiration signal.

The thermocouple transducer successfully recorded respiration data over the duration of each study outlined in Table 3.1. I will note here that during the first three studies (ER119, ER120, and ER121), we were still developing the powering system on the Bionode implant. Because the Bionode implant was not always well powered during these studies, the respiration data recorded is not continuous. The respiration data that does exist during these studies is consistent with more continuous data collected in the subsequent studies listed in Table 3.1. Figure 3.16 presents 10-second snippets of respiration data recorded from the rat ER-119 one week, two weeks, four weeks, and six weeks after we implanted the thermocouple transducer. The signal amplitude and quality did not noticeably change from week-to-week during this study.

I have shown that the thermocouple transducer can measure consistent respiration signals during studies ranging from 12 to 44 days. Furthermore, I successfully recycled two thermocouple transducers from the first six studies to use in the last two. One of these thermocouple transducers (ID = 4, see Table 3.1) has been able to record respiration data for a combined 53 days over the course of two studies. The demonstrated ability of these transducers to record respiration data throughout the duration of these studies validates the transducer as a viable solution for long-term chronic respiration measurements in freely behaving rodents.

3.6   Initial Analysis and Results

Over the course of 26 months, we implanted 51 rats with Bionodes containing a respiration transducer, 2 ECG lead pairs, and one ECoG lead pair. We also injected 45 of these rats with TeNT as described in Section 3.2. Initially, the Bionodes that we implanted had not yet been designed to use the optional batteries for supplemental powering, so they suffered long periods of power loss resulting in daily power fidelity of no more than 20%. While these Bionodes did record some

seizing activity, their poor powering performance made the resultant datasets very difficult to analyze. After we started including batteries in the Bionodes configured to run without negative rails, the power fidelity performance increased to above 95% per day. However, once we had solved the powering issues, we started having difficulty getting the rats to seize. This is due to an unknown issue that affected the efficacy of the TeNT from multiple suppliers. Because of this TeNT efficacy issue, none of the Bionodes implanted during the 8-month period following our fix to the powering system recorded any seizing activity. In spite of these two issues, we have produced a dataset gathered over the past 4 months from 6 rats injected with TeNT containing over 4,700 hours of near-continuous respiration, ECG, ECoG, and video recordings. Table 3.2 summarizes this dataset. Due to the large size of this dataset, we have not analyzed all of the data, so the seizure-count numbers in Table 3.2 are subject to change as the data-set is further analyzed.

Table 3.2: Concurrent Respiration, ECG, ECog, and Video Dataset from Freely Behaving Seizing Rats

Rat ID	Dataset Duration	Confirmed Convulsive Seizures	Confirmed Non-Convulsive Seizures
ER164	45 days	29	29
ER175	22 days	4	8
ER176	13 days	2	0
ER180	42 days	0	1
ER166[1]	30 days	0	0
ER187[2]	45 days	0	0

[1]The ECoG channel of this rat's Bionode became damaged after implantation, making seizure detection difficult. Seizures for this rat must be detected by manually viewing video data.

[2]There was an issue in backing up the video recorded from this rat. I have been unable to confirm any seizures indicated by the ECoG channel because concurrent video data does not exist.

We have recently implanted 3 more rats with Bionodes. All three of these rats are currently seizing and providing us with more data to add to our dataset. An initial analysis of the data shows some promising results. This section will document these initial results and the analysis techniques used to generate them.

3.6.1 Data Analysis Techniques

The 6 rats generated over 4,700 hours of respiration, ECG, ECoG, and video data over the course of 4 months. Because we are most interested in preictal, ictal, and postictal data, locating events in the data where the rats seize is important. While this can be done by either manually scanning the video recordings or the ECoG channel, this method of searching for seizures is very time consuming. We therefore initially flagged all seizures by looking at the running power spectrum of the ECoG channel between 30 and 300 Hz. During seizures, the power spectrum of the ECoG channel is noticeably increased over this range when compared with the power spectrum of non-ictal ECoG (See Figure 3.13). Once seizures have been flagged in the data, we validate them where possible by viewing the concurrently recorded video. The video also allows us to overlay behavioral observations on the recorded biopotential data to further clarify what the rat is experiencing during the recorded signals.

The ability to detect QRS complexes in the ECG algorithmically greatly decreases the amount of manual effort involved in calculating heart rate. Because bradycardia and tachycardia have been associated with epileptic seizures, the ability to calculate this metric efficiently is important [25]. For this reason, I wrote a custom script for Spike 2 that runs a version of the Pan Tompkins algorithm on our dataset to aid in QRS detection [134, 140]. My implementation of the Pan Tompkins algorithm is illustrated in Figure 3.17
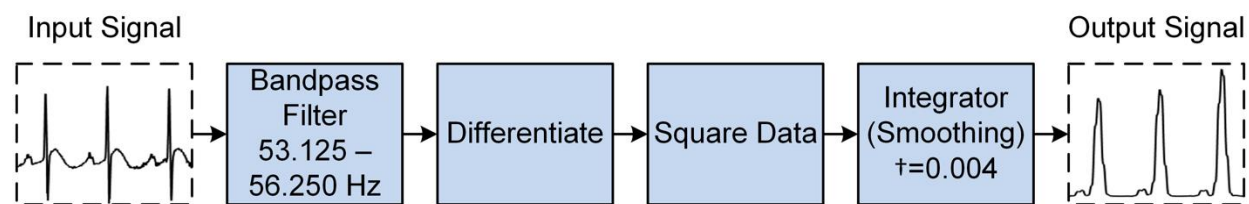
Figure 3.17: The Pan Tompkins algorithm takes an input ECG signal and outputs a signal that makes QRS complex detection easy to do using a simple peak detector. This Pan Tompkins algorithm uses a smoothing filter with a time constant of 0.004 seconds as an integrator. The output of the smoothing filter at time t is the average value of t-0.004 to t+0.004.

The Pan Tompkins algorithm takes the ECG waveform as its input and outputs a waveform with very distinct, prominent peaks that line up with the QRS complex in the ECG waveform. These

peaks can then be used to identify the QRS complexes by using a simple peak detector. I implemented the algorithm by passing the signal through a bandpass filter with cutoff frequencies of 53.125 to 56.250 Hz. It then passes the signal through a differentiator. The output of the differentiator is squared, and then integrated. I implemented the integrator using a smoothing algorithm with a time constant of 0.004 seconds. This smoothing algorithm outputs at time t the average of t-0.004 to t+0.004, which effectively implements an integrator with a scaling factor. I implemented this algorithm using Spike 2's custom scripting language. An example of this Pan Tompkins algorithm output with its associated ECG input is shown in Figure 3.18.
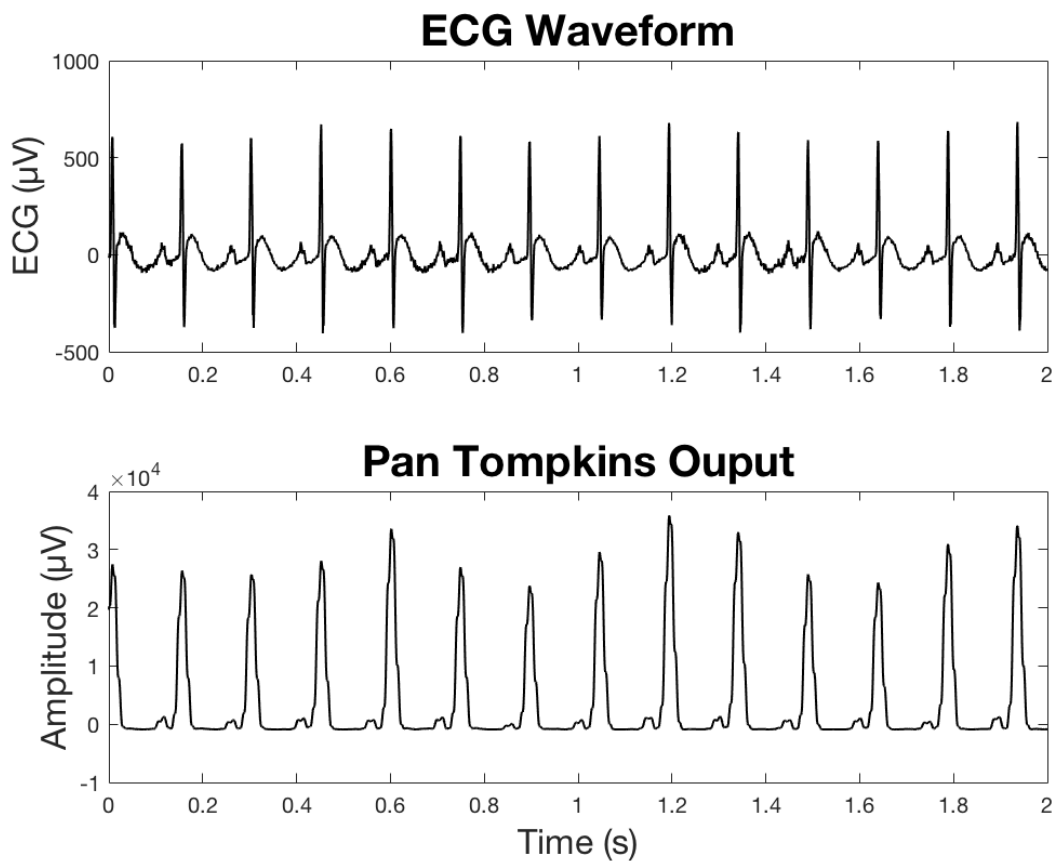
Figure 3.18: The Pan Tompkins algorithm outputs a waveform with distinct, prominent peaks that line up with the QRS complex of the input ECG waveform. This ECG data is from the same data sample shown in Figure 3.10(b).

The Pan Tompkins algorithm can also be used to quickly find periods of stable ECG signals. This is important when looking for periods to measure baseline data during long-term studies. My Pan Tompkins algorithm was used when analyzing such data for a paper (of which I am the 4th author) currently in preparation that reports QT interval changes induced by repeated focal seizures [141].

3.6.2   Suppression of Respiration During Convulsive and Non- Convulsive Seizures

Our initial focus when analyzing our dataset has been on looking for abnormalities on the respiration channel because our dataset is the only dataset containing respiration recordings from freely-behaving rats experiencing chronic, spontaneous seizures. While validating flagged seizures using concurrent video recordings, I observed a general suppression of respiration during both convulsive and non-convulsive seizures. An example of this suppression of respiration is shown in Figure 3.19.
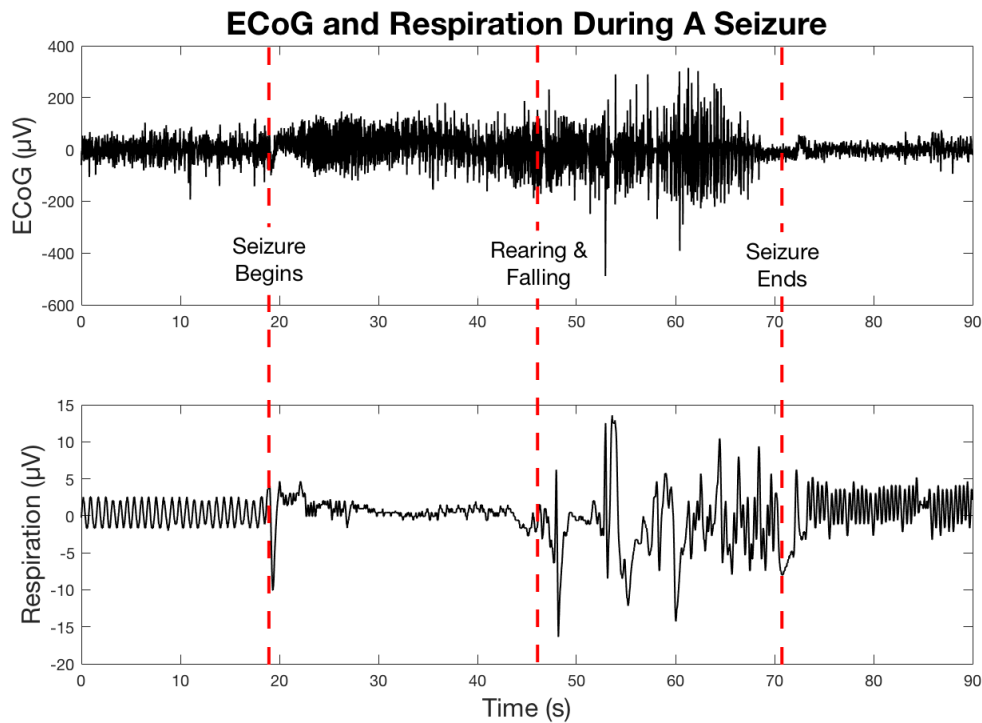
Figure 3.19: This data is from ER164 20 days after implant and TeNT surgery. The start of the seizure was determined initially by electrocorticogram (ECoG) analysis and was later confirmed and refined with concurrent video recordings. The rearing and falling stage was determined by observing video recordings. The end of the seizure was determined by noting the neural suppression in the ECoG signal and the cessation of rearing and falling in the video.

The data shown in Figure 3.19 was recorded from ER164. This rat experienced 24 confirmed seizures during the 24-hour period of time from which the data in Figure 3.19 was recorded. The respiration prior to the seizure shown in Figure 3.19 is regular and stable with a rate of 81 breaths per minute and root mean square (RMS) of 1.44 µV. Immediately upon the onset of the seizure, the rat's respiration is suppressed so much so that respiration rate cannot be calculated. The RMS of the respiration signal is 0.47 µV. During this time, the rat remains tense and motionless except for some twitching of the head and body. During the rearing and falling stage, the rat repeatedly convulses while rearing on its hind legs and falling. We believe that the respiration signal recorded during this phase is mainly comprised of motion artifact due to the physical severity of the rearing and falling activity. Respiration during the recovery phase returns to a regular and stable state, although with a higher amplitude than during the preictal phase (RMS = 1.92 µV) and with an elevated respiration rate of 136 breaths per minute. Figure 3.20 shows 10-second samples of the respiration channel during the preictal, ictal, and postictal phases.
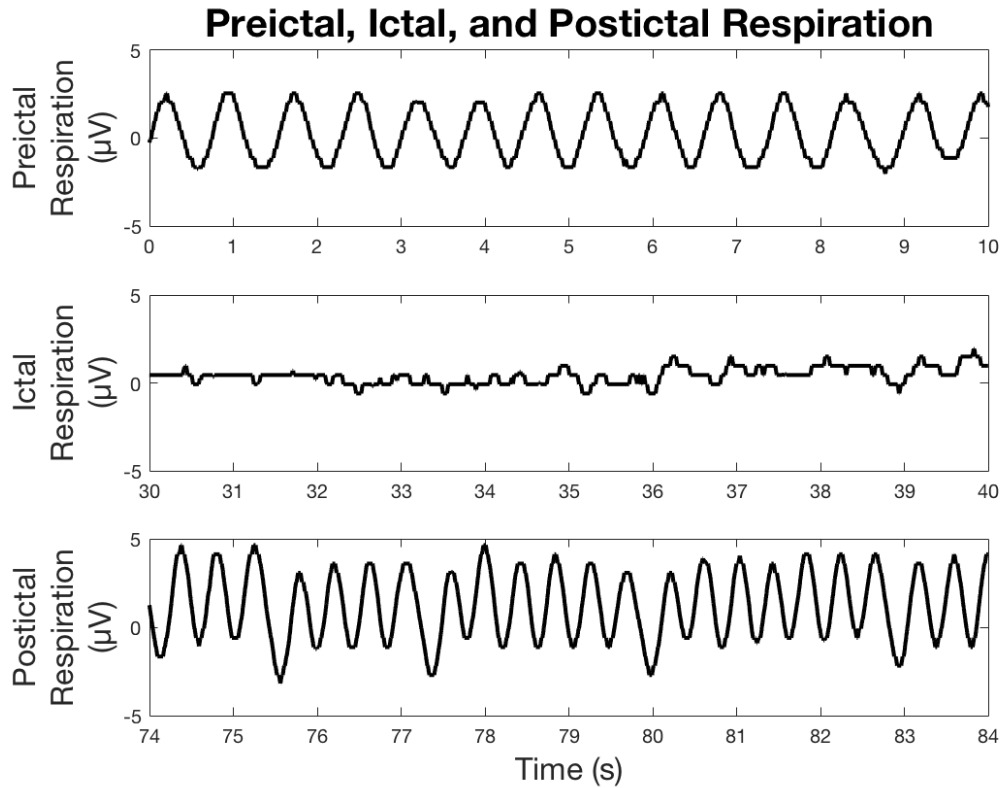
Figure 3.20: This data represents measured respiration from ER164 during a convulsive seizure. The respiration rate before the seizure is 81 breaths per minute with a calculated root mean square (RMS) of 1.44 µV during the displayed 10-second interval. During the seizure, the respiration signal is suppressed so much that it falls below the quantization level of the Bionode's analog-to-digital converter, making it impossible to calculate respiration rate during this time. The RMS of the signal during the ictal phase is 0.47. Respiration during the postictal phase has an increased amplitude of 136 breaths per minute with an RMS of 1.92.

During the preictal, ictal, and postictal phases of this seizure, the ECG indicates that the rat's heart rate increased from the preictal (420 beats per minute) to the ictal stage (440 beats per minute), and then increased again during the postictal phase (480 beats per minute). 3-second samples of the ECG waveforms during these periods is shown in Figure 3.21.
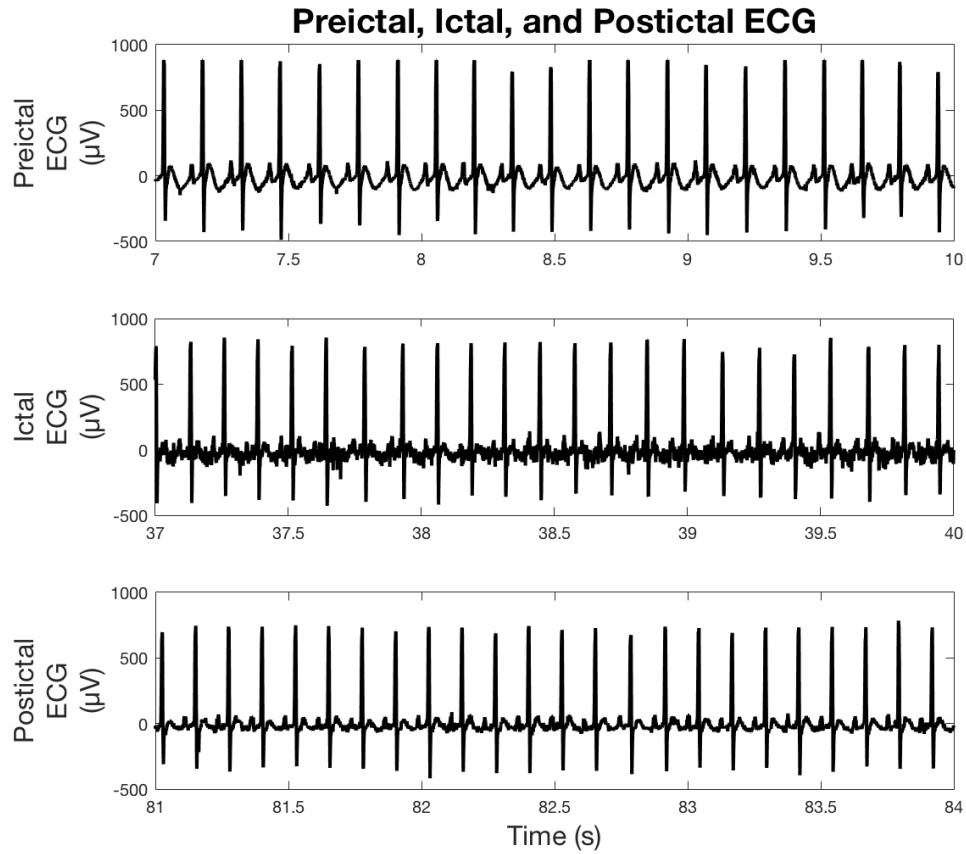
Figure 3.21: This data represents measured respiration from ER164 during a convulsive seizure. Heart rate is calculated by detecting QRS complexes within the electrocardiogram waveform. Preictal heart rate is 420 beats per minute. Ictal heart rate is 440 beats per minute. Postictal heart rate is 480 beats per minute.

We have observed similar respiratory suppression during convulsive seizures detected in two other rats (ER175 and ER176). For comparison, I have included ECoG and Respiration measurements during one of these convulsive seizures observed in ER175 in Figure 3.22.
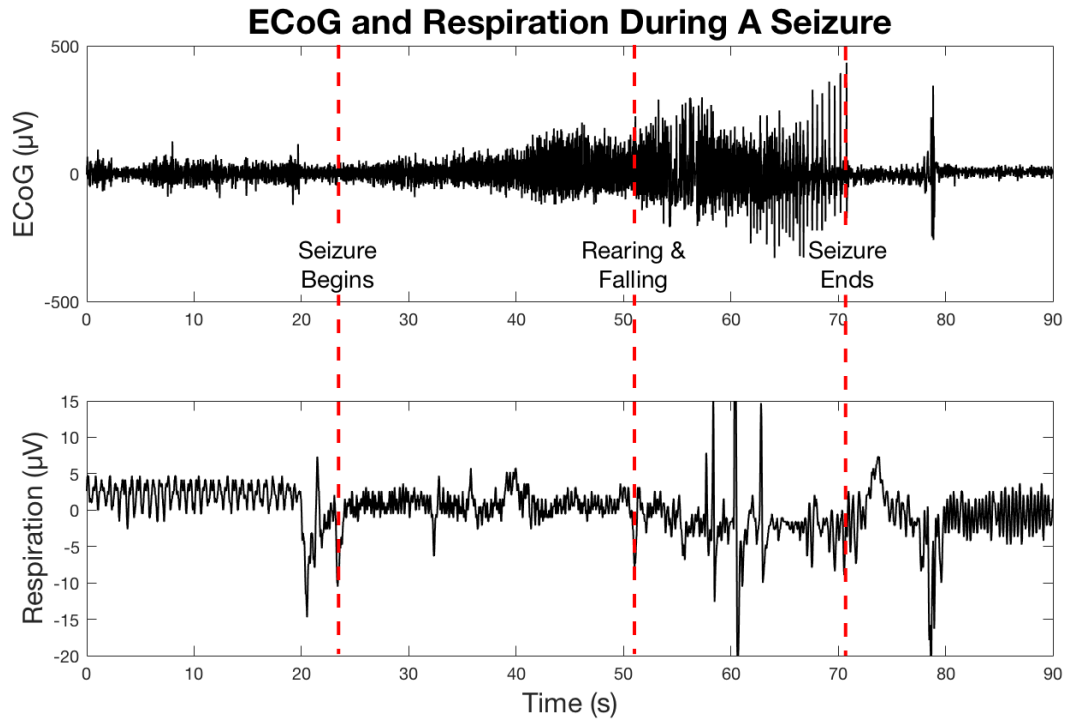
Figure 3.22: This data is from ER175 29 days after implant and TeNT surgery. The start of the seizure was determined initially by electrocorticogram (ECoG) analysis and was later confirmed and refined with concurrent video recordings. The rearing and falling stage was determined by observing video recordings. The end of the seizure was determined by noting the neural suppression in the ECoG signal and the cessation of rearing and falling in the video.

The respiration profile during the preictal, ictal, and postictal phases shown in both Figure 3.19 and Figure 3.22 show a decrease in the respiration signal during the ictal phase followed by an increased respiration rate and amplitude during the postictal phases. Figure 3.23 shows 10-second samples of the respiration channel taken during the preictal, ictal, and postictal phases shown in Figure 3.22.
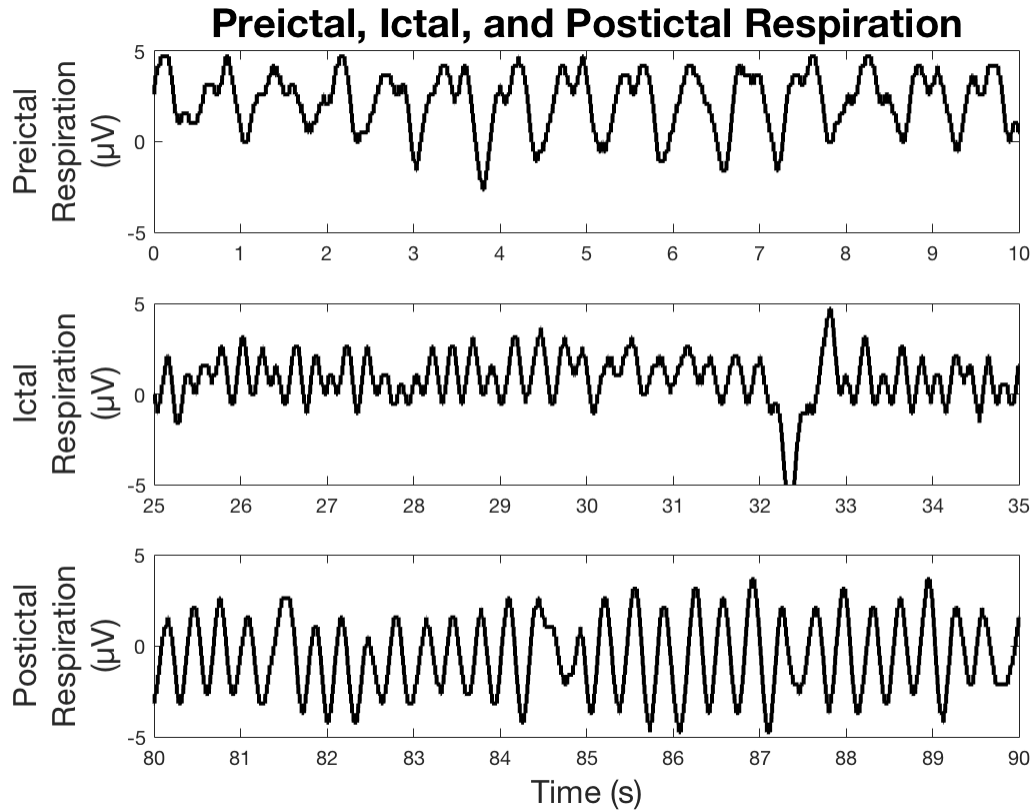
Figure 3.23: This data represents measured respiration from ER175 during a convulsive seizure. The respiration rate before the seizure is 90 breaths per minute with a calculated root mean square (RMS) of 1.61 µV over the displayed 10-second interval. During the seizure, the respiration rate increases to approximately 282 breaths per minute with a measured RMS of 1.38 µV. The respiration rate during the postictal phase is 174 breaths per minute with a calculated RMS of 2.02 µV.

We have observed similar respiratory suppression during non-convulsive seizures as well. Four days after ER164 experienced 24 confirmed convulsive seizures, she experienced 23 confirmed non-convulsive seizures during another 24-hour period. Figure 3.24 shows ECoG and respiration signals measured during one of these non-convulsive seizures.
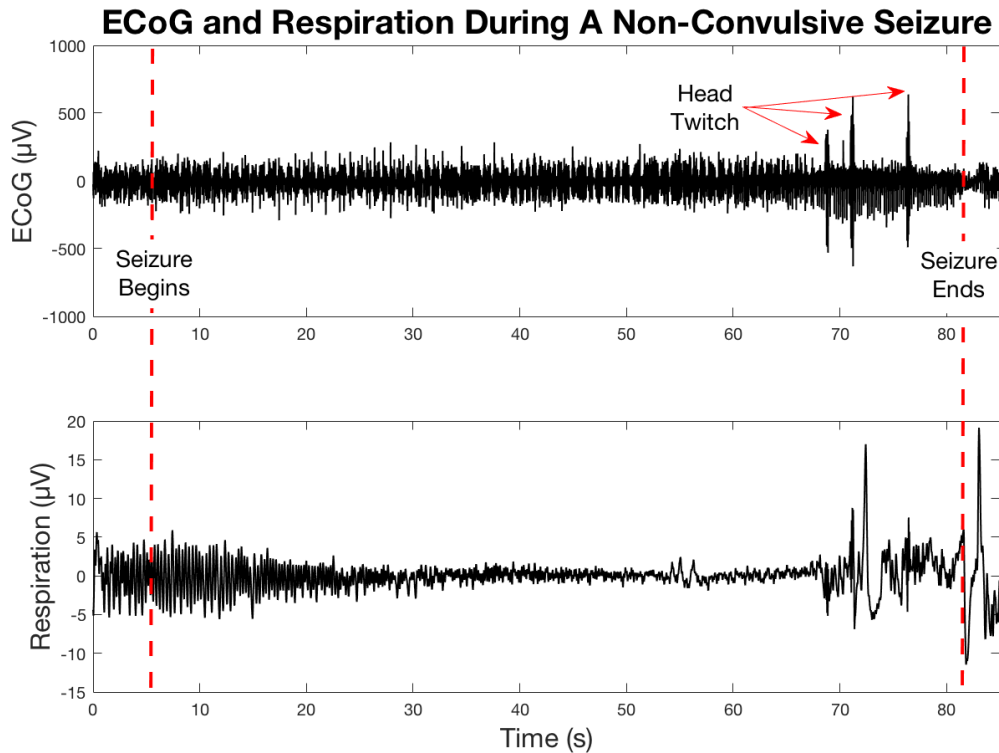
Figure 3.24: This data is from ER164 24 days after implant and TeNT surgery. The start of the seizure was determined initially by electrocorticogram (ECoG) analysis and was later confirmed with concurrent video recordings. Larger than normal head twitches were observed in the video and are annotated in the ECoG data. The end of the seizure was determined by noting the neural suppression in the ECoG signal and the rat resuming motion in the video.

ER164 was very active before the beginning of the non-convulsive seizure presented in Figure 3.24. At the beginning of the seizure, the rat sat motionless and experienced head twitching throughout the duration of the seizure. Unlike the convulsive case, the rat experienced a more gradual suppression of respiration throughout the duration of the seizure. Near the end of the seizure, the rat experienced three larger than normal head twitches which are noticeable on the ECoG channel. Following the third head twitch, the rat immediately started to move around her cage again. Figure 3.25 shows 3-second samples of the respiration and ECG signals measured before and during the seizure.
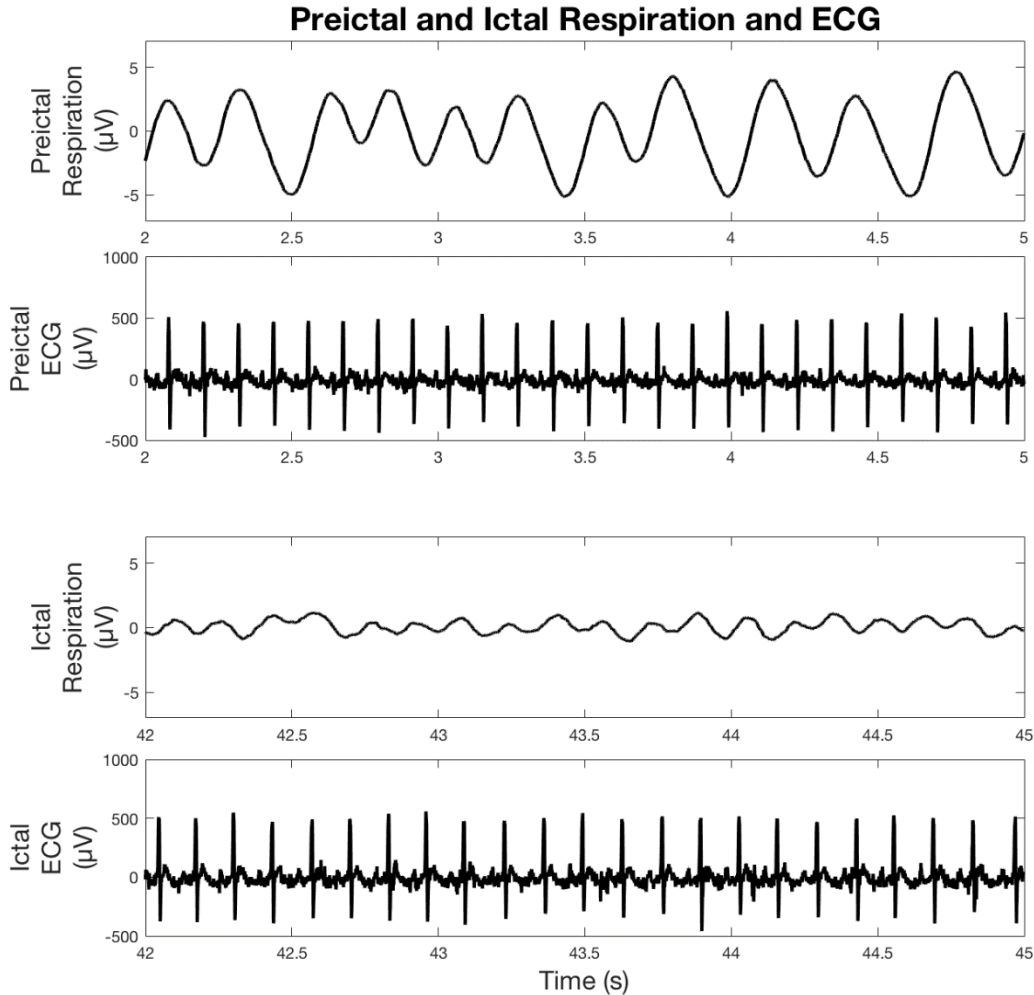
Figure 3.25: Before the seizure, the rat had been very active and had a respiration rate of 132 breaths per minute with a root mean square (RMS) value of 2.58 µV and a heart rate of 300 beats per minute. During the seizure, the rat experienced a gradual suppression of respiration amplitude with an RMS of 0.50 µV and a respiration rate of 228 breaths per minute. The heart rate during the seizure slowed to 264 beats per minute.

To date, we have observed this suppression of respiration during convulsive seizures in multiple rats (ER164, ER175, and ER176). We have also observed a suppression of respiration during non-convulsive seizures in multiple rats as well (ER164, ER175, and ER180). We have detected the most seizures in ER164 and ER175. The average RMS values of the respiration signal during the preictal, ictal, and postictal phases of both convulsive and non-convulsive seizures for each of these rats is shown in Figure 3.26. I calculated the RMS amplitude values of each respiration signal during each phase by first identifying a 2-5 second window of time during each phase where the

respiration signal was most stable and least affected by motion artifact. I then calculated the RMS amplitude of each signal during the stable window using the Spike 2 software application.
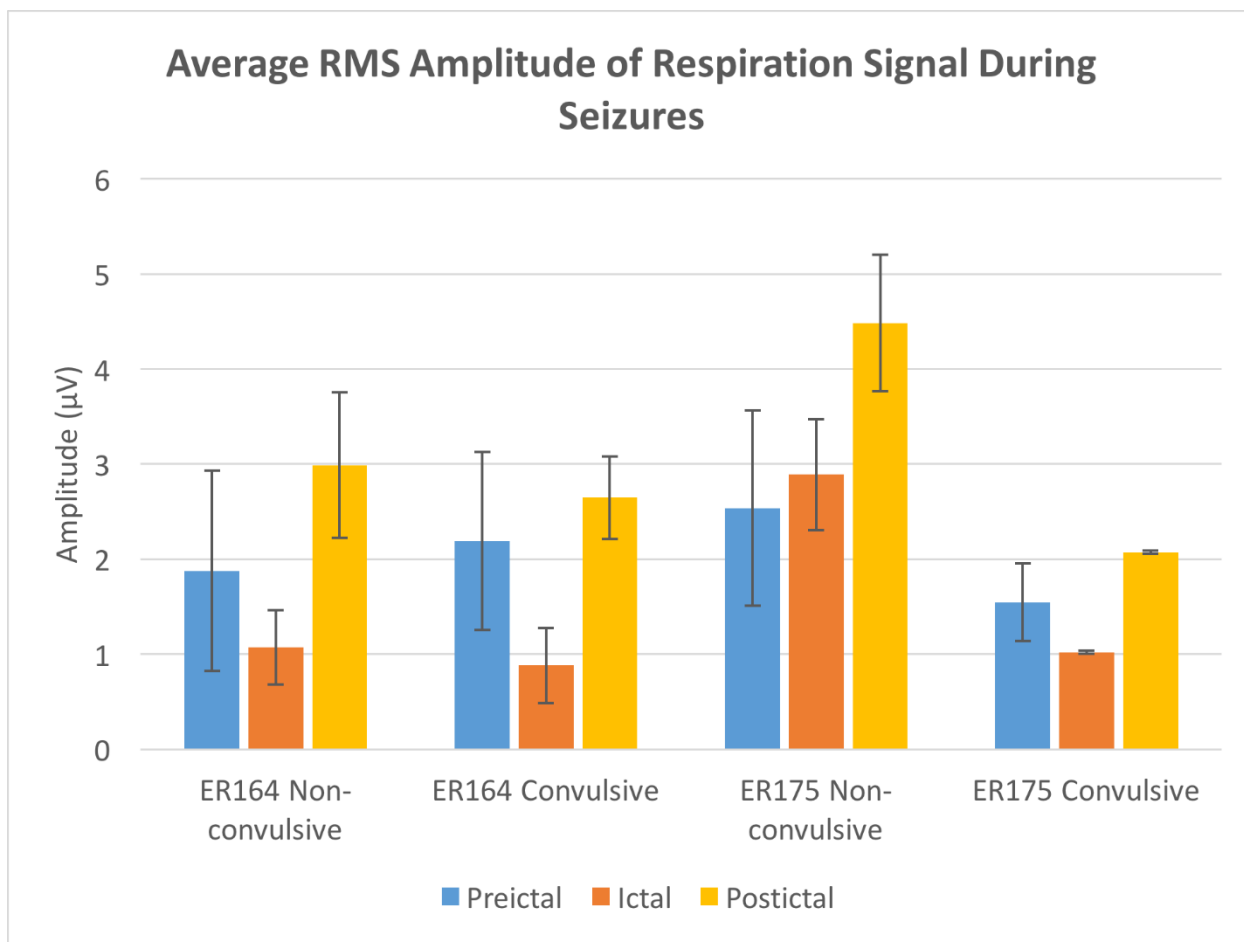
Figure 3.26: Average root mean squared amplitudes of the respiration signal during the preictal, ictal, and postictal phases of both convulsive and non-convulsive seizures for ER164 and ER175. Error bars are equal to the average ±standard deviation.

To determine if the respiration decreases when transitioning from the preictal phase to the ictal phase and increases when transitioning from the ictal phase to the postictal phase, I analyzed the change in respiration amplitude before and after these transitions for each seizure. These changes in amplitude are shown in Figure 3.27.
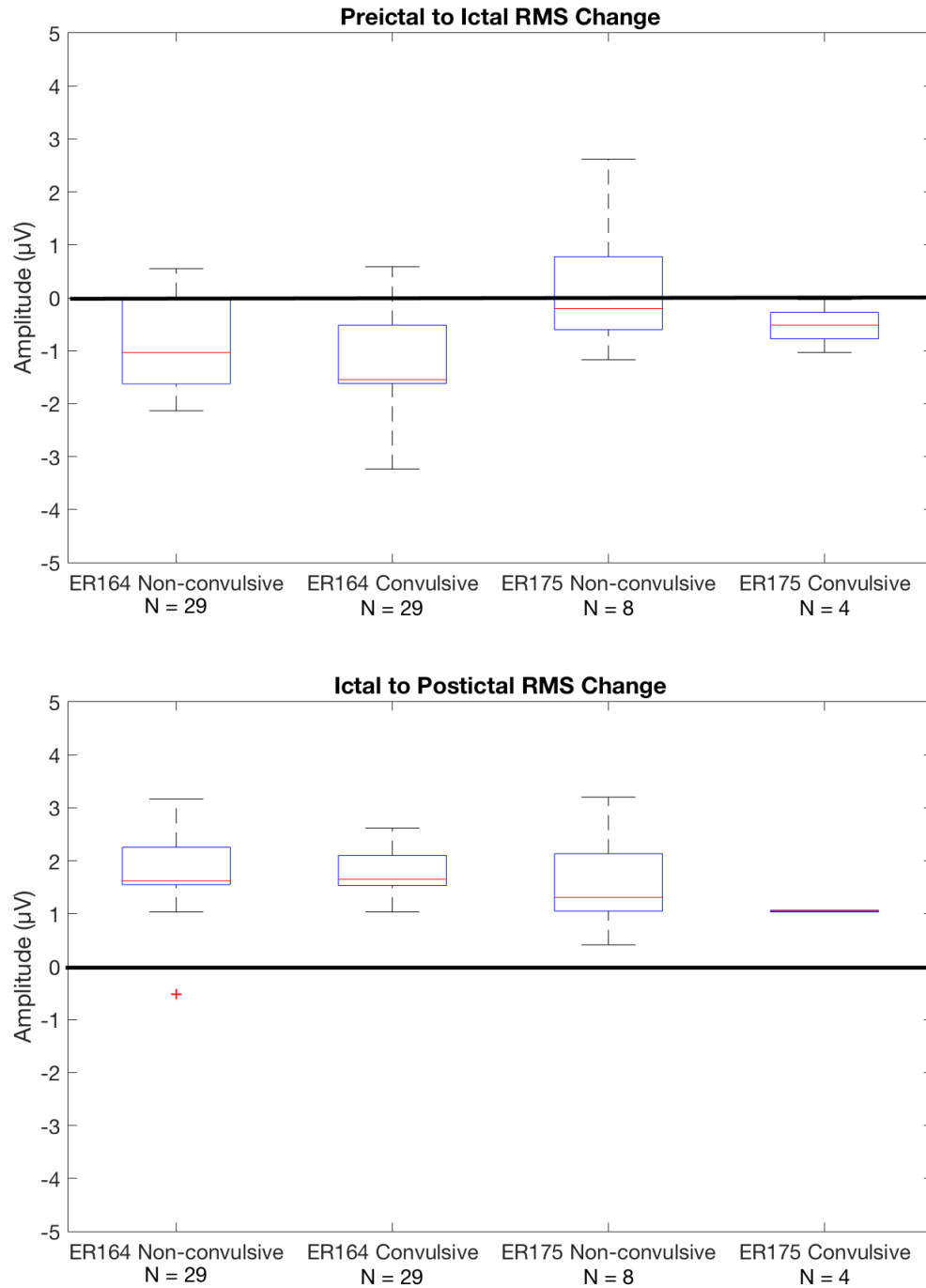
Figure 3.27: Respiration root mean squared amplitude change while transitioning from the preictal phase to the ictal phase (top) and from the ictal phase to the postictal phase (bottom). For each box, the central mark equals the median, and the bottom and top of the box represents the 25th and 75th percentile respectively. The whiskers extend to the most extreme data-points not considered outliers. Outliers are marked with a '+' symbol.

While it is apparent that there is an increase in respiration amplitude from the ictal to the postictal phase, it is not immediately clear if there is a decrease in respiration amplitude from the preictal phase to the ictal phase. Figure 3.26 indicates that the standard deviation of the preictal respiration RMS amplitudes is higher than the standard deviations of the respiration RMS amplitudes for the ictal and postictal phases. This, in turn, leads to the respiration RMS amplitudes measured during the preictal phase having a higher variance than the respiration RMS amplitudes measured during the ictal or postictal phases. This is consistent with the fact that the rat's respiration signal typically increases when the rat is active and decreases during inactivity [142]. Because the ictal and postictal respiration signals occur during similar states respectively (seizing or recovery phases), it follows that the variances of the amplitudes of these signals would be smaller than the variance of the signal measured during the preictal phase when the rat may be active or inactive.

To determine if the respiration RMS amplitude decreases between the preictal and the ictal phases, I filtered out all of the preictal respiration RMS amplitude measurements made while the rat was asleep. This allowed me to analyze what happens to the amplitude of the rat's respiration signal when it is initially active, and then begins to seize. I determined when the rat was active or inactive by viewing the concurrently recorded video to see whether the rat was asleep before the seizure or not. Anytime that I could tell that the rat was not asleep before the seizure started, I determined that the rat was active. These changes in respiration RMS amplitude from the active preictal phase to the ictal phase are shown in Figure 3.28.
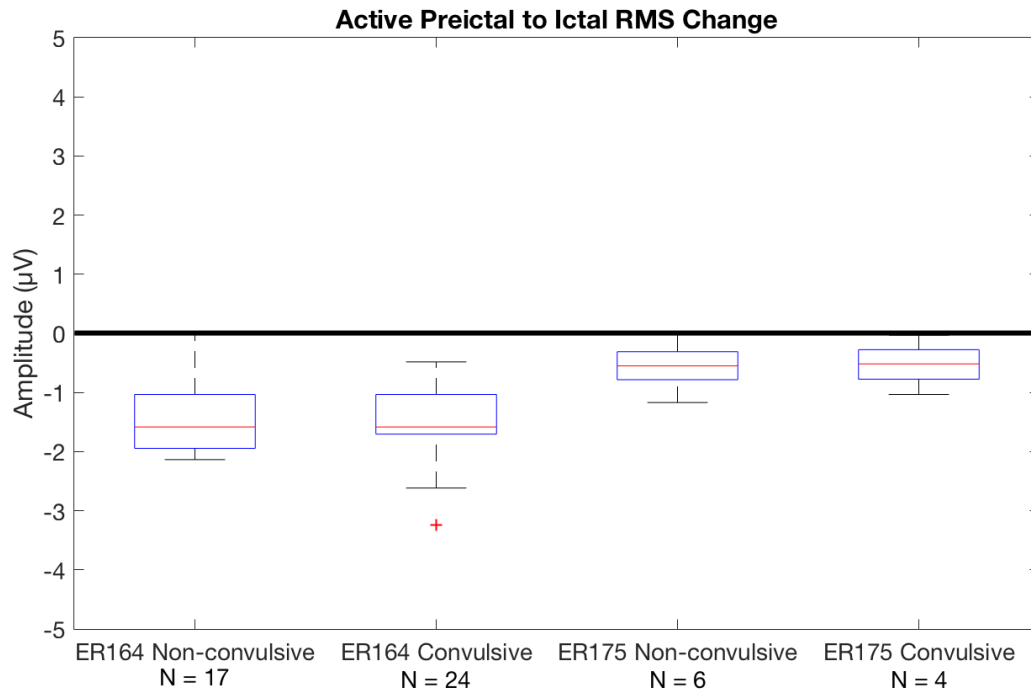
Figure 3.28: Respiration root mean squared amplitude change while transitioning from the preictal phase to the ictal phase when the rat is active during the preictal phase. For each box, the central mark equals the median, and the bottom and top of the box represents the 25th and 75th percentile respectively. The whiskers extend to the most extreme data-points not considered outliers. Outliers are marked with a '+' symbol.

The data displayed in both Figure 3.27 and Figure 3.28 indicate that there is a suppression of respiration during the ictal phase of both convulsive and non-convulsive seizures made especially apparent when analyzing the respiration signals of rats that are active during the preictal period. During a seizure, video data shows that the rats experience various muscle spasms in the head, neck, and body that result in an increase in physical activity especially during convulsive seizures. This increase in activity would typically lead to an increase in mitochondrial oxygen uptake and an autonomic increase in respiration to compensate [143, 144]. Our observations indicate that the rats do not experience this expected autonomic increase in respiration due to physical activity caused by seizures. This is further supported by the subsequent increase in respiration during the postictal phase in which the rats are typically inactive. This indicates that the autonomic increase in respiration to compensate for increased mitochondrial oxygen uptake during the ictal phase resumes during the postictal recovery phase. The cessation of this autonomic respiratory response during the extreme physical activity experienced during a seizure could lead to hypoxia if the

seizure is prolonged, which may contribute to the damage incurred during prolonged seizures and/or status epilepticus [145-147].

I am currently preparing a paper to present this data and analysis. While we have found this suppression of respiration during the ictal phase in two rats, we are still adding to our dataset to identify more seizures in other rats. This will increase our confidence that this reduced ictal respiration is experienced by seizing rats using the TeNT model in general. We plan to include data collected by the 3 rats we have recently implanted that are currently seizing.

If this suppression of respiration is in fact shown to be a common occurrence in rats with chronic seizures, more work should be done to determine the source of this suppression. While the suppression may be centrally mediated (caused by asynchronous signals being sent to the diaphragm and intercostal muscles by the brain), it may also be a peripheral anomaly (caused by over-tension of intercostal muscles). This could be determined by measuring signals in the brain stem responsible for respiration as well as electromyogram (EMG) signals in the diaphragm and intercostal muscles to determine muscle activation activity during the preictal, ictal, and postictal phases. To determine if this respiratory suppression could cause hypoxia, an implantable SpO_2 sensor could be developed to interface with the Bionode and detect harmfully low blood oxygen levels.

3.6.3   Apnea Following Some Seizures

While respiratory abnormalities occurring during the ictal phase may be able to explain some complications experienced during prolonged seizures, we are also interested in analyzing the respiration signal immediately following the end of convulsive seizures. This is because most documented cases of SUDEP occur sometime after the end of a convulsive seizure [22]. While analyzing confirmed seizures for ER164, we observed several instances suggesting that the rat experienced a short apnea during the transition from the ictal phase to the postictal phase. One of these observed apneas is shown in Figure 3.29.
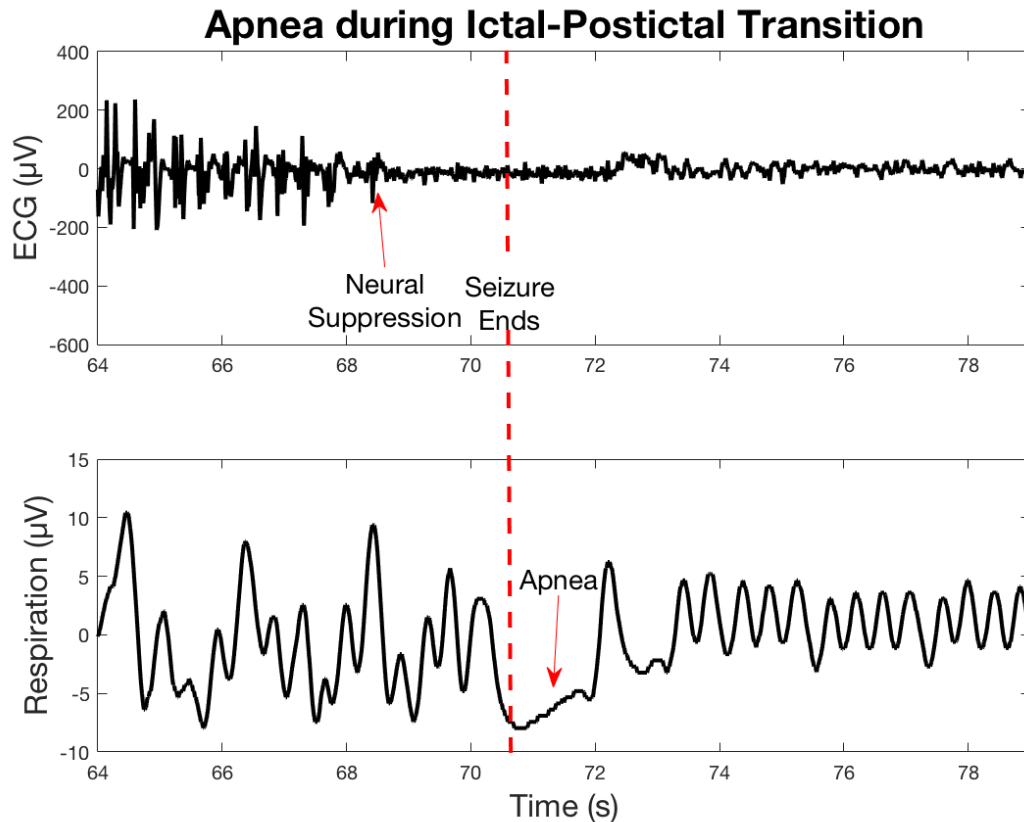
Figure 3.29: The location of the ending of this seizure was determined by inspecting the concurrently recorded video. The apnea is observed immediately upon cessation of the seizure and lasts approximately 2 seconds.

The two second apnea experienced by ER164 occurred immediately after the rat finished rearing and falling. After the apnea, the rat resumed a period of rapid, high amplitude respiration with a respiration rate of 136 breaths per minute. We do not observe this apnea at the end of every convulsive seizure. To date, we have observed apneas lasting 1 to 3 seconds during the ictal to postictal transition in about 20% of the convulsive seizures observed for ER164 (6 out of 28).

Short apneas lasting a few seconds would not typically cause harm to rats. However, in rats experiencing chronic, repeated seizures, these apneas may be indications of possible SUDEP onset. Recent work has indicated that obstructive apneas may be a factor in SUDEP [55-57]. Furthermore, recent unpublished work at the CID at Purdue University performed by Professor John Jefferys of Oxford University, Oxford, UK, and Professor Thelma Lovick of the University of Bristol, Bristol, UK has further indicated that obstructive apnea may be a factor leading to

SUDEP. Figure 3.30 (presented here with permission) shows the recordings that Professor Jefferys and Professor Lovick took during an acute experiment where a seizing rat experienced a 30 second apnea. Brainstem recordings indicate that the apnea was not centrally driven, and was most likely due to a peripheral event.
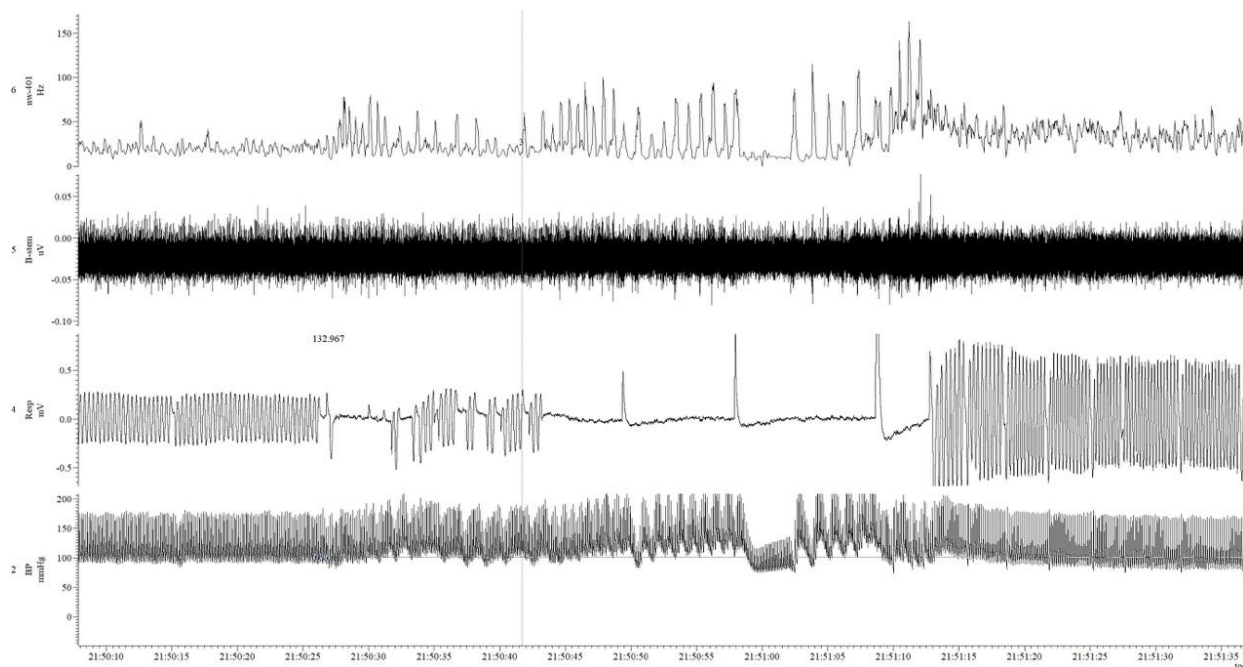
Figure 3.30: These recordings were taken from a rat under urethane anesthesia following an intrahippocampal injection of kainic acid. The signals shown are (from top to bottom) mean firing rate of brainstem neuron, raw recording of brainstem neurons, nasal air temperature, and blood pressure.

I have been directly involved in work led by Ryan Budde at the CID that also indicates obstructive apneas as a cause for death in epilepsy. Our submitted paper, of which I am the third author, documents the possible role of stomach acid-induced laryngospasms in obstructive apnea related to sudden deaths in seizing rats [55]. The treatment and prevention of these laryngospasm driven obstructive apneas is the subject of Chapter 4 of my dissertation.

While obstructive apnea has been observed in acute models of epilepsy in rats, it is difficult to relate these obstructive apneas to SUDEP. This is because SUDEP does not occur during seizures, so it is best studied in chronic models experiencing spontaneous seizures with long periods of

postictal recovery times. This is why it is important to identify any postictal respiratory apneas that may exist in our chronic seizing freely behaving rat dataset.

3.7 Conclusion of Specific Aim 2

My second specific aim was to acquire and analyze cardiac, respiratory, and brain signals from freely behaving rats with induced chronic epilepsy. I used Bionodes equipped with fully implantable thermocouple transducers along with ECG and ECoG leads to measure these signals in freely behaving rats with chronically induced epilepsy by means of the TeNT model. This generated the first dataset of its kind involving concurrent respiration, ECG, and ECoG measurements in freely behaving rats with induced chronic epilepsy. An initial analysis of the data collected during the preictal, ictal, and postictal phases shows reduced respiration during the ictal phase with increased respiration during the post-ictal phase. Additionally, in some cases, I observed short apneas during the transition from the ictal to the postictal phase. While these apneas are short, they may indicate possible SUDEP onset as obstructive apneas due to laryngospasm have been indicated as possible causes of SUDEP [55-57].

4. AIM 3: TREATING AND PREVENTING OBSTRUCTIVE APNEA CAUSED BY LARYNGOSPASM

This chapter contains two major sections. Section 4.3 covers a method of treating laryngospasms by electrically stimulating the RLNs. Section 4.4 covers a method of preventing gastric-acid induced laryngospasm via gastric vagotomies. This method has informed ongoing research into preventing laryngospasm during seizing activity using blocking electrical stimulation on the cervical vagus nerve. Much of the content contained in these sections will be included in a paper, of which I am the first author, titled "Methods and Techniques for Preventing Death in Epilepsy." This paper is currently in preparation with a planned submission date of Q4 2018.

4.1 Motivation/Overview

A laryngospasm is a reflex response typically triggered by harmful manual or chemical stimulation

of the larynx [58]. During a laryngospasm, intrinsic laryngeal muscles contract to force adduction

of the larynx, resulting in the closure of the larynx over the lumen of the trachea [59, 60]. While

laryngospasms are usually observed in anesthesiology, they can also be life-threatening symptoms

of GERD, various neurological diseases, and some genetic disorders [61-68]. Recent work has

indicated that laryngospasms may be a factor in SUDEP [56, 57], and that acid reflux may be the

trigger for some or all of those laryngospasm episodes [55]. This chapter documents our efforts to

both treat and prevent laryngospasms using electrical stimulation. We focused on using electrical

stimulation to treat laryngospasms in an effort make our research more translational to currently

available neuromodulation devices. Because people with implantable neuromodulation devices

typically have medically intractable epilepsy, they represent a population within the epilepsy

community with an increased risk of sudden death in epilepsy [21]. The therapies that we explore

in this chapter inform new possibly life-saving therapies that may be deliverable by VNS devices

currently on the market.

4.2 Bionode Breakout Board

While working on upgrades for the Bionode stimulator, AFE circuitry, and firmware image, I

designed and fabricated a Bionode breakout board based on the Nordic PCA10040 Dev kit for the

NRF52832 ARM M4 microcontroller. This breakout board became widely used in acute

experiments using the Bionode circuitry because it is larger and less delicate than a Bionode

implant and it is more easily modifiable. I used this board to conduct all of the experiments documented in this chapter, so I am providing some brief documentation about the breakout board here.

The Bionode breakout board consists of three stackable boards: The Nordic PCA10040 Dev kit, the Bionode Daughterboard breakout board, and the Bionode Stimulator breakout board (See Figure 4.1).

(a) (b) (c)
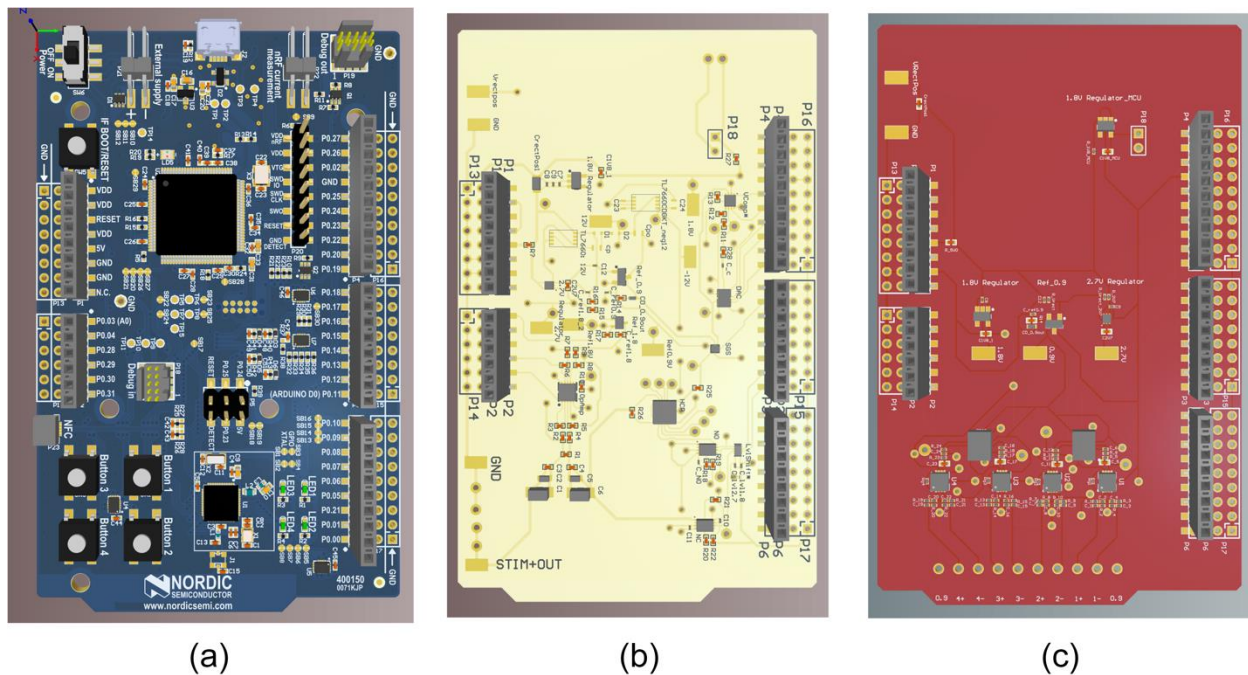
Figure 4.1: (a) The Nordic PCA10040 dev kit and the (b) Bionode Stimulator breakout board and the (c) Bionode Daughterboard breakout board stack together to form the Bionode breakout board. These images are from the Altium design project, and were generated by Jay Shah of the CID.

The Nordic PCA10040 dev kit is a commercially available board that provides full access to all pins on the NRF52832 ARM M4 microcontroller. This is the microcontroller that we have started using in the most up-to-date Bionode implants. I used this dev kit to develop and test all new firmware code for the updated Bionode as well as port all of the old firmware from the NRF51822 ARM M0 to the NRF52832 ARM M4. The dev kit also provides regulated powering for the NRF52832 microcontroller which allows the board to be powered via a USB connection. The Bionode Stimulator breakout board contains all of the Bionode's stimulator circuitry (See Figure

2.10) as well as the regulators, doublers, and inverters located on the Powernode (See Figure 2.22). The presence of both the stimulator circuitry and the Powernode circuitry allows the stimulator circuit to be fully functional when connected to the Nordic PCA10040 dev kit. Logic pins to and from the Nordic PCA10040 control the stimulator circuit exactly the same way that the Bionode microcontroller does on the implant, and the 5 volt USB supply provides power to the Powernode circuitry in the same way that the output of the voltage rectifiers do for the Powernode in the implant. Finally, the Bionode Daughterboard breakout board contains four AFE circuits identical to the ones shown in Figure 2.4. It also contains voltage regulators and voltage references necessary to run the AFE circuits; allowing it to be fully functional when connected to the Nordic PCA10040 without needing any supplemental equipment.

The Bionode Stimulator breakout board and the Bionode Daughterboard breakout board are both 2-layer boards with all components populated on the top layer. This reduces the time it takes to fabricate each board (I have populated each board in less than 1 hour). Because the boards only use 2 layers, they are easily modifiable to test different configurations because all traces are available for cutting and re-routing if needed. I designed the boards to stack on top of the Nordic PCA10040, but they also can stack on top of the Nordic PCA10028 if testing using the original Bionode NRF51822 microcontroller is desired. Because both breakout boards contain their own voltage rail generation circuitry, they can be used either independently or in tandem. Jay Shah and Gang Seo, both of the CID, were responsible for the Bionode Stimulator breakout board layout and the Bionode Daughterboard breakout board layout respectively.

When both the Bionode Stimulator breakout board and the Bionode Daughterboard breakout are stacked on top of the Nordic PCA10040 dev kit, the resulting set of boards forms a USB powered 4-channel biopotential recording device with 1 channel of constant current stimulation and wireless data transfer capabilities that can fit in the palm of your hand (See Figure 4.2). This alone makes the Bionode breakout board a valuable piece of equipment for acute experiments, and has caused the Bionode breakout board to become a popular device at the CID.
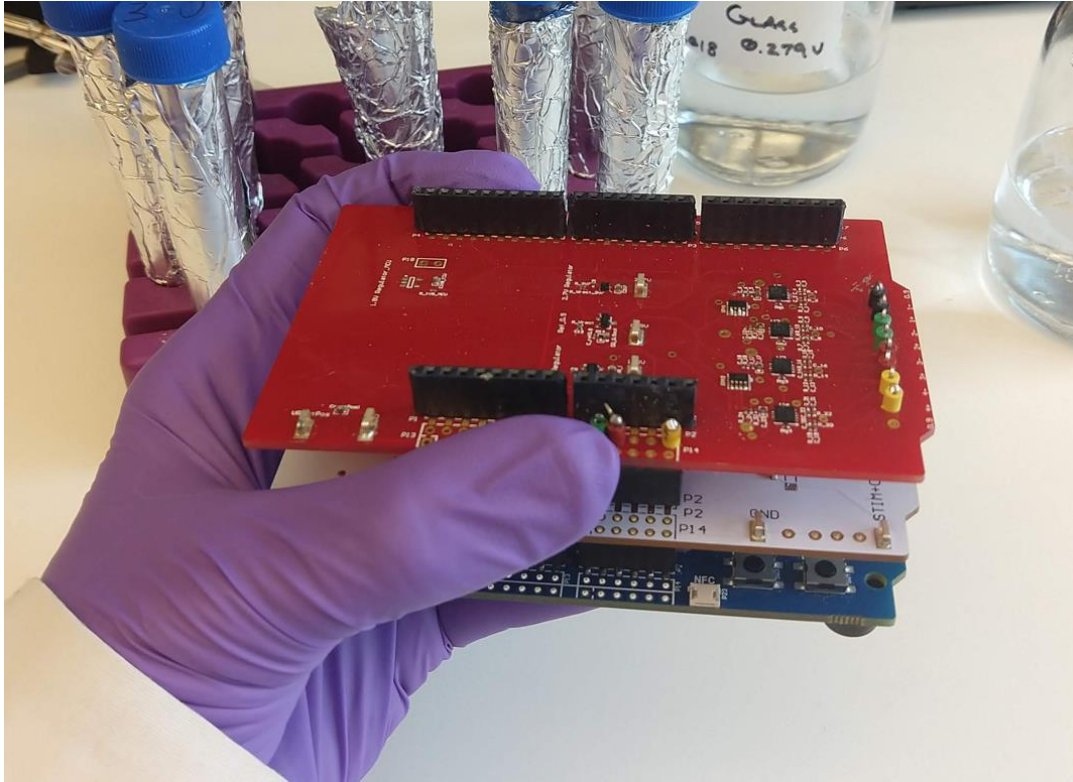
Figure 4.2: The stacked PCA10040 NRF52083 board, Bionode stimulator breakout board, and Bionode daughterboard breakout board is a USB powered 4-channel biopotential recording device with 1 channel of constant current stimulation and wireless data transfer capabilities that can fit in the palm of your hand

4.3 Treating Laryngospasm via Electrical Stimulation in Rats

Opening the larynx during a laryngospasm leads to an opening of the airway which is a potentially life-saving action in people experiencing an untreatable laryngospasm during a seizure. We set out to open the larynx during a laryngospasm by using electrical stimulation to activate abductor muscles in the larynx of rats experiencing laryngospasms. We activated these abductor muscles by electrically stimulating the RLNs in rats after triggering a laryngospasm with hydrochloric acid topically applied to the larynx. The RLNs innervate the majority of the muscles in the larynx, including the PCA muscles which control laryngeal abduction [73, 74]. The RLNs run parallel to the lateral edges of the trachea, making them easy to identify and access for electrical stimulation. In this section, I present a constant-current stimulation waveform that, when applied bilaterally to the RLNs, is able to open the larynx during acid-induced laryngospasms in rats.

4.3.1 Materials and Methods

4.3.1.1 Overview

To determine if the larynx can be opened during a laryngospasm via electrical stimulation, we used a custom designed cuff electrode and stimulator to provide constant-current, alternating phase stimulation of varying amplitudes, pulse widths, and pulse repeat times to both RLNs. We observed the physical effects of these varying stimuli on the larynx using a laryngoscope. Our goal was to find a stimulation waveform that could hold the larynx in a rigid, open position. We determined if the larynx was open both by visually observing the larynx and by measuring airflow using a thermocouple transducer. After finding a waveform that was able to hold the larynx in a rigid open position, we applied the waveform to a rat with both RLNs severed rostral to the stimulating electrode to verify that the laryngeal muscles were being stimulated via the RLNs. We then attempted to open the larynx during laryngospasms in six rats by first topically applying hydrochloric acid to the larynx to provoke a laryngospasm and then applying the waveform to the RLNs. We performed all of the animal work described in this section in accordance with the regulations of the IACUC using procedures approved by the PACUC.

4.3.1.2 Electrical Stimulation

In order to stimulate both RLNs simultaneously, we designed a cuff electrode with a 3-mm inner diameter that fits around the trachea just caudal to the cricoid cartilage (See Figure 4.3). We used silicone tubing for the body of the cuff and 90-10 platinum-iridium wire for the electrical contacts. Because this cuff fits around the entire trachea, the wire makes contact with both the left and right RLNs.
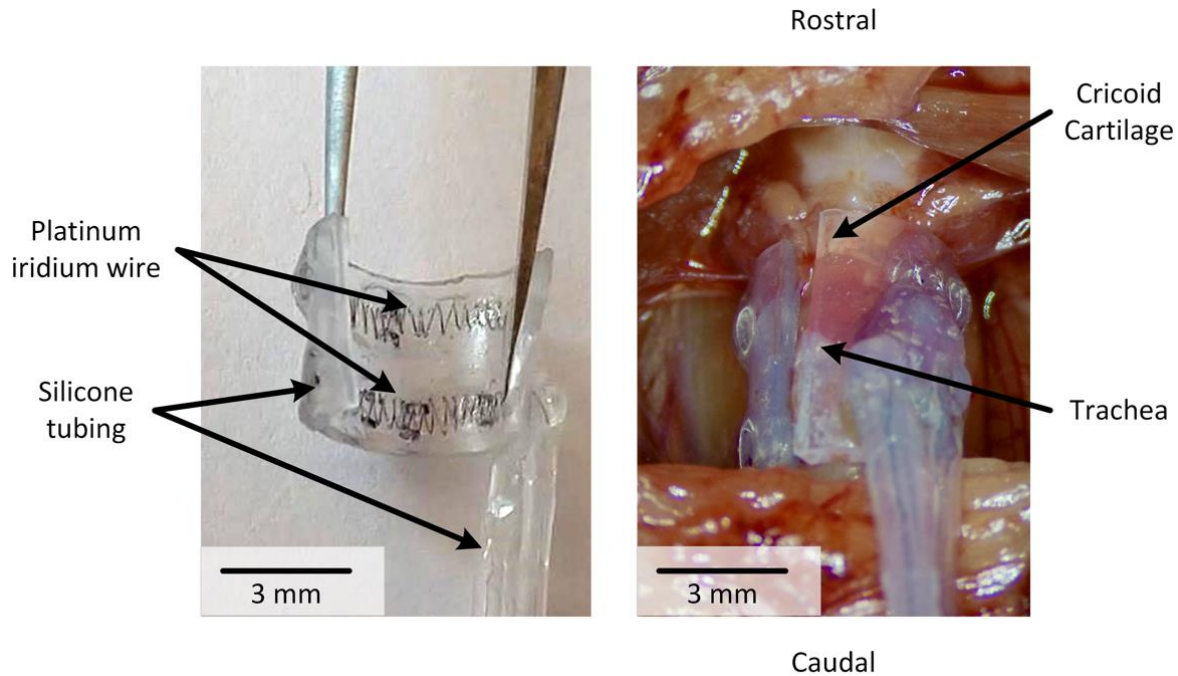
Figure 4.3: The cuff electrode wraps completely around the trachea caudal to the cricoid cartilage. This allows the electrode contacts to interface with both the right and left recurrent laryngeal nerves as they run parallel to the lateral sides of the trachea (See Figure 1.1)

We connected this cuff electrode to the Bionode Stimulator breakout board (See Section 4.2) which was configured to output an alternating phase waveform as shown in Figure 4.4. We searched for a stimulus waveform that could hold the larynx in a rigidly open position using pulse widths ranging from 100 to 1000 µs, pulse repeat times ranging from 200 to 50,000 µs, and amplitudes ranging from 50 to 1,000 µA.
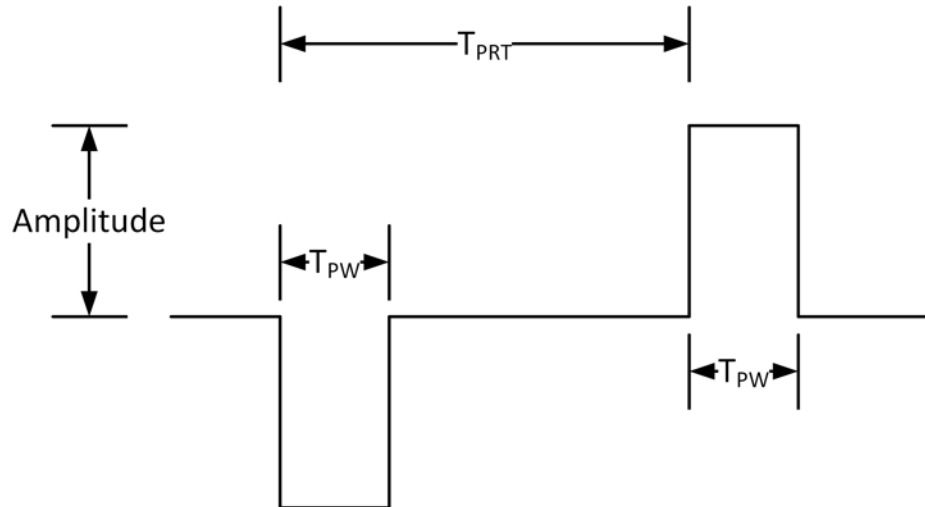
Figure 4.4: We swept amplitude, pulse width (T$_{PW}$) and pulse repeat time (T$_{PRT}$) parameters to determine a suitable stimulation waveform.

4.3.1.3 Inducing Laryngospasm

We induced laryngospasms by topically applying 0.1 mL of 1.6 pH hydrochloric acid in a Tris buffer to the larynx via a cannula. As reported in [58], hydrochloric acid with a pH less than 2 has been shown to reliably induce laryngospasm in canine models, and is consistent with stomach acid. We also chose the topical application of acid to induce laryngospasm because it is consistent with the way laryngospasms are produced in people with GERD [63, 64] and possibly in cases of SUDEP [55].

4.3.1.4 Imaging and Respiration Measurements

We viewed and recorded real-time video of the larynx using a 2.7mm, 30 degree Dyonics 4130 video laryngoscope connected to a GoPro 5 modified with a C-mount by Back-Bone. To provide a clear view of the larynx, we 3D printed a blunt cannula similar to the one described in [148]. This 3D printed blunt cannula was designed and printed by Ethan Biggs. To get a consistent, stable view of the larynx using the laryngoscope and cannula, we first put the rat in a stereotaxic frame in the supine position. We then inserted the 3D printed cannula into the rat's mouth and clamped the cannula to a ring stand to hold it in place. Finally, we inserted the laryngoscope through the cannula to obtain a clear, stable view of the larynx.
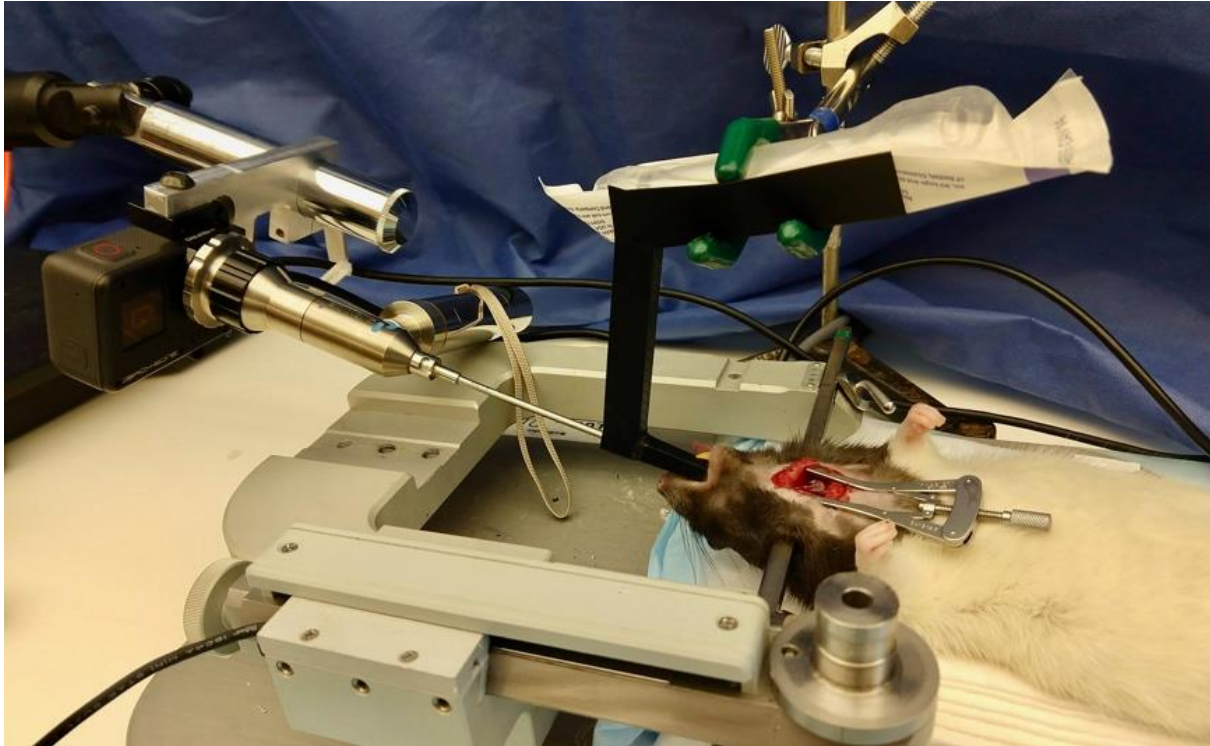
Figure 4.5: The 3D printed cannula holds the rat's mouth open to give the laryngoscope a clear, stable view of the larynx. The GoPro 5 mounted to the laryngoscope provides us with the ability to view real-time video via an HDMI connected monitor as well as the ability to record HD video of the larynx onto a micro SD card in the GoPro. The GoPro 5 has been modified with a C-mount attachment created by Back-Bone.

We measured respiration airflow by inserting a thermocouple into the rat's mouth to sense temperature fluctuations that occur during respiration. The thermocouple and front-end amplification circuitry needed to record the respiration signal are described in Sections 2.2.2 and 2.3.3. We used this airflow measurement along with the arthroscopic views of the larynx when searching for a stimulation waveform that could hold the larynx in a rigid, open position. When attempting to open the larynx during acid-induced laryngospasms, we did not use the thermocouple because the added moisture in the mouth during these experiments desensitized it. For these experiments, we determined if the larynx was open by observing the shape of the larynx, listening for respiration sounds, and watching the chest for evidence of respiration.

4.3.1.5   Surgical Procedures

We performed two surgeries in which we swept stimulus parameters as described in Section 4.3.1.2 to determine the waveform that could hold the larynx in a rigidly open position. In an additional

surgery, we severed the RLNs to verify that the intrinsic laryngeal muscles were being stimulated via signals from the RLNs and not from direct muscle stimulation. Once we had established a waveform that could hold the larynx in a rigidly open position, we performed six surgeries to determine if we could open the larynx during acid-induced laryngospasms. This section provides a description of the surgical procedures we used in these experiments. I performed all of these surgical procedures myself with assistance from Ethan Biggs.

Rats were given butorphanol analgesic (0.5-2 mg/kg SC) and urethane anesthesia (1-1.2 mg/ kg IP). With the rat in the supine position, we made a rostral-caudal incision at the neck. Using retractors, we retracted both the sternomastoid and sternohyoid muscles to expose the trachea. We then separated the trachea from the esophagus using blunt dissection. We then placed the cuff electrode around the trachea as illustrated in Figure 4.3. After cuffing the trachea, we placed the rat in a stereotaxic frame and inserted both the 3D printed cannula and the laryngoscope into the mouth as illustrated in Figure 4.5. At this point, we either swept stimulation parameters as described in Section 4.3.1.2, or we attempted to open the larynx during acid-induced laryngospasms. After inducing a laryngospasm, we electrically stimulated the RLNs and observed the larynx.

4.3.2   Results

We determined that stimulating the RLNs using a constant-current, alternating-phase waveform with a pulse width of 100 µs, pulse repeat time of 500 µs, and amplitude of 500 µA could hold the larynx in a rigidly open position. We refer to this waveform as our established waveform. Figure 4.6 shows airflow measurements and still images of the larynx taken during inhalation and exhalation while stimulating with this waveform using various amplitudes.
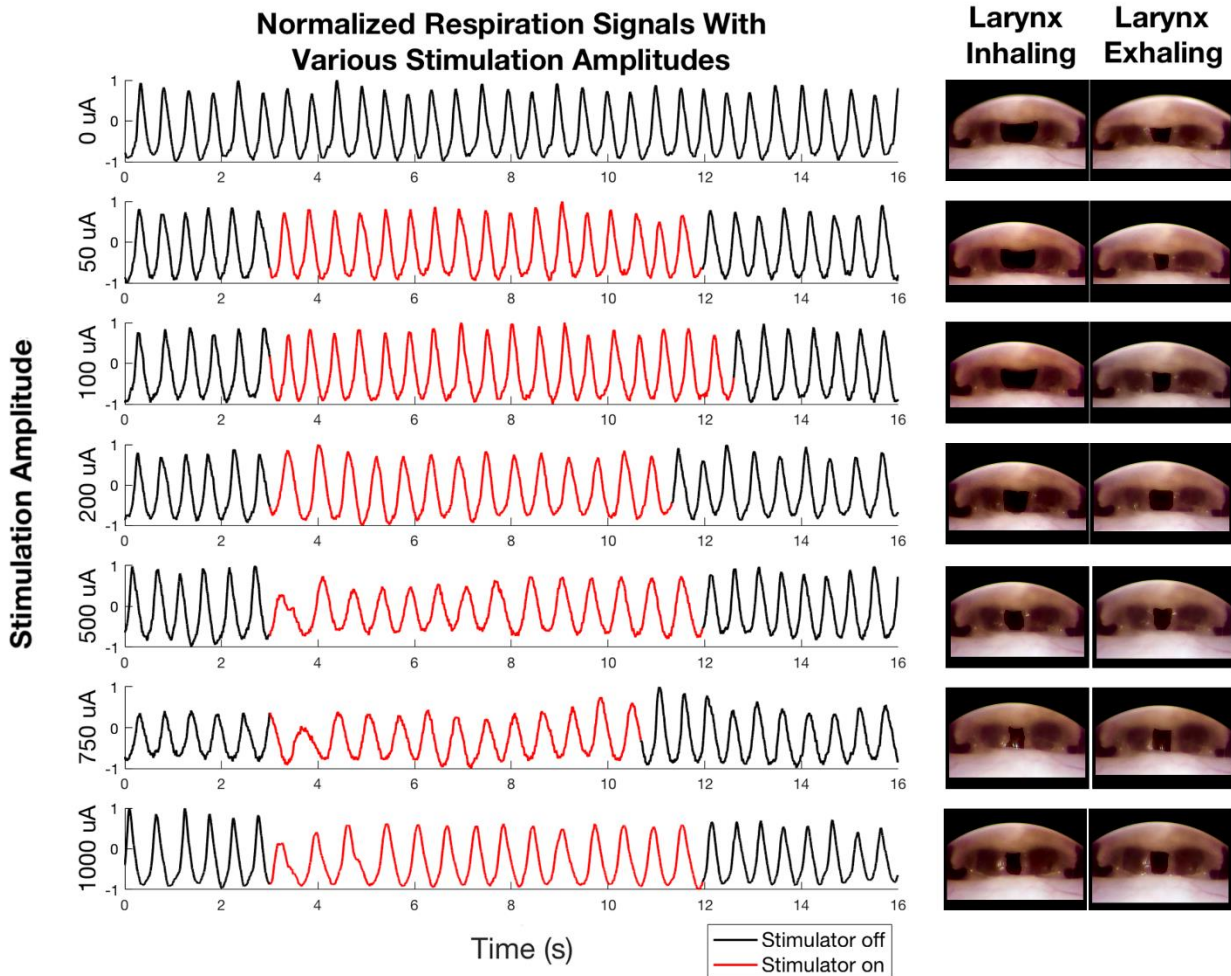
Figure 4.6: We stimulated both of the recurrent laryngeal nerves with a pulse width of 100 µs and a pulse repeat time of 500 µs. The traces show the normalized respiration signal before, during, and after stimulation. We applied stimulation amplitudes of 0, 50, 100, 200, 500, 750, and 1000 µA as indicated to the left of each respiration trace. The images on the right of the figure depict the larynx during inhalation and exhalation while stimulating with each amplitude.

Figure 4.7 shows still images of the larynx taken during inhalation and exhalation before and during our application of the established waveform in rats with either intact or severed RLNs. The rat with intact RLNs immediately responded to the stimulus by contracting its larynx into a rigid, open position. The rat with severed RLNs showed no response to the stimulus and exhibited total vocal cord palsy immediately after we severed the RLNs.

| | **Intact Recurrent Laryngeal Nerves** | **Severed Recurrent Laryngeal Nerves** |
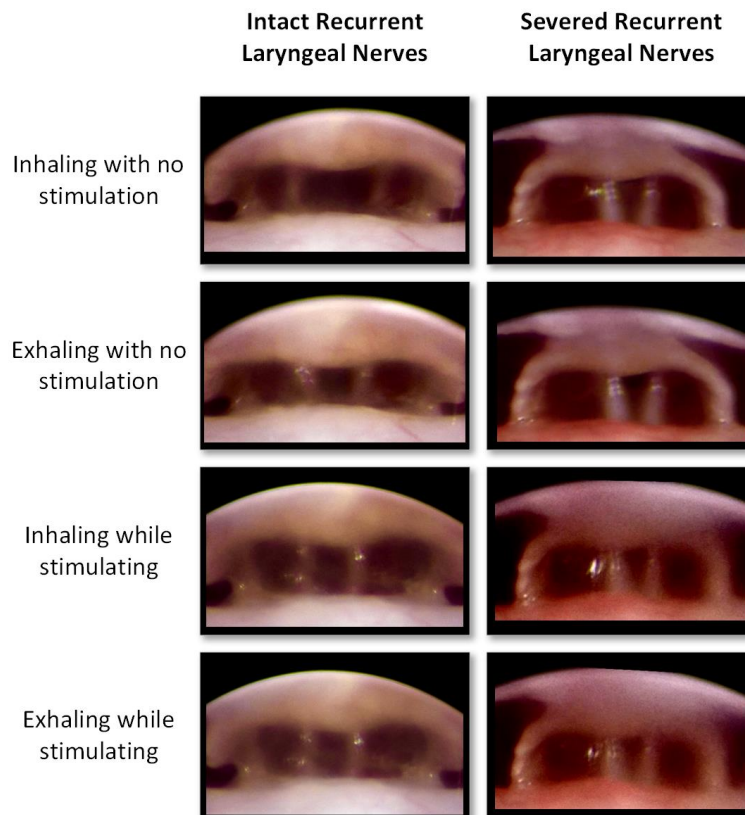
Figure 4.7: The images in the left column of this figure depict the laryngeal responses to electrical stimulation of a rat with intact recurrent laryngeal nerves (RLNs). The images in the right column of this figure depict the laryngeal responses to electrical stimulation of a rat with severed RLNs. In both cases, we used our established waveform.

We attempted to open the larynx in 6 rats with acid-induced laryngospasms. In two rats, we observed partial vocal cord palsy before we applied the acid. In another rat, we were able to open the larynx, but it died a 65 seconds later after inhaling what appeared to be a large quantity of fluid. In all rats, we observed a persistent laryngospasm accompanied by a cessation of respiratory chest movements after applying acid to the larynx. Table 4.1 summarizes the results of these experiments.

Table 4.1: Results of attempting to open the larynx in 6 rats during acid-induced laryngospasms by applying the established waveform to the recurrent laryngeal nerves.

Rat Number	Laryngospasm Induced	Larynx Opened During Laryngospasm	Rat Survived Laryngospasm	Partial Vocal Cord Palsy Observed
1	Yes	Yes	Yes	No
2	Yes	No	No	Yes
3	Yes	Yes	Yes	No
4	Yes	Yes	Yes	No
5	Yes	No	No	Yes
6	Yes	Yes	No	No

Figure 4.8 shows still images taken of the larynx before, during, and after we applied the established waveform to open the larynx during an acid-induced laryngospasm.
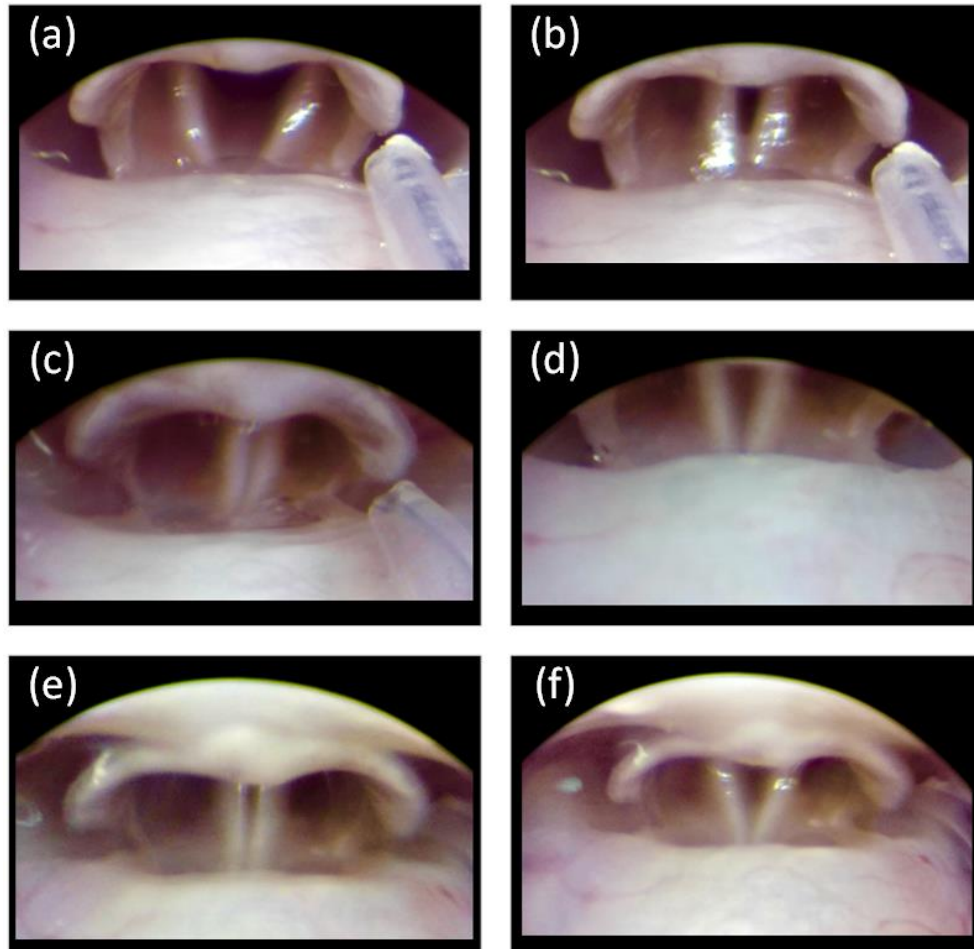
Figure 4.8: (a) and (b) show the larynx during inhalation and exhalation respectively. (c) depicts a laryngospasm that occurred immediately after we applied the acid to the larynx. (d) shows the larynx opened immediately after we applied the established waveform. (e) the larynx returned to a state of laryngospasm after we stopped electrical stimulation. (f) the larynx opened again during a subsequent period of bi-lateral recurrent laryngeal nerve stimulation.

4.3.3   Discussion

Our experiments demonstrate that stimulating the RLNs with a constant-current, alternating-phase waveform with a pulse width of 100 µs and pulse repeat time of 500 µs can make the larynx stay in a rigid open position as long as the amplitude of the stimulus is above a threshold current of 500 µA. To reduce the amount of charge we pushed into the RLNs, we chose to stimulate using the threshold current of 500 µA. We have also shown that stimulating at or above this threshold holds the larynx in a rigidly open position that closely resembles the generally adducted position observed during normal exhalation. The main intrinsic laryngeal muscles involved in adduction

are the ipsilateral thyroarytenoid and the lateral cricoarytenoid muscles while the main intrinsic laryngeal muscle involved in abduction are the PCA muscles [73]. The rigidly open nature of the laryngeal response suggests that our stimulation is activating both the adducting and abducting laryngeal muscles. The generally adducted shape of the larynx is consistent with the fact adducting motor neurons exist at a 4:1 ratio to the abducting motor neurons in the RLNs [73]. This laryngeal response is also consistent with findings reported in [59] that concurrent stimulation of both adducting and abducting intrinsic laryngeal muscles via electrical stimulation of the RLNs leads to overall adduction of the larynx, not abduction. Figure 4.6 demonstrates that while the larynx is in a generally adducted position during stimulation, the larynx is still open.

The intrinsic laryngeal muscle response is most likely caused by signals sent through the RLNs to the muscles and not due to direct electrical stimulation of the muscles, as the response was not observed when the RLNs were severed. Furthermore, as shown in Figure 4.7, we were unable to open the larynx during acid-induced laryngospasms in the two rats where we had observed partial vocal cord palsy. After reviewing our surgical procedure, we determined that we had in both cases inadvertently damaged one or both of the RLNs while separating the trachea from the esophagus.

In all six cases of acid introduction, we observed persistent laryngospasm that was accompanied by cessation of respiratory movements, perhaps caused by diaphragmatic arrest [149]. In all four cases (the animals with undamaged RLNs), we observed that stimulation immediately opened the larynx and normal respiratory movements resumed. Stimulation cessation immediately closed the larynx again, suggesting that electrical stimulation prevents laryngeal closure.

In one case, we observed an opening of the larynx and resumption of respiratory chest movements, but the rat died after 65 seconds. We believe that this rat died of asphyxiation either from inhaling saliva, mucus, acid, or a combination of the three. While the rat did not survive the laryngospasm, we were able to open its larynx during the laryngospasm. We make special note of this death because it highlights a risk of asphyxiation involved with any therapy that attempts to force open the larynx during a laryngospasm, particularly a laryngospasm caused by fluid.

The images shown in Figure 4.8 (d) and (f) indicate that the opening in the larynx during stimulation occurs where the PCA abductor muscles are located as shown in [150]. Electrical stimulation of either the RLNs or the cervical vagus nerves evokes a similar response from the intrinsic laryngeal muscles [151, 152], so our experiments suggest that VNS (applied to the cervical vagus) could open the larynx during a laryngospasm. Electrical stimulation could be a viable alternative treatment for laryngospasm for people with epilepsy who already have a VNS device. Because most VNS devices only stimulate either the left or right cervical vagus nerve, future work should determine if this electrical stimulation can open the larynx during a laryngospasm via unilateral vagus nerve stimulation.

4.3.4   Conclusion

We have shown that a constant-current, alternating-phase stimulation waveform with a pulse width of $100 \, \mu s$, pulse repeat time of $500 \, \mu s$, and amplitude of at least $500 \, \mu A$ can open the larynx during acid-induced laryngospasms in rats when applied bilaterally to the RLNs. Evidence suggests that this stimulation waveform opens the larynx by contracting the PCA abductor muscles in the larynx via signals induced on the RLNs. Adaptation of this stimulation for use in unilateral vagus nerve stimulation could provide a crucial alternative treatment for laryngospasms for people with epilepsy who already have a VNS device.

4.4   Preventing Laryngospasm via Gastric Vagotomy

Laryngospasm can be caused by gastric acid coming into direct contact with the larynx and activating chemoreceptors and/or mechanoreceptors responsible for triggering the laryngospasm reflex [58, 59]. Our recently published work indicates that gastric acid can lead to death in seizing rats by causing obstructive apnea via laryngospasm [55]. While we have shown that this type of laryngospasm can be treated via electric stimulation of the RLNs, understanding the mechanism behind how seizing activity leads to gastric acid induced laryngospasm is important for exploring preventative treatments.

To determine if the vagus nerve plays a role in the mechanism behind how seizing activity leads to stomach acid induced laryngospasm during seizures, we performed a series of gastric vagotomies on rats prior to inducing seizures via systemic kainic acid injections. We found that

performing gastric vagotomies on rats led to a statistically significant reduction in sudden death and incidences of acid reflux.

4.4.1 Materials and Methods

4.4.1.1 Data Acquisition

We acquired pH data from the esophagus using the same dual antimony pH electrodes and silver silver-chloride reference as described in [55]. We acquired ECoG using bone screws (Plastics One E363-20-SPC) connected to the cortex through a bur hole in the skull. We collected respiration signals using the same electrodes as described in Section 2.3. We used the Bionode breakout board (See Section 4.2) to acquire all four signals and saved all of the data using the Bionode DataView application (See Section 2.2.4). We had to build custom analog front end circuits to interface with the pH electrodes because we could not AC couple them from the animal due to the slow nature of the pH signal and the fact that the reference electrode must be grounded to the animal. Figure 4.9 depicts a pH AFE circuit.
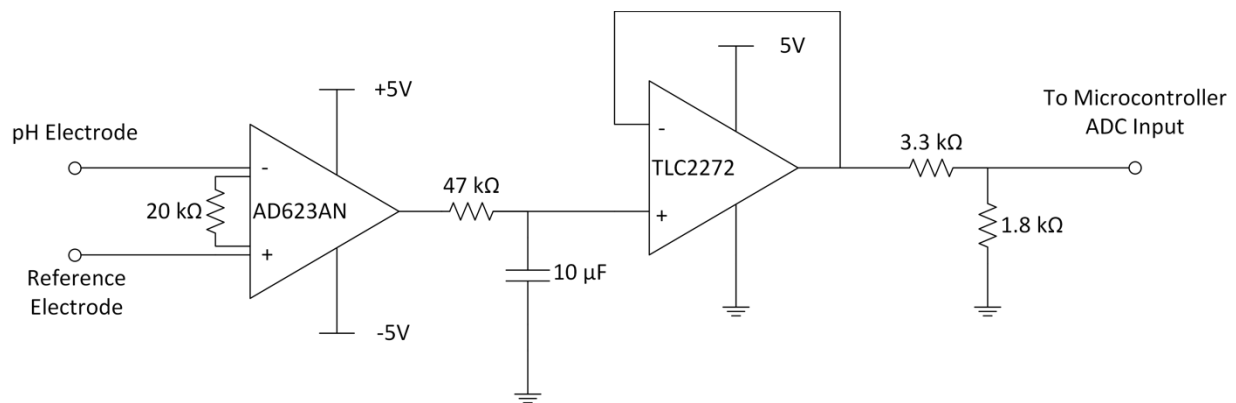
Figure 4.9: The instrumentation amplifier (AD623AN) provides high input impedance with a differential gain of 6 set by the 20 kΩ resistor. A passive RC low-pass filter with a cutoff of 0.4 Hz removes high frequency noise before the signal is inverted using a unity gain inverting amplifier (TLC2272). The resultant signal is attenuated using a resistor divider to ensure that it stays within the 0 to 1.8-volt input range of the microcontroller.

We connected the output of the pH AFE circuits to the Bionode breakout board (See Section 4.2) at the two ADC inputs corresponding to channel 1 and channel 2 of the Bionode AFE input. We configured the remaining two AFE channels to acquire data from the respiration transducer and the ECoG electrodes as outlined in Table 2.2.

4.4.1.2 Inducing Seizures

We induced seizures in rats using the systemic kainic acid (KA) model which has been found to produce recurring seizures an acute setting [33, 56, 153]. We chose this method of inducing seizures specifically because it is what we used to first determine that the presence of acid detected in the esophagus was a prerequisite for sudden death using this model [55]. To induce seizures, we injected a dose of 10 mg/kg of kainic acid in a solution of sterile saline (10 mg/ 5 mL) into the IP space. Seizures were confirmed by analyzing ECoG data as described in Section 3.5.2.

4.4.1.3 Surgical Procedure

Every surgical procedure that we performed was in accordance with the regulations of the IACUC and using procedures approved by the PACUC. All of these surgical procedures were performed by either Ethan Biggs or Adam Scott at the Center for Implantable Devices at Purdue University.

Rats were given urethane anesthesia (1-1.2 mg/ kg IP). We maintained the rat's core temperature using a heating pad with a rectal thermometer feedback sensor (Harvard Apparatus 50-7212). Once the rat was anesthetized, we kept its eyes hydrated using artificial tears (AKORN NDC 17478-062-35). Our first task was to perform the gastric vagotomy. With the rat in the supine position, we made a 2 cm rostral-caudal incision 0.5 cm left of midline starting in line with the apex of the xiphoid process. This incision goes through both the skin and the abdominal wall. We identified the liver and severed the hepatogastric ligament connecting the liver to the stomach. Severing this ligament allowed us to reflect the liver in the rostral direction using retractors which allows us to visualize the esophagus. With the esophagus in view, we identified the left vagus nerve which is visible on the ventral side of the esophagus. We followed the left vagus in the rostral direction until we could identify the bifurcation with the hepatic branch. The gastric branch is 2-3 mm caudal to the hepatic branch. We lift up the gastric branch using a microdissection hook and sever it using electric cautery. The right vagus nerve can be identified by locating it on the dorsal side of the esophagus. Using the location of the hepatic branch of the right vagus as a landmark, we identified the right vagus nerve's junction with the celiac branch. We then severed the gastric branch using the same procedure as before. We closed the wound by suturing the muscle wall together and then suturing the skin together.

Our next task was to place the bone screws on the cortex to acquire ECoG signals. We placed the rat in a stereotaxic frame in the prone position and held its head in place using ear bars and an incisor bar. We then made a rostral-caudal incision on the rat's scalp, exposing the skull. In order to place the ECoG bone screws onto the surface of the cortex, we drilled two bur holes into the skull to expose the dura, making sure to locate the caudal ECoG electrode over the hippocampus (bregma anterior/posterior – 3.5 mm, bregma lateral -3.0 mm). We located the reference ECoG bur hole 3 mm rostral to the caudal electrode. We then screwed the bone screw electrodes into the bur holes until they made contact with the dura.

Our final surgical task was to place the pH electrodes into the esophagus. We did this by removing the rat from the stereotaxic frame and placing it on its side in the recovery position (on its side). We then pushed a food tube into the esophagus until it made contact with the lower esophageal sphincter. Using the food tube as a guide, we threaded the pH electrodes through the food tube until they made contact with the lower esophageal sphincter. We then removed the food tube, taking care to keep the pH electrodes in their place near the esophageal sphincter. Finally, we made a small incision on the side of the rat and inserted the pH reference into the subcutaneous space.

Once the surgical procedures described above were completed, we rotated the rat to the prone position, and connected the ECoG and pH electrodes to the modified Bionode breakout board. We also placed the respiration thermocouple transducer tip immediately in front of the rat's nose and connected its terminals to the respiration channel AFE on the modified Bionode breakout board. At this point, we collected 10 minutes of baseline data. After we had collected the baseline data, we gave the rat an IP injection of kainic acid and resumed data collection. We collected data for 2 hours. If after 2 hours, the rat was not in obvious distress we terminated the experiment. If the rats were in distress after 2 hours, we allowed the experiment to continue for an additional 30 minutes. If at any time during the data collection, we observed a pH level of less than 3 on both electrodes, we recorded that acid had been detected in the esophagus. If acid was detected within 30 minutes of the termination of the experiment, we allowed the experiment to continue for an additional 30 minutes. If the rat survived until the end of data collection, we reported it as surviving the experiment, and then euthanized the rat with a lethal dose of Beuthanasia (200 mg/kg).

4.4.1.4 Acquiring Stomach Contents

To determine if performing gastric vagotomies affects the production of stomach acid and if that production of stomach acid affects the survival of the rats and/or the detection of acid in the esophagus, we collected the stomach contents of each rat immediately after euthanization. To collect both the liquid and solid stomach contents, we first used two pairs of hemostats to clamp off the esophagus and the duodenum to prevent any liquid or solid stomach contents from leaving the stomach. With the hemostats clamped in place, we removed the stomach by severing the esophagus and the duodenum on the side of the hemostats farther from the stomach. We then made an incision in the stomach and transferred the stomach contents into a 12-mL centrifuge tube. We measured the acidity of the liquid in the stomach contents using the pH electrodes to determine that its pH was consistent with the pH of stomach acid. We then stored the stomach contents in a -4°C freezer.

After we had completed all of the surgeries, we thawed out all of the stomach contents and weighed them. We then separated the liquid contents from the solid contents by centrifuging them for 5 minutes at 2500 revolutions per minute and then for 5 minutes at 3000 revolutions per minute. Figure 4.10 shows how the liquid and solid stomach contents separate after they are centrifuged.
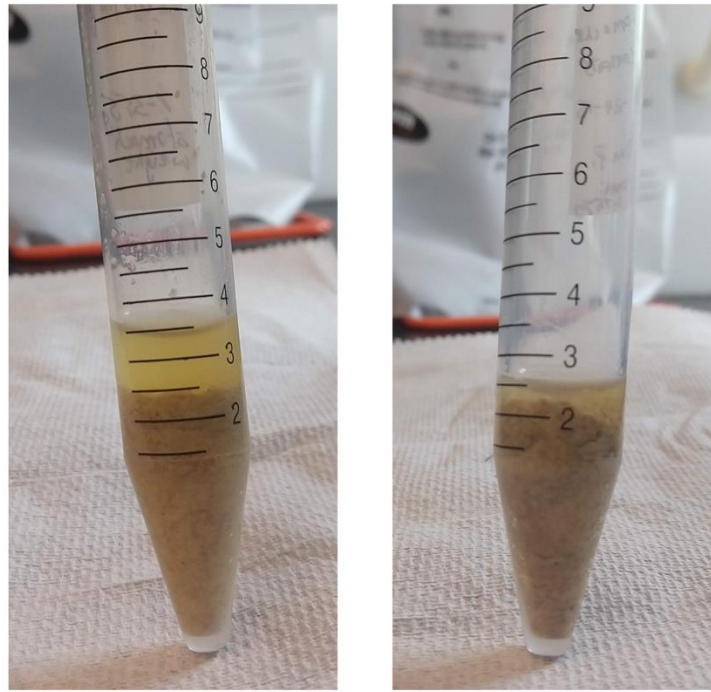
Figure 4.10: Liquid and solid stomach contents after being centrifuged. The stomach contents shown on the left contains more liquid than the stomach contents shown on the right.

We initially removed the liquid stomach contents from the solid stomach contents by pouring the liquid off of the top of each centrifuge tube. We then placed the open centrifuge tubes containing the remaining mostly solid stomach contents into a fume hood and allowed the remaining liquid to evaporate over the course of three days. We finally determined the mass of both the liquid and solid stomach contents via equation (4.1) and

(4.2).

$$Solid\ Stomach\ Content\ Mass = M_{TS} - M_{TE} \tag{4.1}$$
$$where$$
$$M_{TS} = Mass\ of\ tube\ containing\ solid\ stomach\ contents$$
$$M_{TE} = Mass\ of\ empty\ tube$$

$$Liquid\ Stomach\ Content\ Mass = M_{TSL} - M_{TS}$$

$$where$$

$$M_{TSL} = Mass\ of\ tube\ containing\ solid\ and\ liquid\ stomach\ contents \qquad (4.2)$$

$$M_{TS} = Mass\ of\ tube\ containing\ solid\ stomach\ contents$$

4.4.1.5   Statistical Methods

To determine the effects that gastric vagotomies had on the seizing rats, we performed various statistical tests for significance on the measurements we collected during the surgical procedures. These statistical tests are summarized in *Table 4.2*. We ran all statistical tests using R software. For convenience, we labeled the "liquid stomach content mass as a percentage of total stomach content mass" measurement as the "liquid ratio." This is an important measure because we did not control for initial stomach content mass, so the rats had a variable amount of food in their stomachs at the beginning of the experiments. The liquid ratio measurement normalizes the amount of liquid in the stomach to the total amount of stomach contents. We will therefore treat the liquid ratio as a measure of gastric acid production, where a high ratio indicates gastric acid overproduction.

We determined that acid had been detected in the esophagus if both caudal and rostral pH electrodes measured a pH of less than 3. This confirms acid reflux because it shows that acid has been detected traveling up the esophagus.

Table 4.2: Measures tested for statistical significance across various groups.

Group 1	Group 2	Measurement	Test
Gastric vagotomy with KA	No gastric vagotomy with KA	Died suddenly or did not die suddenly	Barnard's test
Gastric vagotomy with KA	No gastric vagotomy with KA	Acid detected or acid not detected	Barnard's test
Gastric vagotomy with KA	No gastric vagotomy with KA	Total stomach content mass	Student's t-test
Gastric vagotomy with KA	No gastric vagotomy with KA	Liquid ratio[1]	Student's t-test
Rats that survived with KA	Rats that did not survive with KA	Liquid ratio[1]	Student's t-test
Acid detected in the esophagus with KA	No acid detected in the esophagus with KA	Liquid ratio[1]	Student's t-test
Control	Gastric vagotomy with KA	Liquid ratio	Student's t-test
Control	No gastric vagotomy with KA	Liquid ratio	Student's t-test

[1]Liquid stomach content mass as a percentage of total stomach content mass

We determined if performing gastric vagotomies led to a statistically significant reduction in sudden death by performing a Barnard's test, which is an exact test used to examine contingency tables [154]. To run this test, we set the outcomes to be how many rats did not survive (Outcome 1) and how many rats did survive (Outcome 2). We specified the treatments to be performing a gastric vagotomy (Treatment 1) or not performing a gastric vagotomy (Treatment 2). We determined if performing gastric vagotomies led to a statistically significant reduction in death if the Barnard's test returned a p value less than 0.05. We used the Barnard's test in a similar fashion when determining if performing gastric vagotomies led to a statistically significant reduction in the incidence of acid reflux.

Before running the Student's t-test on any of the measurements in Table 4.2, we first performed Shapiro-Wilks tests of normality on each group as well as the Bartlett's test on both groups for homoscedasticity. If neither of the Shapiro-Wilks tests indicated that either dataset was not normal ($p > 0.5$), and if the Bartlett's test did not indicate that the datasets had unequal variances ($p > 0.5$), we performed a two tailed Student's t-test assuming normal distributions and equal variances to determine if the datasets contained a statistically significant difference. We determined statistical significance if the t-test returned a p value less than 0.5.

4.4.2   Results

We performed a total of 16 surgeries. Three of these surgeries acted as controls where we injected saline instead of systemic KA and we did not sever the gastric nerve. Seven of these surgeries included both gastric vagotomies and systemic KA injections. The remaining six surgeries did not include gastric vagotomies, but did include systemic KA injections. The results of these surgeries are summarized in Table 4.3.

Table 4.3: Survival, esophageal acid detection, and stomach content mass measurements for kainic acid injected rats with and without gastric vagotomies.

Rat	Gastric vagotomy?	Sudden death?	Acid detected?	Solid stomach contents (g)	Liquid stomach contents (g)	Liquid ratio	Air detected in stomach
Systemic KA Administered							
PH50	No	No	Yes	2.32	2.08	47%	N/A
PH55	No	No	Yes	1.96	1.51	44%	Yes
PH56	No	Yes	Yes	1.26	1.81	59%	Yes
PH61	No	Yes	Yes	5.45	2.85	34%	No
PH63	No	Yes	Yes	3.17	2.58	45%	Yes
PH65	No	Yes	Yes	5.89	4.98	46%	Yes
PH49	Yes	No	No	2.12	0.17	7%	N/A
PH52	Yes	No	No	4.99	1.71	26%	Yes
PH60	Yes	No	No	2.04	0.40	16%	Yes
PH64	Yes	No	No	3.50	1.87	35%	No
PH68	Yes	No	No	4.51	1.76	28%	Yes
PH69	Yes	No	No	3.12	1.54	33%	Yes
PH62	Yes	No	Yes	2.81	1.22	30%	Yes
Controls (No KA Administered)							
PH86	No	No	No	1.69	0.54	24%	No
PH87	No	No	No	2.25	0.38	15%	No
PH88	No	No	No	0.70	0.43	38%	No

As stated in Section 4.4.1, we have labeled the liquid stomach content mass as a percentage of total stomach content mass measurement as the liquid ratio. Because this is a measure of gastric acid production, we will focus much of our analysis on this measure. Figure 4.11 depicts the liquid ratios of all of the rats.
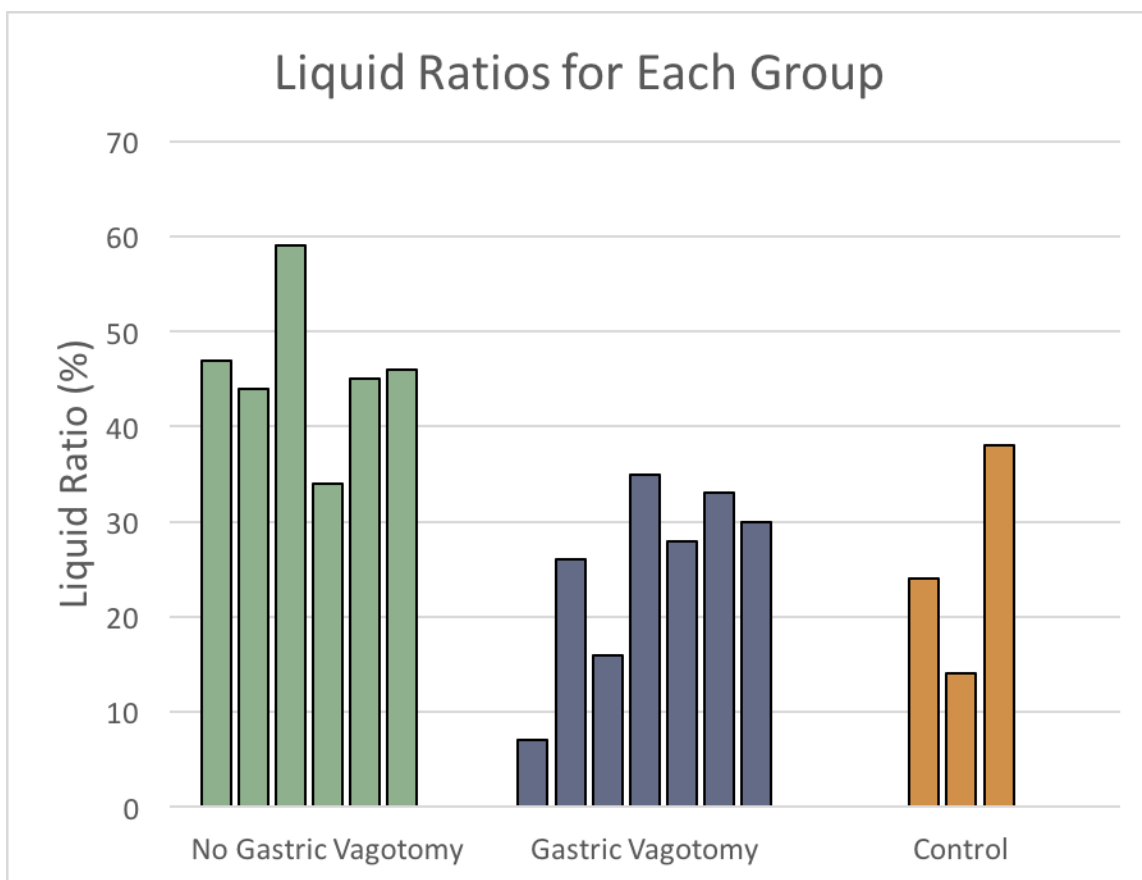
Figure 4.11: The ratio is defined as the liquid stomach content mass as a percentage of total stomach content mass.

Performing the gastric vagotomy on KA injected rats resulted in a statistically significant reduction in sudden death (p = 0.0122) and acid detection (p = 0.0011) (See Figure 4.12). KA injected rats without gastric vagotomies had statistically significantly higher liquid ratios than both KA injected rats with gastric vagotomies (p = 0.0017) and rats in the control group (p = 0.0174). KA injected rats with gastric vagotomies did not have a statistically significantly different liquid ratio than rats in the control group (p = 0.9394). Performing the gastric vagotomy did not result in a statistically significant difference in total stomach content mass (p = 0.3089). Rats that survived had a statistically significantly smaller liquid ratio than rats that died (p = 0.0414). Rats that did not have acid detected in their esophagus by both pH electrodes also had a statistically significantly smaller liquid ratio than rats that did have acid detected by both pH electrodes (p = 0.0047). These results are summarized in Table 4.4.
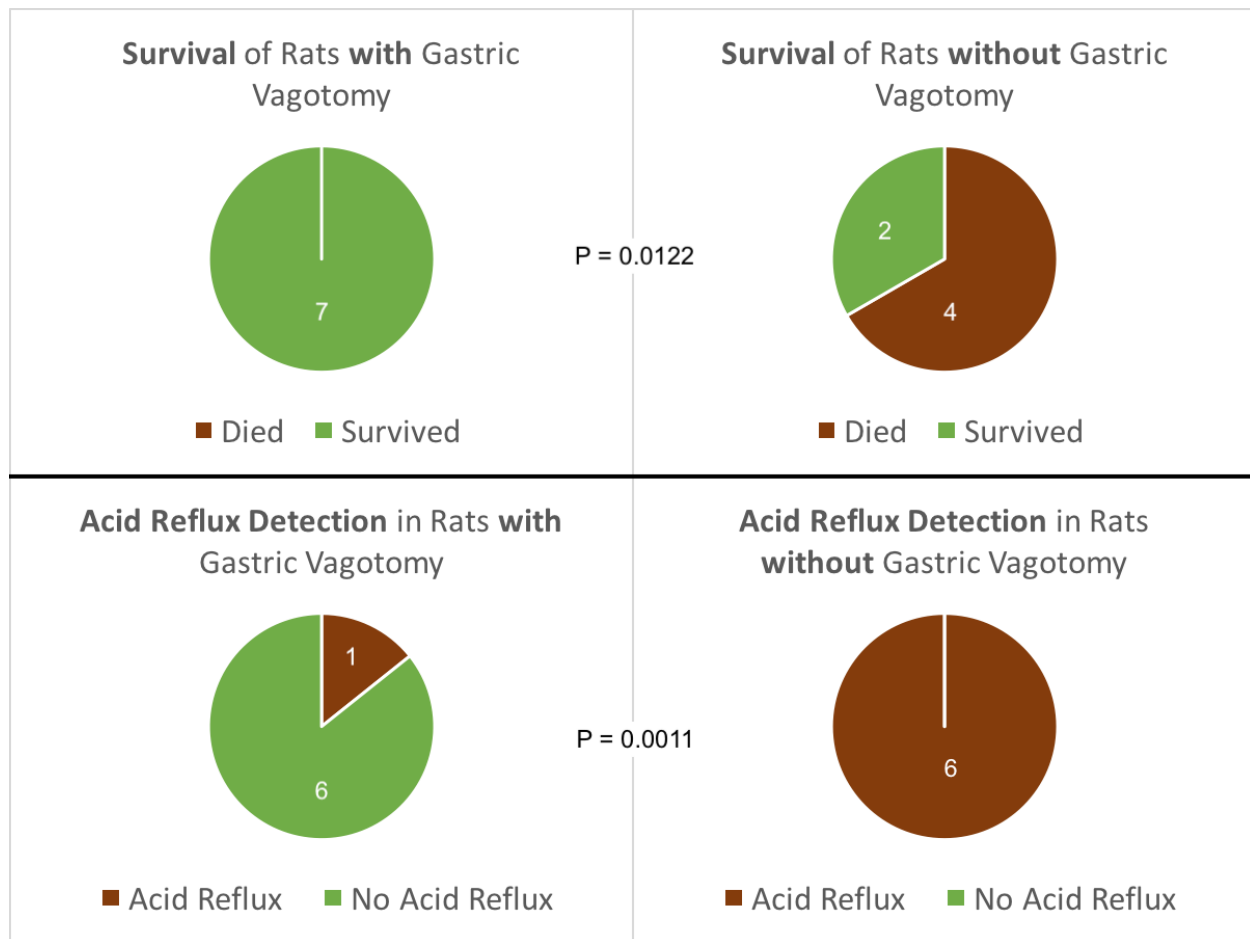
Figure 4.12: Performing the gastric vagotomy on kainic acid injected rats resulted in a statistically significant reduction in death (p = 0.0122) and acid reflux detection (p = 0.0011).

Table 4.4: Statistical results.

Group 1	Group 2	Measurement	Result
Gastric vagotomy	No gastric vagotomy	Died suddenly or did not die suddenly	p = 0.0122
Gastric vagotomy with KA	No gastric vagotomy with KA	Acid detected or acid not detected	p = 0.0011
Gastric vagotomy	No gastric vagotomy	Total stomach content mass	p = 0.3089
Gastric vagotomy	No gastric vagotomy	Liquid ratio[1]	p = 0.0017
Rats that survived	Rats that did not survive	Liquid ratio[1]	p = 0.0414
Acid detected in the esophagus	No acid detected in the esophagus	Liquid ratio[1]	p = 0.0047
Control	Gastric vagotomy with KA	Liquid ratio	p = 0.9394
Control	No gastric vagotomy with KA	Liquid ratio	p = 0.0174

Prior to removing the stomach, we observed distention of the stomach due to air inside the stomach in nine rats. The first time we observed this distention was during the third surgery, so we do not have observations for the first two surgeries (PH49 and PH50) about the presence of air inside the stomach. Figure 4.13 shows the stomach of one of these rats (PH65) as well as a non-distended stomach (PH89). We did not detect any gas in the stomachs of the rats from the control group.
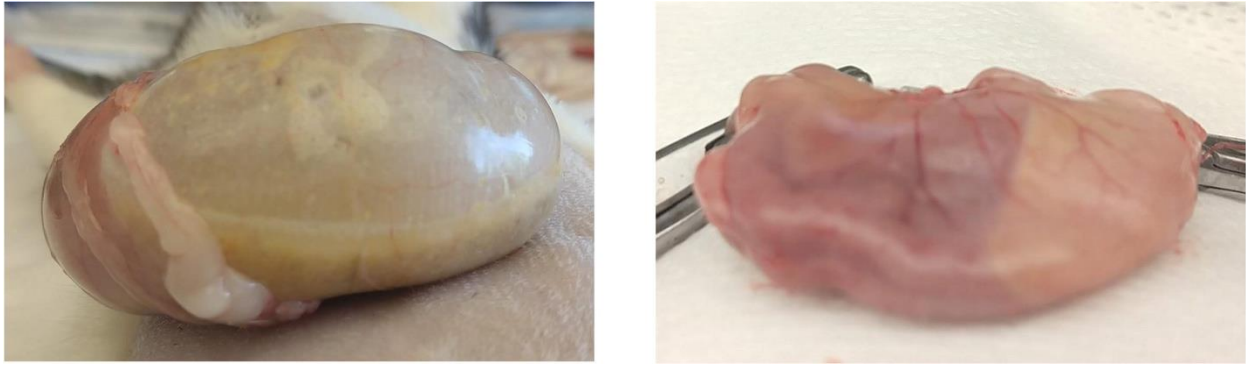
Figure 4.13: (left) Distention of the stomach caused by excessive air inside the stomach. (right) A non-distended stomach.

Figure 4.14 shows all of the signals that we measured from PH61 from the beginning of the experiment through sudden death.
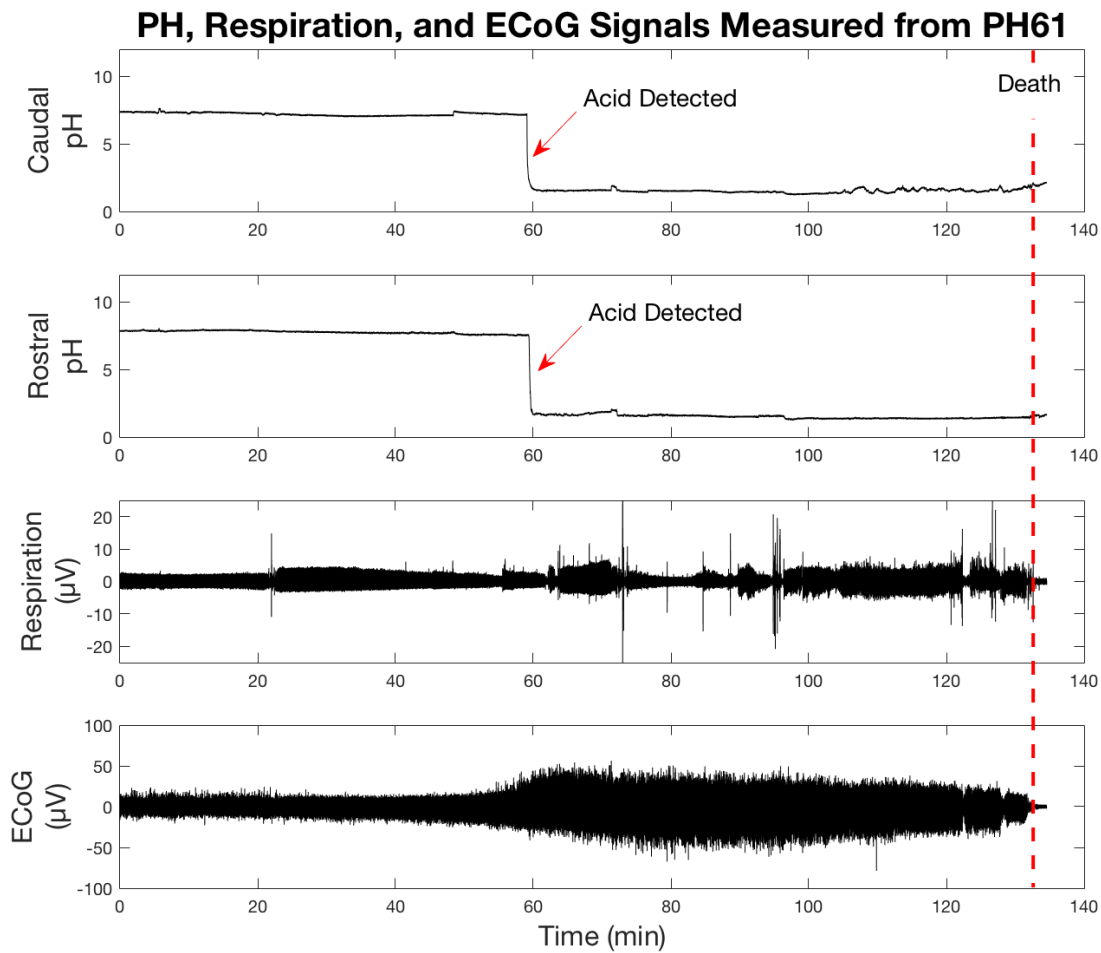
Figure 4.14: Acid was detected on both the caudal and rostral pH electrodes 60 minutes after the beginning of the experiment. Sudden death occurred 132 minutes after the beginning of the experiment.

We observed several obstructive apneas in rats that experienced sudden death. We determined that apneas were obstructive if we observed a cessation of airflow (as measured by the respiration transducer) with concurrent chest movements indicating that the rat was attempting to breath but was unable to. While we did observe transient apneas (apneas without obstruction) in rats that did not suddenly die, we only observed obstructive apneas in rats that suddenly died. Figure 4.15 depicts an obstructive apnea that was experienced by PH61 four minutes prior to sudden death.
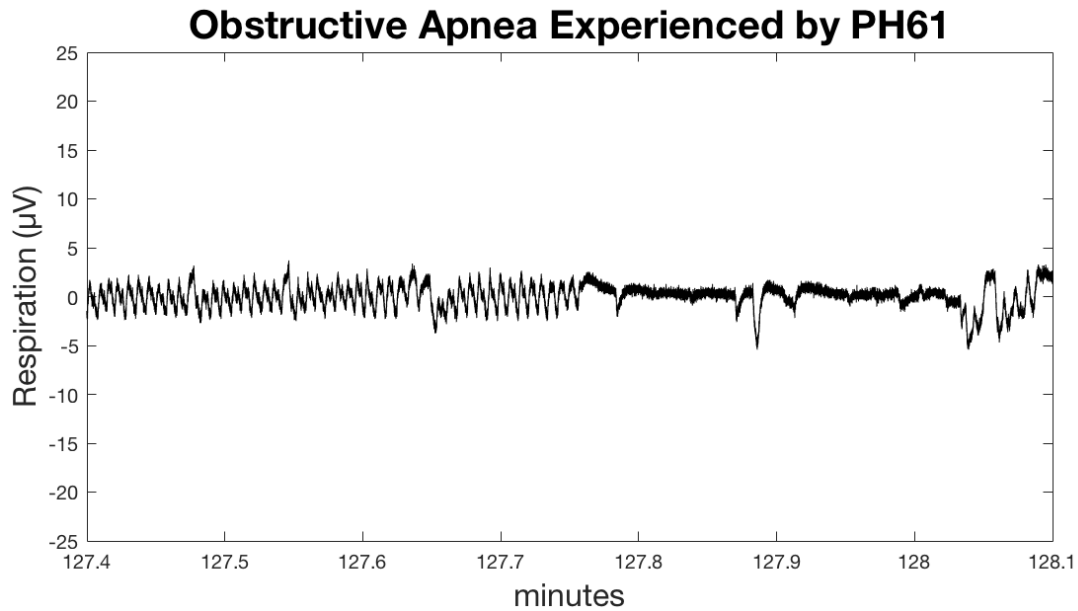
Figure 4.15: This obstructive apnea was experienced by PH61 four minutes prior to sudden death. During the cessation of airflow, the rat's chest movements indicated that it was attempting to breath, and was unable to.

We confirmed seizures by analyzing the PSD of baseline ECoG measurements and comparing it to the PSD of ECoG measurements taken during suspected seizing activity. Figure 4.16 shows 2 minute ECoG samples and their respective PSDs taken during PH61's baseline period as well as during seizing activity. The PSDs were estimated using Welch's method with a Hamming window.
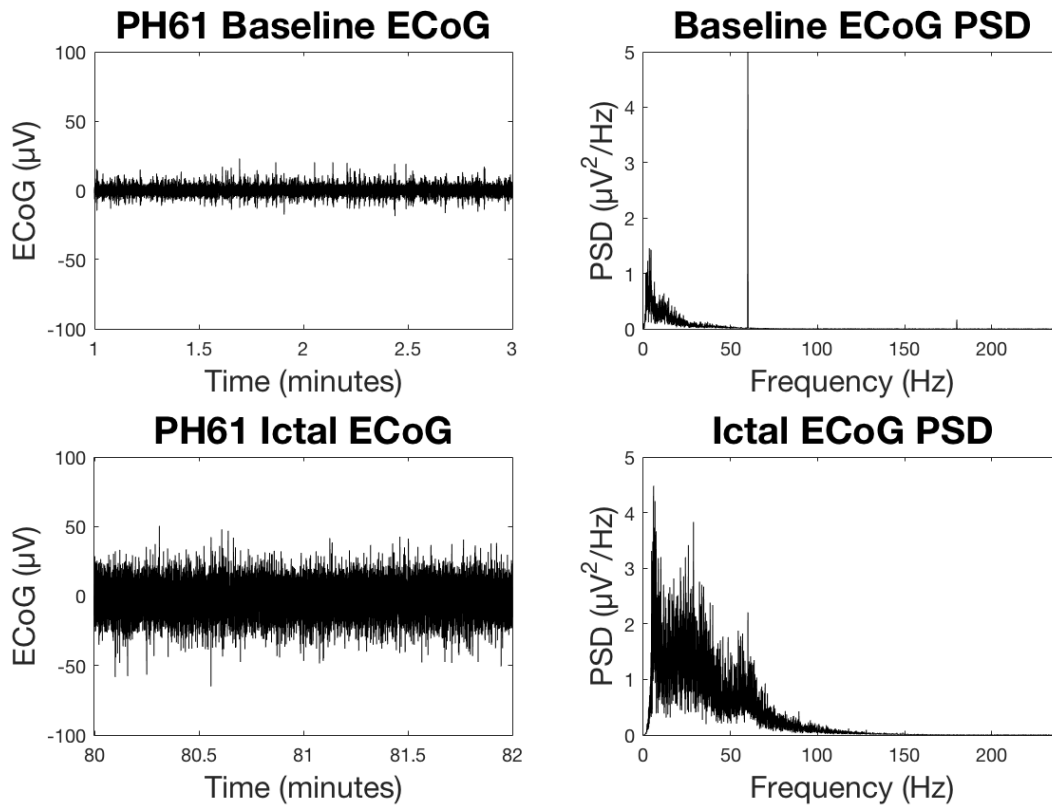
Figure 4.16: Preictal ECoG power spectral density (PSD) compared to ictal ECoG PSD for PH61. PSD is estimated using Welch's method with a Hamming window. Increased power below 40 Hz and specifically near 30 Hz indicates seizing activity.

4.4.3 Discussion

In our experiments, performing gastric vagotomies eliminated sudden death and greatly reduced incidence of acid reflux. Kainic acid increased the liquid ratio in the stomach suggesting gastric acid overproduction. Severing the gastric nerve eliminated this effect. Animals that suddenly died had a higher liquid ratio than animals that did survive. Animals that experience acid reflux had a higher liquid ratio than animals that do not. Our results show that severing the gastric nerve reduces liquid ratio, incidence of acid reflux, and incidence of sudden death.

While our nonparametric statistical methods (via Barnard's test) are robust, our parametric statistical methods (via the Student's t-test) require assumptions about the normality and homoscedasticity of the data sets. We have taken steps to prove these assumptions with the

Shapiro-Wilk test of normality and the Bartlett's test for the homogeneity of variances, but these tests may be disproportionately impacted by our small sample size. Therefore, we are confident in our claims that performing gastric performing gastric vagotomies eliminated sudden death and greatly reduced incidence of acid reflux. However, our claims involving the reduction of the liquid ratio should be taken as indicators of a possible mechanism that require more investigation.

Determining the method by which severing the gastric nerve reduces sudden death in these rats is crucial to developing translational preventative treatments for sudden death in epilepsy in humans. It is apparent that the acid overproduction observed during the experiments is necessary for both acid reflux and sudden death as both of these events occurred in rats with significantly higher liquid ratios in their stomachs at death. Because acid reflux has been shown to be a prerequisite for sudden death [55], it follows from our experiments that stomach acid overproduction is also a prerequisite for sudden death. By severing the gastric nerve, we are preventing sudden death by eliminating the effect that systemic KA injections have on gastric acid overproduction.

The mechanism behind the increase in gastric acid production that we observed during seizing activity is unknown. Our results will be most relevant to epilepsy if acid overproduction is a result of seizing activity as opposed to a side effect of KA. While KA may be able to increase gastric acid production directly by activating glutamate receptors in the stomach [155], the elimination of gastric overproduction via gastric vagotomy indicates that this is not the main mechanism driving gastric acid overproduction. KA injected directly into the medulla has been shown to increase gastric acid production, which suggests that this response may be brain stem mediated [156, 157]. If this is the driving mechanism behind the gastric acid overproduction, this overproduction would be attributed to a side-effect of the systemic KA model and not to epilepsy. However, during a series of exploratory experiments, we detected acid reflux in a rat with KA injected directly into the hippocampus. While this suggests that KA injections can cause acid reflux without directly acting upon the brainstem, this result must be replicated in multiple rats before we can eliminate the effect that KA has on the brainstem as a necessary factor in gastric acid overproduction.

Our proposed mechanism behind the observed stomach acid overproduction is that during seizures, signals originating in the brain generate errant signals on the vagus nerve which may cause an

overproduction of gastric acid in the stomach via the gastric branch of the vagus nerve. This overproduction of gastric acid in the stomach can cause excessive gastric acid to move up the esophagus and contact the larynx, causing a fatal laryngospasm responsible for sudden death in epilepsy. Gastric acid may enter the esophagus passively through regurgitation, via abnormal, vagus mediated relaxation of the gastroesophageal barrier during seizing activity, or via a pressure increase in the stomach due to acid and/or gas buildup. Gastric acid overproduction is supported by the documented comorbidity of GERD and stomach ulcers in people with epilepsy, both of which can be caused by an overproduction of gastric acid [158, 159]. This comorbidity may be partially explained by our proposed mechanism of vagally-mediated gastric acid overproduction.

During some of our experiments, we observed distention of the stomach in rats with KA injected (both with and without gastric vagotomy) (See Figure 4.13). We determined that the distention was caused by air in the stomach. We believe this is caused by the rat swallowing air during seizures. While distention of the stomach can lead to an increase in gastric acid production [76], the presence of air in the stomach did not have a significant effect on either acid reflux or sudden death, suggesting that the mere presence of air does not play a significant role in stomach acid overproduction. It may be the case, however, that extreme levels of distention due to air in the stomach could lead to gastric overproduction. It would be worthwhile to keep track of the volume of air inside the stomach in future studies.

While some people do undergo gastric vagotomy procedures to treat stomach ulcers [91], the risk of sudden death in epilepsy may be too low for patients to pursue invasive preventative surgery. With this in mind, we propose a method of stimulating the left cervical vagus nerve via electrical stimulation to block signals traveling from the brain to the gastric branch of the vagus nerve during seizing activity. This would electrically block any errant signals that might cause stomach acid overproduction from getting to the stomach. Because electrical blocking is reversible, this would result in a "temporary vagotomy" that would reduce the risk of sudden death in epilepsy during seizures and then return the vagus nerve to normal operation after the risk of sudden death has passed. If the risk of sudden death from epilepsy can be mediated by applying blocking electrical stimulation to the left cervical vagus nerve, then patients already outfitted with VNS devices may be able to reduce their risk of death in epilepsy via a modification to the algorithm driving the

stimulation output of their device. I describe my progress toward this method of VNS in Chapter 5.

4.4.4   Conclusion

In our experiments, performing gastric vagotomies eliminated sudden death and greatly reduced incidence of acid reflux. Statistical results suggest that severing the gastric nerve eliminates the gastric acid overproduction that we detected in seizing rats that did not have gastric vagotomies. Our proposed mechanism behind the detected stomach acid overproduction is that during seizures, signals originating in the brain generate errant signals on the vagus nerve which may cause an overproduction of gastric acid in the stomach via the gastric branch of the vagus nerve. This overproduction of gastric acid in the stomach can cause excessive gastric acid to move up the esophagus and contact the larynx, causing a fatal laryngospasm and causing sudden death in epilepsy. We have started exploring a method of stimulating the left cervical vagus nerve via electrical stimulation to block signals traveling from the brain to the gastric branch of the vagus nerve during seizing activity. This would electrically block any errant signals that might cause stomach acid overproduction from getting to the stomach. If the risk of sudden death from epilepsy can be mediated by applying blocking electrical stimulation to the left cervical vagus nerve, then patients already outfitted with implanted VNS devices may be able to reduce their risk of death in epilepsy via a modification to the algorithm driving the stimulation output of their device.

4.5   Conclusion of Specific Aim 3

My third specific aim was to stimulate the nervous system via electrical stimulation to treat and/or prevent the onset of sudden death in epilepsy. I demonstrated that a constant-current, alternating-phase stimulation waveform can open the larynx during acid-induced laryngospasms in rats when applied bilaterally to the RLNs. Because laryngospasms may be a factor in SUDEP [56, 57], and acid reflux may be the trigger for some or all of those laryngospasm episodes [55], I have shown that it may be possible to treat fatal laryngospasms using electrical stimulation. Additionally, I have demonstrated that performing gastric vagotomies eliminated sudden death and greatly reduced incidence of acid reflux in the acute systemic KA model of epilepsy. This suggests that it may be possible to reduce sudden death in epilepsy by applying electrical blocking stimulation to the vagus nerve. I present initial work toward providing this blocking stimulation in chapter 5.

Neither bilateral electrical stimulation of the RLN nor severing the gastric nerve are easily translatable for human use. However, because both of these therapies involve modulation of branches of the vagus nerve, it may be possible to use currently available VNS devices to achieve similar results. My research has paved the way for this translational work.

5. INITIAL WORK TOWARD FUTURE STUDIES

5.1 Validating Nerve Blocking via Electrical Stimulation

Section 4.4 showed that rats with gastric vagotomies had a statistically significant reduction in sudden death while seizing when compared to rats without gastric vagotomies. While this result indicates that errant signals on the vagus nerve may cause gastric acid induced laryngospasms leading to an increased risk of death in epilepsy, it does not directly provide a preventative treatment for increased risk of sudden death in epilepsy. While some people do have gastric vagotomies to treat stomach ulcers [91], the risk of sudden death in epilepsy may be too low for people with epilepsy to pursue invasive preventative surgery. With this in mind, I decided to pursue the idea of stimulating the left cervical vagus nerve via electrical stimulation to block signals traveling from the brain to the gastric branch of the vagus nerve. If the risk of sudden death from epilepsy can be mediated by applying blocking electrical stimulation to the left cervical vagus nerve during seizures, then patients already outfitted with implanted VNS devices may be able to reduce their risk of death in epilepsy via a small modification to the algorithm driving the stimulation output of their device.

To validate that certain electrical stimulation waveforms can block nerve signals, I used one Bionode's stimulator to generate a compound nerve action potential, while I simultaneously used another Bionode's stimulator block it. The setup is shown in Figure 5.1
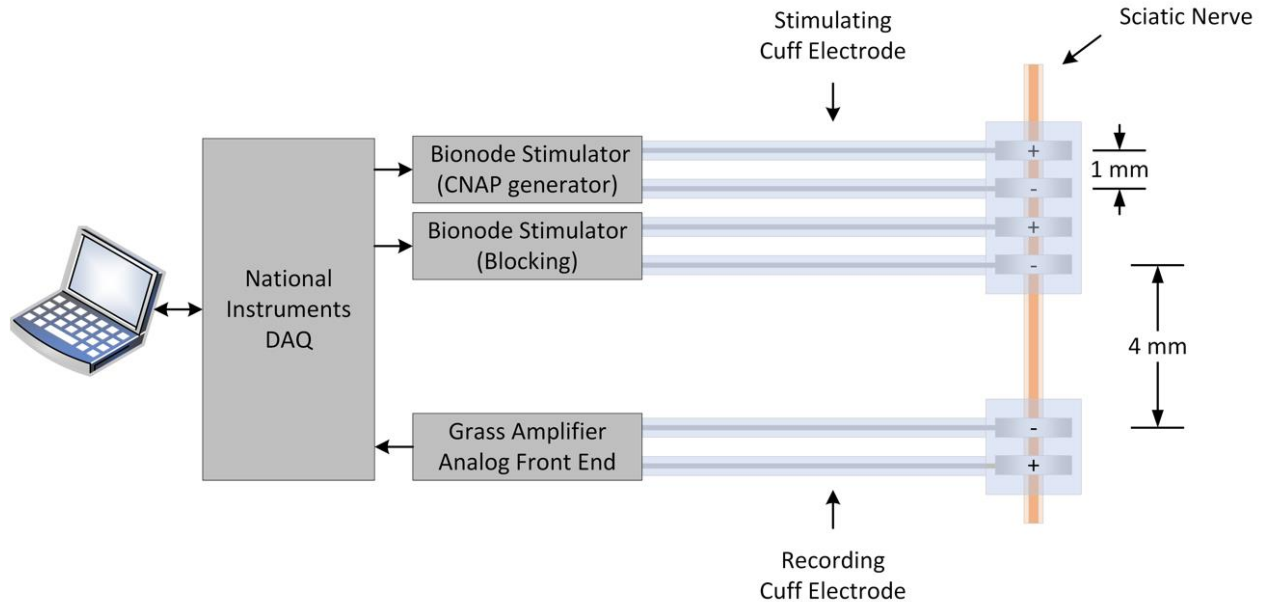
Figure 5.1: Setup for testing and validating the Bionode's ability to block nerve signals. The first stimulator generates compound nerve action potentials on the sciatic nerve via electrical stimulation. The second stimulator generates blocking stimulation. The analog front end records electrical activity on the sciatic nerve downstream from the stimulators.

We attached two Bionode stimulators to the left sciatic nerve of an anesthetized rat using a custom designed cuff electrode with four contacts spaced 1-mm apart. This allowed us to stimulate the nerve with both stimulators in very close proximity. I chose to initially stimulate the sciatic nerve during this validation phase because it is easier to access and cuff than the vagus nerve and has been used in other studies to validate electrical blocking signals [160, 161]. We attached a recording cuff electrode 4 mm caudal to the stimulating cuff electrode and connected it to a Grass Amplifier to condition the recorded signal. We did not use the Bionode's analog front end for this because we wanted the ability to change the filtering parameters during the surgery due to the exploratory nature of this procedure. Both stimulators were driven by a National Instruments data acquisition (NI-DAQ) unit. This NI-DAQ also digitized the output of the analog front end attached to the recording cuff electrode. I designed custom PC software GUI using Python to precisely synchronize the NI-DAQ's input and output. Figure 5.2 displays this GUI.
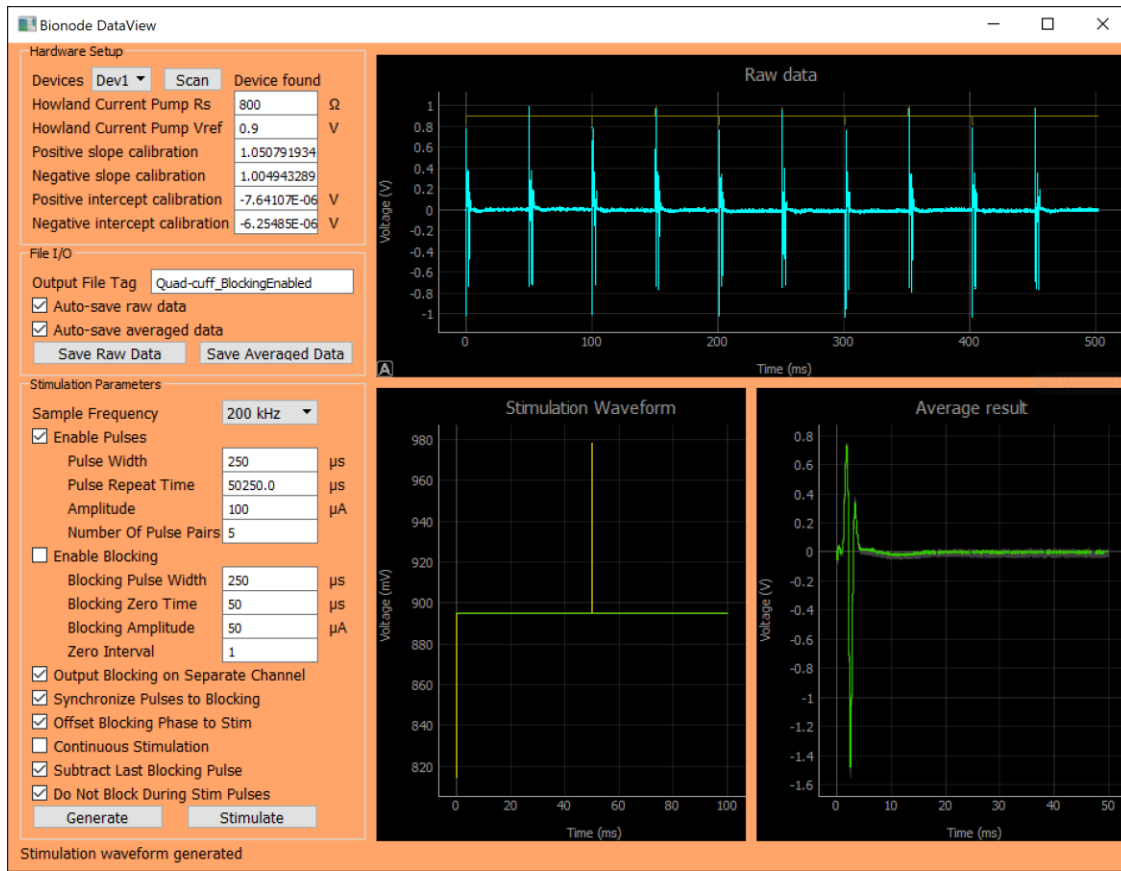
Figure 5.2: Graphical User Interface for synchronizing blocking and compound nerve action potential generating stimulation.

The following protocol outlines how we validated the Bionode's ability to block nerve signals:

1. Stimulate the sciatic nerve with the first stimulator to generate a CNAP

2. Verify that CNAPs have been generated on the sciatic nerve by the first stimulator by looking at signals recorded by the recording cuff electrode.

3. Stimulate the sciatic nerve with the first stimulator to generate a CNAP. Simultaneously stimulate the sciatic nerve with the second stimulator to block nerve signals.

4. Verify that CNAP activity has reduced or ceased on the sciatic nerve by looking at signals recorded by the recording cuff electrode.

5. Re-do steps 1 and 2 to ensure that no damage has been done to the nerve by the blocking stimulation.

We generated CNAPs using an alternating phase waveform with the following parameters:

- Pulse Width (T_{PW}) = 250 µs

- Pulse Repeat Time (T_{PRT}) = 50,250 µs

- Amplitude = 100 µA.

This waveform is depicted in Figure 5.3.
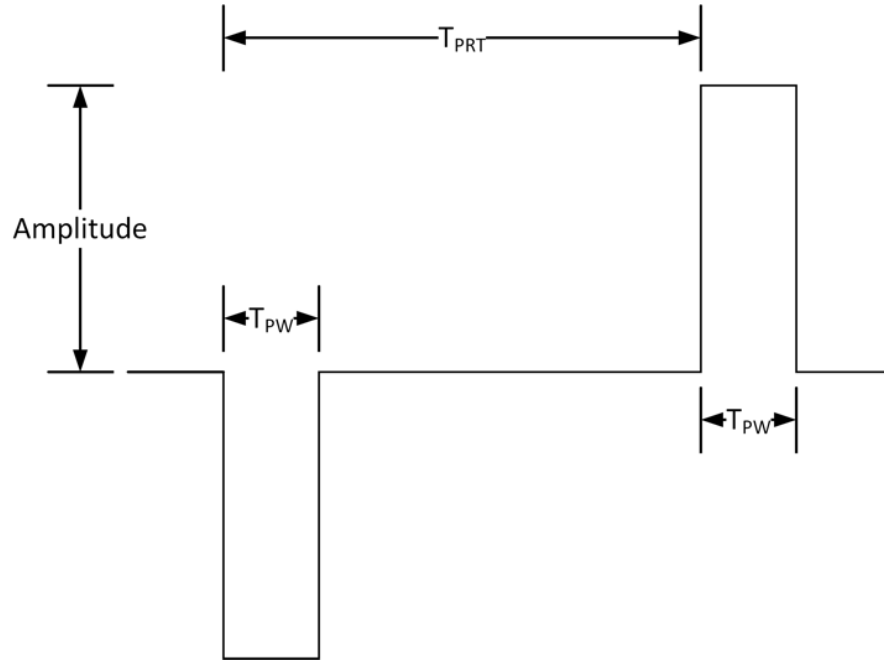
Figure 5.3: Stimulation waveform for generating compound nerve action potentials (CNAPs). To generate CNAPs, we set T_{PW} = 250 µs, T_{PRT} = 50,250 µs, and Amplitude = 100 µA.

After referencing work documented in [160, 161], we generated blocking waveforms using a bi-phasic 2 kHz square wave of various amplitudes (ranging from 0 to 100 µA) with a short, 50 µs period between each rising and falling edge where the output of the stimulator is set to zero amperes. This short period where the stimulator output was zero amperes allowed us to discharge the blocking capacitor on the output of the stimulator (See Section 2.2.3) between each pulse to ensure that the blocking capacitor never becomes saturated. This blocking waveform is shown in Figure 5.4.
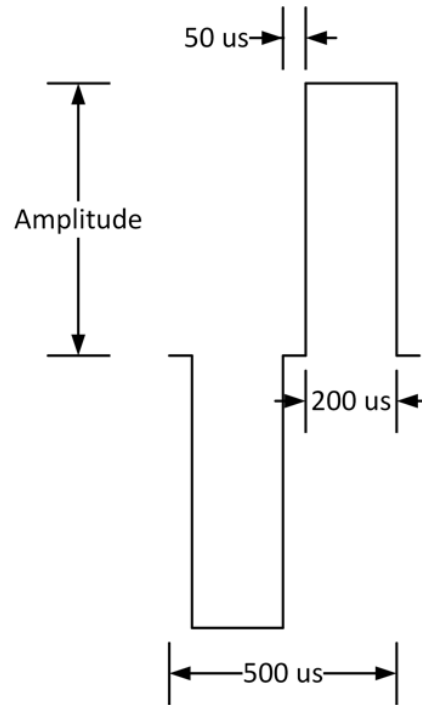
Figure 5.4: Blocking waveform for blocking nerve signals. We attempted to generate blocking stimulation using amplitudes ranging from 0 to 100 µA.

To confirm the existence or non-existence of CNAPs on the sciatic nerve, I had to cancel stimulation artifacts from both the CNAP generating stimulator and the blocking stimulator in post processing. This required me to synchronize both stimulator outputs as well as the digitization of the recorded signal precisely. This is why I chose to use a NI-DAQ to drive the Bionodes' stimulators and the data acquisition. The Bionode's microcontroller can be configured to perform this synchronization, but I decided to verify that the Bionode's hardware was able to block nerve signals before revising the Bionode's firmware. I removed the CNAP generating stimulation artifact and the blocking stimulation artifact using two methods.

To remove the stimulation artifact, I followed a procedure outlined in [162]. I first applied 20 instances of the stimulation waveform show in Figure 5.3. Concurrently, I recorded signals measured from the sciatic nerve by the recording cuff during these stimulation pulses. Because I know the timing parameters of the stimulation waveform, I am able to add the recorded negative and positive stimulation responses together to isolate the CNAP responses generated during the negative stimulation pulse. After adding the positive and negative stimulation responses together, I took the average of the resulting 20 waves to acquire the CNAP response. This is all done

automatically by the software program that I wrote to drive the NI-DAQ. Figure 5.5 shows the raw data recorded during a session of CNAP generation stimulation as the resulting CNAP present after stimulation artifact cancelling. This data was recorded with the Grass Amplifier set to a gain of 1000 with a bandpass filter of 0.3 Hz to 5 kHz.
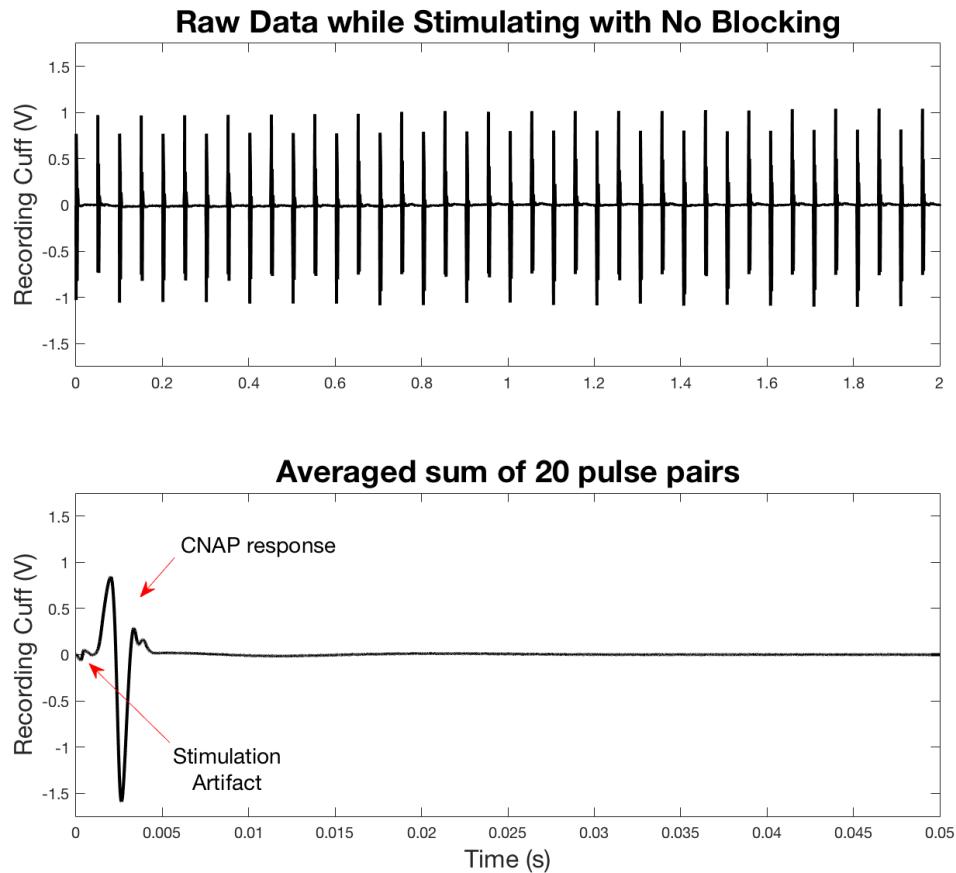
Figure 5.5: (top) Raw data recorded while applying compound nerve action potential (CNAP) generating stimulation. (bottom) CNAP present after cancelling out stimulation artifact.

We verified that the resulting signal in Figure 5.5 was a CNAP by taking into account various nerve fiber propagation velocities. Because the stimulating and recording cuffs are 4mm apart from each other, the resulting pulse at 4ms post stimulation suggests a C-fiber activation which has propagation velocities of between 0.5 and 2 mm/ms [163].

To successfully remove the blocking stimulation artifact, I had to synchronize the blocking waveform with the CNAP generation waveform. If I had not synchronized the waveforms together, then my method of canceling the CNAP generation stimulation artifact would add the blocking stimulation artifacts together out of phase, making them much harder to cancel out. When synchronizing the blocking waveform to the stimulation waveform, I also had to be sure that I was not actively cancelling out the stimulation waveform by applying opposite blocking pulses synchronized with the stimulation pulses. I avoided this problem by applying the blocking stimulation in such a way that it could only add to the stimulation pulse amplitude. This is illustrated in Figure 5.6.
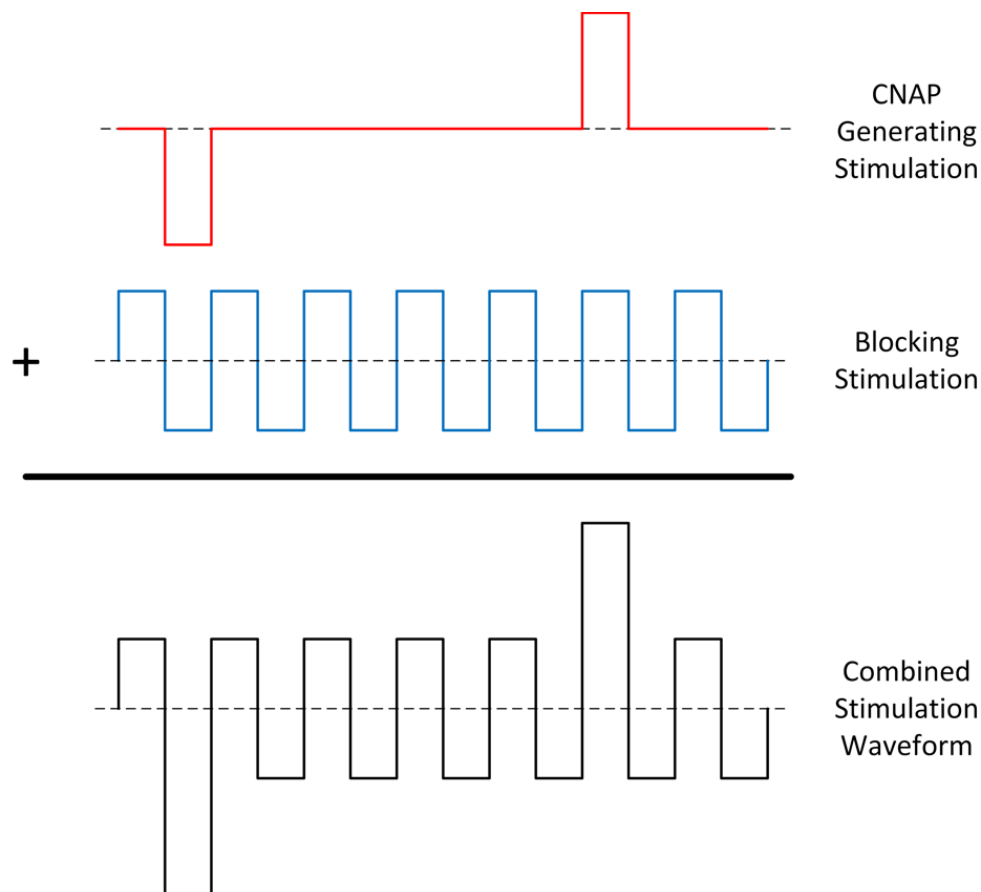
Figure 5.6: The blocking stimulation is synchronized with the compound nerve action potential (CNAP) generation stimulation waveform in such a way that it does not cancel out the CNAP generation stimulation pulses.

To remove both blocking and CNAP generating stimulation artifacts, I applied 20 CNAP generating stimulation pulse pairs as before while concurrently applying the blocking stimulation

as shown in Figure 5.4. During the application of the stimulation and blocking pulses, I simultaneously recorded measurements acquired by the recording electrode. I then canceled out the CNAP generating stimulation artifact using the same method as before by adding the positive and negative stimulation responses together and obtaining an averaged response waveform. Because of how I synchronized the blocking waveform to the stimulation waveform, this method of cancelling out the CNAP generating stimulation artifact also cancels out the blocking stimulation artifact because the blocking stimulation pulses during the positive CNAP generation pulse are exactly 180 degrees out of phase with the blocking stimulation pulses during the negative CNAP generation pulse. To further remove noise from the resultant signal, I obtain a sample at the very end of the averaged waveform equal in length to one period of blocking stimulation, invert it, and add it to the averaged signal. Because nerve responses have ceased by this time, the sampled data at the end of the waveform represents data containing no signal of interest. I have found that this reduces any noise injected into the signal by small asymmetries in the blocking waveform between the negative and positive pulses. Figure 5.7 shows the result of stimulating with both CNAP generation stimulation and blocking stimulation with an amplitude of 50 µA.
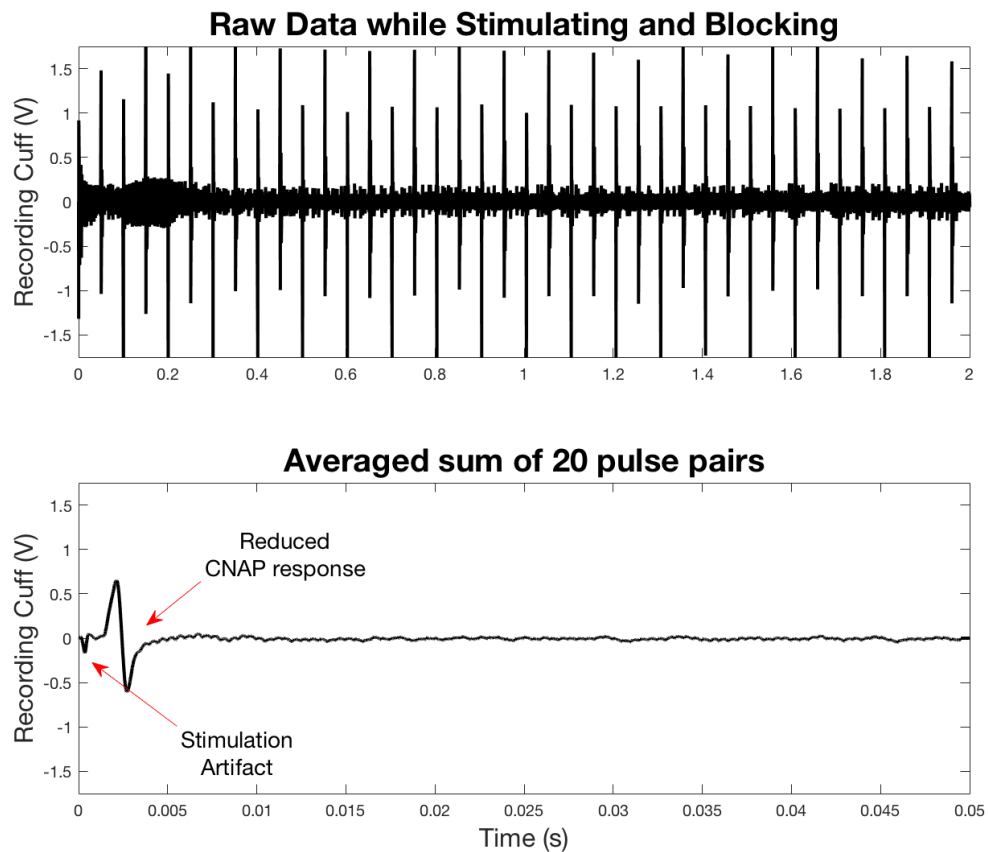
Figure 5.7: The blocking waveform applied here had an amplitude of 50 µA. The top plot shows the raw signal acquired by the recording cuff electrode during all 20 pulse pairs of the compound nerve action potential (CNAP) generating stimulation with concurrent blocking stimulation. The bottom plot shows the resulting CNAP after stimulation and blocking artifacts have been canceled out. Blocking while stimulating results in a reduced compound nerve action potential response when compared to the response shown in Figure 5.5.

I observe that the CNAP responses measured while both stimulating and blocking were smaller in amplitude than the CNAP responses measured while stimulating without blocking. Figure 5.8 shows this more directly by overlaying the CNAP responses to electrical stimulation with and without blocking stimulation applied.

CNAP Responses to Stimulation
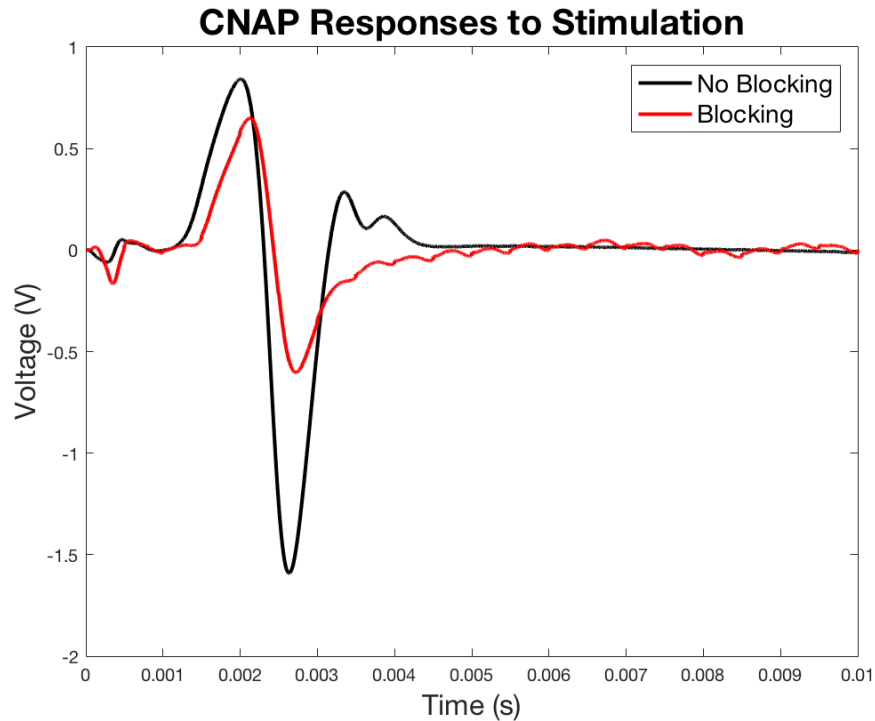
Figure 5.8: The compound nerve action potential (CNAP) response to the stimulation without concurrent blocking is noticeably higher than the CNAP response with concurrent blocking applied.

Note that when applying the blocking stimulation, the CNAP response to the stimulation that occurs between 1 and 3 ms is reduced, and the CNAP response between 3 and 4 ms is completely removed. We have been able to repeat these results in multiple trials including trials stimulating the vagus nerve, which validates the Bionode stimulation hardware's ability to block nerve signals via electrical stimulation.

5.2 Conclusion

I have validated that the Bionode's stimulation hardware is able to produce an electrical stimulation waveform that can block signals traveling down a nerve. The tools that I developed to both drive and validate electrical blocking waveforms are currently being used by members of the CID at Purdue University to explore the possibility of using blocking electrical stimulation to reduce the risk of sudden death in epilepsy.

6. SUMMARY AND CONCLUSIONS

6.1 Specific Aim 1 Conclusions

Aim 1: Design a chronic, wireless implantable device with the ability to acquire long-term cardiac, respiratory, and brain signals in freely behaving rodents as well as provide electrical stimulation to the nervous system.

The Bionode's verified ability to acquire up to four channels of chronic biopotential data from freely behaving rodents as well as concurrently stimulate and record from the nervous system has met this aim, and has also led to its widespread use in research projects at Purdue University and at other institutions. This widespread usage is further facilitated by proven fabrication and packaging methods that make the Bionode a viable low-cost, reusable, and modifiable research tool. The use of only COTS components in the Bionode's design allows all aspects of the Bionode to be replicated and/or modified by a typical university lab.

I was integrally involved in the design and testing of the analog front-end, stimulator, power management circuitry, and packaging of the Bionode. I was also the lead developer of the firmware on the implantable device as well as the graphical user interface PC application used to communicate with the Bionode. I designed the glass case and packaging techniques used to encapsulate the Bionode in our most recent successful implant procedures. I also designed and fabricated the Bionode's ECG and ECoG electrodes, which have been used in multiple projects at Purdue to collect cardiac and brain signals. I designed, fabricated, and used the respiration transducer to produce the novel dataset generated while completing Specific Aim 2.

6.2 Specific Aim 2 Conclusions

Aim 2: Acquire and analyze cardiac, respiratory, and brain signals from freely behaving rats with induced chronic epilepsy.

I used Bionodes equipped with fully implantable thermocouple transducers along with ECG and ECoG leads to measure these signals in freely behaving rats with chronically induced epilepsy by

means of the TeNT model. I built all of the implants used to acquire these signals and was directly involved in developing the implant surgical procedure. After the rats were implanted, I was in charge of all animal husbandry and data collection responsibilities, although I did receive assistance from Ethan Biggs in latter experiments. The systems I created to allow us to gather, store, translate, and synchronize all of the physiological and video data made it possible to generate a novel dataset. This novel dataset is the first dataset of its kind involving concurrent respiration, ECG, and ECoG measurements in freely behaving rats with induced chronic epilepsy. An initial analysis of the data collected during the preictal, ictal, and postictal phases shows reduced respiration during the ictal phase with increased respiration during the post-ictal phase. Additionally, in some cases, I observed short apneas during the transition from the ictal to the postictal phase. While these apneas are short, they may indicate possible SUDEP onset.

6.3   Specific Aim 3 Conclusions

Aim 3: Stimulate the nervous system via electrical stimulation to treat and/or prevent the onset of sudden death in epilepsy.

I demonstrated that a constant-current, alternating-phase stimulation waveform can open the larynx during acid-induced laryngospasms in rats when applied bilaterally to the RLNs. I was the lead developer of these RLN stimulation experiments and performed all of the surgical procedures myself with assistance from Ethan Biggs. Because laryngospasms may be a factor in SUDEP [56, 57], and acid reflux may be the trigger for some or all of those laryngospasm episodes [55], I have shown that it may be possible to treat a possible cause of sudden death in epilepsy using electrical stimulation.

I also had the initial idea that gastric acid overproduction during seizures may lead to fatal acid-induced laryngospasms. I was the lead developer of the gastric vagotomy experiments aimed at preventing sudden death in epilepsy by removing the possible mechanism leading to gastric acid overproduction during seizing activity. I have demonstrated that performing gastric vagotomies eliminated sudden death and greatly reduced incidence of acid reflux in the acute systemic KA model of epilepsy. This suggests that it may be possible to reduce incidents of sudden death in epilepsy by applying electrical blocking stimulation to the vagus nerve. Neither bilateral electrical

stimulation of the RLN nor severing the gastric nerve are easily translatable for human use. However, because both of these therapies involve modulation of branches of the vagus nerve, it may be possible to use currently available VNS devices to achieve similar results. My research has paved the way for this translational work.

APPENDIX

Bionode Manufacturing and Testing Procedure

Figure 6.1: This flow chart outlines the Bionode manufacturing and testing procedure. All steps contained in the groups of blue boxes can be done in parallel. Steps in the white boxes must be done in successive order. I used this flow chart extensively while leading a team of 4 students in the CID to coordinate the building, testing, and assembly six Bionodes.

```mermaid
flowchart

A[Populate Bionode Mainboard] --> B[Program microcontroller on mainboard]
B --> C[Test Bionode Mainboard]
C --> D[Connect Mainboard to feedthrough board]

E[Populate Feedthrough Board] --> D

D --> F[Connect Daughterboard to Mainboard and feedthrough board]

G[Populate Daughterboard] --> H[Test Daughterboard]
H --> F

F --> I[Test all four channels]
I --> J[Attach Powernode]

K[Populate Powernode exempting coils and tuning caps] --> L[Test regulated voltage output]
L --> M[Attach coils and tuning caps to powernode]
M --> N[Test regulated voltage output]
N --> J
```

Populate Bionode Mainboard

Program microcontroller on mainboard

Test Bionode Mainboard

Populate Feedthrough Board

Connect Mainboard to feedthrough board

Populate Daughterboard

Test Daughterboard

Connect Daughterboard to Mainboard and feedthrough board

Test all four channels

Populate Powernode exempting coils and tuning caps

Test regulated voltage output

Attach coils and tuning caps to powernode

Test regulated voltage output

Attach Powernode

```
                    ┌──────────────────────┐      ┌──────────────────────┐
                    │ Strip helical wire and│      │   Trim and strip     │
                    │ stuff in silicone tubes│     │  thermocouple leads  │
                    └───────────┬──────────┘       └───────────┬──────────┘
                                │                              │
┌──────────────────────┐       ▼                              ▼
│ Acquire rechargeable │   ┌──────────────────────┐     ┌──────────────────────┐
│      batteries       │   │  Connect pins to the  │     │  Crimp connectors to  │
└───────────┬──────────┘   │ ends of helical wires │     │  thermocouple leads   │
            │              └───────────┬──────────┘     └───────────┬──────────┘
            ▼                          │                            │
┌──────────────────────┐              ▼                            ▼
│  Test rechargeable   │   ┌──────────────────────┐     ┌──────────────────────┐
│      batteries       │   │ Trim and seal ends of │     │ Attach thermocouple   │
└───────────┬──────────┘   │ ECG, ECoG, and Ground │     │ lead connectors to    │
            │              │     electrodes        │     │ helical leads and coat│
            ▼              └───────────┬──────────┘     │   with parylene       │
┌──────────────────────┐              │                 └──────────────────────┘
│  Put tabs on batteries│             │
└───────────┬──────────┘              │
            │                         │
            ▼                         ▼
```

Strip helical wire and stuff in silicone tubes

Trim and strip thermocouple leads

Acquire rechargeable batteries

Connect pins to the ends of helical wires

Crimp connectors to thermocouple leads

Test rechargeable batteries

Trim and seal ends of ECG, ECoG, and Ground electrodes

Attach thermocouple lead connectors to helical leads and coat with parylene

Put tabs on batteries

Acquire ~300 gram dead rat

Attach batteries → Test battery turn on/ turn off → Connect Electrodes → Test electrodes by feeding signals in via saline bath → Tune Powernode

198

```
┌─────────────────────┐
│ Cut 17mm OD, 15mm ID│
│ glass tube into 45 mm│
│ lengths             │
└─────────────────────┘
          │
          ▼
┌─────────────────────┐
│ Seal one end of the │
│ glass case          │
└─────────────────────┘
          │
          ▼
┌─────────────────────┐
│ Rough-up inside and │
│ outside of glass tube│
│ where epoxy will adhere│
└─────────────────────┘
          │
          ▼
```

| Glue Bionode in glass case | → | Inject initial layer of silicone on top of the blocking-board and cure for 60 minutes | → | Inject initial layer of medical grade epoxy on silicone layer and cure for 60 minutes | → | Grind edge of glass tube and rub on layer of epoxy. Cure for 60 minutes | → | Connect silicone tubes for suture ties with super glue. |

Rub on two more layers of medical grade epoxy. Cure for 60 minutes each layer

Drill open suture tie holes if necessary

Submerge in saline for at least 12 hours

Turn on for final test before implanting

REFERENCES

[1]   M. M. Zack and R. Kobau, "National and state estimates of the numbers of adults and children with active epilepsy--United States, 2015.(Survey)," *Morbidity and Mortality Weekly Report,* vol. 66, no. 31, p. 821, 2017.

[2]   R. S. Fisher *et al.*, "ILAE official report: a practical clinical definition of epilepsy," *Epilepsia,* vol. 55, no. 4, pp. 475-482, 2014.

[3]   R. S. Fisher *et al.*, "The impact of epilepsy from the patient's perspective I. Descriptions and subjective perceptions," *Epilepsy Research,* vol. 41, no. 1, pp. 39-51, 2000.

[4]   M. J. Cook *et al.*, "Prediction of seizure likelihood with a long-term, implanted seizure advisory system in patients with drug-resistant epilepsy: a first-in-man study," *The Lancet. Neurology,* vol. 12, no. 6, p. 563, 2013.

[5]   S. U. Schuele and H. O. Lüders, "Intractable epilepsy: management and therapeutic alternatives," *Lancet Neurology,* vol. 7, no. 6, pp. 514-524, 2008.

[6]   M. J. Brodie, "Road to refractory epilepsy: The G lasgow story," *Epilepsia,* vol. 54, pp. 5-8, 2013.

[7]   D. J. Dlugos, "The early identification of candidates for epilepsy surgery," *Archives of neurology,* vol. 58, no. 10, pp. 1543-1546, 2001.

[8]   S. Spencer and L. Huh, "Outcomes of epilepsy surgery in adults and children," *Lancet Neurology,* vol. 7, no. 6, pp. 525-537, 2008.

[9]   G. Nune, C. DeGiorgio, and C. Heck, "Neuromodulation in the treatment of epilepsy," *Current treatment options in neurology,* vol. 17, no. 10, p. 43, 2015.

[10]   S. C. Schachter and C. B. Saper, "Vagus nerve stimulation," *Epilepsia,* vol. 39, no. 7, pp. 677-686, 1998.

[11]   C. N. Heck, "Two-year seizure reduction in adults with medically intractable partial onset epilepsy treated with responsive neurostimulation: Final results of the RNS System Pivotal trial," *Epilepsia (Series 4),* vol. 55, no. 3, pp. 432-442, 2014.

[12]   A. Handforth, "Vagus nerve stimulation therapy for partial- onset seizures: a randomized active-control trial," *Neurology,* vol. 51, no. 1, p. 48, 1998.

[13]   F. Sun, M. Morrell, and R. Wharen, "Responsive cortical stimulation for the treatment of epilepsy," *Neurotherapeutics,* vol. 5, no. 1, pp. 68-74, 2008.

[14]   J. J. Zielihski, "Epilepsy and Mortality Rate and Cause of Death," *Epilepsia,* vol. 15, no. 2, pp. 191-201, 1974.

[15]   R. Mohanraj, J. Norrie, L. J. Stephen, K. Kelly, N. Hitiris, and M. J. Brodie, "Mortality in adults with newly diagnosed and chronic epilepsy: a retrospective comparative study," *Lancet Neurology,* vol. 5, no. 6, pp. 481-487, 2006.

[16]   N. Hitiris, R. Mohanraj, J. Norrie, and M. J. Brodie, "Mortality in epilepsy," *Epilepsy and Behavior,* vol. 10, no. 3, pp. 363-376, 2007.

[17]   D. H. Lowenstein, T. Bleck, and R. L. Macdonald, "It's time to revise the definition of status epilepticus," *Epilepsia,* vol. 40, no. 1, pp. 120-122, 1999.

[18]   T. Tomson, L. Nashef, and P. Ryvlin, "Sudden unexpected death in epilepsy: current knowledge and future directions," *Lancet Neurology,* vol. 7, no. 11, pp. 1021-1031, 2008.

[19]   J. G. Boggs, "Mortality Associated with Status Epilepticus," *Epilepsy Currents,* vol. 4, no. 1, pp. 25-27, 2004.

[20]   L. Nashef, "Sudden unexpected death in epilepsy: terminology and definitions," *Epilepsia,* vol. 38, pp. S6-S8, 1997.

[21]   R. Kloster and T. Engelskjøn, "Sudden unexpected death in epilepsy (SUDEP): a clinical perspective and a search for risk factors," *Journal of Neurology, Neurosurgery & Psychiatry,* vol. 67, no. 4, pp. 439-444, 1999.

[22]   P. Ryvlin, "Incidence and mechanisms of cardiorespiratory arrests in epilepsy monitoring units (MORTEMUS): A retrospective study," *The Lancet Neurology,* vol. 12, no. 10, pp. 966-978, 2013.

[23]   C. Stöllberger and J. Finsterer, "Cardiorespiratory findings in sudden unexplained/unexpected death in epilepsy (SUDEP)," *Epilepsy Research,* vol. 59, no. 1, pp. 51-60, 2004.

[24]   E. L. So, M. C. Sam, and T. L. Lagerlund, "Postictal Central Apnea as a Cause of SUDEP: Evidence From Near-SUDEP Incident," *Epilepsia,* vol. 41, no. 11, pp. 1494-1497, 2000.

[25]   A. M. J. Ashby - Lumsden, "Ictal bradycardia and tachycardia observed in the tetanus toxin model of temporal lobe epilepsy in the freely moving rat," J. G. R. Jefferys and W.-c. Chang, Eds., ed, 2013.

[26]   W. Löscher, D. Schwartz-Porsche, H. Frey, and D. Schmidt, "Evaluation of epileptic dogs as an animal model of human epilepsy," *Arzneimittel-Forschung,* vol. 35, no. 1, pp. 82-87, 1985.

[27]   C. Á. Szabó, M. M. Leland, K. Knape, J. J. Elliott, V. Haines, and J. T. Williams, "Clinical and EEG phenotypes of epilepsy in the baboon (Papio hamadryas spp.)," *Epilepsy research,* vol. 65, no. 1-2, pp. 71-80, 2005.

[28]   T. Fitzgerald, "Comparison of research cost: man--primate animal--other animal models," *Journal of medical primatology,* vol. 12, no. 3, pp. 138-145, 1983.

[29]   S. Ishida *et al.*, "Kcna1-mutant rats dominantly display myokymia, neuromyotonia and spontaneous epileptic seizures," *Kcna1-mutant rats dominantly display myokymia, neuromyotonia and spontaneous epileptic seizures,* vol. 1435, pp. 154-166, 2012.

[30]   I. Ogiwara *et al.*, "Nav1. 1 localizes to axons of parvalbumin-positive inhibitory interneurons: a circuit basis for epileptic seizures in mice carrying an Scn1a gene mutation," *Journal of Neuroscience,* vol. 27, no. 22, pp. 5903-5914, 2007.

[31]   E. Cavalheiro, D. Riche, and G. L. G. La Salle, "Long-term effects of intrahippocampal kainic acid injection in rats: a method for inducing spontaneous recurrent seizures," *Electroencephalography and clinical neurophysiology,* vol. 53, no. 6, pp. 581-589, 1982.

[32]   J. Mellanby, "Epileptiform syndrome in rats produced by injecting tetanus toxin into the hippocampus," *Journal of Neurology, Neurosurgery & Psychiatry,* vol. 40, no. 4, pp. 404-415, 1977.

[33]   K. Sakamoto *et al.*, "Autonomic consequences of kainic acid–induced limbic cortical seizures in rats: Peripheral autonomic nerve activity, acute cardiovascular changes, and death," *Epilepsia,* vol. 49, no. 6, pp. 982-996, 2008.

[34]   J. Jefferys, "Models and mechanisms of experimental epilepsies," *Epilepsia,* vol. 44, pp. 44-50, 2003.

[35]   N. R. Temkin and G. R. Davis, "Stress as a risk factor for seizures among adults with epilepsy," *Epilepsia,* vol. 25, no. 4, pp. 450-456, 1984.

[36]   D. Young, P. A. Lawlor, P. Leone, M. Dragunow, and M. J. During, "Environmental enrichment inhibits spontaneous apoptosis, prevents seizures and is neuroprotective," *Nature medicine,* vol. 5, no. 4, p. 448, 1999.

[37]   D.-B. S. f. P. s. D. S. Group, "Deep-brain stimulation of the subthalamic nucleus or the pars interna of the globus pallidus in Parkinson's disease," *N Engl J Med,* vol. 2001, no. 345, pp. 956-963, 2001.

[38]   D. M. Labiner and G. L. Ahern, "Vagus nerve stimulation therapy in depression and epilepsy: therapeutic parameter settings," (in eng), *Acta Neurol Scand,* vol. 115, no. 1, pp. 23-33, Jan 2007.

[39]   H. A. Sackeim, "Vagus nerve stimulation (VNSTM) for treatment- resistant depression: Efficacy, side effects, and predictors of outcome," *Neuropsychopharmacology,* vol. 25, no. 5, pp. 713-729, 2001.

[40]   J. Luigjes, "Deep brain stimulation in addiction: a review of potential brain targets," *Molecular Psychiatry,* vol. 17, no. 6, p. 572, 2012.

[41]   M. J. Kane, P. P. Breen, F. Quondamatteo, and O. L. G, "BION microstimulators: a case study in the engineering of an electronic implantable medical device," *Med Eng Phys,* vol. 33, no. 1, pp. 7-16, Jan 2011.

[42]   M. Weiergräber, M. Henry, J. Hescheler, N. Smyth, and T. Schneider, "Electrocorticographic and deep intracerebral EEG recording in mice using a telemetry system," *Brain Research Protocols,* vol. 14, no. 3, pp. 154-164, 2005.

[43]   H. Kassiri *et al.*, "Battery-less Tri-band-Radio Neuro-monitor and Responsive Neurostimulator for Diagnostics and Treatment of Neurological Disorders," *IEEE Journal of Solid-State Circuits,* vol. 51, no. 5, pp. 1274-1289, 2016.

[44]   Q. Xu, D. Hu, B. Duan, and J. He, "A Fully Implantable Stimulator With Wireless Power and Data Transmission for Experimental Investigation of Epidural Spinal Cord Stimulation," *IEEE Trans Neural Syst Rehabil Eng,* vol. 23, no. 4, pp. 683-92, Jul 2015.

[45]   R. G. Dennis, D. E. Dow, and J. A. Faulkner, "An implantable device for stimulation of denervated muscles in rats," *Medical Engineering and Physics,* vol. 25, no. 3, pp. 239-253, 2003.

[46]   S. G. Ewing, W. J. Lipski, A. A. Grace, and C. Winter, "An inexpensive, charge- balanced rodent deep brain stimulation device: A step-by- step guide to its procurement and construction," *Journal of Neuroscience Methods,* vol. 219, no. 2, pp. 324-330, 2013.

[47]   A. Lundt *et al.*, "EEG Radiotelemetry in Small Laboratory Rodents: A Powerful State-of-the Art Approach in Neuropsychiatric, Neurodegenerative, and Epilepsy Research," *Neural Plasticity,* vol. 2016, 2016.

[48]   A. Sgoifo, D. Stilli, D. Medici, P. Gallo, B. Aimi, and E. Musso, "Electrode positioning for reliable telemetry ECG recordings during social stress in unrestrained rats," *Physiology & behavior,* vol. 60, no. 6, pp. 1397-1401, 1996.

[49]   K. Aminian, X. Thouvenin, P. Robert, J. Seydoux, and L. Girardier, "A piezoelectric belt for cardiac pulse and respiration measurements on small mammals," in *Engineering in Medicine and Biology Society, 1992 14th Annual International Conference of the IEEE*, 1992, vol. 6, pp. 2663-2664: IEEE.

[50]   W. I. Welker, "Analysis of Sniffing of the Albino Rat," *Behaviour,* vol. 22, no. 3-4, pp. 223-244, 1964.

[51]   M. M. Kabir, "Respiratory pattern in awake rats: Effects of motor activity and of alerting stimuli," *Physiology & Behavior,* vol. 101, no. 1, pp. 22-32, 2010.

[52]   A. National Research Council . Committee for the Update of the Guide for the Care and Use of Laboratory, *Guide for the care and use of laboratory animals*, 8th ed.. ed. Washington, D.C.: Washington, D.C. : National Academies Press, 2011.

[53]   E. Eisman, "Measurement of Respiratory Rate in the Unrestrained Rat," *Psychophysiology,* vol. 1, no. 4, pp. 360-363, 1965.

[54]   A. Kepecs, N. Uchida, and Z. F. Mainen, "Rapid and precise control of sniffing during olfactory discrimination in rats," *Journal of neurophysiology,* vol. 98, no. 1, p. 205, 2007.

[55]   R. B. Budde, M. A. Arafat, D. J. Pederson, T. A. Lovick, J. G. R. Jefferys, and P. P. Irazoqui, "Acid reflux induced laryngospasm as a potential mechanism of sudden death in epilepsy," *Epilepsy Research,* vol. 148, pp. 23-31, 2018.

[56]   K. Nakase *et al.*, "Laryngospasm, central and obstructive apnea during seizures: Defining pathophysiology for sudden death in a rat model," *Epilepsy Research,* vol. 128, pp. 126-139, 2016.

[57]   N. Lacuey, L. Vilella, J. P. Hampson, J. Sahadevan, and S. D. Lhatoo, "Ictal laryngospasm monitored by video-EEG and polygraphy: a potential SUDEP mechanism," *Epileptic Disorders,* vol. 20, no. 2, pp. 146-150, 2018.

[58]   C. J. Loughlin *et al.*, "Acid-Induced Laryngospasm in a Canine Model," *Laryngoscope,* vol. 106, no. 12, pp. 1506-1509, 1996.

[59]   M. A. Rex, "A review of the structural and functional basis of laryngospasm and a discussion of the nerve pathways involved in the reflex and its clinical significance in man and animals," *British journal of anaesthesia,* vol. 42, no. 10, p. 891, 1970.

[60]   M. Suzuki and C. T. Sasaki, "Laryngeal spasm: a neurophysiologic redefinition," *Annals of Otology, Rhinology & Laryngology,* vol. 86, no. 2, pp. 150-157, 1977.

[61]   F. E. Babl, J. Grindlay, and M. J. Barrett, "Laryngospasm With Apparent Aspiration During Sedation With Nitrous Oxide," *Annals of Emergency Medicine,* vol. 66, no. 5, pp. 475-478, 2015.

[62]   D. Hampson-Evans, P. Morgan, and M. Farrar, "Pediatric laryngospasm," *Pediatric Anesthesia,* vol. 18, no. 4, pp. 303-307, 2008.

[63]   D. Maceri and S. Zim, "Laryngospasm: An atypical manifestation of severe gastroesophageal reflux disease (GERD)," *Laryngoscope,* vol. 111, no. 11, pp. 1976-1979, 2001.

[64]   M. M. S. Roland, A. S. Baran, and A. C. Richert, "Sleep-related laryngospasm caused by gastroesophageal reflux," *Sleep Medicine,* vol. 9, no. 4, pp. 451-453, 2008.

[65]   H. J. Gdynia, J. Kassubek, and A. D. Sperfeld, "Laryngospasm in neurological diseases," *Neurocritical Care,* vol. 4, no. 2, pp. 163-167, 2006.

[66]   G. Fourcade, G. Castelnovo, D. Renard, and P. Labauge, "Laryngospasm as preceding symptom of amyotrophic lateral sclerosis," *Official Journal of the European Neurological Society,* vol. 257, no. 11, pp. 1929-1930, 2010.

[67]   E. Caietta *et al.*, "Diagnosis and outcome of SCN4A-related severe neonatal episodic laryngospasm (SNEL): 2 new cases," *Pediatrics,* vol. 132, no. 3, p. e784, 2013.

[68]   R. R. Singh, S. V. Tan, M. G. Hanna, S. A. Robb, A. Clarke, and H. Jungbluth, "Mutations in SCN4A: a rare but treatable cause of recurrent life-threatening laryngospasm," *Pediatrics,* vol. 134, no. 5, p. e1447, 2014.

[69]   J. J. Ardesch, J. R. Sikken, P. H. Veltink, v. d. H. E. Aa, G. Hageman, and H. P. J. Buschman, "Vagus nerve stimulation for epilepsy activates the vocal folds maximally at therapeutic levels," pp. 227-1211, 2010.

[70]   D. S. Lundy, R. R. Casiano, H. J. Landy, J. Gallo, B. Gallo, and R. Eugene Ramsey, "Effects of vagal nerve stimulation on laryngeal function," *Journal of Voice,* vol. 7, no. 4, pp. 359-364, 1993.

[71]   R. El Tahry *et al.*, "Repeated assessment of larynx compound muscle action potentials using a self-sizing cuff electrode around the vagus nerve in experimental rats," *Journal of Neuroscience Methods,* vol. 198, no. 2, pp. 287-293, 2011.

[72]   K. Vanschandevijl *et al.*, "Functional electrical stimulation of the left recurrent laryngeal nerve using a vagus nerve stimulator in a normal horse," *The Veterinary Journal,* vol. 189, no. 3, pp. 346-348, 2011.

[73]   R. L. Crumley, "Unilateral recurrent laryngeal nerve paralysis," *Journal of Voice,* vol. 8, no. 1, pp. 79-83, 1994.

[74]   K. Inagi, E. Schultz, and C. N. Ford, "An Anatomic Study of the Rat Larynx: Establishing the Rat Model for Neuromuscular Function," *Otolaryngology- Head and Neck Surgery,* vol. 118, no. 1, pp. 74-81, 1998.

[75]   T. Lin and R. Alphin, "Cephalic phase of gastric secretion in the rat," *American Journal of Physiology-Legacy Content,* vol. 192, no. 1, pp. 23-26, 1957.

[76]   T. Noto, M. Nagasaki, and T. Endo, "Role of vagus nerves and gastrin in the gastric phase of acid secretion in male anesthetized rats," *American Journal of Physiology-Gastrointestinal and Liver Physiology,* vol. 272, no. 2, pp. G335-G339, 1997.

[77]   K. Lloyd, H. Raybould, Y. Tache, and J. Walsh, "Role of gastrin, histamine, and acetylcholine in the gastric phase of acid secretion in anesthetized rats," *American Journal of Physiology-Gastrointestinal and Liver Physiology,* vol. 262, no. 4, pp. G747-G755, 1992.

[78]   H. Debas and S. H. Carvajal, "Vagal regulation of acid secretion and gastrin release," *The Yale journal of biology and medicine,* vol. 67, no. 3-4, p. 145, 1994.

[79]   D. Grundy and T. Scratcherd, "Effect of stimulation of the vagus nerve in bursts on gastric acid secretion and motility in the anaesthetized ferret," *The Journal of physiology,* vol. 333, p. 451, 1982.

[80]   R. A. Hatcher, "The mechanism of vomiting," *Physiological Reviews,* vol. 4, no. 3, pp. 479-504, 1924.

[81]   N. Takeda, S. Hasegawa, M. Morita, and T. Matsunaga, "Pica in rats is analogous to emesis: An animal model in emesis research," *Pharmacology, Biochemistry and Behavior,* vol. 45, no. 4, pp. 817-821, 1993.

[82]   H. K. G. C. Y. S. F. Y. T. A. N. Omura, "Establishment of Surgically Induced Chronic Acid Reflux Esophagitis in Rats," *Scandinavian Journal of Gastroenterology,* vol. 34, no. 10, pp. 948-953, 1999.

[83]   S. Montedonico, J. A. Diez-Pardo, and J. A. Tovar, "Gastroesophageal reflux after combined lower esophageal sphincter and diaphragmatic crural sling inactivation in the rat," *Digestive diseases and sciences,* vol. 44, no. 11, pp. 2283-2289, 1999.

[84]   C. Soto, B. Qi, J. A. Diez-Pardo, and J. A. Tovar, "Identification of diaphragmatic crural component of gastroesophageal barrier in the rat," *Digestive diseases and sciences,* vol. 42, no. 12, pp. 2420-2425, 1997.

[85]   T. L. Powley, J. M. Gilbert, E. A. Baronowsky, C. N. Billingsley, F. N. Martin, and R. J. Phillips, "Vagal sensory innervation of the gastric sling muscle and antral wall: implications for gastro-esophageal reflux disease?.(Report)," *Neurogastroenterology and Motility,* vol. 24, 2012.

[86]   A. Hanson, "Why rats can't vomit," *Rat Behavior and Biology,* May 20, 2005 [October 23, 2018]. http://www.ratbehavior.org/vomit.htm

[87]   K. S. Eggleston, B. D. Olin, and R. S. Fisher, "Ictal tachycardia: the head–heart connection," *Seizure,* vol. 23, no. 7, pp. 496-505, 2014.

[88] D. Marshall, B. Westmoreland, and F. Sharbrough, "Ictal tachycardia during temporal lobe seizures," in *Mayo Clinic Proceedings*, 1983, vol. 58, no. 7, pp. 443-446.

[89] O. Devinsky, "Effects of seizures on autonomic and cardiovascular function," *Epilepsy currents,* vol. 4, no. 2, pp. 43-46, 2004.

[90] L. A. Will, J. R. Leininger, and K. J. Donham, "Regurgitation and choke in rats," *Regurgitation and choke in rats,* vol. 49, no. 11, pp. 360-361, 1979.

[91] R. L. Dragstedt, V. P. Harper, B. E. Tovee, and R. E. Woodward, "SECTION OF THE VAGUS NERVES TO THE STOMACH IN THE TREATMENT OF PEPTIC ULCER," *Annals of Surgery,* vol. 126, no. 5, pp. 687-708, 1947.

[92] R. F. Yazıcıoğlu, *Biopotential readout circuits for portable acquisition systems*. Dordrecht]: Dordrecht : Springer, 2009.

[93] R. Schaumann, *Design of analog filters*, 2nd ed.. ed. New York: New York : Oxford University Press, 2010.

[94] R. F. Coughlin, *Operational amplifiers and linear integrated circuits*, 4th ed.. ed. Englewood Cliffs, N.J.: Englewood Cliffs, N.J. : Prentice Hall, 1991.

[95] T. August, M. Harvey, P. Lightfoot, D. Kilbey, T. Papadopoulos, and P. Jepson, "Emerging technologies for biological recording," *Biological Journal of the Linnean Society,* vol. 115, no. 3, pp. 731-749, 2015.

[96] S. Nag and N. V. Thakor, "Implantable neurotechnologies: electrical stimulation and applications," *Medical & Biological Engineering & Computing,* vol. 54, no. 1, pp. 63-76, Jan 2016.

[97] A. C. Thompson, P. R. Stoddart, and E. D. Jansen, "Optical stimulation of neurons," *Current molecular imaging,* vol. 3, no. 2, pp. 162-177, 2014.

[98] S. T. Lee, P. A. Williams, C. E. Braine, D. T. Lin, S. W. John, and P. P. Irazoqui, "A Miniature, Fiber-Coupled, Wireless, Deep-Brain Optogenetic Stimulator," *IEEE Trans Neural Syst Rehabil Eng,* vol. 23, no. 4, pp. 655-64, Jul 2015.

[99] J. E. Arle, *Essential Neuromodulation*. Burlington: Burlington : Elsevier Science, 2011.

[100] D. R. Merrill, M. Bikson, and J. G. R. Jefferys, "Electrical stimulation of excitable tissue: design of efficacious and safe protocols," *Journal of Neuroscience Methods,* vol. 141, no. 2, pp. 171-198, 2005.

[101] "AN-1515 A Comprehensive Study of the Howland Current Pump," Texas Instruments2013.

[102] U.S.G.S., "PhreeqC," *Hydrochemistry software*.

[103] H. M. Brace, J. G. R. Jefferys, and J. Mellanby, "Long-term changes in hippocampal physiology and leaning ability of rats after intrahippocampal tetanus toxin," *Journal of Physiology,* vol. 368, pp. 343-57, 1985.

[104] J. G. Proakis, *Digital signal processing*, 4th ed.. ed. Upper Saddle River, N.J.: Upper Saddle River, N.J. : Pearson Prentice Hall, 2007.

[105] A. B. Amar, A. B. Kouki, and H. Cao, "Power Approaches for Implantable Medical Devices," *Sensors (Basel),* vol. 15, no. 11, pp. 28889-914, 2015.

[106] H. Mei and P. P. Irazoqui, "Miniaturizing Wireless Implants," *Nature Biotechnology,* vol. 32, no. 10, pp. 1008-1010, Oct 2014.

[107] A. Kim, "Acoustically powered wireless medical implants," *Purdue University. Electrical and Computer Engineering,* Electronic Resource (97 pages).

[108] H. Mei, K. Thackston, R. Bercich, J. Jefferys, and P. Irazoqui, "Cavity Resonator Wireless Power Transfer System for Freely Moving Animal Experiments," *IEEE Trans Biomed Eng,* Jun 07 2016.

[109] H. Mei, Y. W. Huang, K. A. Thackston, and P. P. Irazoqui, "Optimal Wireless Power Transfer to Systems in an Enclosed Resonant Cavity," *IEEE Antennas and Wireless Propagation Letters,* vol. 15, pp. 1036-1039, 2016.

[110] K. A. Thackston, "Optimization of wireless power networks for biomedical applications," *Purdue University. Biomedical Engineering,* (electronic resource).

[111] D. J. Dohyuk Ha, W. J. Tsung-Chieh Lee, W. J. Webery, and W. J. Chappell, "Power distribution to multiple implanted sensor devices using a multiport bandpass filter (BPF) approach," ed, 2014, pp. 1-4.

[112] T. C. Beh, M. Kato, T. Imura, S. Oh, and Y. Hori, "Automated Impedance Matching System for Robust Wireless Power Transfer via Magnetic Resonance Coupling," *IEEE Transactions on Industrial Electronics,* vol. 60, no. 9, pp. 3689-3698, 2013.

[113] J. P. Somann, "A Study of Techniques of Vagus Nerve Stimulation for Treatment of Inflamation, (PhD diss.)," *Purdue University,* 2018.

[114] K. Stokes, "The biocompatibility and biostability of new cardiovascular materials and devices," in *Implantable Neural Prostheses 2*: Springer, 2009, pp. 1-26.

[115] G. Jiang and D. D. Zhou, "Technology advances and challenges in hermetic packaging for implantable medical devices," in *Implantable Neural Prostheses 2*: Springer, 2009, pp. 27-61.

[116] F. Boeser, J. S. Ordonez, M. Schuettler, T. Stieglitz, and D. T. Plachta, "Non-hermetic encapsulation for implantable electronic devices based on epoxy," in *Engineering in Medicine and Biology Society (EMBC), 2015 37th Annual International Conference of the IEEE*, 2015, pp. 809-812: IEEE.

[117] C. K. Bjune *et al.*, "Package architecture and component design for an implanted neural stimulator with closed loop control," in *Engineering in Medicine and Biology Society (EMBC), 2015 37th Annual International Conference of the IEEE*, 2015, pp. 7825-7830: IEEE.

[118] P. Wang *et al.*, "Long-term evaluation of a non-hermetic micropackage technology for MEMS-based, implantable pressure sensors," in *Solid-State Sensors, Actuators and Microsystems (TRANSDUCERS), 2015 Transducers-2015 18th International Conference on*, 2015, pp. 484-487: IEEE.

[119] L. Lonys *et al.*, "Silicone rubber encapsulation for an endoscopically implantable gastrostimulator," *Medical & biological engineering & computing,* vol. 53, no. 4, pp. 319-329, 2015.

[120] A. Kalaijakis, "Medical device interconnects must address harsh environments and durability challenges.(The Main Circuit)," *ECN-Electronic Component News,* vol. 55, no. 7, p. 20, 2011.

[121] S. Grob, P. A. Tass, and C. Hauptmann, "Capacitive Feedthroughs for Medical Implants," *Frontiers in neuroscience,* vol. 10, p. 404, 2016.

[122] R. Stevenson, "Feedthrough EMI filter with ground isolation for cardiac pacemakers and implantable cardioverter defibrillators," in *Engineering in Medicine and Biology Society, 1998. Proceedings of the 20th Annual International Conference of the IEEE*, 1998, vol. 6, pp. 3319-3323: IEEE.

[123] M. J. Kane, P. P. Breen, F. Quondamatteo, and G. ÓLaighin, "BION microstimulators: A case study in the engineering of an electronic implantable medical device," *Medical engineering & physics,* vol. 33, no. 1, pp. 7-16, 2011.

[124] J. R. Lachapelle *et al.*, "An implantable, designed-for-human-use peripheral nerve stimulation and recording system for advanced prosthetics," in *Engineering in Medicine and Biology Society (EMBC), 2016 IEEE 38th Annual International Conference of the*, 2016, pp. 1794-1797: IEEE.

[125] S. F. Hulbert, F. A. Young, R. S. Mathews, J. J. Klawitter, C. D. Talbert, and F. H. Stelling, "Potential of ceramic materials as permanently implantable skeletal prostheses," *Journal of Biomedical Materials Research,* vol. 4, no. 3, pp. 433-456, 1970.

[126] Q. Xu, J. Li, W. Han, and H. Zhou, "A fully implantable stimulator with wireless power and data transmission for experimental use in epidural spinal cord stimulation," in *2011 Annual International Conference of the IEEE Engineering in Medicine and Biology Society*, 2011, pp. 7230-7233: IEEE.

[127] A. Lay-Ekuakille, G. Griffo, A. Massaro, F. Spano, and G. Gigli, "Experimental characterization of an implantable neuro-packaging for EEG signal recording and measurement," *Measurement,* vol. 79, pp. 321-330, 2016.

[128] A. Örnberg, J. Pan, M. Herstedt, and C. Leygraf, "Corrosion resistance, chemical passivation and metal release of 35N LT and MP35N for biomedical material application," *Journal Of The Electrochemical Society,* vol. 154, no. 9, pp. C546-C551, 2007.

[129] S. Clarke, J. Panksepp, and J. Trowill, "A method of recording sniffing in the free-moving rat," *Physiology & Behavior,* vol. 5, no. 1, pp. 125-126, 1970.

[130] J. G. Jefferys, "Chronic focal epilepsy induced by intracerebral tetanus toxin," *Italian Journal Of Neurological Sciences,* vol. 16, no. 1-2, p. 27, 1995.

[131] J. G. Jefferys, "Physiological and behavioural consequences of seizures induced in the rat by intrahippocampal tetanus toxin," *Brain: A Journal Of Neurology,* vol. 110 (Pt 2), p. 517, 1987.

[132] L. P. Tilley, *ECG for the small animal practitioner* (ECG electrocardiography for the small animal practioner). Jackson, Wyo.: Jackson, Wyo. : Teton NewMedia, 1999.

[133] G. Paxinos, "C., Watson (1986) The Rat Brain in Stereotaxic Coordinates," *New York: Academic*.

[134] R. M. Rangayyan, *Biomedical signal analysis*, Second edition.. ed. (Biomedical signal analysis, second edition). Hoboken, New Jersey : IEEE Press : Wiley, 2015.

[135] D. Dubin, *Rapid Interpretation of EKG's*. Cover Publishing Company Tampa (FL), 1996.

[136] W. Franks, I. Schenker, P. Schmutz, and A. Hierlemann, "Impedance characterization and modeling of electrodes for biomedical applications," *IEEE Transactions on Biomedical Engineering,* vol. 52, no. 7, pp. 1295-1302, 2005.

[137] P. Welch, "The use of fast Fourier transform for the estimation of power spectra: A method based on time averaging over short, modified periodograms," *Audio and Electroacoustics, IEEE Transactions on,* vol. 15, no. 2, pp. 70-73, 1967.

[138] G. T. Finnerty and J. G. Jefferys, "9-16 Hz oscillation precedes secondary generalization of seizures in the rat tetanus toxin model of epilepsy," *Journal of neurophysiology,* vol. 83, no. 4, p. 2217, 2000.

[139] R. W. Berg, D. Whitmer, and D. Kleinfeld, "Exploratory whisking by rat is not phase locked to the hippocampal theta rhythm," *The Journal of neuroscience : the official journal of the Society for Neuroscience,* vol. 26, no. 24, p. 6518, 2006.

[140] J. Pan and W. J. Tompkins, "A real-time QRS detection algorithm," *IEEE Trans. Biomed. Eng,* vol. 32, no. 3, pp. 230-236, 1985.

[141] A. M. Saleh *et al.*, "Repeated focal seizures induced by intrahippocampal tetanus toxin leads to prolonged QT interval and altered cardiac expression of mitochondrial and calcium homoeostasis proteins.," 2018 (In preparation).

[142] F. Snyder, J. A. Hobson, D. F. Morrison, and F. Goldfrank, "CHANGES IN RESPIRATION, HEART RATE, AND SYSTOLIC BLOOD PRESSURE IN HUMAN SLEEP," *Journal of applied physiology,* vol. 19, pp. 417-422, 1964.

[143] F. L. Eldridge, D. E. Millhorn, and T. G. Waldrop, "Exercise Hyperpnea and Locomotion: Parallel Activation from the Hypothalamus," *Science,* vol. 211, no. 4484, pp. 844-846, 1981.

[144] J. O. Holloszy, "Biochemical adaptations in muscle effects of exercise on mitochondrial oxygen uptake and respiratory enzyme activity in skeletal muscle," *Journal of biological chemistry,* vol. 242, no. 9, pp. 2278-2282, 1967.

[145] E. C. Wirrell, E. A. Armstrong, L. D. Osman, and J. Y. Yager, "Prolonged seizures exacerbate perinatal hypoxic-ischemic brain damage," *Pediatric research,* vol. 50, no. 4, p. 445, 2001.

[146] R. DeLorenzo *et al.*, "A prospective, population-based epidemiologic study of status epilepticus in Richmond, Virginia," *Neurology,* vol. 46, no. 4, pp. 1029-1035, 1996.

[147] D. M. Treiman *et al.*, "A comparison of four treatments for generalized convulsive status epilepticus," *New England Journal of Medicine,* vol. 339, no. 12, pp. 792-798, 1998.

[148] N. Mor *et al.*, "Quantitative Video Laryngoscopy to Monitor Recovery from Recurrent Laryngeal Nerve Injury in the Rat," *Otolaryngology–Head and Neck Surgery,* vol. 150, no. 5, pp. 824-826, 2014.

[149] S. G. Duke, G. Postma, W. McGuirt, D. Ririe, D. Averill, and J. Koufman, "Laryngospasm and diaphragmatic arrest in immature dogs after laryngeal acid exposure: A possible model for sudden infant death syndrome," *Ann. Otol. Rhinol. Laryngol.,* vol. 110, no. 8, pp. 729-733, 2001.

[150] M. J. Pitman, P. Weissbrod, R. Roark, S. Sharma, and S. D. Schaefer, "Electromyographic and histologic evolution of the recurrent laryngeal nerve from transection and anastomosis to mature reinnervation," *Laryngoscope,* vol. 121, no. 2, pp. 325-331, 2011.

[151] W. Liddy *et al.*, "The electrophysiology of thyroid surgery: electrophysiologic and muscular responses with stimulation of the vagus nerve, recurrent laryngeal nerve, and external branch of the superior laryngeal nerve," *Laryngoscope,* vol. 127, no. 3, pp. 764-771, 2017.

[152] C. W. Wu *et al.*, "Investigation of optimal intensity and safety of electrical nerve stimulation during intraoperative neuromonitoring of the recurrent laryngeal nerve: A prospective porcine model," *Head & Neck,* vol. 32, no. 10, pp. 1295-1301, 2010.

[153] I. Naggar and M. Stewart, "A rat model for exploring the contributions of ventricular arrhythmias to sudden death in epilepsy," in *Sudden Unexpected Death in Epilepsy: Mechanisms and New Methods for Analyzing Risks*: Taylor & Francis Boca Raton, FL, 2015, pp. 241-250.

[154] G. Barnard, "A new test for 2× 2 tables," *Nature,* vol. 156, p. 177, 1945.

[155] L. H. Tsai and J. Y. Wu, *Glutamate receptors in the stomach and their implications*. 2005, pp. 179-190.

[156] Y. Watanabe, T. Okumura, A. Uehara, and K. Tsuji, "Kainic acid injection into medullary raphe produces gastric lesions through the vagal system in rats," *American Journal of Physiology,* vol. 27, no. 4, p. G655, 1993.

[157] H. Kaneko, H. Yang, G. Ohning, and Y. Tache, "Medullary TRH is involved in gastric protection induced by low dose of kainic acid into the raphe pallidus," *American Journal of Physiology - Gastrointestinal and Liver Physiology,* vol. 268, no. 4, pp. G548-G552, 1995.

[158] J. F. Téllez-Zenteno, S. Matijevic, and S. Wiebe, "Somatic comorbidity of epilepsy in the general population in Canada," *Epilepsia,* vol. 46, no. 12, pp. 1955-1962, 2005.

[159] D. A. Wilson, A. M. Malek, J. L. Wagner, B. B. Wannamaker, and A. W. Selassie, "Mortality in people with epilepsy: A statewide retrospective cohort study," *Epilepsy Research,* vol. 122, pp. 7-14, 2016.

[160] K. Kilgore and N. Bhadra, "Nerve conduction block utilising high-frequency alternating current," *Medical and Biological Engineering and Computing,* vol. 42, no. 3, pp. 394-406, 2004.

[161] N. Bhadra, N. Bhadra, K. Kilgore, and K. J. Gustafson, "High frequency electrical conduction block of the pudendal nerve," *High frequency pudendal nerve block,* vol. 3, no. 2, pp. 180-187, 2006.

[162] M. P. Ward, K. Y. Qing, K. J. Otto, R. M. Worth, S. W. M. John, and P. P. Irazoqui, "A Flexible Platform for Biofeedback- Driven Control and Personalization of Electrical Nerve Stimulation Therapy," *Neural Systems and Rehabilitation Engineering, IEEE Transactions on,* vol. 23, no. 3, pp. 475-484, 2015.

[163] D. Purves, *Neuroscience*, 3rd ed.. ed. Sunderland, Mass.: Sunderland, Mass. : Sinauer Associates, Publishers, 2004.

VITA

Daniel Pederson has been working toward his PhD in the Electrical and Computer Engineering Department at Purdue University since August 2013. His focus at Purdue has been studying epilepsy using medical implantable devices. Daniel was born and raised in Pomeroy, Washington, and attended Washington State University (WSU) in Pullman, Washington where he obtained B.S. degrees in both Computer Engineering and Bioengineering. After graduating from WSU in 2008, Daniel worked for a startup company called NeuroVista in Seattle, Washington that was developing a Class III medical implantable device for seizure prediction in patients with epilepsy. It was at this time that Daniel dedicated his professional career to studying and treating epilepsy. After NeuroVista closed its doors due to insufficient funding in 2012, Daniel applied for and was accepted into the PhD program in the department of Electrical and Computer Engineering at Purdue University with the intent of continuing his work in the field of epilepsy. In 2014, Daniel was awarded an NSF Graduate Research Fellowship that funded the next three years of his research. He was subsequently awarded the Purdue Bilsland Dissertation Fellowship to fund his remaining year of research at Purdue.

Upon graduating from Purdue University, Daniel plans to return to industry and continue working on implantable devices for the treatment of epilepsy in the Seattle, Washington area. He also plans to teach engineering classes at local colleges and universities wherever he lives.